Annual to Millennial Scale Oxygen Minimum Zone Expansion on the Southern California Margin: Proxies and Drivers

by

Yi Wang

A dissertation submitted in partial fulfillment
of the requirements for the degree of
Doctor of Philosophy
(Earth and Environmental Sciences)
in the University of Michigan
2020

Doctoral Committee:

Professor Ingrid L. Hendy, Chair
Professor Brian K. Arbic
Professor Julia E. Cole
Associate Professor Rose M. Cory
Associate Professor Gregory Dick
Assistant Professor Brian R. Ellis
Professor Nathan D. Sheldon

Yi Wang

ellawang@umich.edu

ORCID iD: 0000-0001-5633-3312

Dedication

This dissertation is dedicated to my late grandma who genuinely supported me.

Acknowledgements

Firstly, I would like to thank Ingrid for taking me as a student, providing me with an opportunity of studying paleoceanography, being patient in teaching me, and constantly pushing me to deal with new challenges (and deadlines!). Thank you for encouraging me to step out of my comfort zone, developing my own ideas, and bringing them to fruition. I would also like to thank my committee – Brian Arbic, Julie, Rose, Greg, Brian Ellis, and Nathan – for their guidance and all the encouragement during my committee meetings. I especially want to thank Rose and Julie for their help in my postdoc applications and inspiring conversations both on academics and life. I would also like to thank my co-authors: Dario Bilardello, Jen Latimer, Bob Thunell, and Jiang Zhu, who have broadened my knowledge, provided technical support, and read my drafts for many times.

My thesis would never be done without many hands that help. Special thanks to Angela Dial who taught me how to run mass spec and be a meticulous analytical chemist. Without her taking care of the mass specs I would never be able to finish running through my analyses in months. I want to thank Tiffany, Allie, and Tim for teaching me how to process bulk sediments and show me how to run Fe speciation. Thanks to two undergrads, Alex and Madeline, who helped me grind and load many, many samples for organic carbon analyses.

Everyone in the Hendy, Sheldon, and Smith lab has been supportive as officemates. I want to thank Allie Tessin, Tiffany Napier, Katy Rico, Xiaojing Du, Mark Robbins, Madelyn Cook, Molly Ng, Becca Dzombak, and Bekah Stein for reading my manuscripts and providing suggestions for my presentations. I've thrown you with many long drafts and thank you all for giving insightful advice that helped me improve them. Many thanks to my new friends at the University of Michigan for being so supportive during my PhD. Thanks to Youngjae Kim, Phoebe Aron, Jenny Bowen, Molly Ng, Sooyeon Kim, Jackie Wrage, Alice Zhou, Chrissie Nims, Li Guan, Yang Qu, and Yuan Zhang for the encouragement, discussions, and fun. Special thank you to the Chinese community in this department (Xiaofei Pu, Hong (Dora) Shen, Bian Wang, Sha Chen, Guolei Han, Yanhan Si, Meichen Liu, Xue Su, and Chengwei Zhang) who has

organized many group activities (parties, board games, and room escapes!) and allows me to have some place to complain about life.

Last but not the least, I would like to thank my family to whom this thesis is dedicated to, especially my grandma who I missed the last chance of seeing almost five years ago and grandpa who took care of me in my childhood. Thanks to my parents who always support me to chase after what I determined to. Thank you to Yi Niu, my partner, for simply staying with me and listening to me when I feel hopeless during my last year. More importantly, thanks for reading half of my thesis within two days and serving as the proofreading person for me.

Acknowledgement is made to the National Science Foundation, the University of Michigan Rackham Graduate School, and the University of Michigan Earth and Environmental Sciences Department for funding that made this work possible.

Table of Contents

List of Tables

List of Figures

List of Appendices

Abstract

The limited timespan (several decades) of dissolved oxygen (DO) instrumental records precludes a complete picture of how DO in seawater have changed in the past, and thus high-resolution paleo-DO reconstructions are essential for revealing DO variability on centennial to millennial timescales. A rapid and simultaneous bulk sediment elemental analysis method for determining multiple elemental concentrations was thus developed for future high-resolution paleoceanographic reconstructions in **Chapter 2**. To identify appropriate redox proxies minimizing post-depositional overprints, we applied Fe speciation to quantify reactive Fe towards sulfide. The results were cross-validated using magnetic analyses that characterize preserved Fe phases. We confirmed in **Chapter 3** that instantaneous depositional events (e.g., flood and turbidite layers) could initiate post-depositional pyrite formation, and result in 'false-positive' sulfidic (no DO and HS^- present) interpretations, compromising redox reconstructions. In contrast, redox-sensitive trace metals (Re, Mo, and U) seem to be unaffected by instantaneous depositional events. A post-Industrial oxygenation history was then constructed from redox-sensitive trace metal records from the Santa Barbara Basin (SBB), Southern California in **Chapter 4**. We demonstrated that the gradually intensified Southern California OMZ since the 20^{th} century is associated with the anthropogenic warming.

To further explore the natural variability on multi-centennial to millennial timescales, I explored a Common Era core (~2 – 5 year resolution) in SBB. Bulk sedimentary N isotopic composition was reconstructed in **Chapter 5**, which revealed competing tropical and subarctic waters that transport nitrate to Southern California. We confirmed more tropical water influences during the Medieval Climate Anomaly (MCA, 1000 – 1100 CE). However, stronger connections with the subarctic water transport during the Little Ice Age (LIA, 1670 – 1840 CE) coincided with the strongest Aleutian Low (AL), suggesting nitrogen cycling responses to atmospheric forcing. In **Chapter 6**, we generated the highest-resolution DO record (4 – 9 years) to date in the North Pacific using the same core, which revealed the lowest DO during the MCA corresponding to the warmest pre-Industrial interval in the Common Era. The natural OMZ deoxygenation rates

were significantly faster than the post-Industrial reconstruction in Chapter 4, suggesting that the post-Industrial OMZ intensification is not unprecedented. Additionally, a low-oxygen interval during the cold LIA (1550 – 1750 CE) was inconsistent with either climate or productivity. We suggest that this low-oxygen interval was due to less ventilated North Pacific Intermediate Water (NPIW) that propagates to the east. A comparison of proxies (sea ice, oxygenation, and AL proxies) and the Last Millennium Reanalysis corroborates that a weaker/westward AL and weakened Siberian High resulted in weaker wind stress and prevailing easterlies over the Sea of Okhotsk, reducing the sea ice production and NPIW ventilation despite the relatively cold period.

A similar oxygenation response to atmospheric teleconnections was indicated for the Holocene in **Chapter 7,** with much lower DO in the early- to mid-Holocene (~6 ka before present) than the post-Industrial. A state-of-the-art model corroborates basin-wide low DO responses due to NPIW oxygenation changes that are associated with reduced sea ice brine rejection tying to a weakened AL under mid-Holocene orbital forcing. These results demonstrate a nuanced mid-depth ventilation and OMZ response to climate change in the Holocene, and underline the role of atmospheric circulation in controlling natural OMZ variations. The dissertation thus calls for additional high-resolution reconstructions to constrain the natural OMZ variability, especially in the background of anthropogenic climate change.

Chapter 1

Introduction

Dissolved oxygen (DO) in the ocean is fundamental for marine ecosystems, as DO modulates biodiversity, productivity, nutrient cycling, and geochemical processes (Breitburg et al., 2018; Diaz and Rosenberg, 2008; Keeling et al., 2010; Schmidtko et al., 2017). Reduced DO in the water column leads to loss of suitable habitats for benthic fauna and the subsequent loss of biodiversity (Bopp et al., 2002; Rabalais et al., 2014; Rabalais et al., 2002). In the past several decades, oceanic deoxygenation has been widely observed in both the open ocean and coastal waters from the instrumental records, expanding and intensifying oxygen minimum zones (OMZs). More than 500 coastal sites have reported hypoxia (DO < 61 μmol/kg, a DO threshold suppressing fauna survival) since the 1950s, and many affected sites intersect with high primary productivity regions that support important fisheries (Breitburg et al., 2018; Schmidtko et al., 2017).

Reduced DO can be associated with reduced supply and/or increased consumption via organic carbon (OC, generated by photosynthesis) decay. Modeling and modern observations have attributed aggravated deoxygenation to a warming ocean since the 20th century, which reduces subsurface DO supply by decreasing oxygen solubility and intensifies water-column stratification (Bopp et al., 2013; Stramma et al., 2010). In addition to surface DO supply, low-oxygen waters can be ventilated by intermediate waters, whose oxygen concentrations are controlled by intermediate water formation rates and/or modification by organic carbon respiration along the circulation path. DO consumption in the water column is controlled by export productivity (organic carbon fluxes exported to the deep ocean) as oxygen is gradually depleted by aerobic respiration. Thus, high primary productivity waters are usually associated with low-oxygen waters at the mid-depth (~200 – 800 m, Brandes et al. (1998)). For the coastal OMZs, eutrophication caused by nutrient-rich river discharge can further stimulate

phytoplankton growth that enhances export productivity and leads to consequent DO depletion (e.g., Chesapeake Bay and Gulf of Mexico, (Brush, 2008); Rabalais et al. (2002)). The complex nature of DO controls renders it sensitive to both climate shifts and anthropogenic impacts, as manifested from the large magnitude of interannual variability overlying the multidecadal trend in modern observations (Wang et al., 2017; Whitney et al., 2007). The short duration of available instrument records (~60 years) and cruise data, however, makes detecting longer-term (multidecadal to centennial) OMZ oscillations difficult. Sufficiently long and high-resolution oxygenation records are thus needed to better understand the magnitude of OMZ shifts on various timescales (interannual to centennial).

Sediment archives provide invaluable information on past climatology and are often used to reconstruct the oxygenation beyond the instrumental records, because sedimentary geochemistry (e.g., redox-sensitive trace metal preservation, isotope fractionation) is controlled by ambient DO concentrations (redox potential, Fig. 1-1). However, complications remain as post-depositional redox potential changes in the ambient waters can lead to preservation/remobilization of redox proxies (sedimentary diagenesis), overprinting the original redox signal preserved. For instance, occurrences of instantaneous depositional events that perturb the normal depositional environment can initiate diagenesis and compromised the redox interpretations (Chaillou et al., 2008; McKay and Pedersen, 2014; Mucci et al., 2003; Wang et al., 2019). Thus, identifying a suite of sedimentary redox proxies that subject to minimized diagenesis is required prior to accurate oxygenation reconstructions. Additionally, to disentangle the complex interplay among driving forces underlying the oxygen oscillations, it is essential that a multi-proxy approach be applied to cross check the validity of redox reconstructions and provide insights on oxygen supply/consumption evolution through time.

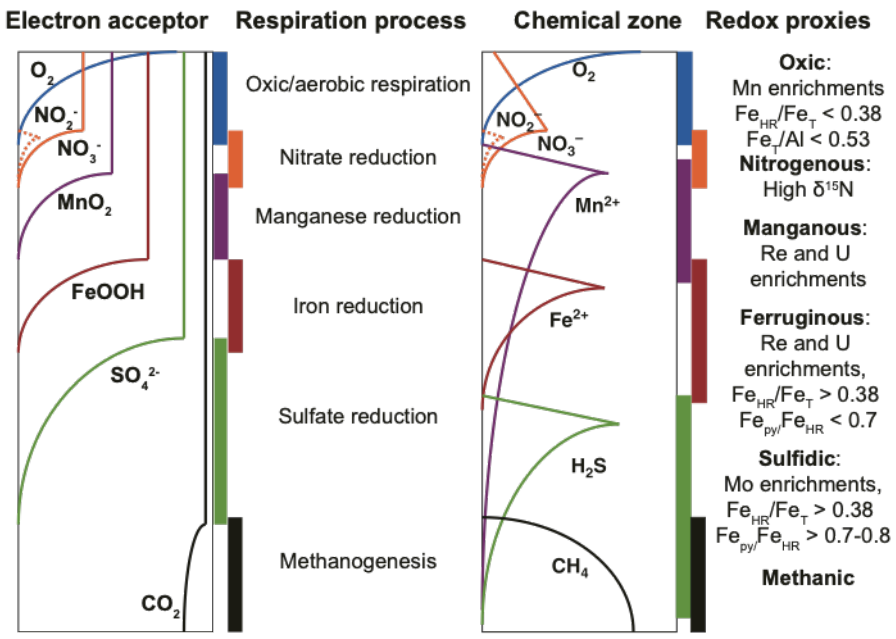

Figure 1-1 Redox tower and chemical zones modified from Canfield and Thamdrup (2009). On the left shows the dominant electron acceptors with the associated respiration processes listed in the middle. The right column shows the chemical zones and expected redox proxy responses from nitrogen isotopes, Fe speciation, and redox sensitive trace metals.

In this thesis, I focus on the Southern California margin off the US west coast. The Southern California margin is under the influence of the California Current System (CCS), an Eastern Boundary Upwelling system extending from Southern California to Washington that supports important marine industries (e.g., tourism and fisheries). High primary productivity induced by extensive upwelling results in intense coastal OMZs on the Southern California margin. The thesis aims to (1) identify valid redox proxies that can be applied to the Southern Califonria OMZ reconstructions, (2) to document Southern California OMZ oscillations on interannual to millennial timescales during the Holocene, and (3) to understand how coastal OMZs (Southern California as a case) would respond to large-scale climate and anthropogenic forcing via comparison with model realizations.

1.1 Reduction-oxidation (redox) reactions and proxies

In the oxic water columns, aerobic respiration is the dominant pathway for organic carbon decay. As DO draws down, redox potential decreases and the favorable electron acceptor for organic carbon decay becomes nitrate, Mn oxides, Fe (oxyhydr)oxides, sulfate, and finally CO_2 (Fig. 1-1). Redox potential (depending on DO) in the ambient waters controls the dominant reduction processes (e.g., NO_3^-, Mn, Fe, and SO_4^{2-} reduction or methanogenesis). Geochemical

proxies sensitive to these reduction processes thus have the potential of recording past redox variability if they are preserved in the sediments.

Sedimentary nitrogen isotopic composition ($\delta^{15}N_{sed}$) has shown to respond to intensity of nitrate reduction. Microbial denitrification (nitrate reduction to nitrogen gas) preferentially removes ^{14}N in the water column, gradually enriching ^{15}N in the subsurface nitrate pool. Upwelled ^{15}N-enriched nitrate is then incorporated into particulate OC in the photic zone, which is then exported to seafloor. The subsurface high-^{15}N denitrified signal can thus be preserved as elevated $\delta^{15}N_{sed}$ (Altabet, 2006; Altabet and François, 1994; Ganeshram et al., 2002). Complete nitrate utilization in the photic zone is required to exclude $\delta^{15}N_{sed}$ complications associated with preferential uptake of ^{14}N in photosynthesis that leads to increased $\delta^{15}N$ as well (Altabet and François, 1994). This assumption of complete surface nitrate utilization can be validated using modern surface nitrate measurements. Additionally, careful prescreening of sedimentary diagenesis is necessary prior to redox applications of $\delta^{15}N_{sed}$ (Prokopenko et al., 2006). Another controlling factor for $\delta^{15}N_{sed}$ is the contribution of different N sources that have unique $\delta^{15}N$ signatures. The fixed N sources include N fixation ($\delta^{15}N = -2 – 0‰$), atmospheric deposition ($\delta^{15}N \approx -2‰$), terrestrial input ($\delta^{15}N \approx 4‰$), and remote water masses with different $\delta^{15}N$ that advect to upwelling regions (Altabet, 2006; Sigman et al., 2009). Denitrification reconstructions from $\delta^{15}N_{sed}$ thus require a comprehensive understanding of the local nitrogen cycle.

As DO decreases, Fe reduction becomes prevalent in the surrounding waters and iron speciation was thus developed as a redox proxy. Fe speciation extracts Fe carbonate, Fe (oxyhydr)oxides, magnetite, and pyrite, and defines three parameters (Fe_T [total Fe]/Al, Fe_{HR} [highly-reactive Fe]/Fe_T, and Fe_{py} [pyrite Fe]/Fe_{HR}) to distinguish between oxic (DO rich), ferruginous (no DO and free Fe^{2+} presence), and euxinic conditions (Clarkson et al., 2014; Lyons and Severmann, 2006; Poulton and Canfield, 2011; Poulton and Raiswell, 2005). Fe_{py}, Fe carbonate, and Fe (oxyhydr)oxides are defined as the highly-reactive iron pool towards sulfide (Fe_{HR}) because they are either preserved as pyrite or readily reduced by HS^- in the early diagenetic stages (März et al., 2008a; Poulton and Raiswell, 2005; Raiswell and Canfield, 2012). Fe_{HR}/Fe_T and Fe_T/Al are used as anoxia indicators, representing authigenic Fe enrichment relative to lithogenic input (Clarkson et al., 2014; Lyons and Severmann, 2006; Raiswell and Canfield, 1998). $Fe_{HR}/Fe_T > 0.38$ and $Fe_T/Al > 0.53 \pm 0.11$ are used as anoxia (no oxygen present) thresholds (Clarkson et al., 2014; Lyons and Severmann, 2006; Poulton and Raiswell, 2005).

Fe_{py}/Fe_{HR} measures the portion of highly-reactive iron that has been converted to pyrite (FeS_2). When the water column is anoxic ($Fe_{HR}/Fe_T > 0.38$), Fe_{py}/Fe_{HR} was used to distinguish euxinic ($Fe_{py}/Fe_{HR} > 0.7$~0.8, free sulfide present) from ferruginous ($Fe_{py}/Fe_{HR} < 0.7$, anoxic with free Fe(II) present) conditions (Clarkson et al., 2014; Li et al., 2015; März et al., 2008b; Poulton and Canfield, 2011; Poulton et al., 2015). These thresholds, however, can be different depending on the paleo-archives studied (e.g., $Fe_{HR}/Fe_T > 0.22$ for the Phanerozoic rock records vs. > 0.38 for the modern sediments, Hardisty et al. (2018)).

Tandem use of multiple redox-sensitive trace metals can also be used to reconstruct a range of redox conditions (Fig. 1-1). Sedimentary Mn enrichment is frequently used to suggest oxic waters because Mn is preserved as insoluble Mn(IV) oxides (Calvert and Pedersen, 2007). As DO decreases, Mn oxides can be reduced to free Mn(II) that diffuses out of sediments. Rhenium and U have similar redox potentials and are conservative in oxic waters. In low DO conditions, sedimentary Re and U are enriched compared to crustal values due to formation of Re(IV) oxides/sulfides and U(IV) precipitates (Calvert and Pedersen, 2007; Crusius et al., 1996; McManus et al., 2006; Tribovillard et al., 2006). Molybdenum is usually conservative in oxic water columns despite complexation with dissolved organic carbon (Tessin et al., 2018; Wagner et al., 2017) and co-precipitation with Fe and Mn oxides (Fe/Mn shuttles, Scott et al. (2008); Tribovillard et al. (2006)). In reducing environments, sedimentary Mo enrichments requires the presence of free sulfide (Crusius et al., 1996; Zheng et al., 2000), and thus are usually interpreted to suggest ambient sulfidic environments provided that coeval U/Re enrichments are observed and Fe/Mn shuttle effects (Chapter 3) are not prominent (Calvert and Pedersen, 2007; McKay et al., 2007; Rico et al., 2019; Scott et al., 2008; Tribovillard et al., 2006).

1.2 Santa Barbara Basin on the Southern California margin

The thesis is focused on sediment archives retrieved from the Santa Barbara Basin, a semi-closed basin (~590 m depth) located on the Southern California margin with a high sedimentation rate (~4 mm/y, Reimers et al. (1996)) suitable for high-resolution reconstructions (Fig. 1-2b). The bottom of SBB is located at the center depth of the Southern California OMZ. SBB sediments preserve annual couplets (i.e., varves) with alternation of a biogenic (sourced from organisms) and a siliciclastic (sourced from rocks) layer (Soutar and Crill, 1977; Thunell et al., 1995). The biogenic component is usually deposited in spring and summer under intensified upwelling, when the North Pacific High (NPH) intensifies and migrates poleward. The

northward displacement of NPH then drives upwelling-favorable alongshore winds and induces extensive coastal upwelling, which transports nutrients to the surface ocean and stimulates primary productivity (Checkley and Barth, 2009; Chelton et al., 2007). Additionally, in the southern CCS, a broad offshore upwelling (up to 200 km) caused by the positive wind stress curl also plays a role in driving nutrient-rich waters to the surface (Checkley and Barth, 2009; Pickett, 2003; Rykaczewski and Checkley, 2008). In winter, NPH weakens and migrates towards the equator, diminishing upwelling and allowing the strengthened Aleutian Low (AL) to steer precipitation in Southern California. Higher winter precipitation usually leads to increasing river runoff and subsequent deposition of siliciclastic component (Thunell, 1998; Thunell et al., 1995; Warrick and Farnsworth, 2009). The low-oxygen bottom waters suppress macrofauna activities and reduce bioturbation, which contribute to varve (annualy-resolved laminations) preservation and allow generation of a high-fidelity age model for oxygenation reconstructions (Du et al., 2018; Hendy et al., 2013; Schimmelmann et al., 1990).

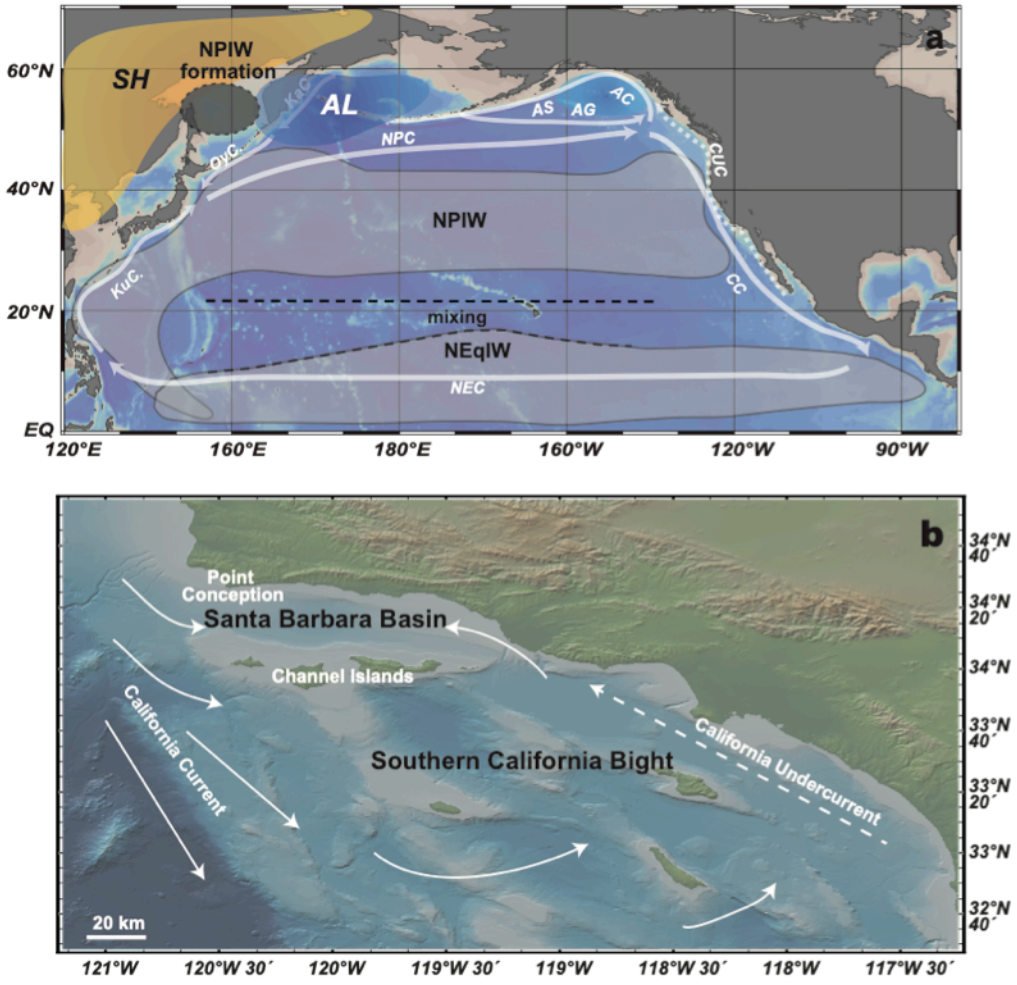

Figure 1-2 Santa Barbara Basin and circulation patterns. (a) The figure shows relative position of a westward/weakened Aleution Low (AL) and Siberian High (SH). Intermediate water masses (light gray shading circled in gray) and formation regions (dark gray shading with the dashed outline) are adapted from Bostock et al. (2010); Bostock et al. (2013); Talley (2008). Ocean currents are shown in white arrows. KaC: Kamchatka Current; OyC.: Oyashio Current; KuC.: Kuroshio Current; NEC: North Equatorial Current; CC: California Current; CUC: California Undercurrent; GoA: Gulf of Alaska; AC: Alaska Current; AS: Alaska Stream. NPIW: North Pacific Intermediate Water; NEqPIW: North Equatorial Intermediate Water; (b) The SBB map with ocean circulations modified from Hickey (1992). The base maps are generated from the Ocean data View in (a) and the GeoMapApp (http://www.geomapapp.org, Ryan et al., 2009), respectively.

In addition to the interactions with atmosphere pressure systems (e.g., AL and NPH), the Southern California margin is affected by the oceanic currents in the CCS that transports nutrients: the equatorward California Current (CC) and the poleward California Undercurrent (CUC) (Fig. 1-2). As the east limb of the North Pacific Gyre, CC carries cold and fresh water from the subpolar region (Hickey, 1978). CC intensity is largely dependent on the North Pacific Current (NPC) transport, with a stronger CC corresponding to an intensified NPC and enhanced Ekman pumping in the subpolar/subtropical gyres (Cummins and Freeland, 2007). The CUC is a subsurface poleward flow (core depth 200 – 300 m), advecting warm, salty, and low-oxygen

waters to the Southern California margin (Hickey, 1978). The CUC intensity has been suggested to be associated with coastal-trapped Kelvin waves that are propagated from the equator (Gómez-Valdivia et al., 2017). The Southern California margin is thus sensitive to both tropical and subarctic variations.

Furthermore, bottom waters in SBB are ventilated by two intermediate water masses: the more oxic North Pacific Intermediate Water (NPIW) from the northwest Pacific and the Equatorial Pacific Intermediate Water (EqPIW) (Fig. 1-2a). As the densest water mass currently formed in the North Pacific, NPIW (water depth of 300 – 800 m) is formed between the Kuroshio Extension and the Oyashio Fronts and then migrates eastward across the North Pacific basin (Miyao and Ishikawa, 2003; Talley, 1993; Yasuda, 1997; You, 2003). NPIW ventilates from the Okhotsk Sea (Fig. 1-2a), where sea ice brine rejection leads to formation of well-oxygenated intermediate waters (Shcherbina et al., 2004a; Shcherbina et al., 2004b; Talley, 1993; Watanabe and Wakatsuchi, 1998). EqPIW (water depth of 600 – ~1300 m) originates from the tropics and is transported to Southern California following the CUC. As EqPIW flows from the Eastern Equatorial Pacific where extensive DO consumption under high primary productivity deprives DO, EqPIW usually has lower DO compared to NPIW. Thus, ventilation variability of the NPIW and EqPIW would affect Southern California OMZ by alternating the mid-depth DO supply. The close association with atmospheric forcing (e.g., NPH intensity controls coastal upwelling intensity), oceanic currents (e.g., CC and CUC advect nutrients), and remote ventilation via the intermediate waters makes Southern California OMZ an ideal region to systematically investigate complex coastal OMZ responses to various forcing mechanisms.

1.3 Sedimentary proxies and analytical methods

The geochemical proxies in this thesis include redox proxies for oxygen reconstructions (e.g., iron speciation, redox-sensitive trace metals, nitrogen isotopes), export productivity proxies for oxygen consumption reconstruction (e.g., total organic carbon, Ba, and Br/Cl), and other elemental composition of the bulk sediments. Data using this multi-proxy approach are evaluated for sedimentary diagenesis, and the least affected proxies are further compared with other published flora/faunal abundance (e.g., diatoms, dinoflagellates, and foraminifera) and climatology (e.g., sea surface temperature and sea level pressure) records to investigate the OMZ driving forces. The elemental composition of SBB sediments is measured by the inductively coupled plasma mass spectrometry (ICP-MS) or atomic emission spectrometry (ICP-AES). Both

ICP-MS and ICP-AES use the argon plasma as the ion source, but MS and AES measure mass-to-charge ratio and the characteristic emission spectra, respectively. The spectrometry methods are implemented with scanning X-ray fluorescence measurements, which is a semi-quantitative and non-destructive approach to high-resolution (200 μm) records (Croudace et al., 2006). 2 – 7 data points per year can thus be achieved in SBB sediments (Hendy et al., 2015), compared to the at best 4 – 8 year resolution of mass spectrometry. Diagenesis of redox proxies is investigated by determining Fe mineralogy from qualitative magnetic analyses and comparing with core fabric observations.

1.4 Thesis structure

The thesis is divided into a method chapter (Chapter 2) and five data chapters (Chapter 3 – 7). Chapter 2 provides a detailed description on the quantitative elemental analysis method using ICP-MS, and serves as the methodology groundwork for other data chapters. A fast and economic bulk elemental analysis method (for ~40 elements) is established in the Michigan Elemental Analysis Lab (MEAL) at the University of Michigan, using a mixture of concentrated HCl, HNO_3, and HF to digest bulk samples in a microwave digestion system. The method is tested against sediment reference materials (MESS-3, PAC-2, and HISS-1) to determine its accuracy and precision. A data comparison between this MEAL method for data in Chapter 6, and the ALS Global (Brisbane, Australia) method for data presented in Chapter 3, 4, and 7 is also presented to make sure the datasets are comparable.

Chapter 3 presents a ground truthing study for iron speciation and redox-sensitive trace metals as redox proxies. Magnetic analyses were used to determine Fe mineralogy shifts that are associated with post-depositional diagenetic processes. The tandem application of magnetic analyses and Fe speciation thus allows an evaluation of digenetic overprinting on the original redox signal in the SBB.

In Chapter 4, I applied redox-sensitive trace metal enrichments and modern oxygen observations to reconstruct post-Industrial Revolution OMZ oscillations in Southern California on interannual to centennial timescales. Paired with export productivity data, the centennial OMZ responses to the anthropogenic warming trend are evaluated. Comparison between recent instrumental observations and high-resolution scanning XRF data also allow the investigation of how intermediate water ventilation replenishes DO in the SBB on an interannual scale.

Starting from Chapter 5, the thesis turns its focus to longer records on millennial timescales. Extended records allow us to understand natural OMZ variability prior to anthropogenic impacts on decadal to centennial timescales and its evolution throughout the Holocene. Chapter 5 and 6 focus on the Common Era, whereas Chapter 7 further expands the record coverage to most of the Holocene (9 ka before present/BP). Chapter 5 presents a high-resolution (~2 – 4 year) denitrification and export productivity records on the Southern California margin. Through comparison with published upwelling-related diatom assemblages, the upwelling regime shifts (e.g., coastal vs. wind curl upwelling) in the SBB are investigated. Local (e.g., productivity) and regional (e.g., remote nitrate advection) dentrification controls are also evaluated in this chapter to provide insights on how coastal OMZ nitrogen cycling would have responded to climate shifts. In particular, the regional control from tropics and subarctic regions are suggested by comparison with another denitrification record from the Gulf of California (as the tropical end member of nitrate) and an AL reconstruction from the Yukon Territory (as an indicator of subarctic nitrate transport via the California Current).

Having understood the export productivity variability during the Common Era, Chapter 6 continues on oxygenation reconstruction with redox-sensitive trace metal enrichments. This new Common Era redox record allows us to assess the natural OMZ variability in terms of the magnitude and frequency on the highest temporal resolution in the North Pacific to date (4 – 8 years). Paired with the export productivity record from Chapter 5 and remote ventilation records from the NPIW and EqPIW source regions, the impacts of remote ventilation are evaluated. Additionally, reconstructed OMZ oscillations are compared with updated Last Millennium Reanalysis product to unveil the physical mechanisms responsible for OMZ expansions that are not following local solubility (oxygen supply) and productivity (oxygen consumption) control.

Chapter 7 aims to resolve the waxing and waning of OMZ prior to the Common Era. In this chapter, redox records are presented as fluxes to account for sedimentation rate change across the mid-Holocene (6 ka). The new record implements a vertical transect spanning the whole depth range of Southern California OMZ, allowing a comprehensive evaluation of benthic responses to OMZ intensification in the early to mid Holocene. A similar comparison with local solubility and productivity control is conducted to separate local drivers from remote intermediate water influences. Additionally, state-of-the-art model (Community Earth System

Model, CESM) simulations are used to reveal the physical processes that may have controlled remote intermediate water ventilation.

Finally, a summary of the conclusions in this thesis and future research directions are presented in Chapter 8. This dissertation uses multiple marine sediment archives on the Southern California margin to investigate OMZ variability from interannual to millennial timescales and the underlying mechanisms. Modern redox proxy validation and export productivity variations (Chapter 3 and 5) provide the foundation for Southern California OMZ reconstructions in the following chapters that contributes to understanding anthropogenic and/or natural drivers of OMZ oscillations through the Holocene (Chapter 4, 6, and 7). This work thus has important implications for future OMZ projections under current climate change, fishery management, and ecosystem adaptation, by providing insights on the past OMZ variability from the sedimentary records.

1.5 References

Altabet, M.A., 2006. Isotopic Tracers of the Marine Nitrogen Cycle: Present and Past. The Handbook of Environmental Chemistry, 2N: 251-293.

Altabet, M.A., François, R., 1994. Sedimentary nitrogen isotopic ratio as a recorder for surface nitrate utilization. Global Biogeochemical Cycles, 8(1): 103-116.

Bopp, L., Le Quéré, C., Heimann, M., Manning, A.C., Monfray, P., 2002. Climate-induced oceanic oxygen fluxes: Implications for the contemporary carbon budget. Global Biogeochemical Cycles, 16(2): 1-13.

Bopp, L. et al., 2013. Multiple stressors of ocean ecosystems in the 21st century: projections with CMIP5 models. Biogeosciences, 10(10): 6225-6245.

Bostock, H.C., Opdyke, B.N., Williams, M.J.M., 2010. Characterising the intermediate depth waters of the Pacific Ocean using δ13C and other geochemical tracers. Deep Sea Research Part I: Oceanographic Research Papers, 57(7): 847-859.

Bostock, H.C., Sutton, P.J., Williams, M.J.M., Opdyke, B.N., 2013. Reviewing the circulation and mixing of Antarctic Intermediate Water in the South Pacific using evidence from geochemical tracers and Argo float trajectories. Deep Sea Research Part I: Oceanographic Research Papers, 73: 84-98.

Brandes, J.A., Devol, A.H., Yoshinari, T., Jayakumar, D.A., Naqvi, S.W.A., 1998. Isotopic composition of nitrate in the central Arabian Sea and eastern tropical North Pacific: a tracer for mixing and nitrogen cycles. Limnology and Oceanography, 43(7): 1680-1689.

Breitburg, D. et al., 2018. Declining oxygen in the global ocean and coastal waters. Science, 359(6371).

Brush, G.S., 2008. Historical Land Use, Nitrogen, and Coastal Eutrophication: A Paleoecological Perspective. Estuaries and Coasts, 32(1): 18-28.

Calvert, S.E., Pedersen, T.F., 2007. Elemental Proxies for Palaeoclimatic and Palaeoceanographic Variability in Marine Sediments: Interpretation and Application, Developments in Marine Geology, pp. 567-644.

Canfield, D.E., Thamdrup, B., 2009. Towards a consistent classification scheme for geochemical environments, or, why we wish the term 'suboxic' would go away. Geobiology, 7(4): 385-92.

Chaillou, G., Schäfer, J., Blanc, G., Anschutz, P., 2008. Mobility of Mo, U, As, and Sb within modern turbidites. Marine Geology, 254(3-4): 171-179.

Checkley, D.M., Barth, J.A., 2009. Patterns and processes in the California Current System. Progress in Oceanography, 83(1-4): 49-64.

Chelton, D.B., Schlax, M.G., Samelson, R.M., 2007. Summertime Coupling between Sea Surface Temperature and Wind Stress in the California Current System. Journal of Physical Oceanography, 37(3): 495-517.

Clarkson, M.O., Poulton, S.W., Guilbaud, R., Wood, R.A., 2014. Assessing the utility of Fe/Al and Fe-speciation to record water column redox conditions in carbonate-rich sediments. Chemical Geology, 382: 111-122.

Croudace, I.W., Rindby, A., Rothwell, R.G., 2006. ITRAX: description and evaluation of a new multi-function X-ray core scanner. Geological Society, London, Special Publications, 267(1): 51-63.

Crusius, J., Calvert, S., Pedersen, T., Sage, D., 1996. Rhenium and molybdenum enrichments in sediments as indicators of oxic, suboxic and sulfidic conditions of deposition. Earth and Planetary Science Letters, 145: 65-78.

Cummins, P.F., Freeland, H.J., 2007. Variability of the North Pacific Current and its bifurcation. Progress in Oceanography, 75(2): 253-265.

Diaz, R.J., Rosenberg, R., 2008. Spreading dead zones and consequences for marine ecosystems. Science, 321(5891): 926-9.

Du, X., Hendy, I., Schimmelmann, A., 2018. A 9000-year flood history for Southern California: A revised stratigraphy of varved sediments in Santa Barbara Basin. Marine Geology, 397: 29-42.

Ganeshram, R.S., Pedersen, T.F., Calvert, S.E., François, R., 2002. Reduced nitrogen fixation in the glacial ocean inferred from changes in marine nitrogen and phosphorus inventories. Nature, 415: 156-159.

Gómez-Valdivia, F., Parés-Sierra, A., Laura Flores-Morales, A., 2017. Semiannual variability of the California Undercurrent along the Southern California Current System: A tropical generated phenomenon. Journal of Geophysical Research: Oceans, 122(2): 1574-1589.

Hendy, I.L., Dunn, L., Schimmelmann, A., Pak, D.K., 2013. Resolving varve and radiocarbon chronology differences during the last 2000 years in the Santa Barbara Basin sedimentary record, California. Quaternary International, 310: 155-168.

Hendy, I.L., Napier, T.J., Schimmelmann, A., 2015. From extreme rainfall to drought: 250 years of annually resolved sediment deposition in Santa Barbara Basin, California. Quaternary International, 387: 3-12.

Hickey, B.M., 1978. The California current system—hypotheses and facts. Progress in Oceanography, 8(4): 191-279.

Keeling, R.E., Kortzinger, A., Gruber, N., 2010. Ocean deoxygenation in a warming world. Ann Rev Mar Sci, 2: 199-229.

Li, C. et al., 2015. Marine redox conditions in the middle Proterozoic ocean and isotopic constraints on authigenic carbonate formation- Insights from the Chuanlinggou Formation, Yanshan Basin, North China. Geochimica et Cosmochimica Acta, 150(2015): 90-105.

Lyons, T.W., Severmann, S., 2006. A critical look at iron paleoredox proxies: New insights from modern euxinic marine basins. Geochimica et Cosmochimica Acta, 70(23): 5698-5722.

März, C., Hoffmann, J., Bleil, U., de Lange, G.J., Kasten, S., 2008a. Diagenetic changes of magnetic and geochemical signals by anaerobic methane oxidation in sediments of the Zambezi deep-sea fan (SW Indian Ocean). Marine Geology, 255(3-4): 118-130.

März, C. et al., 2008b. Redox sensitivity of P cycling during marine black shale formation-Dynamics of sulfidic and anoxic, non-sulfidic bottom waters. Geochimica et Cosmochimica Acta, 72(2008): 3703-3717.

McKay, J., Pedersen, T., Mucci, A., 2007. Sedimentary redox conditions in continental margin sediments (N.E. Pacific) — Influence on the accumulation of redox-sensitive trace metals. Chemical Geology, 238(3-4): 180-196.

McKay, J.L., Pedersen, T.F., 2014. Geochemical response to pulsed sedimentation: Implications for the use of Mo as a paleo-proxy. Chemical Geology, 382: 83-94.

McManus, J. et al., 2006. Molybdenum and uranium geochemistry in continental margin sediments: Paleoproxy potential. Geochimica et Cosmochimica Acta, 70(18): 4643-4662.

Miyao, T., Ishikawa, K., 2003. Formation, distribution and volume transport of the North Pacific Intermediate Water studied by repeat hydrographic observations. Journal of Oceanography, 59(6): 905-919.

Mucci, A., Boudreau, B., Guignard, C., 2003. Diagenetic mobility of trace elements in sediments covered by a flash flood deposit: Mn, Fe and As. Applied Geochemistry, 18(7): 1011-1026.

Pickett, M.H., 2003. Ekman transport and pumping in the California Current based on the U.S. Navy's high-resolution atmospheric model (COAMPS). Journal of Geophysical Research, 108(C10).

Poulton, S.W., Canfield, D.E., 2011. Ferruginous conditions: a dominant feature of the ocean through Earth's history. Elements, 7: 107-112.

Poulton, S.W. et al., 2015. A continental-weathering control on orbitally driven redox-nutrient cycling during Cretaceous Oceanic Anoxic Event 2. Geology, 43(11): 963-966.

Poulton, S.W., Raiswell, R., 2005. Chemical and physical characteristics of iron oxides in riverine and glacial meltwater sediments. Chemical Geology, 218(3-4): 203-221.

Prokopenko, M. et al., 2006. Nitrogen cycling in the sediments of Santa Barbara basin and Eastern Subtropical North Pacific: Nitrogen isotopes, diagenesis and possible chemosymbiosis between two lithotrophs (Thioploca and Anammox)—"riding on a glider". Earth and Planetary Science Letters, 242(1-2): 186-204.

Rabalais, N. et al., 2014. Eutrophication-Driven Deoxygenation in the Coastal Ocean. Oceanography, 27(1): 172-183.

Rabalais, N.N., Turner, R.E., Wiseman, W.J., 2002. Gulf of Mexico Hypoxia, A.K.A. "The Dead Zone". Annual Review of Ecology and Systematics, 33(1): 235-263.

Raiswell, R., Canfield, D.E., 1998. Sources of iron for pyrite formation in marine sediments. American Journal of Science, 298(3): 219-245.

Raiswell, R., Canfield, D.E., 2012. Geochemical Perspectives: The Iron Biogeochemical Cycle Past and Present, 1.

Reimers, C.E., Ruttenberg, K.C., Canfield, D.E., Christiansen, M.B., Martin, J.B., 1996. Porewater pH and authigenic phases formed in the uppermost sediments of the Santa Barbara Basin. Geochimica et Cosmochimica Acta, 60(21): 4037-4057.

Rykaczewski, R.R., Checkley, D.M., Jr., 2008. Influence of ocean winds on the pelagic ecosystem in upwelling regions. Proc Natl Acad Sci U S A, 105(6): 1965-70.

Schimmelmann, A., Lange, C.B., Berger, W.H., 1990. Climatically controlled marker layers in Santa Barbara Basin sediments and fine-scale core-to-core correlation. Limnology and Oceanography, 35(1): 165-173.

Schmidtko, S., Stramma, L., Visbeck, M., 2017. Decline in global oceanic oxygen content during the past five decades. Nature, 542(7641): 335-339.

Scott, C. et al., 2008. Tracing the stepwise oxygenation of the Proterozoic ocean. Nature, 452(7186): 456-9.

Shcherbina, A.Y., Talley, L.D., Rudnick, D.L., 2004a. Dense water formation on the northwestern shelf of the Okhotsk Sea: 1. Direct observations of brine rejection. Journal of Geophysical Research: Oceans, 109(C9).

Shcherbina, A.Y., Talley, L.D., Rudnick, D.L., 2004b. Dense water formation on the northwestern shelf of the Okhotsk Sea: 2. Quantifying the transports. Journal of Geophysical Research: Oceans, 109(C9).

Sigman, D.M., Karsh, K.L., Casciotti, K.L., 2009. Nitrogen Isotopes in the Ocean, Encyclopedia of Ocean Sciences (Second Edition). Academic Press, Oxford, pp. 40-54.

Soutar, A., Crill, P.A., 1977. Sedimentation and climatic patterns in the Santa Barbara Basin during the 19th and 20th centuries. Geological Society of America Bulletin, 88(8): 1161-1172.

Stramma, L., Schmidtko, S., Levin, L.A., Johnson, G.C., 2010. Ocean oxygen minima expansions and their biological impacts. Deep Sea Research Part I: Oceanographic Research Papers, 57(4): 587-595.

Talley, L.D., 1993. Distribution and formation of North Pacific Intermediate Water. Journal of Geophysical Oceanography, 23: 517-537.

Talley, L.D., 2008. Freshwater transport estimates and the global overturning circulation: Shallow, deep and throughflow components. Progress in Oceanography, 78(4): 257-303.

Thunell, R.C., 1998. Particle fluxes in a coastal upwelling zone: sediment trap results from Santa Barbara Basin, California. Deep Sea Research Part II: Topical Studies in Oceanography, 45(8): 1863-1884.

Thunell, R.C., Tappa, E.J., Andersen, D.M., 1995. Sediment fluxes and varve formation in Santa Barbara Basin, offshore California. Geology, 23(12): 1083-1086.

Tribovillard, N., Algeo, T.J., Lyons, T., Riboulleau, A., 2006. Trace metals as paleoredox and paleoproductivity proxies: An update. Chemical Geology, 232(1-2): 12-32.

Wang, Y., Hendy, I., Napier, T.J., 2017. Climate and Anthropogenic Controls of Coastal Deoxygenation on Interannual to Centennial Timescales. Geophysical Research Letters, 44(22): 11528–11536.

Wang, Y., Hendy, I.L., Latimer, J.C., Bilardello, D., 2019. Diagenesis and iron paleo-redox proxies: New perspectives from magnetic and iron speciation analyses in the Santa Barbara Basin. Chemical Geology, 519: 95-109.

Warrick, J.A., Farnsworth, K.L., 2009. Sources of sediment to the coastal waters of the Southern California Bight. The Geological Society of America Special Paper, 454: 39-52.

Watanabe, T., Wakatsuchi, M., 1998. Formation of 26.8–26.9 σθ water in the Kuril Basin of the Sea of Okhotsk as a possible origin of North Pacific Intermediate Water. Journal of Geophysical Research: Oceans, 103(C2): 2849-2865.

Whitney, F.A., Freeland, H.J., Robert, M., 2007. Persistently declining oxygen levels in the interior waters of the eastern subarctic Pacific. Progress in Oceanography, 75(2): 179-199.

Yasuda, I., 1997. The origin of the North Pacific Intermediate Water. Journal of Geophysical Research, 102(C1): 893.

You, Y., 2003. The pathway and circulation of North Pacific Intermediate Water. Geophysical Research Letters, 30(24).

Zheng, Y., Anderson, R.F., Geen, A.V., James, K., 2000. Authigenic molybdenum formation in marine sediments: A link to pore water sulfide in the Santa Barbara Basin. Geochimica et Cosmochimica Acta, 64(24): 4165-4178.

Chapter 2

Development of a Rapid Elemental Analysis Procedure for High-resolution Paleoceanographic Reconstructions

2.1 Introduction

Accurate and precise determination of elemental compositions in natural samples is essential to improving our understanding of element sources, sinks, and distribution in sediments via different pathways. For high-resolution paleoceanographic studies, it is essential to develop a rapid elemental analysis procedure that allows simultaneous determination of a suite of elements from sediments and provides valuable information on past variability within a range of redox conditions (e.g., Re, Mo, U, Cd, and Ag as redox sensitive-trace metals, Calvert and Pedersen (2007)), primary productivity (e.g., Ca, Si, and Ba, Cullen et al. (1999)), lithogenic input (e.g., Al and Ti), and possible anthropogenic inputs (e.g., Pb and As, Bruland (1980)).

Inductively coupled plasma mass spectrometry (ICP-MS) is a powerful tool for performing simultaneous analyses of multiple elements. Yet, simultaneous elemental analyses of sediments via ICP-MS is challenging due to the low concentrations of some trace elements (e.g., several ppb in the sediments) relative to others, and the complex matrix effects introduced following sediment digestion (Dial et al., 2015). Isobaric interferences can be generated by polyatomic ions from Ar, O_2, N_2, and C in the plasma, and metal oxides from the sample matrix (Table 2-1). These interferences have similar mass to charge ratios (m/z) with the analytes and can lead to significant analytical errors. This issue is especially serious in the sediment matrix when the concentrations of charged metal oxides are magnitudes higher than the analytes (e.g., a 200-fold higher concentration of Zr compared to Ag in the Santa Barbara Basin [SBB] sediments).

Table 2-1 Monitored isotopes, interferences and element calibration ranges

Major elements	Isotope	Interferences
		Calibration curve range: 0.5 – 10 ppb
Ba	^{138}Ba	–
Mn	^{55}Mn	$^{40}Ar^{14}N^{1}H^{+}$, $^{39}K^{16}O^{+}$, $^{37}Cl^{18}O^{+}$, $^{40}Ar^{15}N+$, $^{38}Ar^{17}O+$, $^{36}Ar^{18}O^{1}H^{+}$, $^{38}Ar^{16}O^{1}H^{+}$, $^{37}Cl^{17}O^{1}H^{+}$, $^{23}Na^{32}S^{+}$, $^{36}Ar^{19}F^{+}$
P	^{31}P	$^{14}N^{16}O^{1}H^{+}$, $^{15}N^{15}N^{1}H^{+}$, $^{15}N^{16}O^{+}$, $^{14}N^{17}O^{+}$, $^{13}C^{18}O^{+}$, $^{12}C^{18}O^{1}H^{+}$
Sr	^{86}Sr	$^{85}Rb^{1}H^{+}$
		Calibration curve range: 20 – 400 ppb
K	^{39}K	$^{38}Ar^{1}H^{+}$
Mg	^{24}Mg	$^{12}C_2^{+}$
Na	^{23}Na	$^{9}Be^{14}N^{+}$, $^{7}Li^{16}O^{+}$, $^{11}B^{12}C^{+}$
S	^{34}S	$^{15}N^{18}O^{1}H^{+}$, $^{16}O^{18}O^{+}$, $^{17}O_2^{+}$, $^{16}O^{17}O^{1}H^{+}$, $^{34}S^{+}$, $^{33}S^{1}H^{+}$
Ti	^{48}Ti	$^{32}S^{16}O^{+}$, $^{34}S^{14}N^{+}$, $^{33}S^{15}N^{+}$, $^{14}N^{16}O^{18}O^{+}$, $^{14}N^{17}N^{2+}$, $^{12}C_4^{+}$, $^{36}Ar^{12}C^{+}$
Ca	^{44}Ca	$^{12}C^{16}O_2$, $^{14}N_2{}^{16}O^{+}$, $^{28}Si^{16}O^{+}$
		Calibration curve range: 100 – 800 ppb
Al	^{27}Al	$^{12}C^{15}N^{+}$, $^{13}C^{14}N^{+}$, $^{14}N_2$ spread, $^{1}H^{12}C^{14}N^{+}$
Fe	^{57}Fe	$^{40}Ar^{16}O^{1}H^{+}$, $^{40}Ca^{16}O^{1}H^{+}$, $^{40}Ar^{17}O^{+}$, $^{38}Ar^{18}O^{1}H^{+}$, $^{38}Ar^{19}F^{+}$
		Minor/trace elements
		Calibration curve range 0.01 – 1 ppb
Bi	^{209}Bi	$^{193}Ir^{16}O^{+}$
Ge	^{72}Ge	$^{36}Ar_2^{+}$, $^{37}Cl^{17}O^{18}O^{+}$, $^{35}Cl^{37}Cl^{+}$, $^{36}S^{18}O_2^{+}$, $^{36}S_2^{+}$, $^{36}Ar^{36}S^{+}$, $^{56}Fe^{16}O^{+}$, $^{40}Ar^{16}O_2^{+}$, $^{40}Ca^{16}O_2^{+}$, $^{40}Ar^{32}S^{+}$
Re	^{187}Re	
Te	^{126}Te	$^{110}Pd^{16}O^{+}$
		Calibration curve range 0.1 – 10 ppb
Hf	^{177}Hf	$^{161}Dy^{16}O^{+}$
Sb	^{123}Sb	$^{94}Zr^{16}O_2^{+}$
Ta	^{181}Ta	$^{165}Ho^{16}O^{+}$
W	^{184}W	
		Calibration curve range 1 – 40 ppb
As	^{75}As	$^{40}Ar^{35}Cl^{+}$, $^{59}Co^{16}O^{+}$, $^{36}Ar^{38}Ar^{1}H^{+}$, $^{38}Ar^{37}Cl^{+}$, $^{36}Ar^{39}K$, $^{43}Ca^{16}O_2^{+}$, $^{23}Na^{12}C^{40}Ar$, $^{12}C^{31}P^{16}O_2^{+}$
Co	^{59}Co	$^{43}Ca^{16}O^{+}$, $^{42}Ca^{16}O^{1}H^{+}$, $^{24}Mg^{35}Cl^{+}$, $^{36}Ar^{23}Na^{+}$, $^{40}Ar^{18}O^{1}H^{+}$, $^{40}Ar^{19}F^{+}$
Cs	^{133}Cs	$^{101}Ru^{16}O_2^{+}$
Mo	^{98}Mo	$^{81}Br^{17}O^{+}$, $^{41}K_2O^{+}$
Nb	^{93}Nb	$^{14}N^{79}Br^{+}$, $^{12}C^{81}Br^{+}$
Pb	^{208}Pb	$^{192}Pt^{16}O^{+}$
Se	^{78}Se	$^{64}Zn^{14}N^{+}$
Sn	^{120}Sn	$^{104}Ru^{16}O^{+}$, $^{104}Pd^{16}O^{+}$
Th	^{232}Th	$^{40}Ar^{192}Os^{+}$

U	^{238}U	
Calibration curve range 10 – 150 ppb		
Ce	^{140}Ce	
Cr	^{52}Cr	$^{35}Cl^{16}O^{1}H^{+}$, $^{40}Ar^{12}C^{+}$, $^{36}Ar^{16}O^{+}$, $^{37}Cl^{15}N^{+}$, $^{34}S^{18}O^{+}$, $^{36}S^{16}O^{+}$, $^{38}Ar^{14}N^{+}$, $^{36}Ar^{15}N^{1}H^{+}$, $^{35}Cl^{17}O^{+}$
Cu	^{65}Cu	$^{31}P^{16}O_2^{+}$, $^{40}Ar^{23}Na^{+}$, $^{47}Ti^{16}O^{+}$, $^{23}Na^{40}Ca^{+}$, $^{46}Ca^{16}O^{1}H^{+}$, $^{36}Ar^{12}C^{14}N^{1}H^{+}$, $^{14}N^{12}C^{37}Cl^{+}$, $^{16}O^{12}C^{35}Cl^{+}$
Ga	^{69}Ga	$^{35}Cl^{16}O^{18}O^{+}$, $^{35}Cl^{17}O_2^{+}$, $^{37}Cl^{16}O_2^{+}$, $^{36}Ar^{33}S^{+}$, $^{33}S^{18}O_2^{+}$, $^{34}S^{17}O^{18}O^{+}$, $^{36}S^{16}O^{17}O^{+}$, $^{33}S^{36}S^{+}$
La	^{139}La	$^{12}C^{127}I^{+}$
Li	^{7}Li	$^{14}N^{2+}$
Ni	^{60}Ni	$^{44}Ca^{16}O^{+}$, $^{23}Na^{37}Cl^{+}$, $^{43}Ca^{16}O^{1}H^{+}$
Y	^{89}Y	$^{14}N^{75}As^{+}$, $^{88}Sr^{1}H^{+}$
Zr	^{90}Zr	$^{89}Y^{1}H^{+}$
Calibration curve range 50 – 300 ppb		
Rb	^{85}Rb	$^{40}Ar^{45}Sc^{+}$
V	^{51}V	$^{34}S^{16}O^{1}H^{+}$, $^{35}Cl^{16}O^{+}$, $^{38}Ar^{13}C^{+}$, $^{36}Ar^{15}N^{+}$, $^{36}Ar^{14}N^{1}H^{+}$, $^{37}Cl^{14}N^{+}$, $^{36}S^{15}N^{+}$, $^{33}S^{18}O^{+}$, $^{34}S^{17}O^{+}$
Zn	^{68}Zn	$^{36}S^{16}O_2^{+}$, $^{34}S^{16}O^{18}O^{+}$, $^{40}Ar^{14}N_2^{+}$, $^{35}Cl^{16}O^{17}O^{+}$, $^{34}S_2^{+}$, $^{36}Ar^{32}S^{+}$, $^{34}S^{17}O_2^{+}$, $^{33}S^{17}O^{18}O^{+}$, $^{32}S^{18}O_2^{+}$, $^{32}S^{36}S^{+}$
Isotope dilution		
Ag	^{109}Ag	$^{92}Zr^{16}O^{1}H^{+}$
	^{107}Ag	$^{91}Zr^{16}O^{+}$
Cd	^{111}Cd	$^{95}Mo^{16}O^{+}$, $^{94}Zr^{16}O^{1}H^{+}$, $^{39}K_2{}^{16}O_2{}^{1}H^{+}$
	^{113}Cd	$^{96}Zr^{16}O^{1}H^{+}$, $^{40}Ca_2{}^{16}O_2{}^{1}H^{+}$, $^{40}Ar_2{}^{16}O_2{}^{1}H^{+}$, $^{96}Ru^{17}O^{+}$

To overcome isobaric interferences, multiple techniques have been applied, including high-resolution (HR)-ICP-MS, matrix separation, and the collision/reaction cell (CRC). HR-ICP-MS achieves a higher mass resolution (mass of the analyte [m]/resolvable mass difference [Δm]) to distinguish the spectral interferences from the analytes, yet in some cases the resolution required (e.g., 23600 for ^{107}Ag, Guo et al. (2011)) is significantly higher than the currently achieved on available instruments (m/Δm of ~8000 – 10000). The second option is to apply column chemistry procedures that separate and/or concentrate analytes from other interferences prior to ICP-MS analyses. Additionally, quadrupole (Q)-ICPMS equipped with a collision/reaction cell (CRC) has proved effective in removing spectral interferences by kinetic energy discrimination (KED; Iglesias et al. (2002); McCurdy and Woods (2004); Tanner et al. (2002); Yamada (2015)). As the isobaric interferences (e.g., polyatomic and metal oxide ions) have larger collision cross sections than the analyte ions, they collide more frequently with the cell gas (He), leading to more energy loss. This preferential energy loss of interferences allows their removal from the ion beam (McCurdy and Woods, 2004; Yamada, 2015), whereas the analyte ions (monoatomic) still retain the kinetic energy to exit the collision cell. Implementation

of the collision cell could thus achieve higher sensitivity and lower blanks for elemental analyses in a complex sample matrix.

Here, we document a bulk sediment analysis method that utilizes matrix separation (column chemistry) and CRC to achieve simultaneous and rapid measurements of multiple elements (major, minor, and trace) from one microwave digested sample. A modified column procedure to separate Ag and Cd from other inferences is calibrated to achieve a better performance (ions with less interferences) using a simpler procedure. Additionally, a comparison with ALS Global (Brisbane, Australia) methodology is included to demonstrate that measured elemental compositions at ALS are comparable with those analyzed using our method, enabling direct comparison among different records in later chapters.

2.2 Experimental

2.2.1 Reagents, standards, and sample matrix

All reagents were prepared using ultrapure water (resistivity > 18 MΩ cm^{-1}). 2% (wt/vol) Optima grade (Fisher Scientific, Hampton, NH, USA) nitric acid (HNO_3) was used on the ICP-MS for washing between samples. Trace Metal (TM) grade (Fisher Scientific, Hampton, NH, USA) acids (HNO_3, HCl, and HF) were used for bulk sediment sample digestion, column procedure, and analyte matrix preparation. Acid blanks were closely monitored throughout the experiment and no significant difference was observed between Optima and TM grade acids. All labware (e.g., Teflon beakers, plastic containers, columns, and pipet tips) was cleaned in the reagent grade 3M HNO_3 for > 12 hours and rinsed with ultrapure water for 3 times. Teflon vessels used in sample digestion additionally went through microwave cleaning using concentrated TM grade HNO_3 and HCl. Calibration standards were prepared either gravimetrically (Re, U, and Mo mixing standard) or volumetrically (multi-element standards for other analytes) using high-purity standards from either SCP Science (for Re, Mo, and U) or High-Purity Standards (HPS). Each digested sample was measured in three matrices: 1% (wt/vol) HNO_3 for Ag and Cd analyses, 0.5M HCl + 1% HNO_3 (1:4 mixture) for minor and trace elements, and 0.5M HCl + 1% HNO_3 (1:19 mixture) for major elements.

2.2.2 Isotope dilution

Isotope dilution mass spectrometry (ID-MS) is considered as the most accurate and precise technique for determining analyte concentrations in a sample (Sargent et al., 2002). ID-

MS relies on a known relative abundance of the spike isotope (usually rare in nature) to the reference isotope (typically abundant in nature) by adding isotope-enriched spikes to samples (Morford, 1999). As elemental concentrations are determined based on the measured ratios between the reference and spike isotopes, total recovery of the analyte is not required once the isotopic equilibrium is achieved. Any analyte transformation during sample preparation can then be compensated by the spike isotope that serves as an internal standard. Thus, accuracy of this method is dependent on the precision of this measured isotopic ratio (Patterson et al., 1994; Sargent et al., 2002). Elemental concentrations can be calculated using the following equation:

$$c_{elemental,natural} = \left(\frac{c_{element,spike} \times m_{spike}}{m_{natural}}\right)\left(\frac{M_{element,natural}}{M_{element,spike}}\right)\left(\frac{Ab_s^A - R \cdot Ab_s^B}{R \cdot Ab_N^B - Ab_N^A}\right) \qquad \text{(Eq. 2-1)}$$

Ab_N^A and Ab_s^A respectively denote the abundance of the *spike* isotope in natural samples and spikes, whereas Ab_N^B and Ab_s^B represent the abundance of *reference* isotope in natural samples/spikes. R is the measured isotopic ratio for the mixture. $c_{natural}$ and c_{spike} are concentrations of an element for the sample and isotope spikes, while $m_{natural}$ and m_{spike} denote mass of natural samples and spikes, respectively (Sargent et al., 2002). Finally, $M_{natural}$ and M_{spike} are the elemental molecular weight for the natural samples or spikes.

In this method we apply the isotope dilution technique to Ag and Cd analyses as both elements suffer from severe matrix interferences (Table 2-1) and recoveries following the sample preparation (digestion and column chemistry) is variable. Enriched isotope spikes of ^{109}Ag and ^{111}Cd in the metal form were obtained from the Oak Ridge National Laboratory (ORNL). The spiked metals were first dissolved in 2M TM grade HNO_3 to make concentrated spike stock solutions, and a mixed Ag and Cd spike (containing ~0.2 µg/g [ppm] of Ag and ~0.1 ppm of Cd) was obtained by further diluting the concentrated spikes using 2M HNO_3. Exact Ag and Cd spike concentrations were monitored by the 'reversed' IDMS, where the spike concentrations were repeatedly determined using natural calibration standards.

2.2.3 Sample spiking and digestion

Approximately 10 mg of freeze-dried and ground sediments was accurately weighed into a 10 mL EasyPrep (CEM Corporation, Matthews, NC) Teflon digestion vessel. 25 µL of the Ag and Cd mixed spike was then pipetted into the vessel, and the weight of the spike was recorded. The spike volume was determined to minimize the error propagation factor during spiking by

targeting the optimal isotope ratios for the spike and reference isotopes in the spiked samples (~5 for Ag Sargent et al. (2002) and ~1 for Cd Morford (1999)). TM grade acid mixtures (0.8 mL HNO_3, 0.1 mL HCl, and 0.2 mL HF) were then pipetted to the vessel in the laminar flow hood for the 1st microwave digestion. A marine sediment digestion program was created on the MARS 6 microwave digestion system (CEM Corporation). During the 1st digestion, temperature was ramped to 180 °C within 20 – 25 min, and was held at 180 °C for 20 min before cooling down. The digested mixture was then dried down on a graphite hotplate at 165 °C. 1.5 mL 0.5M TM grade HCl was then added to the digestion vessels for the 2nd digestion, with a 20 – 25 min ramp to 175°C and 15 min hold before cooling down. The final digested mixture was again brought to dryness at 165°C prior to final addition of another 1.5 mL 0.5M TM grade HCl for elemental analysis. The digested sample was divided into three aliquots: 400 µL for minor and trace elements by diluting to 2 mL with 1% (wt/vol) HNO_3; 100 µL for major elements diluted to 2 mL with 1% HNO_3; and the remaining 1000 µL for Ag and Cd column chemistry. A batch of 40 samples can be digested in one run, including 4 sediment reference materials and 4 procedural blanks. PACS-2, MESS-3, and HISS-1 obtained from National Research Council of Canada are used as reference materials for quality control.

Comparison with the ME-MS61 method used in ALS was also conducted by digesting 9 sediment samples from the core MV0811-14JC (34°16.906'N, 120°2.162'W, 582 m water depth) retrieved from the SBB, California. ALS used an acid mixture of HF, HNO_3, and $HClO_4$ to digest 0.25 g of samples on a hotplate. After evaporating the digested sample, the residue was then leached with diluted HCl and diluted to volume prior to analysis. All elements were measured using external calibration on either ICP-atomic emission spectrometer (AES) or quadrupole ICP-MS. Lab standard materials (GBM908-10, GBM908-5, MRGEO08, and OREAS 90) are used to monitor the accuracy and precision. No column chemistry or isotope dilution was performed. We targeted both high and low redox-sensitive metal concentrations (e.g., Mo) from the ALS data and measured the same suite of elements using the microwave digestion method at the University of Michigan.

2.2.4 Column chemistry

Prior to application on sediment samples, a column calibration was performed to validate the modified column procedure. Both the procedure used by the Prof. Thomas Pedersen Lab (University of Victoria, BC, Canada) and the one described in this chapter, use a Bio-rad Poly-

Prep column (2 mL bed volume and 10 mL reservoir) packed with Bio-rad AG 1-X8 resin (100 mesh, chloride form). The modified procedure reduces acid usage by replacing 8M HNO_3 with 4M HNO_3 (Fig. 2-1). Validation of the columns was performed with a digested PACS-2 sample and two high-purity standard mixtures with interferences (Nb, Zr, and Mo) of expected concentrations in the SBB sediments. The standard mixtures contain 0.07 ppm Nb, 0.27 ppm Zr, 0.03 ppm Mo, 1.33 ppb Ag, and 13.33 ppb Cd. For column calibration, we collected every 2-mL of elution in separate Savillex Teflon beakers. Post-column samples were dried to one drop on the hotplate at ~160 °C. 1.5 mL 1% HNO_3 was finally added prior to ICP-MS analysis. For real sediment sample Ag/Cd analyses, only the Ag/Cd portion eluted by 4M HNO_3 was collected into the Teflon beaker.

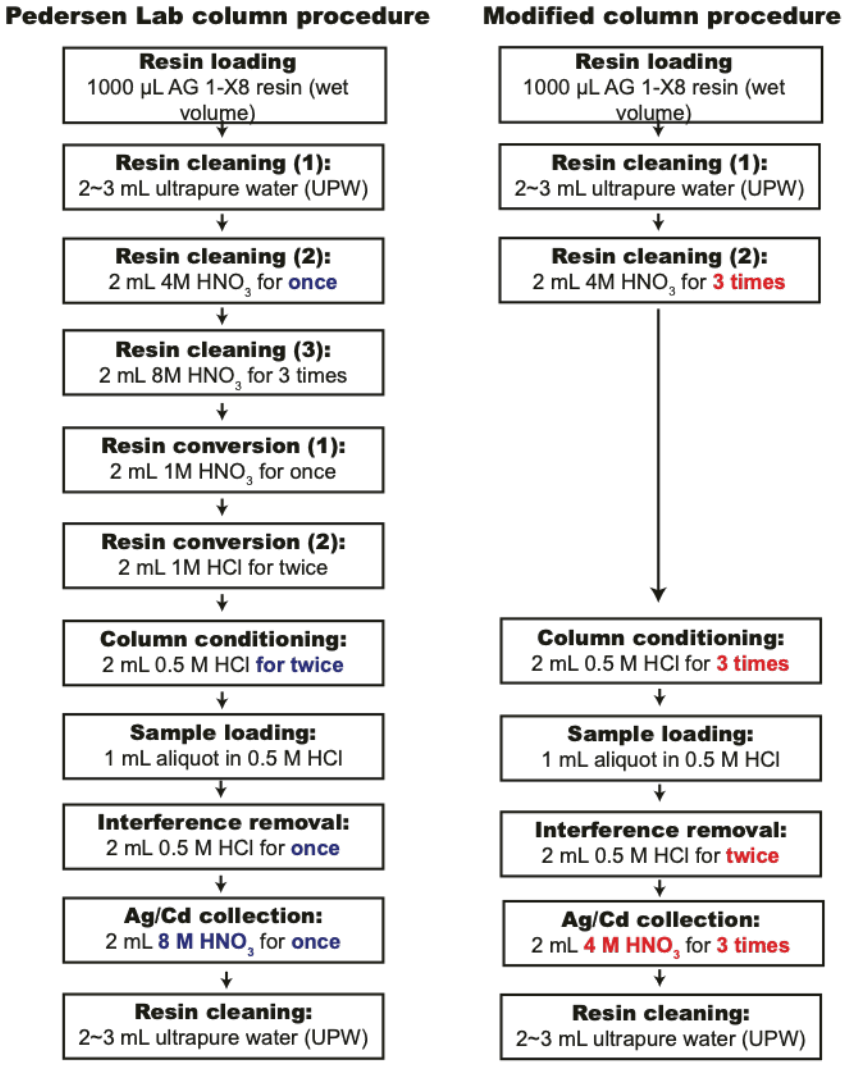

Figure 2-1 Column procedure comparison. Original column procedures were from Prof. Thomas Pedersen (University of Victoria) and the modified procedures were modified at the University of Michigan.

2.2.5 Quadrupole ICP-MS

The major and minor/trace aliquots were measured on the iCAP Q ICP-MS (Thermo Scientific, Bremen, Germany) equipped with a collision cell (He as the cell gas) at the Michigan Elemental Analysis Lab (MEAL), University of Michigan. The PrepFAST autosampling system (Elemental Scientific Inc., Omaha, NE, USA) with a 0.5 mL loop was used for sample introduction through a quartz spray chamber, as well as nickel sample and skimmer cones. For daily operation, the instrument sensitivity and stability (relative standard deviation [RSD] ≤ 2%) were optimized for $^{7}Li^{+}$, $^{59}Co^{+}$, $^{238}U^{+}$, $^{209}Bi^{+}$, and $^{115}In^{+}$. To minimize polyatomic interferences, the instrument was adjusted to have < 2% oxide formation ($^{140}Ce^{16}O^{+}/^{140}Ce^{+}$) and doubly charged ion formation ($^{137}Ba^{2+}/^{137}Ba$). Tuning of the instrument (peak resolution, peak shape, and resolution axis) and detector calibration (linearity of pulse to analog counting mode) was performed via auto-tune. Internal standards (^{9}Be, ^{45}Sc, ^{115}In, ^{133}Cs, and ^{205}Tl) were introduced simultaneously to increase stability for minor/trace element analysis. Most elements were measured using the KED mode except for Li and Be, for which the standard mode was used instead. For minor and trace elements, no auto-dilution was applied, and a multi-element standard was prepared to cover a wide range of analyte concentrations (Table 2-1). Three runs were performed for each sample with the dwell time of 0.01 s for each monitored isotope. For major element analyses, a 50-fold PrepFAST auto-dilution using 2% Optima HNO_3 was applied with 3 runs for each sample, and the dwell time was set as 0.07 s for each isotope. Major element standards were prepared based on the analyte concentrations after auto-dilution (Table. 2-1). For both major and minor/trace element analyses, bracketing standards were run every 7 samples to correct for instrument drift. Instrumental blanks (0.5M HCl + 1% HNO_3 for trace/minor elements and 1% HNO_3 for major elements) were also regularly measured to watch for contamination. The RSD for each sample was < 10% (usually < 5%).

2.2.6 High-resolution ICP-MS

After the column procedure, Ag and Cd were measured on the Thermo Scientific high-resolution Element 2 ICP-MS in MEAL. The sample was introduced using a quartz spray chamber, and nickel sample and skimmer cones. Tuning of the instrument was performed by adjusting the torch position, sample gas flow, and the focus lenses to optimize instrument stability and sensitivity (RSD < 2%) for $^{7}Li^{+}$, $^{115}In^{+}$, and $^{238}U^{+}$ in the low-resolution mode, $^{56}Fe^{+}$ in the medium-resolution mode, as well as $^{39}K^{+}$ in the high-resolution mode. The instrument

mass bias was calibrated using a mixed high-purity natural Cd and Ag standard solution on a day-to-day basis. Four isotopes were monitored (^{109}Ag and ^{111}Cd as spiked isotopes, ^{107}Ag and ^{113}Cd as reference isotopes) in the low-resolution mode. Analyzed isotopes were detected under both the analog and counting mode with a mass window of 125%, search window of 80%, and an integration window of 80%. Mass bias throughout the run was monitored by the analyses of Cd and Ag standards every 7 samples, which was used to correct measured isotopic ratios (^{109}Ag/^{107}Ag, ^{111}Cd/^{113}Cd) in ID-MS. Additionally, instrumental blank (1% HNO_3) was also analyzed regularly. Each sample were measured with 3 runs and 8 passes, and the RSD was < 2% (usually < 1%).

2.3 Results and Discussions

2.3.1 Column calibration

Column elution patterns were similar for mixed high-purity standards and digested sediment reference materials (Figs. 2-2a vs. 2c, and 2-2b vs. 2d), suggesting that more complex sediment matrices only have minor impacts on the column performance. 0.5M HCl proved to be efficient in rinsing out Zr, Nb, and Mo (Zr especially, Fig. 2-2) without significant Ag/Cd elution. Zr was least retained by the column and eluted instantaneously upon sample loading. 4 mL of 0.5M HCl is shown to be sufficient to remove Zr (Fig. 2-2b and d). No elution peak was shown for Mo and Nb as low abundance prevailed in all elutions, except a Nb elution peak following the PACS-2 sediment standard sample (Fig. 2-2d). Both 4M and 8M HNO_3 are efficient in eluting Ag and Cd, yet the Ag elution peak occurred earlier when using 8M HNO_3 (2 mL 8M HNO_3 vs. 4 mL 4M HNO_3). Conversely, Cd is eluted faster with 4M HNO_3 (peak at 2 mL) than using 8M HNO_3 (peak at 4 mL). The Pedersen Lab procedure only collects the first 2 mL 8M HNO_3 for Ag/Cd analyses, but an additional 8M HNO_3 step suggested that subsequent elutions still contained higher Cd and Ag (Figs. 2-2a and c), which might have affected Ag/Cd recovery. The modified column procedures, however, extended the Ag/Cd aliquot collection to 6 mL of 4M HNO_3 to cover the entire Cd elution peak and the majority of Ag peak. The modified procedures thus increased Cd recovery from ~50 – 60% to 85 – 100%, and Ag recovery from ~50% to 75%. It is important to note that ^{109}Ag/^{107}Ag varies for each collection (e.g., 0 – 2 mL 4M HNO_3 vs. 4 – 6 mL 4M HNO_3 elution), indicating that a high Ag column recovery is needed to accurately capture the sample ^{109}Ag/^{107}Ag for isotope dilution. This modified procedure thus

improves the existing protocol by reducing acid usage with simplified steps and increasing analyte recoveries (Figs. 2-1 and 2-2).

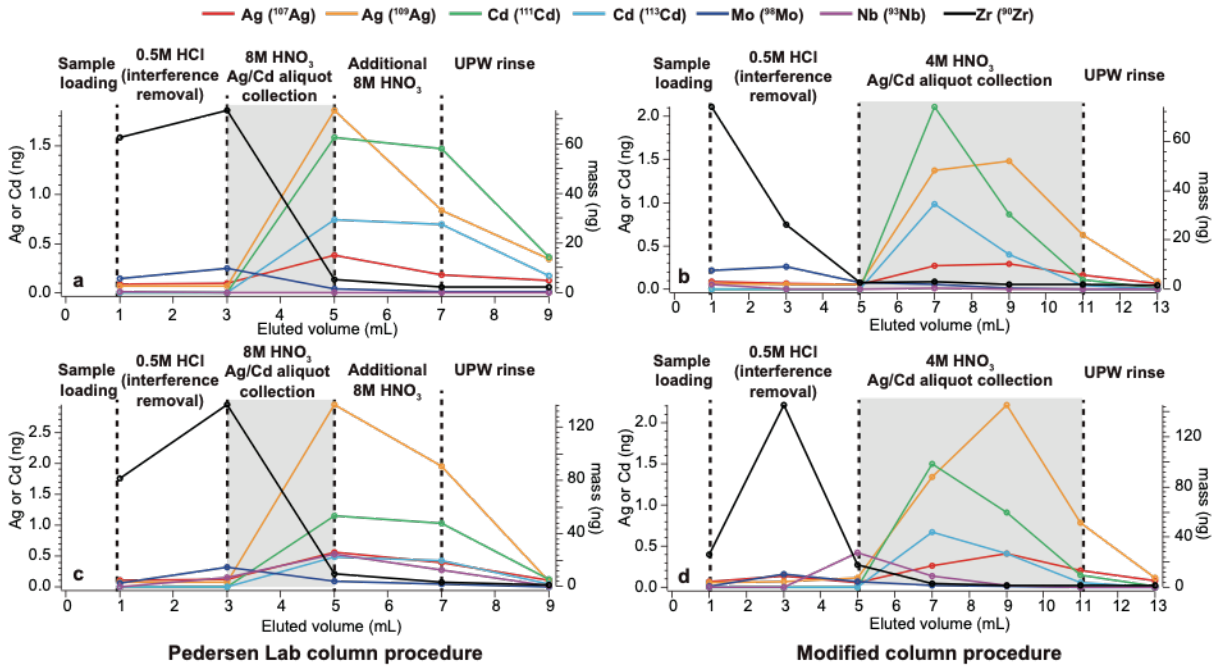

Figure 2-2 Column calibration for the Pedersen Lab and the modified procedures. Red, yellow, green, light blue, dark blue, purple, and black lines denote eluted masses of Ag measured from ^{107}Ag, Ag from ^{109}Ag, Cd from ^{111}Cd, Cd from ^{113}Cd, Mo from ^{95}Mo, Nb from ^{93}Nb, and Zr from ^{90}Zr, respectively.

2.3.2 Sensitivity and sensitivity to blank (S/B) ratios

Estimated concentration ranges (Table 2-1) for digested sediment samples are 5 (e.g., P) to 10000 (e.g., Ba) times higher than the limits of detection (LoD, 3SD of the instrumental blanks) shown in Table 2-2. Among all isotopes monitored, ^{34}S (not shown here) failed to show any linear relationship, which excludes the possibility of quantitatively determining sulfur using the iCAP Q ICP-MS. Some elements suffer from low sensitivity to blank ratios (S/B) and higher LoD due to high instrumental blanks (e.g., Na and K) and/or low sensitivity (e.g., P, Ca). However, due to the relatively high abundance of those major elements and thus high signals relative to the blanks, these elements could still be measured after testing against the sediment reference materials.

Table 2-2 Sensitivity, sensitivity to blank ratios (S/B), and limit of detection (LoD)

Major element analytes	Sensitivity (cps/(μg L^{-1}))	S/B	LoD (ng L^{-1})
^{23}Na	3225	0.65	0.12
^{24}Mg	1832	2.22	0.051
^{27}Al	1150	3.38	0.059
^{31}P	66	0.17	0.64
^{39}K	2659	0.05	0.74
^{44}Ca	154	0.63	0.35
^{48}Ti	8080	107	0.011
^{55}Mn	20550	448	0.0009
^{57}Fe	573	5.57	0.06
^{88}Sr	35101	1011	0.0005
^{138}Ba	81987	961	0.0005
Minor/trace element analytes			
^{7}Li	25653	51.25	0.026
^{51}V	15655	1.22	0.64
^{52}Cr	17855	36.13	0.18
^{59}Co	25741	669	0.021
^{60}Ni	6262	93.67	0.10
^{65}Cu	7761	41.83	0.39
^{68}Zn	3041	1.39	1.35
^{69}Ga	12781	121	0.26
^{72}Ge	4126	130	0.023
^{75}As	2307	35.11	0.048
^{78}Se	462	2.96	0.12
^{85}Rb	19824	89.45	0.19
^{89}Y	48317	476	0.03
^{90}Zr	68218	417	0.085
^{93}Nb	47880	313	0.025
^{98}Mo	18133	62.67	0.041
^{120}Sn	29258	61.83	0.032
^{123}Sb	17638	111	0.018
^{126}Te	2852	465	0.0065
^{139}La	108699	555	0.046
^{140}Ce	122316	278	0.11
^{177}Hf	38005	808	0.0047
^{181}Ta	137327	847	0.0041
^{184}W	48766	59.0	0.01
^{187}Re	102836	3840	0.0007
^{208}Pb	95445	85.61	0.20
^{209}Bi	152144	615	0.0066
^{232}Th	198873	408	0.021
^{238}U	184223	16355	0.0091

2.3.3 Accuracy and reproducibility

Repeated measurements of three sediment reference materials (SRM; MESS-3, PACS-2, and HISS-1) demonstrate the accuracy and reproducibility of our method for different sediment types. MESS-3 was obtained from the Beaufort Sea and represents continental margin sediments similar to the SBB sediments. PACS-2 was collected from a coastal region (Harbor of Esquimalt) subjected to heavy metal contamination, whereas HISS-1 was sampled from the Hibernia Shelf sediments associated with much lower organic carbon content and trace metal concentrations.

The RSD of certified elemental compositions in the SRMs can be highly variable (10 – 20%) and such heterogeneity of the SRMs is thus expected to introduce uncertainty in sample recoveries.

The digestion method used in this chapter results in variable recoveries for different SRMs (Tables 2-3, 2-4, and 2-5). New data reported here provide information on data validity for different elements, and caution should thus be taken when applying the same digestion method to different sediment types. Throughout an analyses period of ~2 – 3 months (September to December 2019), most major elements achieved a recovery of 90 – 110% for all three SRMs, with the exception of > 120% recovery for P, which might be due to low P sensitivity on the instrument. Measured Na and Ti concentrations for HISS-1 were also much higher than the certified values (Table 2-5). Despite these differences, our major element results are consistent with other studies using different digestion methods (e.g., diluted HCl in Townsend et al. (2007) and higher microwave temperatures employed in Roje (2010)), suggesting that our method provides comparable results with other published data. However, some minor/trace elements have significantly lower concentrations than certified values and previously published data, notably Cu, Li, and Pb (Table 2-5). Cu recovery was below 80% for the three SRMs, which may indicate a systematic Cu loss during the digestion process. Li and Pb show < 80% recoveries in one SRM (MESS-3 and PAC-2, respectively), and may be associated with either digestion efficiency for the specific SRM and/or heterogeneity of the SRM. Other lower recovery (80 – 90%) elements (e.g., Co, Cr, Mo, Ni, V, and U) are not significantly different from published results (Townsend et al., 2007). For U in particular, only informational values have been provided for SRMs, and measured values with long time stability should be more informative for elemental compositions in sediments. Ag and Cd analyses that applied the isotope dilution and column separation achieved great recovery (95 – 120%) for MESS-3 and HESS-1 sediments, yet low Ag recovery (< 80%) was observed for PACS-2. It is likely that incomplete Ag elution from the column in this high Ag concentration case may have led to $^{109}Ag/^{107}Ag$ uncertainties (Fig. 2-2). Our sediment samples, however, have Ag concentrations similar to MESS-3 (~200 ppb) and should therefore be less affected by the $^{109}Ag/^{107}Ag$ error produced by the column elution. More column calibration studies are needed to achieve higher Ag recovery before this methodology should be applied for Ag-rich settings.

Table 2-3 Elemental concentrations measured for MESS-3

Major elements	Certified	Observed (n = 23)	1SD	Recovery (%)	Townsend et al. (2007)	Roje (2010)
Al (%)	8.59 ± 0.23	7.92	0.84	92	8.89 ± 2.5	3.07 ± 0.32
Ca (%)	1.47 ± 0.06	1.27	0.15	86		
Fe (%)	4.34 ± 0.11	3.97	0.43	91	4.09 ± 0.36	3.73 ± 0.092
K (%)	(2.6)	2.47	0.27	95		1.55 ± 0.15
Mg (%)	(1.6)	1.61	0.17	100		
Na (%)	(1.6)	1.62	0.15	101		1.57 ±0.1
Ti (%)	0.44 ± 0.06	0.43	0.05	97		0.43 ± 0.1
Mn (ppm)	324 ± 12	298.51	29.17	92	322 ± 34	306 ± 4.84 (sic)
P (ppm)	(0.12)	0.14	0.02	117		
Sr (ppm)	129 ± 11	131.29	14.51	102	133 ± 6	92.6 ± 1.59
Ba (ppm)	-	953.04	104.0			575 ± 25.6
Minor/trace elements						
Sb (ppm)	1.02 ± 0.09	1.03	0.13	101	1.05 ± 0.06	0.73 ± 0.00
As (ppm)	21.2 ± 1.1	20.18	1.48	95	23 ± 6	20 ± 0.59
Cr (ppm)	105 ± 4	86.55	11.06	82	107 ± 20	104 ± 6.63
Co (ppm)	14.4 ± 2.0	12.07	0.85	84	14 ± 3	13.2 ± 0.44
Cu (ppm)	**33.9 ± 1.6**	**26.84**	**2.04**	**79**	**33 ± 14**	**31.1 ± 0.22**
Pb (ppm)	21.1 ± 0.7	17.52	1.50	83	20 ± 2	23.3 ± 0.06
Li (ppm)	**73.6 ± 5.2**	**53.60**	**10.40**	**73**		**67.8 ± 3.65**
Mo (ppm)	2.78 ± 0.07	2.38	0.18	86	2.6 ± 0.2	2.03 ± 0.09
Ni (ppm)	46.9 ± 2.2	39.26	3.34	84	46 ± 9	45.0 ± 0.02
Sn (ppm)	2.50 ± 0.52	2.06	0.22	82	2.4 ± 0.1	2.35 ± 0.11
U (ppm)	(4)	3.45	0.48	86	3 ± 0.3	3.79 ± 0.06
V (ppm)	243 ± 10	197.45	43.45	81	248 ± 34	234 ± 4.79
Zn (ppm)	159 ± 8	187.21	14.20	118	168 ± 20	145 ± 4.27
Ga (ppm)		165.11	28.86			
Ge (ppm)		6.83	0.76			
Y (ppm)		18.97	2.61			
Zr (ppm)		98.01	18.87			
Nb (ppm)		13.43	0.89			
Cs (ppm)		7.80	0.80			
La (ppm)		34.96	3.17			
Ce (ppb)		62.05	6.94			
Hf (ppm)		3.01	0.30			
Ta (ppm)		1.06	0.17			
W (ppm)		1.28	0.11			
Re (ppb)		3.23	0.40			
Bi (ppb)		257.17	18.24			
Th (ppm)		10.67	1.49			
Ag/Cd aliquot (IDMS)						

Ag (ppb)	180 ± 20	172.53	19.92	96		
Cd (ppb)	240 ± 10	234.35	14.50	98	220 ± 10	350

*Certified concentrations in parentheses are only informational values.
**Elements with a recovery lower than 80% or higher than 120% are bolded.

Table 2-4 Elemental concentrations measured for PACS-2

Major elements	Certified	Observed (n=9)	1SD	Recovery (%)	Townsend et al. (2007)
Al (%)	6.62 ± 0.32	6.24	0.46	94	6.55 ± 1.06
Ca (%)	1.96 ± 0.18	1.88	0.21	96	
Fe (%)	4.09 ± 0.06	3.97	0.34	97	3.94 ± 0.23
K (%)	1.24 ± 0.05	1.25	0.11	100	
Mg (%)	1.47 ± 0.13	1.38	0.10	94	
Na (%)	3.45 ± 0.17	3.42	0.29	99	
Ti (%)	0.443 ± 0.032	0.446	0.023	101	
Mn (ppm)	440 ± 19	422.32	27.67	96	431 ± 42
P (ppm)	**0.096 ± 0.004**	**0.120**	**0.017**	**125**	
Sr (ppm)	276 ± 30	268.25	20.38	97	270 ± 8
Ba (ppm)		894.10	81.80		
Minor/trace elements					
Sb (ppm)	11.3 ± 2.6	10.50	1.14	93	11.4 ± 1
As (ppm)	26.2 ± 1.5	25.22	1.89	96	29.4 ± 6
Cr (ppm)	90.7 ± 4.6	76.06	8.47	84	90 ± 15
Co (ppm)	11.5 ± 0.3	10.20	0.77	89	12 ± 2
Cu (ppm)	**310 ± 12**	**230.13**	**42.20**	**74**	**306 ± 25**
Pb (ppm)	**183 ± 8**	**132.72**	**31.56**	**73**	**158 ± 17**
Li (ppm)	32.2 ± 2.0	26.35	2.14	82	
Mo (ppm)	5.43 ± 0.28	4.79	0.50	88	4.9 ± 0.6
Ni (ppm)	39.5 ± 2.3	34.91	3.65	88	43 ± 6
Sn (ppm)	19.8 ± 2.5	17.94	2.91	91	20 ± 3
U (ppm)	**(3.)**	**2.12**	**0.19**	**71**	**1.97 ± 0.08**
V (ppm)	133 ± 5	106.83	17.00	80	138 ± 20
Zn (ppm)	364 ± 23	360.69	24.18	99	366 ± 28
Ga (ppm)		150.83	34.53		
Ge (ppm)		5.85	0.62		
Y (ppm)		12.47	1.01		
Zr (ppm)		52.59	5.49		
Nb (ppm)		7.53	0.54		
Cs (ppm)		1.75	0.25		
La (ppm)		16.08	5.09		
Ce (ppb)		28.66	11.04		
Hf (ppm)		1.63	0.15		
Ta (ppm)		0.62	0.10		

W (ppm)		1.07	0.09		
Re (ppb)		5.07	0.61		
Bi (ppb)		268.15	30.89		
Th (ppm)		3.42	0.32		
Ag/Cd aliquot (IDMS)					
Ag (ppb)	**1220 ± 140**	**945.31**	**112.68**	**77**	
Cd (ppb)	2110 ± 150	2381.04	145.85	113	2100 ± 30

*Certified concentrations in parentheses are only informational values.
**Elements with a recovery lower than 80% or higher than 120% are bolded.

Table 2-5 Elemental concentrations measured for HISS-1

Major elements	Certified	Observed (n=9)	1SD	Recovery (%)
Al (%)	0.73 ± 0.05	0.69	0.06	94
Ca (%)	1.14 ± 0.10	0.99	0.08	87
Fe (%)	0.246 ± 0.009	0.24	0.05	99
K (%)	0.332 ± 0.013	0.33	0.02	98
Mg (%)	0.075 ± 0.016	0.08	0.01	111
Na (%)	**0.373 ± 0.026**	**0.58**	**0.08**	**155**
Ti (%)	**0.076 ± 0.004**	**0.11**	**0.02**	**143**
Mn (ppm)	66.1 ± 4.2	66.66	10.04	101
Sr (ppm)	96.9 ± 11.2	98.51	8.21	102
P (ppm)		335.96	112.30	
Ba (ppm)		167.99	29.72	
Minor/trace elements				
Sb (ppm)	(0.13)	0.10	0.02	74
As (ppm)	0.801 ± 0.099	0.89	0.06	111
Cr (ppm)	**30.0 ± 6.8[1]**	**9.17**	**1.15**	**31**
Co (ppm)	**(0.65)**	**0.51**	**0.03**	**79**
Cu (ppm)	**2.29 ± 0.37**	**1.79**	**0.10**	**78**
Pb (ppm)	3.13 ± 0.40	2.59	0.16	83
Li (ppm)	2.83 ± 0.54	2.64	0.17	93
Mo (ppm)	(0.13)	0.11	0.04	83
Ni (ppm)	2.16 ± 0.29	1.74	0.16	81
Sn (ppm)	(0.11)	0.10	0.03	92
U (ppm)	(0.26)	0.26	0.05	100
V (ppm)	6.80 ± 0.78	5.75	0.69	85
Zn (ppm)	**4.94 ± 0.79**	**12.79**	**3.70**	**259**
Ga (ppm)		26.33	4.91	
Ge (ppm)		482.77	73.42	

Y (ppm)		2.28	0.18	
Zr (ppm)		19.12	4.27	
Nb (ppm)		1.44	0.32	
Ag/Cd aliquot (IDMS)				
Ag (ppb)	16 ± 2	18.01	3.85	113
Cd (ppb)	24 ±9	23.35	2.84	97

*Certified concentrations in parentheses are only informational values.
**Elements with a recovery lower than 80% or higher than 120% are bolded.
[1] The low Cr recovery for HISS-1 is expected as it contains a significant recalcitrant Cr and the certified value can only be obtained by extensive high-temperature chemical treatment using $HClO_4$ and H_2SO_4.

2.3.4 Comparison with ALS methodology

Due to the different acid matrices ($HF + HClO_4 + HNO_3$ in ALS vs. $HF + HCl + HNO_3$ in MEAL), digestion method (hotplate vs. microwave), instruments (ICP-AES and Q-IC-MS vs. HR-ICP-MS and Q-ICP-MS), and analysis method (isotope dilution), observed elemental concentrations may be significantly different. The majority of elemental concentrations are consistent within ~10% on average, especially for major elements (e.g., Al and Fe agree within 5%, Table 2-6). For minor and trace elements, > 20% inconsistencies can occur due to multiple reasons. One possibility is the lack of accuracy and precision in ALS results due to their analysis methods. No column chemistry or isotope dilution was applied in ALS, and thus Ag concentrations from ALS could be overestimated due to interferences – the negative difference values for most samples provides evidence of this potential problem. Rare earth elements are not fully digested in the ALS method as the company disclaims and our higher Hf concentrations indicate an incomplete Hf recovery from ALS. Additionally, the lack of precision in ALS results is prominent for several trace elements (e.g., Bi, Ta, Te, and Re). This may have contributed to the inconsistencies between the two methods. Another error source is our digestion method, which shows low (< 80%) recovery for Pb (in PACS-2) and high recovery (> 120%) for P (PACS-2) and Zn (HISS-1). It is possible that errors in our digestion method recovery may have led to inconsistent Pb, P, and Zn concentrations. Two elements, Ga and Ge, show much higher concentrations using the MEAL method. It is likely that the digestion efficiency for these elements is low when the ALS method is applied. It is also noteworthy that the ALS instrument blank for Ge can be comparable (0.13 ppm) to the reported data, and thus Ge concentrations from ALS are less valid. Since neither of the two elements was certified by SRMs, more information is required to determine the error sources of Ga and Ge.

Table 2-6 Data comparison between ALS method and the MEAL method

Elements	Sample ID									
	6_12	**6_147**	**7_86**	**8_45**	**1_53**	**2_197**	**3_275**	**4_42**	**6_110**	Average (%)
Ag (ppb)	*220*	*190*	*220*	*180*	*250*	*220*	*190*	*220*	*200*	
	169.57	163.0	149.6	184.0	226.3	212.9	211.0	165.8	180.7	
Difference (%)	**-22.92**	-14.21	**-32.02**	2.23	-9.47	-3.24	11.02	**-24.66**	-9.66	-11.43
Al (%)	*6.77*	*6.84*	*6.4*	*6.09*	*8.16*	*6.44*	*8.43*	*8.01*	*8.69*	
	6.13	6.74	6.16	6.57	8.51	6.18	8.14	7.23	8.57	
Difference (%)	-9.39	-1.41	-3.74	7.92	4.28	-3.99	-3.38	-9.72	-1.34	-2.31
As (ppm)	*20.7*	*14*	*13*	*10.9*	*6.6*	*17.2*	*3.9*	*5.1*	*5.8*	
	13.45	12.73	13.82	11.70	7.94	17.40	4.72	5.32	6.67	
Difference (%)	**-35.02**	-9.04	6.32	7.31	**20.36**	1.15	21.05	4.25	15.03	3.49
Ba (ppm)	*580*	*560*	*550*	*550*	*620*	*510*	*610*	*590*	*650*	
	512	554	519	588	629	476	578	501	606	
Difference (%)	-11.73	-1.13	-5.61	6.92	1.42	-6.71	-5.28	-15.06	-6.77	-4.88
Bi (ppb)	*190*	*200*	*200*	*190*	*310*	*160*	*280*	*270*	*300*	
	127.8	149.3	137.3	151.3	247.8	148.0	232.0	193.8	253.0	
Difference (%)	**-32.74**	**-25.34**	**-31.33**	**-20.38**	**-20.07**	**-7.53**	**-17.14**	**-28.23**	**-15.68**	**-22.05**
Ca (%)	*4.89*	*3.88*	*4.65*	*5.45*	*1.77*	*4.14*	*1.45*	*2.04*	*1.73*	
	4.19	3.63	4.07	5.35	1.68	3.73	1.23	1.63	1.56	
Difference (%)	-14.26	-6.45	-12.40	-1.80	-4.83	-9.91	-15.46	**-20.06**	-9.98	-10.57
Cd (ppb)	*2070*	*1800*	*2830*	*2880*	*1620*	*2240*	*1420*	*1770*	*1120*	
	2258	1974	2902	3183	1781	2064	1456	2012	1395	
Difference (%)	9.08	9.68	2.53	10.54	9.92	-7.85	2.52	13.66	**24.54**	8.29
Ce (ppm)	*67.7*	*68.4*	*59.5*	*60.5*	*92.1*	*63.8*	*92.1*	*78.6*	*88.1*	
	53.02	56.00	54.28	55.68	86.84	57.80	80.84	74.58	86.77	
Difference (%)	**-21.68**	-18.12	-8.78	-7.96	-5.71	-9.40	-12.22	-5.12	-1.50	-10.06
Co (ppm)	*8.8*	*9.7*	*9.1*	*9.1*	*15.4*	*9.3*	*13.8*	*11.5*	*12.6*	
	8.54	8.99	9.00	8.97	16.49	9.58	14.09	11.79	14.57	
Difference (%)	-2.91	-7.33	-1.14	-1.46	7.06	2.98	2.09	2.55	15.62	1.94
Cr (ppm)	*92*	*84*	*92*	*85*	*91*	*88*	*98*	*98*	*86*	
	84.56	81.17	94.84	90.41	101.1	86.05	104.7	98.62	89.73	
Difference (%)	-8.09	-3.37	3.09	6.37	11.12	-2.22	6.88	0.63	4.34	2.08
Cu (ppm)	*31.1*	*28.5*	*29.3*	*28*	*44.4*	*31.9*	*45.2*	*42.9*	*40.3*	
	23.42	22.31	25.15	23.91	39.03	26.98	37.31	34.09	35.71	
Difference (%)	**-24.69**	**-21.72**	-14.17	-14.60	-12.10	-15.43	-17.46	**-20.55**	-11.39	-16.90
Fe (%)	*4.56*	*4.47*	*3.83*	*4.03*	*4.34*	*4.41*	*4.04*	*4.13*	*4.54*	
	3.79	4.44	3.68	4.26	4.48	4.17	3.87	3.55	4.44	
Difference (%)	-16.85	-0.69	-3.83	5.81	3.33	-5.49	-4.13	-13.97	-2.20	-4.23
Ga (ppm)	*19.15*	*18.1*	*17.05*	*16.6*	*22.4*	*17.35*	*24.2*	*23.8*	*23.5*	
	78.45	115.8	88.15	91.08	144.4	82.14	99.10	87.33	138.2	

Difference (%)	**309.67**	**539.6**	**417.0**	**448.7**	**544.5**	**373.4**	**309.5**	**267.0**	**488.0**	**410.83**
Ge (ppm)	*0.07*	*0.14*	*0.13*	*0.15*	*0.18*	*0.16*	*0.2*	*0.08*	*0.09*	
	6.96	7.01	6.97	7.51	8.67	7.82	7.59	7.48	7.74	
Difference (%)	**9838**	**4909**	**5262**	**4904**	**4718**	**4786**	**3694**	**9250**	**8503**	**6207**
Hf (ppm)	*1.2*	*1.2*	*1.2*	*1.2*	*1.3*	*1.1*	*1.4*	*1.3*	*1.2*	
	1.23	1.16	1.35	1.29	1.49	1.27	1.42	1.38	1.52	
Difference (%)	2.53	-3.38	12.42	7.32	14.49	15.27	1.17	6.46	**26.91**	9.24
K (%)	*2.06*	*2.05*	*1.9*	*1.85*	*2.59*	*1.98*	*2.65*	*2.49*	*2.68*	
	1.91	2.10	1.85	2.04	2.76	1.93	2.57	2.27	2.68	
Difference (%)	-7.39	2.62	-2.84	10.08	6.75	-2.30	-3.14	-9.01	-0.01	-0.58
La (ppm)	*34.9*	*35.1*	*30.9*	*31.2*	*45.8*	*33.2*	*46.5*	*38.4*	*44*	
	26.90	28.19	27.84	28.68	42.81	29.20	40.15	37.35	42.26	
Difference (%)	**-22.93**	-19.69	-9.90	-8.08	-6.54	-12.06	-13.67	-2.74	-3.96	-11.06
Li (ppm)	*50.9*	*45.5*	*43.8*	*41.4*	*61.3*	*46.4*	*64*	*67.5*	*69.3*	
	41.52	5.98	46.53	40.45	62.35	41.62	58.33	55.06	64.78	
Difference (%)	-18.42	**-86.87**	6.24	-2.30	1.72	-10.30	-8.86	-18.44	-6.52	-15.97
Mg (%)	*1.68*	*1.6*	*1.6*	*1.56*	*1.84*	*1.64*	*1.87*	*1.98*	*1.93*	
	1.50	1.57	1.54	1.66	1.91	1.57	1.83	1.74	1.90	
Difference (%)	-10.46	-1.88	-3.95	6.57	3.63	-4.30	-2.12	-12.31	-1.69	-2.95
Mn (ppm)	*303*	*314*	*282*	*281*	*357*	*296*	*333*	*340*	*387*	
	279.3	317.6	275.1	305.6	383.0	299.1	333.6	302.9	393.4	
Difference (%)	-7.81	1.14	-2.46	8.75	7.28	1.05	0.17	-10.92	1.65	-0.13
Mo (ppm)	*24.7*	*13.75*	*16.65*	*15.65*	*4.58*	*11.3*	*2.16*	*2.65*	*1.79*	
	19.03	11.17	15.59	13.55	4.43	9.82	2.15	2.30	1.76	
Difference (%)	**-22.97**	-18.74	-6.38	-13.42	-3.28	-13.08	-0.60	-13.17	-1.51	-10.35
Na (%)	*2.39*	*2.39*	*2.28*	*2.29*	*2.33*	*2.73*	*2.13*	*2.31*	*2.24*	
	2.28	2.44	2.32	2.50	2.54	2.71	2.24	2.10	2.24	
Difference (%)	-4.77	2.04	1.86	9.03	8.90	-0.59	5.29	-9.05	0.06	1.42
Nb (ppm)	*11.7*	*11.3*	*10.4*	*10.3*	*15*	*10.7*	*14.5*	*14.5*	*14.5*	
	10.62	11.06	11.07	11.08	15.89	11.20	14.52	14.04	15.35	
Difference (%)	-9.27	-2.09	6.45	7.62	5.96	4.67	0.15	-3.19	5.88	1.80
Ni (ppm)	*51.2*	*45.6*	*49.9*	*44.8*	*55.6*	*50.4*	*58.2*	*43.7*	*42.9*	
	42.49	39.20	46.91	42.71	54.12	45.37	52.64	37.64	42.66	
Difference (%)	-17.02	-14.03	-5.99	-4.67	-2.66	-9.99	-9.56	-13.86	-0.56	-8.70
P (ppm)	*1120*	*1120*	*1150*	*1140*	*1080*	*1110*	*1070*	*1160*	*1050*	
	1205	1249	1202	1523	1327	1375	1298	1306	1273	
Difference (%)	7.60	11.56	4.51	**33.61**	**22.89**	**23.87**	**21.28**	12.58	**21.21**	17.68
Pb (ppm)	*13.2*	*13.5*	*12*	*12.4*	*19.1*	*12.8*	*19.3*	*17.6*	*17.9*	
	9.23	10.33	9.67	10.34	15.58	10.23	14.73	12.85	15.66	
Difference (%)	**-30.09**	**-23.47**	-19.45	-16.58	-18.42	**-20.09**	**-23.67**	**-27.00**	**-12.52**	**-21.26**
Rb (ppm)	*110.5*	*112.5*	*103*	*100.5*	*145.5*	*106*	*151.5*	*121.5*	*142*	
	102.0	103.3	106.4	106.8	156.2	108.0	148.9	135.2	147.4	

Difference (%)	-7.71	-8.22	3.30	6.24	7.36	1.91	-1.70	11.24	3.81	1.80
Re (ppb)	*23*	*10*	*20*	*12*	*6*	*10*	*5*	*7*	*4*	
	20.91	11.91	21.49	15.25	7.58	9.77	5.85	7.36	5.66	
Difference (%)	-9.10	19.09	7.43	**27.12**	**26.38**	-2.33	16.95	5.14	**41.53**	14.69
Sb (ppm)	*1.9*	*1.58*	*1.59*	*1.24*	*1.48*	*2.16*	*1.28*	*1.64*	*1.28*	
	1.39	1.45	1.53	1.14	2.15	2.07	1.25	1.59	1.40	
Difference (%)	**-26.77**	-7.96	-3.53	-8.36	**45.24**	-4.24	-2.26	-3.32	9.65	-0.17
Sn (ppm)	*2*	*1.9*	*1.8*	*1.8*	*2.4*	*1.9*	*2.5*	*2.4*	*2.2*	
	1.69	1.65	1.73	1.82	2.65	1.77	2.23	2.37	2.38	
Difference (%)	-15.38	-13.15	-4.05	1.30	10.53	-6.86	-10.84	-1.43	8.31	-3.51
Sr (ppm)	*385*	*329*	*360*	*413*	*219*	*338*	*199.5*	*233*	*214*	
	313.2	301.2	323.2	398.0	211.6	299.2	182.4	187.9	197.4	
Difference (%)	-18.64	-8.45	-10.24	-3.62	-3.38	-11.47	-8.59	-19.37	-7.77	-10.17
Ta (ppb)	*750*	*760*	*730*	*730*	*1020*	*720*	*980*	*940*	*950*	
	910	964	966	1008	1378	977	1257	1197	1373	
Difference (%)	**21.38**	**26.85**	**32.34**	**38.05**	**35.13**	**35.67**	**28.27**	**27.40**	**44.53**	**32.18**
Te (ppb)	*60*	*60*	*60*	*70*	*<0.05*	*50*	*60*	*<0.05*	*60*	
	45.16	33.69	45.45	47.57	52.99	51.37	36.02	38.38	34.89	
Difference (%)	**-24.74**	**-43.85**	**-24.24**	**-32.04**	**-**	2.74	**-39.97**	**-**	**-41.86**	**-29.14**
Th (ppm)	*11.7*	*11.1*	*9.9*	*9.9*	*15.9*	*10.9*	*16*	*14.4*	*15.3*	
	9.27	9.82	9.42	9.68	14.58	10.16	13.69	13.19	15.22	
Difference (%)	**-20.75**	-11.49	-4.88	-2.22	-8.32	-6.77	-14.46	-8.42	-0.53	-8.65
Ti (%)	*0.384*	*0.384*	*0.37*	*0.346*	*0.462*	*0.364*	*0.465*	*0.465*	*0.486*	
	0.39	0.42	0.41	0.43	0.52	0.41	0.49	0.45	0.52	
Difference (%)	1.82	9.39	11.03	**24.24**	13.06	12.46	5.81	-2.49	7.22	9.17
U (ppm)	*9.8*	*5.4*	*7.1*	*6.1*	*4.1*	*4.7*	*4.6*	*3.8*	*3.6*	
	8.21	4.71	6.41	5.56	3.82	3.84	3.99	3.41	3.63	
Difference (%)	-16.26	-12.70	-9.67	-8.83	-6.83	-18.25	-13.23	-10.15	0.96	-10.55
V (ppm)	*155*	*138*	*149*	*142*	*167*	*146*	*174*	*181*	*167*	
	159.9	132.2	159.8	159.7	193.6	165.5	188.0	188.7	175.5	
Difference (%)	3.13	-4.16	7.21	12.45	15.92	13.38	8.08	4.24	5.07	7.26
W (ppm)	*1.2*	*1.3*	*1.2*	*1.2*	*1.7*	*1.3*	*1.7*	*1.5*	*1.6*	
	1.09	1.14	1.15	1.19	1.69	1.19	1.53	1.41	1.71	
Difference (%)	-8.91	-12.61	-4.55	-0.94	-0.72	-8.15	-10.09	-5.94	7.17	-4.97
Y (ppm)	*20.7*	*21.4*	*20.3*	*20.6*	*24.8*	*23*	*24.5*	*20.6*	*22*	
	17.42	14.68	18.26	18.83	24.15	20.48	21.31	19.68	21.10	
Difference (%)	-15.82	**-31.41**	-10.07	-8.60	-2.63	-10.96	-13.03	-4.45	-4.09	-11.23
Zn (ppm)	*116*	*106*	*103*	*99*	*138*	*112*	*140*	*150*	*144*	
	119.0	118.2	127.8	125.2	167.3	130.3	158.1	154.0	156.0	
Difference (%)	2.60	11.55	**24.03**	**26.47**	**21.20**	16.35	12.93	2.70	8.34	14.02
Zr (ppm)	*39.2*	*43.6*	*42.4*	*39.7*	*41.7*	*38.1*	*43*	*40.1*	*37*	
	41.10	39.58	44.60	38.74	48.03	39.89	45.99	39.49	47.15	

Difference (%)	4.85	-9.23	5.20	-2.42	15.19	4.69	6.96	-1.51	**27.43**	5.68

* Data from ALS Global and Michigan Elemental Analysis Lab (MEAL) are in italic and regular font style, respectively. The concentration difference for each element was determined by (concentration from MEAL – concentration from ALS)/ concentration from ALS × 100%. Values with > 20% difference are bolded.

2.4 Conclusions

High-resolution paleoceanographic reconstructions require development of a bulk sediment elemental analysis method that allows rapid and simultaneous measurements of multiple elements. Prominent challenges, however, include low concentrations of some trace metals and severe interferences caused by the argon plasma and matrix effects. To overcome these difficulties, we modified the existing redox-sensitive trace metal analysis method (Morford, 1999) and developed a new method to measure major, minor, and trace elements from one digested sample using the quadrupole ICP-MS equipped with a collision cell. Repeated measurements of 3 sediment reference materials (SRM) suggest good recoveries (80 – 120%, mostly within 90 – 110%) for most elements. However, low recoveries (< 80%) of Cu, Li, and Pb and high P recoveries (> 120%) indicate that this method may not completely digest these elements and/or the quadrupole ICP-MS has difficulty to accurately determine these elemental compositions because of high instrumental blank or low sensitivity values. Additionally, we simplified the column procedure for Ag/Cd matrix separation by replacing 8M HNO_3 with 4M HNO_3, which improves Ag and Cd recoveries (to near 100% for Cd) and reduces acid usage. Isotopic dilution ICP-MS suggests great recovery for Ag and Cd (95% – 115%) in two sediment reference materials (MESS-3 and HISS-1), yet low Ag recovery (< 80%) for PACS-2 suggests caution should be employed when using our column procedure for high Ag sediments (> 1000 ppb).

A further comparison between the bulk sediment analytical method from ALS Global and the MEAL was conducted by comparing elemental composition data from the same set of Santa Barbara basin sediment samples. Overall the two methods show agreement within 10% for the majority of elements. The ALS method may have poor accuracy and precision for Ag, Bi, Hf, Re, Ta, and Te compared to the MEAL method, and P, Pb, and Zn from our method may not be accurate for comparison due to recovery issues. This bulk sediment element analysis method achieves rapid and simultaneous data collection for a suite of elements and can thus contribute to more high-resolution elemental reconstructions, especially for records from a continental margin setting.

2.5 References

Bruland, K.W., 1980. Oceanographic distributions of cadmium, zinc, nickel, and copper in the north Pacific. Earth and Planetary Science Letters, 47(1980): 176-198.

Calvert, S.E., Pedersen, T.F., 2007. Elemental Proxies for Palaeoclimatic and Palaeoceanographic Variability in Marine Sediments: Interpretation and Application, Developments in Marine Geology, pp. 567-644.

Cullen, J.T., Lane, T.W., Morel, F.M.M., Sherrell, R.M., 1999. Modulation of cadmium uptake in phytoplankton by seawater CO2 concentration. Nature, 402(6758): 165-167.

Dial, A.R., Misra, S., Landing, W.M., 2015. Determination of low concentrations of iron, arsenic, selenium, cadmium, and other trace elements in natural samples using an octopole collision/reaction cell equipped quadrupole-inductively coupled plasma mass spectrometer. Rapid Commun Mass Spectrom, 29(8): 707-18.

Guo, W., Hu, S., Zhang, J., Zhang, H., 2011. Elimination of oxide interferences and determination of ultra-trace silver in soils by ICP-MS with ion-molecule reactions. Sci Total Environ, 409(15): 2981-6.

Iglesias, M., Gilon, N., Poussel, E., Mermet, J.-M., 2002. Evaluation of an ICP-collision/reaction cell-MS system for the sensitive determination of spectrally interfered and non-interfered elements using the same gas conditions. Journal of Analytical Atomic Spectrometry, 17(10): 1240-1247.

McCurdy, E., Woods, G., 2004. The application of collision/reaction cell inductively coupled plasma mass spectrometry to multi-element analysis in variable sample matrices, using He as a non-reactive cell gas. Journal of Analytical Atomic Spectrometry, 19(5): 607-615.

Morford, J.L., 1999. The geochemistry of redox-sensitive trace metals, University of Washington.

Patterson, K.Y., Veillon, C., O'Haver, T.C., 1994. Error Propagation in Isotope Dilution Analysis As Determined by Monte Carlo Simulation. Analytical Chemistry, 66(18): 2829-2834.

Roje, V., 2010. Multi-elemental analysis of marine sediment reference material MESS-3: one-step microwave digestion and determination by high resolution inductively coupled plasma-mass spectrometry (HR-ICP-MS). Chemical Papers, 64(4).

Sargent, M., Harte, R., Harrington, C., 2002. Guidelines for Achieving High Accuracy in Isotope Dilution Mass Spectrometry (IDMS), Guidelines for Achieving High Accuracy in Isotope Dilution Mass Spectrometry (IDMS). The Royal Society of Chemistry, pp. 1-34.

Tanner, S.D., Baranov, V.I., Bandura, D.R., 2002. Reaction cells and collision cells for ICP-MS: a tutorial review. Spectrochimica Acta Part B: Atomic Spectroscopy, 57(9): 1361-1452.

Townsend, A.T. et al., 2007. Trace metal characterisation of marine sediment reference materials MESS-3 and PACS-2 in dilute HCl extracts. Mar Pollut Bull, 54(2): 236-9.

Yamada, N., 2015. Kinetic energy discrimination in collision/reaction cell ICP-MS: Theoretical review of principles and limitations. Spectrochimica Acta Part B: Atomic Spectroscopy, 110: 31-44.

Chapter 3

Diagenesis and Iron Paleo-redox Proxies: New Perspectives from Magnetic and Iron Speciation Analyses in the Santa Barbara Basin[1]

3.1 Abstract

Sedimentary redox proxies are usually employed to reconstruct the paleo-redox conditions of bottom water environments, assuming that porewater and bottom water dissolved oxygen concentrations are similar. Using a combination of geochemical and magnetic techniques, we investigate the relationship between iron speciation and mineralogy in recent (~1760 – 2009 CE) sediments retrieved from the Santa Barbara Basin (SBB) — a modern silled basin with low-oxygen (dissolved $O_2 < 10$ μmol/kg) and sporadically anoxic (no O_2 detected) bottom waters. Magnetic analyses reveal that biogenic magnetite is preserved in SBB sulfidic porewaters on at least decadal to centennial time scales. Highly-reactive Fe (oxyhydr)oxides remain preserved despite observed sulfidic porewaters, indicating incomplete pyrite conversion, and producing low Fe_{py} [pyrite Fe]/Fe_{HR} ratios. We attribute this observation to restricted porewater reaction kinetics under high sedimentation rates. Our results also reveal non-steady state diagenesis caused by instantaneous depositional events (e.g., turbidites and flood layers). The most reducing water column suggested by Fe speciation coincided with the *Macoma* layer, where *in situ* colonization of hypoxia-intolerant bivalve shells argues for the most oxygenated bottom water in the 250 year record. A turbidite potentially introduced fresh unsulfidized Fe_{HR} that buffered upward-diffusing sulfide from underlying sediments. Subsequent pyrite precipitation following re-establishment of sulfidic porewaters could have facilitated a "false positive" interpretation. In comparison, redox-sensitive metal enrichments (Mo_{EF}, U_{EF}, and Re_{EF}) were not obscured by post-depositional diagenesis and appear to accurately record redox geochemistry at the sediment-water interface.

[1] Published under the citation: Wang, Y., Hendy, I.L., Latimer, J.C., Bilardello, D., 2019. Diagenesis and iron paleo-redox proxies: New perspectives from magnetic and iron speciation analyses in the Santa Barbara Basin. Chemical Geology, 519: 95-109.

3.2 Introduction

Redox environments are central to both paleo- and modern oceanographic studies due to their relationship with atmospheric and/or oceanic oxygenation through geologic time. However, the limited timespan (several decades) of dissolved oxygen (DO) instrumental records in the oceans is insufficient to identify the potential extremes or full magnitude of DO change. To reconstruct past DO changes in the ocean, numerous approaches have been applied, of which sedimentary geochemical proxies (e.g., redox-sensitive metal enrichments, isotopes and speciation) are the most widely used. Geochemistry of these proxies depends directly on the ambient anoxic (no O_2 detected)/euxinic (sulfide-rich anoxic) conditions under which they were generated and then preserved. Iron speciation techniques in particular (Poulton and Canfield, 2005) have been widely used on sedimentary rocks as a redox proxy that can distinguish oxic, ferruginous (iron-rich anoxic water column), and euxinic water columns on different time scales (Cheng et al., 2016; Li et al., 2010; Li et al., 2015; Lyons et al., 2014; Lyons and Severmann, 2006; Reinhard et al., 2009; Tessin et al., 2016).

Extensive calibration on modern surface marine sediments has proven that Fe speciation can provide critical insights for identification of anoxic water columns. Aside from anoxic and fully-oxygenated depositional environments, low-oxygen water columns (dissolved $O_2 < 10$ μmol/kg) represent another important scenario for oceanic Fe cycling. These water column conditions are usually associated with redox processes in bottom waters and porewaters (e.g., nitrate, Mn, Fe oxyhydroxide, and sulfate reduction) and varied Fe mineral preservation in underlying sediments. Few investigations of Fe speciation exist in highly oscillatory low-O_2 water columns (Raiswell and Canfield, 1998; Scholz et al., 2014) with little attention given to understanding how Fe mineralogy diagenetically shifts down-core under such conditions. Iron mineralogy generated by overlying water columns may change in response to post-depositional diagenesis following shifts in porewater redox environments and/or instantaneous depositional events (e.g., flood layers and turbidites), which could obscure geochemical interpretations of ambient redox environments. Finally, there are few calibration studies of Fe speciation where independent mineralogy techniques were employed, all of which limits understanding of Fe proxy behavior in reducing sediments.

To investigate responses of Fe proxies (speciation and mineralogy) to ambient porewater redox conditions on centennial time scales down-core, we examined a recent sedimentary record

from Santa Barbara Basin (SBB), California. New insights into the behavior of Fe diagenesis in this continental borderland basin are provided by the prevailing low-oxygen (O_2 < 10 μmol/kg) and sporadically anoxic (no oxygen detected) bottom water conditions. Iron speciation measurements were made on a box core (SPR0901-04BC) to generate a high-resolution down-core geochemical record spanning the last 250 years. Paired to this record, rapid and non-destructive magnetic techniques were employed to identify specific Fe-bearing minerals and to investigate the response of these minerals to ambient porewater redox environments (Liu et al., 2012), thus providing independent Fe mineralogy to validate Fe speciation interpretations. Finally, using redox-sensitive metals (Re, U, Mo) as independent paleo-redox indicators, we compare different approaches to reconstructing DO change in SBB since ~1760 CE. Together, this multi-proxy approach allows us to revisit interpretations of Fe speciation and mineralogy results that have implications for reconstructing past oxygenation of ocean water columns.

3.3 Background

3.3.1 Site description

Located in the Southern California Bight, the Santa Barbara Basin is a near-shore silled basin with a maximum depth of ~590 m, and a sill depth of 475 m to the west and 230 m to the east (Fig. 3-1).

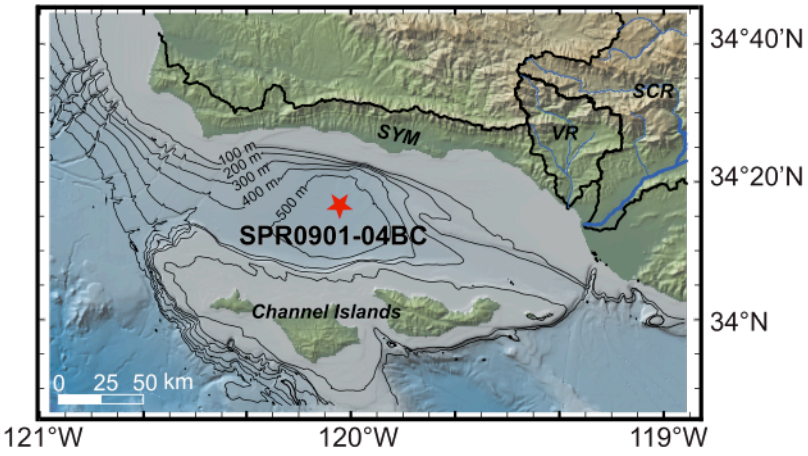

Figure 3-1 Map of the Santa Barbara Basin, California. The red star denotes the location of the SPR0901-04BC core site and river catchments are outlined in black: Santa Clara River (SCR), Ventura River (VR), Santa Ynez Mountain (SYM), and Channel Islands. Main stems of selected rivers are indicated by thick blue lines.

Low-oxygen (dissolved O_2 < 10 μmol/kg) subsurface water entering the basin becomes bathymetrically isolated and further depleted by the oxidant demand of high regional primary

productivity. Together, these features lead to a low-oxygen water column below 550 m water depth. Prevailing low-oxygen conditions with sporadic anoxia in SBB bottom waters contributes to intensive oxidant substitution near the sediment-water interface (SWI) and the subsequent preservation of laminated sediments (Schimmelmann et al., 1990; Soutar and Crill, 1977). The penetration depth of bottom water oxygen is typically less than 1 cm below the SWI in SBB, and a rapid succession of electron acceptors (from NO_3^- to Mn(IV), Fe(III), and SO_4^{2-}) occurs within the upper 5 cm of the sediment (Kuwabara et al., 1999; Reimers et al., 1990; Reimers et al., 1996). Sharp shifts of geochemical gradients in SBB sediments facilitate numerous biogeochemical processes (e.g., denitrification, microbe-mediated iron, manganese, and sulfate reduction), which in turn control redox-sensitive element geochemistry. Biogenic methane – the product of methanogenesis – starts to accumulate in the sulfate methane transition zone (SMTZ) at ~100 – 150 cm in SBB (Harrison et al., 2009; Komada et al., 2016). Both anoxic oxidation of methane (AOM) and sulfate reduction for anaerobic organic carbon degradation occur within the SMTZ, resulting in continued production of free sulfide (Berelson et al., 2005; Harrison et al., 2009). These low-oxygen yet highly variable bottom water redox environments make SBB an ideal location for examining high-resolution responses of sedimentary redox proxies (iron speciation and redox-sensitive trace metals) to water column DO changes. Typical box core lengths (62 cm for SPR0901-04BC) are insufficient to penetrate to the SMTZ (~100 – 150 cm depth), and thus diagenetic impacts of additional sulfide production by AOM in SMTZ could not be evaluated.

3.3.2 Paleo-redox proxies

3.3.2.1 Iron mineralogy

Preservation of Fe-bearing minerals and their responses to sedimentary diagenesis provide valuable information about redox conditions in their ambient environments. In oxic conditions, Fe (oxyhydr)oxides are frequently found in sediments including amorphous ferrihydrite, lepidocrocite (γ-FeOOH), crystalline and nanoparticulate goethite (α-FeOOH) (Poulton and Raiswell, 2005; van der Zee et al., 2003), hematite (α-Fe_2O_3), maghemite (γ-Fe_2O_3), and magnetite (Fe_3O_4) (Berner, 1981; Schwertmann, 2008). When free sulfide is present in porewaters or the water column, these minerals can be reductively dissolved and progressively converted to Fe sulfides including mackinawite (FeS), greigite (Fe_3S_4), and pyrite (FeS_2), although reactivity toward H_2S varies among different minerals (Poulton et al., 2004; Raiswell

and Canfield, 2012; Roberts, 2015). In addition, excessive reactive Fe can be trapped by Fe carbonate ($FeCO_3$, siderite) in strongly reducing conditions, notably in methanic environments where H_2S is absent (Berner, 1981; Roberts, 2015). Porewaters need to be supersaturated in HCO_3^- to form siderite (e.g., during methane oxidation in the presence of Fe(II)); however, these conditions are difficult to achieve in marine environments where sulfate concentrations are frequently high.

3.3.2.2 Iron speciation

Iron speciation is commonly employed in DO reconstructions because Fe reduction/oxidation is closely associated with redox potential. This technique extracts four groups of iron minerals (Fe carbonate, Fe oxyhydroxides, magnetite, and pyrite) to target three parameters — Fe_T [total Fe]/Al, Fe_{HR} [highly-reactive Fe]/Fe_T, and Fe_{py} [pyrite Fe]/Fe_{HR} — which can be used to distinguish between oxic, ferruginous, and euxinic conditions (Clarkson et al., 2014; Lyons and Severmann, 2006; Poulton and Canfield, 2011; Poulton and Raiswell, 2005). Carbonate-bearing Fe and Fe (oxyhydr)oxides are commonly considered to be highly reactive because these forms of Fe readily react with HS^- in early diagenetic stages. When combined with pyrite iron (Fe_{py}), carbonate-bearing Fe, and Fe (oxyhydr)oxides are collectively defined as the highly-reactive iron pool (Fe_{HR}) (März et al., 2008a; Poulton and Raiswell, 2005; Raiswell and Canfield, 2012). Fe_{HR}/Fe_T and Fe_T/Al proxies measure authigenic Fe enrichment relative to lithogenic input and are used as anoxia indicators to distinguish oxic from anoxic water columns (Clarkson et al., 2014; Lyons and Severmann, 2006; Raiswell and Canfield, 1998). Calibration studies on modern sediments indicate a threshold of $Fe_{HR}/Fe_T > 0.38$ for anoxic water columns (Poulton and Canfield, 2011; Raiswell and Canfield, 1998), while a lower Fe_{HR}/Fe_T threshold value of 0.22 has been suggested following calibration studies on Phanerozoic rocks (Poulton and Raiswell, 2002). In this study we use the modern anoxic water column calibration ($Fe_{HR}/Fe_T = 0.38$) due to the centennial timescale of our record. Fe_T/Al requires a baseline value to assess enrichments, and oxic Phanerozoic shale values (0.53 ± 0.11) are commonly applied to indicate anoxic environments (Clarkson et al., 2014; Lyons and Severmann, 2006; Poulton and Raiswell, 2005). Nevertheless, local lithogenic background values of Fe_T/Al should be used when location-specific anoxic thresholds are available (Clarkson et al., 2014; Lyons and Severmann, 2006), and thus a local anoxia threshold $Fe_T/Al = 0.54$ is used. This threshold is based on geochemical analysis of silt sized (grain size < 63 μm) SBB river sediments adjusted

for catchment contribution to SBB (Wang et al., 2017). Fe_{py}/Fe_{HR} measures the extent to which highly-reactive iron is sulfidized to pyrite. Under anoxic regimes ($Fe_{HR}/Fe_T > 0.38$), Fe_{py}/Fe_{HR} can differentiate euxinic ($Fe_{py}/Fe_{HR} > 0.7$~0.8, free sulfide present) from ferruginous ($Fe_{py}/Fe_{HR} <$ 0.7, anoxic with free Fe(II) present) water columns (Clarkson et al., 2014; Li et al., 2015; März et al., 2008b; Poulton and Canfield, 2011; Poulton et al., 2015). When $Fe_{HR}/Fe_T < 0.38$, high Fe_{py}/Fe_{HR} values (> 0.8) have also been used to indicate oxic water columns with porewater sulfide accumulation in organic carbon-rich sediments (e.g., the Friends of Anoxic Mud site (FOAM), Canfield et al. (1992); Hardisty et al. (2018); Raiswell and Canfield (1998); Raiswell et al. (2018)).

3.3.2.3 Trace metal enrichments

Independent of Fe proxies, redox-sensitive metals – notably Mn, Re, U, and Mo – can be used to reconstruct redox conditions, because their geochemical behavior differs as DO conditions change. In the presence of oxygen, Mn exists as insoluble Mn(IV) oxides and is readily scavenged into sediments; whereas in reducing environments, Mn (oxyhydr)oxides are subject to reductive dissolution to form Mn(III)-L (soluble Mn(III) complexed by inorganic or organic ligands) in low-oxygen porewaters (Madison et al., 2013) and to Mn(II) which can diffuse out of sediments as porewaters become more reducing. Thus, sedimentary Mn enrichment is frequently used to support an oxygenated water column (Calvert and Pedersen, 2007). Used jointly, multiple redox-sensitive elements (proxy suites) can improve interpretations of redox conditions. For example, free Mn(II) can also precipitate as $MnCO_3$ and/or co-precipitate with authigenic calcite in reducing porewaters with high alkalinity (Calvert and Pedersen, 1996; Mucci, 2004) to provide a false positive for oxic conditions, and thus Mn should be evaluated simultaneously with other redox-sensitive elements. Both Re and U have low detrital flux and behave conservatively in oxygenated waters (existing as ReO_4^- and $UO_2(CO_3)_2^{2-}$, respectively), and therefore are frequently used as tracers of low-DO conditions (Crusius and Thomson, 2000; Hendy and Pedersen, 2005; McManus et al., 2005; Morford and Emerson, 1999). In low-oxygen waters, Re and U have similar redox potentials and tend to be significantly enriched compared to crustal values as reduction produces Re(IV) oxides/sulfides and U(IV) precipitates (Calvert and Pedersen, 2007; Crusius et al., 1996; McManus et al., 2006; Tribovillard et al., 2006). Additionally, Re preservation in sediments may be associated with thiolation of ReO_4^- to particle-reactive $ReO_nS_{4-n}^-$ and/or co-precipitation with the Fe-Mo-S phase

in sulfidic waters. However, free sulfide levels in most euxinic water columns are usually insufficient to support thiolated ReO_4^- as major species (Helz and Dolor, 2012; Vorlicek et al., 2015).

Molybdenum primarily behaves conservatively in oxygenated water columns in the form of molybdate (MoO_4^{2-}) despite co-precipitation with Mn (oxyhydr)oxides (Scott et al., 2008; Tribovillard et al., 2006). In contrast to Re and U, however, Mo precipitation requires the presence of free sulfide (Crusius et al., 1996; Zheng et al., 2000). A key step in converting unreactive molybdate to authigenic Mo is the progressive formation of a thiomolybdate series ($MoO_xS_{4-x}^{2-}$, x=0~4) in the presence of free sulfide (Erickson and Helz, 2000; Helz et al., 1996; Tribovillard et al., 2006; Vorlicek et al., 2004), which are highly particle-reactive and readily scavenged into sediments. The subsequent removal/sequestration is thought to be associated with Fe-Mo-S cluster formation (Helz et al., 2011) and/or absorption onto sulfide-rich organic matter (Helz et al., 1996). Since the rate of Mo scavenging in sulfidic environments is significantly faster than in oxic ones, Mo enrichment is interpreted as an indicator of euxinic environments provided that coeval U enrichments are observed (Calvert and Pedersen, 2007; McKay et al., 2007; Scott et al., 2008; Tribovillard et al., 2006).

3.4 Methods

Box core SPR0901-04BC (34°16.895'N, 120°02.489'W, 588 m water depth) was collected in SBB in January 2009. The core contains an olive layer deposited by a turbidite associated with the 1812 Santa Barbara earthquake at a depth of 43 – 49 cm below the core top (cmbct) and two gray layers associated with flood events (a 0.7-cm-thick layer dated to 1861 – 62 CE at 38 cmbct and a 1.5-cm-thick layer dated to 1761 at 59 cmbct; Hendy et al. (2015)). SPR0901-04BC was stored at 4 °C until core splitting took place in January 2010. Porewater loss was observed in the cold room but visual inspections upon core splitting confirmed that the core interior had maintained its original appearance with dark sulfide-rich laminations. The split cores were encased in multiple layers of plastic wrap to minimize evaporation during storage at 4 °C. In 2013, the core was sampled at continuous 1-cm intervals (capturing ~2 – 7 years per sample) to obtain 62 bulk sediment samples. Discrete samples were immediately frozen to avoid oxidation and were then freeze-dried. Dried samples were ground to <75 μm for geochemical and magnetic analyses.

3.4.1 Magnetic measurements

Magnetic measurements on discrete freeze-dried samples were conducted at the Institute for Rock Magnetism, University of Minnesota. Magnetic measurements are summarized here. Detailed procedures are given in Appendix A. To quantify concentrations of magnetic minerals in bulk sediments, low-field mass magnetic susceptibility (χ) was determined at 1-cm intervals using an AGICO Kappabridge MFK1 susceptometer at room temperature, followed by measurements of anhysteretic remanent magnetization (ARM) and saturation isothermal remanent magnetization (SIRM, after application of a 1 T direct current field) on a 2G Enterprises superconducting quantum interference device (SQUID) passthrough magnetometer located in a magnetically shielded laboratory. ARMs were imparted using a 0.1 mT DC bias field and a 100 mT alternating field (AF).

Magnetic hysteresis properties were measured to produce first-order reversal curve (FORC) diagrams to illustrate the magnetic domain state of magnetic minerals and to allow further insights into Fe mineralogy. Hysteresis loops were measured on a Princeton Measurements Corporation MicroMag vibrating sample magnetometer (VSM) at room temperature with a maximum field of 1 T. Saturation magnetization (M_s), saturation remanence (M_{rs}), coercive force (B_c), and coercivity of remanence (B_{cr}) were determined from hysteresis loops (after a paramagnetic slope correction following Jackson and Solheid (2010)) and back-field remanence curves. 'Hard' isothermal remanent magnetization (HIRM, (SIRM+IRM_{-300})/2) and S-ratio (S_{-300} = -IRM_{-300mT}/SIRM) were obtained from hysteresis measurements. The L-ratio was then calculated following Liu et al. (2007) as HIRM/[0.5×(SIRM + IRM_{-100mT})], which is used to demonstrate relative contributions from hard (saturation field > 300 mT) with respect to intermediate-coercivity (saturation field between 100 mT and 300 mT) magnetic minerals. Additionally, first-order reversal curve (FORC) diagrams (Pike et al., 1999; Roberts et al., 2014; Roberts et al., 2000) were determined for selected samples on the VSM with an averaging time of 1-1.5 s and a saturating field of 0.7 T. On average, 170 – 200 individual FORCs were acquired for each sample. FORC diagrams were calculated and optimized using the variable smoothing approach (VARIFORC) (Egli, 2013) in the FORCinel package 3.0.3 (Harrison and Feinberg, 2008).

Temperature-dependent magnetic properties were also measured on selected samples to identify magnetic minerals with characteristic low-temperature transitions. Low-temperature

measurements were undertaken using a Quantum Design Magnetic Properties Measurement System (MPMS-5S). For zero-field-cooled (ZFC) and field-cooled (FC) remanence curves, samples were cooled to 10 K either in the absence of a magnetic field (ZFC) or in the presence of a 2.5 T field (FC). For FC measurements, the 2.5 T field was then switched off and the magnetic remanence was measured upon warming back to room (300 K) temperature in 5 K intervals. For ZFC, a low-temperature SIRM (LTSIRM) was imparted at 10 K, and remanence was measured every 5 K during warming. For low temperature cycling (LTC) remanence curves, a room temperature SIRM (RTSIRM) was first imparted on the sample, then the remanence was measured at 5 K steps during cooling (from room temperature to 10 K) and warming back to 300 K in a zero field. High-temperature measurements were performed on a Kappabridge susceptometer. For each sample run, ~200 – 300 mg of sample was weighed, heated from room temperature to 700 °C in air, and cooled to room temperature while measuring χ in 3 °C steps.

3.4.2 Iron speciation

The iron speciation method used has been adapted from the sequential Fe extraction protocol of Poulton and Canfield (2005) and chromium reducible sulfide extraction (CRS) following Canfield et al. (1986). Sequential Fe extraction was performed on 150~200 mg of the bulk sediment sample, and a further ~300 mg of the sample was used to trap chromium reducible sulfides. This procedure operationally defines four Fe pools as listed in Table 3-1. Each step in the sequential Fe extraction (the first three steps) was followed by centrifugation on a Thermo Scientific Sorvall Legend XT system (with the Thermo Scientific TX-750 rotor) at 3500 rpm (2684 × g) for 5 min before proceeding to the next treatment. Iron extracted in sequential Fe extraction was determined on a Perkin Elmer Optima 2100 DV inductively-coupled plasma optical-emission spectrometer (ICP-OES) at Indiana State University. Prior to analyzing the samples, optics was peaked using a 1 ppm Mn solution. Fe concentrations were determined following a standard 4-point calibration curve from a Perkin Elmer stock standard solution. Analytical precision was evaluated by comparison with replicate samples, which all agreed within 10%. Analytical accuracy was determined by incorporating known samples into the analysis and knowns agreed within 2%. The analytical detection limit for Fe was 0.06 ppm.

Table 3-1 Iron speciation procedure and intended target phases

Extraction procedure	Intended extracted Fe phases
10 mL 1 M sodium acetate solution (pH 4.5; buffered with acetic acid; shake for 24 h)	Fe_{ace}: Fe bound with carbonate
10 mL 50 g L^{-1} sodium dithionite solution (pH 4.8; buffered with 0.35 M acetic acid and 0.2 M sodium citrate; shake for 2 h)	Fe_{dith}: Fe (oxyhydr)oxides, (e.g., ferrihydrite, lepidocrocite, goethite, and hematite)
10 mL 0.2 M ammonium oxalate, and 0.17 M oxalic acid solution (pH 3.2, buffered with ammonium hydroxide, shake for 6 h)	Fe_{ox}: magnetite
40 mL 1 M $CrCl_2$ solution acidified to 0.5 M HCl (boiling for 2 h; bubbled with N_2, H_2S precipitated in zinc acetate trap)	Fe_{py}: assume that all chromium reducible sulfur is bound as pyrite

Operationally CRS measures ZnS precipitated from chromium reducible sulfide, which extracts all inorganic sulfur, including acid-volatile sulfur (AVS, e.g., mackinawite, pyrrhotite, and greigite), elemental sulfur (S^0), and pyrite. AVS extraction was not attempted because only freeze-dried samples were available, and thus AVS oxidation/loss during freeze-drying could not be excluded. CRS, as an alternative, measures all inorganic sulfur species and it is unaffected by potential Fe sulfide oxidation. Replicates on selected samples (15% of total samples) agree within ~6%. Previous work has shown that AVS is oxidized to a phase (e.g., elemental sulfur) that can still be extracted by CRS (Canfield et al., 1986; Lyons and Severmann, 2006; Raiswell and Canfield, 1998). In observational data, pyrite-bound sulfur always dominates inorganic sulfur in SBB with minor AVS (AVS-S/pyrite-S values of 0.06 – 0.12, Kaplan et al. (1963); Rickard and Morse (2005)) and negligible elemental sulfur contributions (< 2% of the total sulfur, Kaplan et al. (1963)), and thus the stoichiometrically determined pyrite-associated iron (Fe_{py}) from CRS provides the maximum pyrite abundance in the core with likely significant overestimation near the core top (Canfield et al., 1986). Highly-reactive Fe (Fe_{HR}) is thus defined as $Fe_{ace} + Fe_{dith} + Fe_{ox} + Fe_{py}$, which corresponds to Fe carbonate, Fe (oxyhydr)oxides, and pyrite. Total Fe (Fe_T) in bulk sediment was determined by ICP-MS and ICP-OES at ALS Laboratories in Vancouver, British Columbia (Hendy et al., 2015). Samples were digested with a hydrofluoric, nitric, perchloric, and hydrochloric cocktail. Lab standard (GBM908-10 and MRGeo08) replicates were used to verify elemental concentrations, and agreed within 2%. Unreactive silicate bound Fe (Fe_{UR}) is only reactive on 10^6-year or longer time scales and is determined from Fe_T-Fe_{HR}. Although the CRS protocol also extracts sulfur bound to other trace metals, this additional contribution should be negligible due to relatively low concentrations of those metals

(März et al., 2008a). Possible core oxidation will not affect Fe_{HR} and Fe_T measurements as oxidized Fe sulfides can be extracted as Fe_{dith} (Raiswell and Canfield, 1998).

To assess the extent of core oxidation after collection, Fe_{dith} in this study is compared to Raven et al. (2016), where dithionite extraction was performed on SBB sediments stored under nitrogen. Near the core top (above 23.5 cm), the two datasets agree within 10% (Table A-1). Higher Fe_{dith} values observed down-core (below 23.5 cm) in 04BC, relative to Raven et al. (2016), might result from pyrite oxidation. However, as CRS measures inorganic sulfur dominated by pyrite, the down-core Fe_{py} record should not be significantly altered. Additionally, possible Fe (oxyhydr)oxide inputs by instantaneous depositional events, inter-core variability, and seasonal changes in bottom water and porewater environments cannot be excluded and may have led to higher Fe_{dith} values in this study.

3.5 Results

3.5.1 Magnetic measurements

Magnetic properties used for Fe mineral identification are summarized in Table 3-2. High-temperature magnetic susceptibilities suggest that Fe sulfide is present (e.g., pyrite) throughout the core (Fig. A-4)(Passier et al., 2001), but neither siderite nor pyrrhotite are present in significant concentrations based on results from ZFC and FC remanence curves (Fig. A-2). Low-temperature cycling of a RTSIRM also indicates the presence of magnetite, maghemite, and a small amount of goethite, as do the FC-ZFC curves (Appendix A, Figs. A-2 and A-3). Based on down-core changes in magnetic mineralogy and magnetic mineral concentrations, the core has been subdivided into three distinct zones defined by a gradual decrease of stable magnetic minerals, coercivity (concentration-independent) shifts, and magnetic grain size changes (Appendix A).

Table 3-2 Magnetic properties for iron minerals (following Hunt et al. (1995))

Mineral	Magnetic properties	Saturation field (T)	Saturation magnetization (M_s, Am^2/kg)	Low-T cycling	Curie/Néel temperature (°C)
Magnetite (Fe_3O_4)	Ferrimagnetic		90 – 92	~120 K (Verwey transition, T_v)	580
Goethite (α-FeOOH)	Antiferromagnetic	Very high (> 1 T), B_c tail to > 700 mT in FORC distribution (Roberts et al., 2006)	~0.5	Large difference between FC and ZFC, with large (×2) and reversible RTSIRM increase at low-T (Dekkers, 1989a; Liu et al., 2006)	120 (Özdemir and Dunlop, 1996)
Hematite	Antiferromagnetic	High, B_c tail to >	~0.5	260 K (Morin transition)	675

(α-Fe_2O_3)	at room temperature	150 mT in FORC distribution (Roberts et al., 2006)			
Maghemite (γ-Fe_2O_3)	Ferrimagnetic	A quasi-circular peak centered at B_c = ~40 mT in FORC for SD particles (Carvallo et al., 2004)	~80	Hump-shaped RTSIRM curves (Özdemir and Dunlop, 2010)	645 (Özdemir and Banerjee, 1984)
Pyrite (FeS_2)	Paramagnetic				
Greigite (Fe_3S_4)	Ferrimagnetic	B_c peak at 70 – 85 mT for SD particles (Roberts et al., 2006)	~25	No transitions (Chang et al., 2009)	> 400 (Roberts et al., 2011)
Pyrrhotite ($Fe_{1-x}S$)	Ferrimagnetic (monoclinic)		~20	Besnus transition at 34 K for monoclinic type (Dekkers, 1989b) but no transition for hexagonal type (Horng and Roberts, 2018)	
Siderite ($FeCO_3$)	Paramagnetic			Sharp decay in FC warming curve until 37 K (Frederichs et al., 2003)	

In Zone 1 (0 – 35 cm below core top, cmbct), samples contain relatively high concentrations of stable ferrimagnetic minerals (Fig. 3-2). Notably, there is a significant contribution from single domain/vortex state (SD/vortex) mixtures of maghemite (formed by magnetite oxidation) in addition to biogenic and inorganic magnetite (Figs. 3-3, A-1, and A-3) (Roberts et al., 2017; Roberts et al., 2018). Interactive SD behavior in Zone 1 (e.g., 15 – 16 cm) could be attributed to collapse of biogenic magnetite chains (Harrison and Lascu, 2014). A trend toward coarser-grained ferrimagnetic Fe oxides with depth in Zone 1 is also indicated by the increased distribution along the B_u axis in the FORC diagrams (Fig. 3-3).

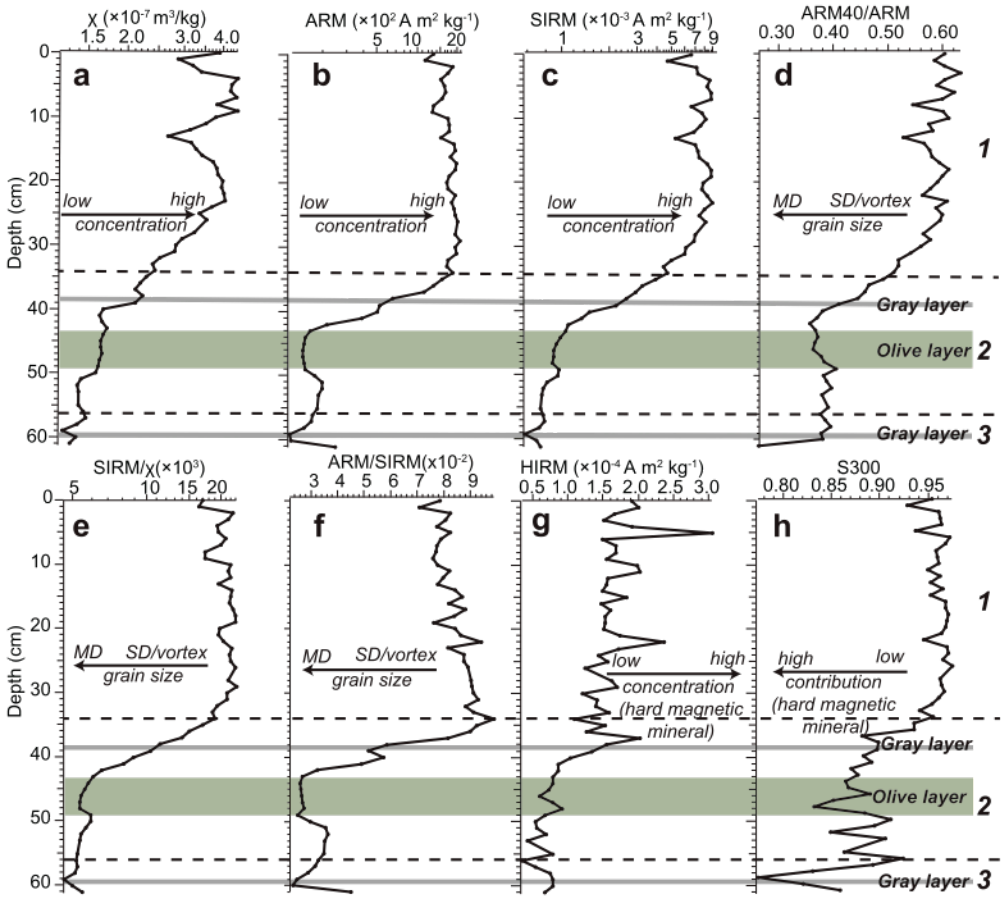

Figure 3-2 Down-core comparison of magnetic parameters for SPR0901-04BC from the Santa Barbara Basin. (a) Magnetic susceptibility χ; (b) anhysteretic remanent magnetization (ARM); (c) saturation isothermal remanent magnetization (SIRM); (d) ARM40 (ARM after demagnetization at 40 mT)/ARM; (e) SIRM/χ; (f) ARM/SIRM; (g) hard isothermal remanent magnetization (HIRM); (h) S300. Zonation (dashed lines) based on changes in magnetic mineral concentrations and concentration-independent properties is as follows: Zone 1 (0 – 35 cmbct), Zone 2 (35 – 56 cmbct), and Zone 3 (56 – 61 cmbct). Gray and olive layers are shaded in gray and dark green, respectively. Arrows indicate higher concentrations of magnetic minerals (a-c), larger magnetic grain sizes (d-f), higher concentrations of hard magnetic materials (g) or higher contributions from magnetically hard minerals (h). Susceptibility χ, ARM, SIRM, and SIRM/χ are plotted on logarithmic scales.

In Zone 2 (Fig. 3-2, 35 – 56 cmbct), samples undergo a major transition toward significantly lower magnetic mineral concentrations and a coarser magnetic grain size distribution (Fig. A-2). The dominant SD/vortex state mineral assemblages found in the core top are gradually replaced by vortex state/multi-domain (vortex/MD) magnetic minerals (Fig. 3-3) with an additional relatively higher contribution from high-coercivity minerals (e.g., hematite, Fig. 3-2h). Low-temperature measurements also reveal increased coarse detrital magnetite concentrations in sediments from the two instantaneous depositional events (Fig. A-2, the olive

turbidite layer associated with the 1812 Santa Barbara earthquake, and the 1861 – 62 gray layer associated with a flood deposit, Hendy et al. (2015)).

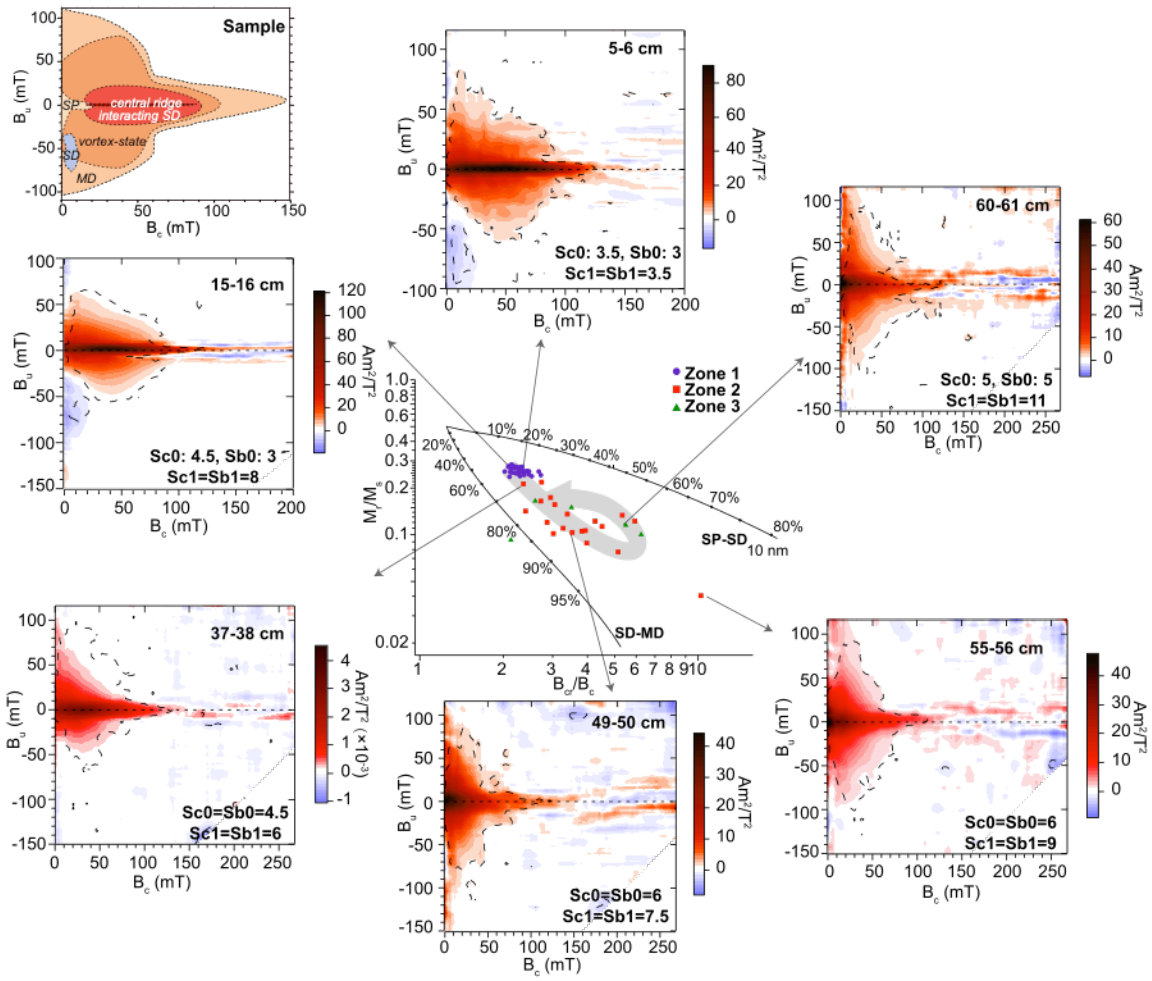

Figure 3-3 Day plot (Day et al. (1977)) and FORC distributions for selected samples from SPR0901-04BC. Samples from the three magnetic mineral zones are represented by purple circles (Zone 1: 0 – 35 cmbct), red squares (Zone 2: 35 – 56 cmbct), and green triangles (Zone 3: 56 – 61 cmbct), respectively. The Day plot is used to evaluate the down-core variation of hysteresis parameters. Theoretical SD-MD and SD-SP mixing lines for (titano-)magnetite are modified from Dunlop (2002) and are plotted for reference only. Selected FORC diagrams in each zone are shown surrounding the Day plot to further demonstrate mineralogy shifts down-core. A sample FORC distribution is shown on the top left to demonstrate typical patterns for different domain sizes following Roberts et al. (2014). Depths and VARIFORC parameters (Sc0, Sc1, Sb0, and Sb1) used are indicated on each FORC distribution following Egli (2013), and black dashed lines indicate 95% confidence envelope of the data.

Samples in Zone 3 (Fig. 3-2, 56 – 61 cmbct) have the lowest concentrations of magnetic minerals, yet the highest contribution of high-coercivity Fe oxides like hematite (Fig. 3-4). Similar to other instantaneous sediment depositional events in Zone 2, the 1.5-cm-thick gray layer associated with the 1761 flood (Hendy et al., 2015) exhibits coarser magnetic grain sizes and an abrupt but small increase in high-coercivity minerals (Figs. 3-2 and 3-4). Nevertheless, the slope (95% confidence level) of the L-ratio regression line in Zone 3 is significantly higher

than in Zone 2, indicating deposition of a 'harder' (higher-coercivity) mineral assemblage in the Zone 3 flood layer (1761 CE) relative to the turbidite (Fig. 3-4). Additionally, a reversal trend to lower B_{cr}/B_c values is observed in Zone 3. Similar trends have been reported in reducing diagenetic environments, including the northern California and Oman margins (Roberts, 2015; Rowan et al., 2009), where the reversal is associated with growth of SP greigite into the stable SD particles. Although SP greigite formation could occur, there is little evidence for a significant SD greigite contribution in Zone 3 as S-ratio and ARM/SIRM do not increase down-core (except the last data point, Fig. 3-2h and f), which would occur if 'soft' ferrimagnetic minerals have increased contributions (see Appendix A). Complete descriptions of the magnetic measurements are provided in Appendix A.

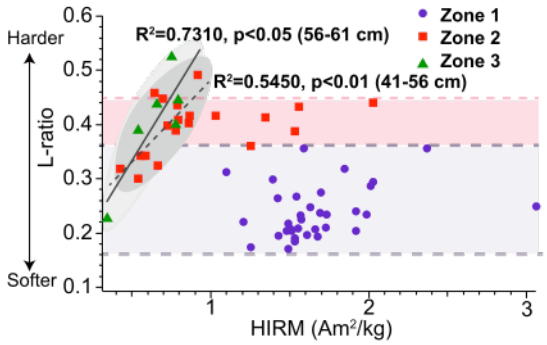

Figure 3-4 Cross-plot of magnetic parameters, L-ratios, and HIRM for core SPR0901-04BC. Samples from the three magnetic mineral zones are denoted by purple circles (Zone 1: 0 – 35 cmbct), red squares (Zone 2: 35 – 56 cmbct), and green triangles (Zone 3: 56 – 61 cmbct), respectively. The light purple and red shaded rectangles represent subsets of data for which L-ratios and HIRM are not correlated in Zone 1 and Zone 2, respectively. The dark and light gray shaded eclipses indicate subsets of data whose L-ratios and HIRM are correlated in Zone 2 and Zone 3. The gray dashed line and solid line represent the linear regression lines for data included by shaded eclipses for the Zone 2 (41 – 56 cm, including an olive turbidite layer at 43 – 49 cm) and Zone 3 (56 – 61 cm, including a gray flood layer at 59 – 60 cm), respectively. R^2 and p-values with depths for each zone are shown beside the regression lines. Correlations between L-ratios and HIRM indicate variable hematite coercivity and the possibility of hematite source shifts in the sediment record.

3.5.2 Geochemical Fe speciation

Carbonate-bound Fe isolated by acetate-extracted Fe (Fe_{ace}) varies from 0.02 to 0.20 wt. %, with the highest value occurring at the top of the core (Fig. 3-5a). Below 2 cm, Fe_{ace} sharply decreases and then oscillates within the range of ~0.04 – 0.15 wt. %. Minima occur in all three instantaneous sediment deposition events. A major decrease is observed below the gray layer at 38 cm, while the lowest value occurs within the olive layer (Fig. 3-5a). Below this layer, Fe_{ace} returns to values similar to Zone 1 samples, but declines again at 54 cm in association with the gray layer at 59 – 60 cm. Relative to Fe_{ace}, Fe (oxyhydr)oxides extracted by dithionite (Fe_{dith}) are more significant contributors to the reactive iron pool (Fe_{HR}). Although concentrations are more

variable (0.10 – 0.87 wt. % range), dithionite-extracted Fe typically accounts for ~30 – 60% of reactive iron (Table. A2). Fe_{dith} undergoes a gradual yet highly variable decline from 0.66 to 0.31 wt. % through Zones 2 and 3 (Fig. 3-5b). Concentrations of oxalate-extracted Fe (Fe_{ox}, likely associated with magnetite) are comparable to Fe_{ace} and range between 0.01 and 0.20 wt. % with no significant trend down-core (Fig. 3-5c).

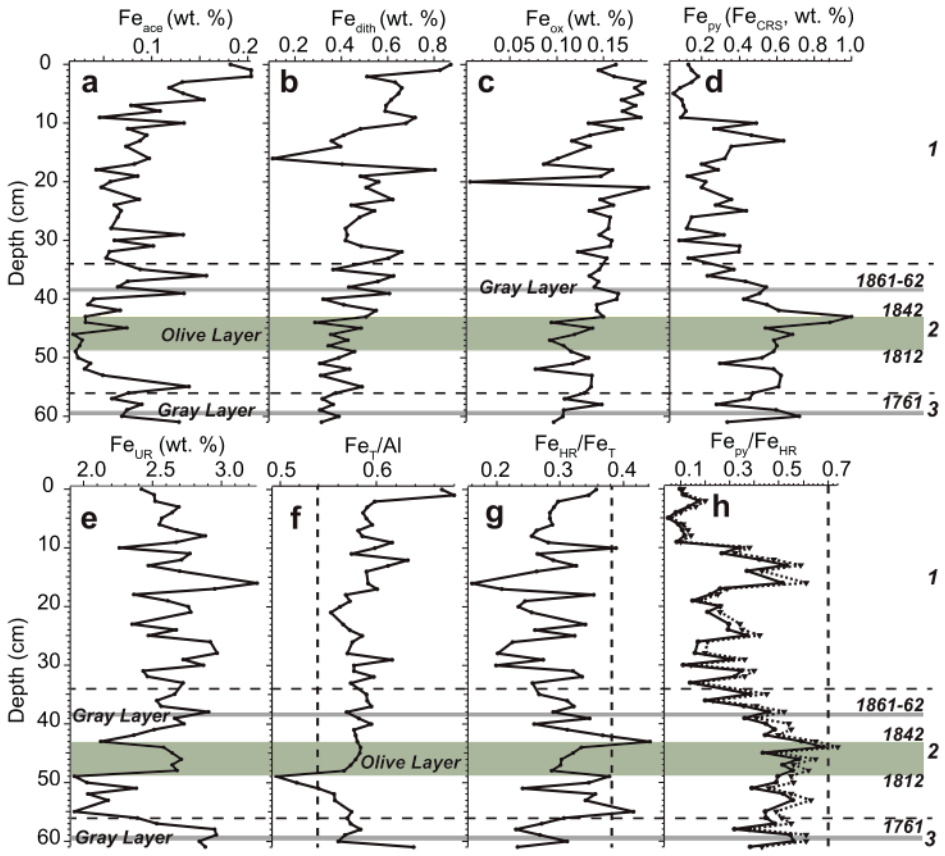

Figure 3-5 Down-core comparison of iron speciation profiles in SPR09091-04BC. (a) acetate extracted iron (Fe_{ace}); (b) dithionite extracted iron (Fe_{dith}); (c) oxalate extracted iron (Fe_{ox}); (d) chromium-reducible sulfur bound iron (Fe_{py} when assumed to be in pyrite form with stoichiometry of Fe:S=1:2); (e) unreactive iron (presumed to be silicate bound iron); (f) Fe_T (total iron)/Al, and the vertical dashed line shows the crustal value of 0.54; (g) Fe_{HR} (highly-reactive iron)/Fe_T, and the vertical dashed line denotes the anoxic threshold of 0.38; (h) Fe_{py}/Fe_{HR}. The dashed line denotes the high-FeS_2 (pyrite) scenario, where all magnetite is assumed to form from pyrite oxidation to demonstrate possible core oxidation effects. Zonation (dashed lines) based on changes in magnetic mineral concentrations and concentration-independent properties is as follows: Zone 1 (0 – 35 cmbct), Zone 2 (35 – 56 cmbct), and Zone 3 (56 – 61 cmbct). Gray bars represent gray layers (1761 CE and 1861 – 1862 CE) in the core while the turbidite layer (1812 – 1842 CE) is shaded in dark green.

Chromium reducible sulfur is used to represent Fe bound in pyrite (Fe_{py}) due to pyrite dominance. Fe_{py} generally follows the opposite trend to Fe_{ace} (correlation coefficient r = -0.4531, p = 0.0004), with the lowest values occurring at the core top (0.05 wt. %) and a local maximum at 10 cm (Fig. 3-5d). Below 13 cm, Fe_{py} returns to ~0.10 – 0.30 wt.% in Zone 1 but increases

again in Zone 2, reaching a maximum value of 1.00 wt.% above the olive layer (43 cm). In contrast to Fe_{ace}, local Fe_{py} maxima occur within both gray and olive layers. Unreactive iron (Fe_{UR}) is consistently dominant with a > 50% contribution to the total Fe throughout the core (Fig. 3-5e), and local maxima are shown in both gray layers. The olive layer, however, has two local minimum Fe_{UR} values at its top and bottom (2.12 and 1.93 wt.%, respectively) but Fe_{UR} values (~2.6 wt.%) remain consistent with background values within this layer (Fig. 3-5e).

An indicator of Fe enrichment – Fe_T/Al – suggests sustained elevated Fe preservation with respect to the local lithogenic background of 0.54 (Wang et al., 2017) with a range of 0.50 – 0.68 (Fig. 3-5f). The uppermost 2 cm has the highest Fe_T/Al ratio, below which Fe_T/Al varies around 0.6. There is no consistent trend down-core but declines are observed in instantaneous depositional events (gray and olive layers), notably a sharp decrease at the bottom of the olive layer where Fe_T/Al reaches its minimum value of 0.50. Although Fe enrichment is observed throughout the core, Fe_{HR}/Fe_T values are usually below the proposed anoxic threshold of 0.38 (Anderson and Raiswell, 2004; Canfield et al., 2007; Poulton and Canfield, 2011). Exceptions occur at 10 cm, 43 cm (top of the olive layer), and 55 cm, with the highest value (0.44) corresponding to the maximum Fe_{py} value at 43 cm (Fig. 3-5g). Local maxima are observed at the base of all three instantaneous depositional events and at the top of the turbidite. Finally, the proposed euxinic indicator (Fe_{py}/Fe_{HR}) ranges from 0.05 to 0.68, with the lowest values at the core top (0 – 10 cm) and the highest at the top of the olive layer (Fig. 3-5h). Again, discrete Fe_{py} maxima occur within the gray layers (Fig. 3-5d). The depositional redox environments according to the Fe proxies are summarized in a cross plot of Fe_{HR}/Fe_T and Fe_{py}/Fe_{HR} (Fig. 3-6). Most data fall within the oxic regime with the notable exception of three samples at 10, 43, and 55 cm, of which the 43-cm sample corresponds to the top of the olive layer. No systematic shifts between zones defined by magnetic parameters are observed in the cross plot.

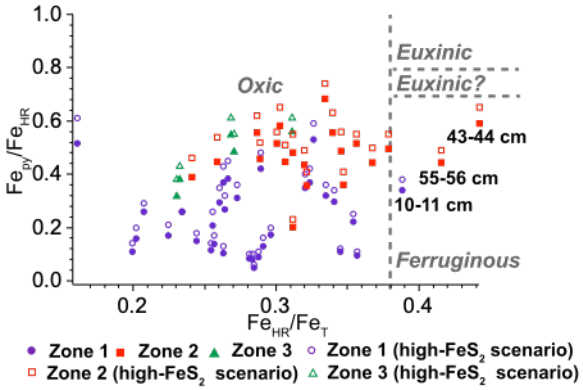

Figure 3-6 Cross-plot of Fe_{py}/Fe_{HR} vs. Fe_{HR}/Fe_T in core SPR0901-04BC. Samples from the three magnetic mineral zones are represented by purple circles (Zone 1: 0 – 35 cmbct), red squares (Zone 2: 35 – 56 cmbct), and green triangles (Zone 3: 56 – 61 cmbct), respectively. The hollow markers represent the high- FeS_2 (pyrite) scenario. The vertical dashed line indicates the threshold between oxic and anoxic water columns ($Fe_{HR}/Fe_T = 0.38$), respectively. In the anoxic regime, the horizontal dashed lines denote the threshold of euxinia at $Fe_{py}/Fe_{HR} = 0.7$~0.8. Depths for the three data points in the ferruginous region are indicated.

3.6 Discussion

3.6.1 Iron mineral identification from magnetic measurements

As magnetic measurements target specific Fe-bearing minerals, additional down-core mineralogical information can be used to constrain and inform geochemical Fe speciation results (summarized in Fig. 3-7). Both magnetic and Fe speciation measurements indicate that Fe oxides remain present throughout the core, yet magnetic measurements identify specific Fe-bearing mineral sources (e.g., maghemite and biogenic magnetite) that are not specifically targeted and/or addressed by Fe speciation techniques. Dithionite-extractable iron (Fe_{dith}) in sequential Fe extraction is often interpreted as the hematite and goethite contribution to the Fe mineral pool (Poulton and Raiswell, 2005; Tessin et al., 2016). In SBB sediments, magnetic measurements indicate only a minor contribution from hematite and goethite (especially in Zone 1, Appendix A), consistent with previous southern California Borderland basin studies (Leslie et al., 1990).

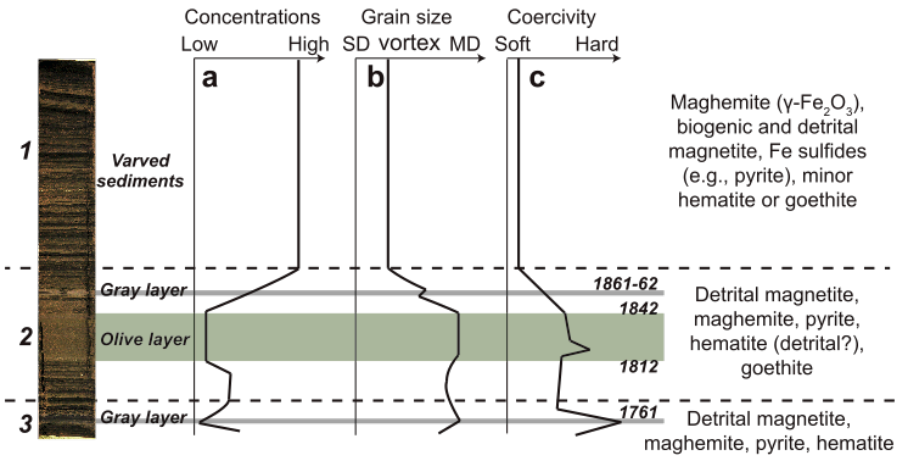

Figure 3-7 Summary of down-core mineralogy from magnetic measurements in core SPR0901-04BC. As in Fig. 3-2, zonation (dashed lines) based on changes in magnetic mineral concentrations and concentration-independent properties is as follows: Zone 1 (0 – 35 cmbct), Zone 2 (35 – 56 cmbct) and Zone 3 (56 – 61 cmbct), respectively. Left, core photo of SPR0901-04BC. Right, minerals identified in each zone according to magnetic measurements. (a) Concentration profile of magnetic minerals; (b) grain size profile: SD, vortex and MD denote single-domain, vortex-state and multi-domain particles, respectively; (c) coercivity of magnetic minerals. Gray bars (1761 CE and 1861-1862 CE) represent gray layers in the core while the turbidite layer (1812-1842 CE) is shaded in dark green.

Given that Fe_{dith} remains a significant contributor to Fe_{HR} (~30 – 60%, Fig. 3-5b), minerals other than hematite or goethite have likely been extracted as Fe_{dith} during sequential digestion. Hump-shaped RTSIRM curves and the shape of high-temperature χ curves suggest a significant contribution from maghemite (γ-Fe_2O_3) formed by magnetite oxidation (Figs. A-1 and A-2) (Chang et al., 2013; Özdemir and Dunlop, 2010). It is possible that Fe_{dith} reflects the presence of maghemite resulting from magnetite oxidation as the core was exposed to O_2 in storage, especially near the core top where magnetite oxidation is more significant (Appendix A, Fig. A-3). However, Fe_{dith} values in 04BC are similar to a nearby multicore that was stored under N_2 (Raven et al., 2016), which argues against maghemite formation from core oxidation. Instead, the significant contribution of maghemite with minor contributions from goethite and hematite in Fe_{dith} is likely sourced from detrital lithogenic sediments. With the same chemical formula as hematite (α-Fe_2O_3) but a different crystal structure, maghemite preservation has likely been overlooked in sulfidic marine environments.

Both FC and ZFC remanence curves contain a double-peak Verwey transition (T_v) feature (at ~100 °C and 120 °C), indicating the possible existence of biogenic magnetite near the core top (Fig. A-2, Zone 1) (Chang et al., 2016a). Transmission electron microscope (TEM) observations confirm the presence of intact cuboidal or prismatic single domain (SD) biogenic magnetite crystal chains in surficial SBB sediments (Chang and Kirschvink, 1989; Stolz et al.,

1986). These observations are consistent with the 'central ridge' feature in FORC diagrams for the samples near the SWI (e.g., Egli et al. (2010); Roberts et al. (2012), Fig. 3-3), further corroborating the presence of biogenic magnetite in Zone 1 of the SBB sediments (Fig. A-2). Similar patterns in FC and ZFC derivatives have been reported in north Arabian Sea oxygen minimum zone sediments (Chang et al., 2016a; Chang et al., 2016b) associated with sulfidic porewater environments similar to SBB. Together, these observations indicate that biogenic magnetite preservation in low-oxygen (suboxic) sedimentary environments might be more common than predicted by abiotically-controlled geochemistry in reducing environments, on the decadal to centennial timescale of recent/modern sediments. However, fine-grained biogenic magnetite remains unstable in sulfidic porewater environments (e.g., the lack of double-peak T_v in Zone 2 and 3), and should be dissolved completely as diagenesis continues (e.g., additional sulfide production in SMTZ via AOM and anaerobic organic carbon degradation) over longer time scales (Roberts, 2015). Further study of Fe minerals over millennial- and longer time scales is needed, however, to support biogenic magnetite preservation under sulfidic porewater conditions in the geologic record.

Biogenic magnetite production has been attributed to either biologically-controlled mineralization by magnetotactic bacteria or biologically-induced mineralization by dissimilatory Fe-reducing bacteria. Magnetotactic bacteria produce magnetite with highly-controlled grain sizes and morphology (Bazylinski and Frankel, 2004; Roberts, 2015). Based on non-interacting SD behavior (Fig. 3-3) (Egli et al., 2010; Roberts et al., 2012), observed SD biogenic magnetite in SBB sediments in Zone 1 are likely associated with nitrate-reducing magnetotactic bacteria that occupy sharp redox gradients near the base of nitrogenous zones (e.g., near the sediment-water interface in SBB) (Bazylinski and Frankel, 2004; Kopp and Kirschvink, 2008; Roberts, 2015).

3.6.2 Iron mineral preservation in rapidly-accumulated reducing sediments

Although highly-reactive Fe (oxyhydr)oxides are widely preserved in most marine sediments, under sulfidic porewater conditions it is assumed that they readily dissolve and are reduced to generate Fe sulfides (Raiswell and Canfield, 2012). It has been proposed that porewater sulfide does not increase to detectable levels until highly-reactive Fe (oxyhydr)oxides are completely consumed, based on field observations at the FOAM site, Long Island Sound, Connecticut (Canfield, 1989; Canfield et al., 1992). Poulton et al. (2004) used synthetic Fe

(oxyhydr)oxides and estimated reduction half lives ($t_{1/2}$) of hours (e.g., 12.3 h for ferrihydrite) to months (182 days for crystalline hematite) at pH=7.5 and 1000 μM dissolved sulfide. Maghemite reactivity to reducing conditions was not tested in this study but should be similar to hematite according to field observations of maghemite dissolution across Fe redox boundaries (Kawamura et al., 2012; Smirnov and Tarduno, 2000). Magnetite preservation on centennial scales has previously been reported in reducing porewaters, an observation that is attributed to the smaller surface area (larger grain sizes) of natural relative to synthetic magnetite (Canfield and Berner, 1987; Canfield et al., 1992; Poulton et al., 2004). However, hematite, goethite, and maghemite all have reduction half-lives consistent with both field observations and lab experiments (Canfield and Berner, 1987; Canfield et al., 1992; Poulton et al., 2004). Thus, this Fe mineral reactivity to free sulfide scheme, though derived from synthetic minerals, should be broadly applicable to natural sediments because the synthesis techniques produce morphologically similar Fe minerals to those in natural environments (Poulton et al., 2004).

Free sulfide usually accumulates within porewaters of the upper ~5 cm of SBB sediments regardless of the sampling season (Kuwabara et al., 1999; Reimers et al., 1996), such that at ~10 cm below the SWI, porewater sulfide concentrations are typically several hundreds of μM (Komada et al., 2016; Reimers et al., 1996; Zheng et al., 2000). Additionally, Raven et al. (2016) report ~1000 μM dissolved sulfide at ~60 cm below the SWI in SBB in October, 2013. Based on porewater geochemistry and a centennial age of the sediments (< 1759 CE with a ~4 mm/yr sedimentation rate) that is much longer than measured reduction half lives, any highly-reactive Fe (oxyhydr)oxides should have been rapidly converted to sulfides at sediment depths >5 cm below the SWI. A general decreasing Fe_{dith} trend down-core suggests continual dissolution of highly-reactive Fe (oxyhydr)oxides below the top 2 – 3 cm where the dissolved Fe peak was observed in SBB porewaters (Kuwabara et al., 1999; Reimers et al., 1996). Yet contributions from Fe_{dith} and Fe_{ox} throughout the core suggest that highly-reactive Fe (oxyhydr)oxides are preserved on centennial timescales, corroborated by magnetic analysis results (Fig. A-2 and A-3). Preservation of highly-reactive Fe (oxyhydr)oxides is also consistent with the results of Raven et al. (2016), where Fe_{dith} still accounts for ~1/3 of Fe_{HR} (defined as Fe_{dith} + Fe_{py}) at 61 cmbct. Thus, Fe_{dith} preservation in highly sulfidic porewaters below the dissolved Fe peak appears incompatible with complete/rapid reduction of Fe (oxyhydr)oxides and pyrite formation in ambient sulfidic environments.

Dissolution reaction kinetics of specific Fe minerals varies with surface area, sedimentation rates, and sulfide concentrations (Canfield and Berner, 1987; Canfield et al., 1992; Karlin, 1990a; Karlin, 1990b; Roberts and Turner, 1993). Sulfide concentrations found in SBB porewaters are similar to those used in lab experiments (Poulton et al., 2004), and thus should not be the main control of dissolution reaction kinetics. Similar morphology of synthetic and natural Fe (oxyhydr)oxides (except magnetite) makes surface area impacts less likely. In SBB, high sedimentation rates may play a role in Fe (oxyhydr)oxide preservation down-core. The sedimentation rate (~4 mm/y) in SBB is significantly higher than sedimentation rates found at other well-studied anoxic marine environments (Reimers et al., 1990; Reimers et al., 1996; Zheng et al., 2000), being ~ two orders of magnitude higher than the Black Sea sediments (0.063 mm/y, from Degens et al. (1978)), and ~4x higher than Cariaco Basin (~0.3 – 1 mm/y, Peterson et al. (2000)). We posit that high sedimentation rates in SBB significantly reduce the exposure of detrital minerals to sulfidic porewaters within the active diagenesis zone (several cm below the SWI), where the highest microbe-mediated sulfate reduction rates are observed and maximum Fe monosulfide formation occurs (Reimers et al., 1996). Down-core below this horizon, subsequent rapid sediment compaction lowers porosity, which hinders further reactions between porewater sulfide and sedimentary Fe (oxyhydr)oxides. Additionally, the lab experiments providing Fe oxide reduction kinetics were performed under continuously stirred conditions at 25 °C (Poulton et al., 2004), similar perhaps to the well bioturbated environment in the FOAM field experiments (Goldhaber et al., 1977). Oxic water columns in the FOAM site allow mega- and macro-fauna to bioturbate sediments despite the presence of sulfidic porewaters, which in turn reworks sediments, thereby increasing sediment-porewater interactions (e.g., irrigation fluxes of Fe(II) and sulfide) (Boudreau, 1984). This is not the case in SBB benthic environment with presence of laminations indicates the lack of bioturbation by macrofauna, which could contribute to incomplete reduction of Fe (oxyhydr)oxides in addition to the high-sedimentation rate in SBB.

3.6.3 The impact of water-column and porewater redox conditions on Fe speciation

Elevated Fe_T/Al ratios are typically associated with Fe sulfide formation in anoxic water columns (Lyons and Severmann, 2006). The down-core Fe_T/Al profile in SBB exhibits a consistent enrichment (Fe_T/Al of ~0.6) relative to the local lithogenic background ratio of 0.54 (except at the base of the olive layer), which suggests that anoxic bottom waters prevailed

throughout the last 250 years and facilitated Fe-sulfide precipitation. Yet most downcore Fe_{HR}/Fe_T values (< 0.38) fall outside the anoxic regime. As the Fe_{HR}/Fe_T threshold value (0.38) is strictly calibrated in perennially anoxic waters, Fe_{HR}/Fe_T values in low-oxygen/oscillatory anoxic environments (inhospitable for mega- and macrofauna) are indistinguishable to those in fully-oxygenated waters, and thus Fe_{HR}/Fe_T threshold values should be applied with caution when inferring oxic/oxygenated water columns (Raiswell and Canfield, 1998; Raiswell et al., 2018). Similarly enriched Fe_T/Al associated with low Fe_{HR}/Fe_T values (< 0.38) are found in the Kau Bay, Indonesia – a water column which alternates between low-oxygen and sporadic anoxia (Middelburg, 1991). Compared to Fe_T/Al from the Kau Bay (0.87 ± 0.08) (Raiswell and Canfield, 1998), however, SBB Fe_T/Al is only weakly enriched (0.58 ± 0.03, 1SD).

Although the SBB water column is not sulfidic, significant particulate Fe enrichments ($Fe_T/Al > 0.7$) exist in the water column below sill depth (475 m) (Shiller et al., 1985). These enrichments have been attributed to mobilized Fe(II) from underlying reducing sediments, which could reprecipitate as Fe (oxyhydr)oxides in the overlying subsurface waters. Additionally, ferric hydroxo-phosphates that accumulated in coastal salt marshes could be an occasional source of Fe-rich particulates that may be transformed into Fe (oxyhydr)oxides in SBB bottom waters (Fig. 3-1, Shiller et al. (1985)). During regional rainfall events, ferric hydroxo-phosphates can be dispersed in surface and hyperpycnal plumes, and are subsequently transported to SBB via floc formation, particle settling, storm wave transport, gravity currents, and mass movement processes (Hendy et al., 2015; Warrick and Farnsworth, 2009a; Warrick and Farnsworth, 2009b). Under the Mediterranean climate in Southern California, Fe (oxyhydr)oxide addition via this mechanism is sporadic.

At/close to the SWI where upward diffusing sulfide fluxes have been observed, Fe-rich particulates are partially converted to Fe sulfides, which contributes to sedimentary Fe_T enrichments (Kuwabara et al., 1999; Zheng et al., 2000). Fe sulfide formation at/near the SWI is also indicated by the presence of authigenic pyrite framboids in near-surface sediments (Raven et al., 2016). Similarly, mobilized Fe addition from reducing sediments with pyrite formation at/near the SWI may have produced high Fe_T/Al in the sporadically euxinic Kau Bay (bottom water sulfide concentrations of 13 μM, Middelburg (1991)), where Fe-rich particulates in bottom waters are also reported (Middelburg et al., 1988). Mobilized Fe(II) from underlying sediments,

however, is insufficient to produce significant Fe_{HR} enrichments, leading to low oxic Fe_{HR}/Fe_T values in SBB.

Fe_{py}/Fe_{HR} follows the extent of Fe_{HR} conversion to pyrite. In non-euxinic depositional environments ($Fe_{HR}/Fe_T < 0.38$), Fe_{py}/Fe_{HR} may be a proxy for sulfidic porewaters (e.g., FOAM) (Hardisty et al., 2018; Raiswell and Canfield, 1998), where complete conversion of sedimentary Fe_{HR} to pyrite leads to high Fe_{py}/Fe_{HR} ratios (> 0.7 – 0.8). In SBB where sulfidic porewaters prevail, the observed Fe_{py}/Fe_{HR} values are relatively low (~0.2 – 0.6, Figs. 3-5h and 3-6). One explanation for the low Fe_{py}/Fe_{HR} values is that pyrite oxidation during core storage converted Fe_{py} back to unsulfidized Fe_{HR}. Comparison with Raven et al. (2016) seems to suggest that Fe_{dith} in this core is not overprinted by severe pyrite oxidation to dithionite-extracted Fe (oxyhydr)oxides (Table. A1, at least near the core top). We thus include an extreme scenario (high-FeS_2 scenario, Fig. 3-6), where we assume that all measured magnetite is formed from pyrite oxidation and therefore we remove Fe_{ox} (magnetite portion) from Fe_{HR}. Fe_{py}/Fe_{HR} calculated in this scenario represents an extreme upper limit because our magnetic analyses confirm the presence of both biogenic and lithogenic magnetite in SBB (Figs. 3-3 and 3-4). Yet, even in this high-FeS_2 scenario, low Fe_{py}/Fe_{HR} (< 0.7) persists except at the top of the turbidite layer (Fig. 3-5h).

Alternatively, low Fe_{py}/Fe_{HR} values could be caused by incomplete Fe_{HR} conversion to pyrite in the depositional enviroment. Fe (oxyhydr)oxide preservation downcore (Section 5.1 and 5.2) indicates the sustained occurrence of unsulfidized highly-reactive Fe despite sulfide accumulation in SBB porewaters (Reimers et al., 1996) (Fig. 3-5). In SBB, high sedimentation rates combined with sluggish sediment-porewater interaction appear to have greatly restricted the reaction kinetics of Fe_{HR} reductive dissolution (Schimmelmann and Kastner, 1993), resulting in low Fe_{py}/Fe_{HR} values in sulfidic porewaters, at least on a centennial timescale.

3.6.4 Instantaneous depositional events and post-depositional diagenesis — an internal "iron shuttle" process

In addition to reaction kinetics, non-steady state diagenesis, such as the response to instantaneous sedimentary deposition events, creates another complication for Fe speciation interpretations. Two categories of instantaneous sedimentary deposition events are preserved in the SBB sedimentary record: flood-induced gray layers (e.g., the 1861 and 1761 floods) and homogenous olive layers (e.g., the turbidite triggered by the 1812 Santa Barbara earthquake) (Du

et al., 2018; Hendy et al., 2015; Schimmelmann et al., 1992). Flood and turbidite layers are usually characterized by low total organic carbon (TOC), low Fe_T/Al ratios, and a concurrent Fe_{py} increase, although the magnitude of these shifts varies depending on layer thickness.

The olive turbidite layer at 43 – 49 cmbct provides an opportunity to observe possible post-depositional diagenetic overprinting on Fe proxies. The base of the olive layer (49 cm) contains the lowest Fe_T/Al value in the core (Fig. 3-5f) but the immediate overlying sample (48 cm) recovers to a typical ratio value of ~0.6. Concurrently, Fe_{py} increases within the olive layer and reaches a maximum at the top of the layer (43 cm, Fig. 3-5g and h) while Fe_{ace} (carbonate-bound Fe) decreases. Fe proxies suggest that the most reducing environment within the core occurred during this interval ($Fe_{HR}/Fe_T = 0.44$; ferruginous according to Fe speciation threshold values). Nevertheless, this apparent anoxic water column coincides with the basin-wide bed of *Macoma* that inhabited SBB around 1840 CE (Schimmelmann et al., 1992; Schimmelmann et al., 1990). *Macoma* spp. are a genus of bivalve intolerant of hypoxia ($O_2 < 65$ μmol/kg) such that it cannot survive typical basin conditions (Myhre et al., 2017). *Macoma* preservation *in situ* provides strong evidence of an unusually oxygenated benthic environment at ~1840 CE, which directly contradicts the Fe speciation interpretation. Our results suggest a "false positive" scenario where "more reducing conditions" caused by post-depositional diagenesis overprint the original oxygenated environment.

Two processes may have played a role in producing non-steady state diagenesis. Instantaneous depositional events (flood or turbidite layers) can attenuate O_2 diffusion into underlying sediments. This 'coffin-lid' effect (reduced O_2 penetration) facilitates establishment of reducing conditions in relatively organic-rich sediments immediately below the instantaneous depositional events, including Mn/Fe oxide reductive dissolution and microbial sulfate reduction (MSR) below the newly formed SWI (Anschutz et al., 2002; McKay and Pedersen, 2014; Schimmelmann, 2011). Rapid buildup of reducing conditions has been observed within weeks to months after instantaneous depositional events (Anschutz et al., 2002; Deflandre et al., 2002) and burndown is prevented for significant periods of time (McKay and Pedersen, 2014). As suggested by coercivity and S300 changes in magnetic mineral assemblages (Figs. 3-2h and 3-4), turbidite deposition introduces an external input of high-coercivity reactive Fe minerals (e.g., hematite), which are readily reduced by either microbial iron reduction (MIR), and/or ambient free sulfide (Meyers, 2007; Severmann et al., 2008).

For the newly deposited turbidite layer, porewater sulfide could come either from MSR and/or from upward sulfide diffusion out of the underlying sediments. If Fe (oxyhydr)oxide reduction outpaces sulfide production from MSR (when porewater sulfate is completely reduced) and diffusion supply, the second widely accepted process – *in situ* remobilization of Fe(II) from newly introduced Fe and Mn oxides – could occur (Chaillou et al., 2008; Lyons and Severmann, 2006; Meyers, 2007; Mucci et al., 2003; Raiswell et al., 2008). This process leads to diffusion and transport of Fe(II) and Mn(II), resulting in less reducing porewater conditions (i.e., the sulfide buffer of Meyers (2007)).

Complete porewater sulfate consumption has been suggested in SBB gray flood layers from $\delta^{34}S$ measurements on bulk sediments and individual pyrite aggregates. The irregular pyrite aggregates (dominant in the flood layers) have more enriched $\delta^{34}S$ values (24.2 ± 2.9‰) with respect to typical pyrite framboids ($\delta^{34}S$ = -24.4‰) found in the intervening laminated sediments (Berelson et al., 2019; Bryant et al., 2019). The enriched irregular pyrite aggregates thus have a similar $\delta^{34}S$ with the original sulfate (~21‰), indicating that pyrite was formed with sulfide generated from complete sulfate reduction. In the observed SPR0901-04BC turbidite layer, a similar scenario might occur given that the sediment layer is also instantaneously deposited. Minimum Fe/Al values at the base of the olive turbidite layer (Fig. 3-5h) further support Fe remobilization after buffering with available sulfide. Thus, upon turbidite deposition, relative rapid responses (rapid MSR, porewater sulfate consumption, and Fe remobilization) may have contributed to development of a short-duration sulfide-free environment that enabled *Macoma* to colonize the SWI for a few years.

Fe remobilization alone is insufficient to explain the maximum Fe_{py} and Fe_{py}/Fe_{HR} at the top of the turbidite layer. Since *Macoma* spp. are intolerant of hypoxia ($O_2 < 65$ μmol/kg), and *Macoma* occupied the SWI for ~3 years (Schimmelmann et al., 1992), bottom waters must have been oxygenated long enough to allow shuttling of upward diffusing Fe(II). Although no burrowing is observed at the *Macoma* layer, the briefly oxygenated bottom waters would have allowed some macrofaunal bioturbation to facilitate Fe(II) diffusion in the porewaters. Free Fe(II) could then have been reoxidized at the top of the turbidite layer and/or repeatedly recycled near the SWI (Anderson and Raiswell, 2004; Raiswell and Anderson, 2005; Wijsman et al., 2001). Subsequent re-establishment of low-oxygen bottom water conditions could have re-initiated vigorous sulfide production near the SWI. High sedimentation rates quickly buried the turbidite

layer in the following years, further contributing to sulfide accumulation in ambient porewaters. This longer-term response of porewater sulfide re-accumulation would then result in post-depositional pyrite conversion of Fe_{HR} and the Fe_{py}/Fe_{HR} peak at the upper boundary of the turbidite layer. This internal "shuttle-like" mechanism involves the reduction of fresh Fe (oxyhydr)oxides introduced by the turbidite layer that produces a local Fe_T/Al depletion, the upward diffusion and oxidation of Fe(II), and finally re-precipitation as pyrite when sulfidic porewaters re-established during the years following turbidite deposition. A further possibility is that *Macoma* spp., freshly suffocated by low-oxygen bottom water, may have provided extra highly-reactive organic carbon contributing to reductive dissolution of Fe (oxyhydr)oxides and pyrite conversion at the top of the turbidite layer (Emiroğlu et al., 2004). Yet, the *Macoma* layer coincides with lower than average TOC values (Wang et al., 2017).

While intense Fe(II) migration in the other two much-thinner flood layers is not evident in the Fe speciation results (except slight Fe_T/Al reduction), these layers contain similar pyrite peaks and local Fe_{py}/Fe_{HR} maxima. The flood sediments also rapidly deposit a new source of Fe_{HR} as demonstrated by L-ratios (Fig. 3-4), therefore, Fe(II) mobilization and sulfide buffering should occur similar to the 1812 turbidite, followed by pyrite conversion in the ambient sulfidic porewaters. Different slopes on the L-ratio vs. HIRM plot (Fig. 3-4) demonstrate that the 1761 flood layer contains a magnetically harder mineral assemblage (e.g., higher-coercivity hematite) than the turbidite layer. Subtle differences in iron mineral assemblages are likely in each turbidite and flood layer due to sediment source variations (downslope submarine landslides relative to different river catchment contributions). Thus, instantaneous depositional events can perturb porewater redox conditions that control later diagenetic processes, initiating non-steady state diagenesis and erasing the original redox record. This post-depositional non-steady state diagenesis likely significantly altered the steady-state redox signal in Fe proxies, leading to "false positive" anoxic interpretations. Given widespread occurrence of instantaneous depositional events in the geological record (e.g., turbidites triggered by submarine landslides, storms, etc.), care should be taken when interpreting diagenetic redox environments.

3.6.5 Trace metal enrichments in the Santa Barbara Basin

To further understand porewater redox chemistry and Fe enrichments, trace metal enrichments (Wang et al., 2017) are compared with Fe speciation results from the same samples. Manganese is consistently depleted in the core; its relatively constant low enrichment factor

(~0.4) indicates that porewaters were always sufficiently reducing to remobilize Mn. Rhenium and U enrichments behave similarly as expected ($r = 0.6384$, $p < 0.0001$), given the typically low-oxygen bottom water in the central SBB (Fig. 3-8). Molybdenum enrichments are not correlated with Fe_{HR}/Fe_T ($r = -0.1695$, $p = 0.2076$) and are negatively correlated to Fe_{py}/Fe_{HR} ($r = -0.2821$, $p < 0.05$), indicating disagreement between the two euxinic indicators. In contrast to Fe_{py} and Fe_{py}/Fe_{HR}, the enrichment factor of Mo (Mo_{EF}) reaches its minimum within the turbidite-triggered olive layer, where Mo is close to or slightly depleted with respect to the lithogenic background, consistent with well-oxygenated bottom water as indicated by the presence of *Macoma* (Tables 3.3 and 3.4). Mo has been shown to precipitate near the SWI in SBB (Zheng et al., 2000), and thus this metal should record the original bottom-water redox chemistry in the basin (Wang et al., 2017).

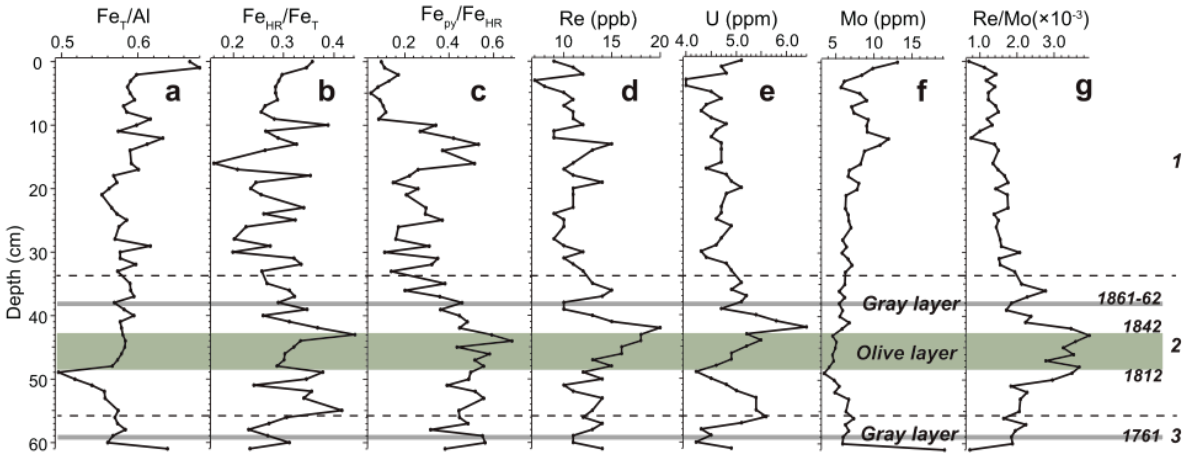

Figure 3-8 Down-core comparison of iron redox proxies and trace metals in SPR0901-04BC. (a) Fe_T/Al; (b) Fe_{HR}/Fe_T; (c) Fe_{py}/Fe_{HR}; (d) Rhenium (ppb); (e) Uranium (ppm); (f) Molybenum (ppm); (g) Re/Mo ratios ($\times 10^{-3}$). Zonation (dashed lines) based on changes in magnetic mineral concentrations and concentration-independent properties is as follows: Zone 1 (0 – 35 cmbct), Zone 2 (35 – 56 cmbct) and Zone 3 (56 – 61 cmbct), respectively. Gray bars (1761 CE and 1861 – 1862 CE) represent gray layers in the core while the turbidite layer (1812 – 1842 CE) is shaded in dark green.

Molybdenum enrichment in sediments is controlled by enhanced Mo delivery via particulate shuttles (i.e., Fe-Mn shuttle effects), changes in water-column trace metal concentrations, and bottom water redox conditions (Algeo and Tribovillard, 2009; Cheng et al., 2016; Tribovillard et al., 2012). In the particulate shuttle process, Mo is readily adsorbed onto Fe-Mn oxides, thus precipitation and reduction of Fe-Mn oxides could strongly accelerate Mo delivery to sediments (Algeo and Tribovillard, 2009; Tribovillard et al., 2012). Uranium affinity with Fe-Mn oxides, however, is much more limited, and thus an efficient Fe-Mn shuttle could result in a higher Mo_{EF} than would be expected from euxinic water columns (e.g., Cariaco Basin,

Tribovillard et al. (2012)). Variations in water-column trace metal concentrations can impact enrichment in sediments. This occurs in the Black Sea where Mo is depleted in the water column and as a result Black Sea sediments have lower than expected Mo_{EF} (Algeo and Tribovillard, 2009). Finally, Mo precipitation is suggested to be initiated at a H_2S threshold of ~0.1 μM at the SWI (Zheng et al., 2000), but a threshold of 11 μM is required for MoO_4^{2-} to abruptly switch to MoS_4^{2-} (Erickson and Helz, 2000). Given the typically low sulfide concentration near the SWI in SBB, partial conversion to intermediate thiomolybdate phases ($MoO_xS_{4-x}^{2-}$) is expected (Cheng et al., 2016; Erickson and Helz, 2000; Helz et al., 1996).

The cross-plot of Mo_{EF} vs. U_{EF} provides insights into the contribution of the three processes in the SBB (Fig. 3-9, Algeo and Tribovillard (2009); Cheng et al. (2016)). Molybdenum and U enrichment factors mostly fall between 0.1×SW (seawater value of Mo:U weight ratio for present Pacific seawater is ~3.2; Tribovillard et al. (2012)) and 0.3×SW, consistent with prevailing low-oxygen water columns. However, Fe and Mn particulate shuttle effects are not observed in the cross-plot (Fig. 3-9), which suggests that particulate shuttles only have, if any, minor impacts on Mo precipitation in SBB sediments. Additionally, Zheng et al. (2000) reported gradually depleted porewater Mo below 5 cm depth, which suggests that there is not a significant amount of post-depositional release of Mo from Fe-Mn oxides. Molybdenum depletion in the SBB water column has not been observed (Zheng et al., 2000), and thus trace metal precipitation in the basin should be primarily related to porewater redox chemistry and/or vigorous redox reactions at the SWI. Thus, trace metal enrichments in the SBB contain a primary signal that provides information on water-column redox conditions at the time of deposition, while the primary Fe enrichment signal is overprinted by post-depositional non-steady state diagenesis.

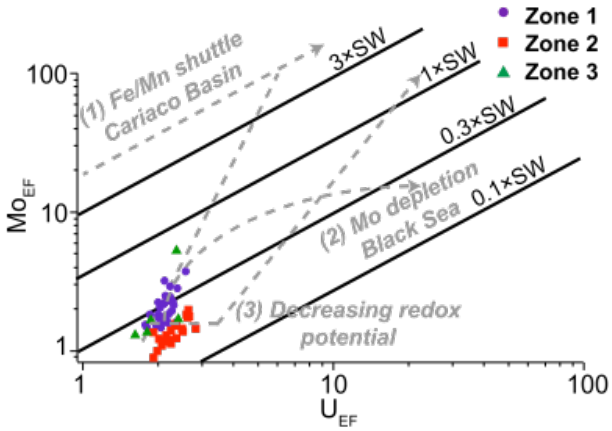

Figure 3-9 Cross-plot of Mo_{EF} vs. U_{EF} in core SPR0901-04BC. Purple circles (Zone 1: 0 – 35 cmbct), red squares (Zone 2: 35 – 56 cmbct), and green triangles (Zone 3: 56 – 61 cmbct), respectively, represent enrichment factors (EF) for samples from the three magnetic mineral zones. Diagonal solid lines represent multiples (0.3, 1, and 3) of SW (seawater) lines in the modern seawater (average weight ratio of Mo:U of ~3.2). Gray dashed lines highlight general patterns of U_{EF} and Mo_{EF} in the unrestricted marine environment, Black Sea (Mo depletion in the water column) and Cariaco Basin ("particulate shuttle" trend) modified from Tribovillard et al. (2012).

3.7 Conclusions and implications

Sedimentary redox-sensitive metal responses to redox conditions are assumed to be directly linked to the overlying water column. Under certain circumstances, this linkage can be compromised because redox conditions are also closely associated with ambient porewater chemistry. The geochemical setting of the Santa Barbara Basin (SBB), California – a weakly-silled, high productivity basin overlain by low-oxygen bottom waters and containing sulfidic porewaters – represents an intermediate environment between oxic and euxinic water columns. Geochemistry/magnetism records from the box core SPR0901-04BC provide a centennial-scale snapshot on how Fe speciation results can be obscured by high sedimentation rates and post-depositional diagenesis, with more diagenetic processes likely affecting the down-core Fe mineralogy on longer time scales. Unlike the Cariaco Basin or the Black Sea where euxinia is observed in the water column (Algeo and Rowe, 2012; Lyons and Severmann, 2006; Raiswell and Anderson, 2005), only porewaters in SBB are sulfidic and the redoxcline (oxic versus anoxic) is at or close to the sediment water interface (SWI). In SBB, vigorous redox reactions occur near the SWI; therefore, enrichments of redox sensitive metals should reflect water column dissolved oxygen (Reimers et al., 1996; Zheng et al., 2000).

Mineralogical shifts related to local geochemistry and diagenesis in SBB sediments can be observed by combining magnetic measurements with iron speciation. Fe_T/Al indicates a sustained anoxic depositional environment (except at the base of the turbidite layer) due to

enrichment by authigenic Fe sulfide formation at or close to the SWI. Our results also demonstrate that biogenic magnetite can be temporarily preserved in sulfidic porewaters and there are frequent instances of highly-reactive Fe (oxyhydr)oxides escaping reduction, at least on decadal to centennial time scales. We suggest that highly-reactive Fe reduction kinetics could be inhibited by the high sedimentation rates and minimal bioturbation, which reduce sediment-porewater interactions and prevent complete/rapid pyrite conversion in porewaters. Caution should, therefore, be taken when using Fe_{py}/Fe_{HR} as a sulfidic porewater proxy in recently deposited sediments (Hardisty et al., 2018); mineralogy should be checked for complete/rapid pyrite conversion. In addition, non-steady state diagenesis following instantaneous sediment depositional events perturbs the geochemistry of the depositional environment, notably through the increased supply of fresh highly-reactive Fe that results in sulfide buffering. Within the 1812 turbidite layer, recently introduced reactive Fe (oxyhydr)oxides buffered upward diffusing free sulfide from underlying sediments and were reduced to Fe(II) that subsequently diffused upward in porewaters. In the SBB, this turbidite deposition created a less reducing (sulfide free) benthic environment that allowed a brief ~3 year colonization of the bivalve, *Macoma* spp. With the greater availability of shuttled Fe, subsequent re-establishment of sulfidic porewater resulted in rapid pyrite precipitation and thus led to a "false positive" (more reducing conditions) in Fe speciation results, overprinting the original oxygenated bottom water responses. Trace metal (Mo, Re, and U) precipitation in SBB appears to be primarily controlled by reducing conditions at the SWI and is not overprinted by down-core diagenesis.

Instantaneous depositional events such as turbidites are common in marginal marine sedimentary environments (Hensen et al., 2003; Otero et al., 2003; Robinson and Sahota, 2000; Robinson et al., 2000; Yücel et al., 2010), and yet are rarely considered in geochemical redox reconstructions of past marine environments. Frequent instantaneous depositional events in SBB, in addition to low-oxygen water conditions and the centennial scale of the record, make Fe speciation a poor proxy choice for local redox reconstructions. Trace metals, however, preserve original redox shifts in the bottom waters of the basin. Despite observed complications in this centennial-scale reconstruction, Fe speciation still deserves some consideration and may provide valuable information on deep-time redox history.

3.8 Acknowledgements

This work is supported by the National Science Foundation (grant number OCE-1304327) awarded to I.H., the Scott Turner Award to Y.W., and by the Rackham Graduate School of the University of Michigan. Part of this work was performed as a US Visiting Student Fellow at the Institute for Rock Magnetism (IRM) at the University of Minnesota. The IRM is a US National Multi-user Facility supported through the Instrumentation and Facilities program of the National Science Foundation, Earth Sciences Division, and by funding from the University of Minnesota. We thank Mike Jackson and Peter Solheid for thoughtful discussions and technical support at the IRM. This is IRM publication 1708. We acknowledge Arndt Schimmelmann for helpful discussions. We appreciate comments from Andrew P. Roberts and other two anonymous reviewers, which greatly improved this manuscript. All geochemical data can be accessed from the Appendix A.

3.9 References

Algeo, T.J., Rowe, H., 2012. Paleoceanographic applications of trace-metal concentration data. Chemical Geology, 324-325(2012): 6-18.

Algeo, T.J., Tribovillard, N., 2009. Environmental analysis of paleoceanographic systems based on molybdenum–uranium covariation. Chemical Geology, 268(3-4): 211-225.

Anderson, T.F., Raiswell, R., 2004. Sources and mechanism for the enrichment of highly reactive iron in euxinic Black Sea sediments. American Journal of Science, 304: 203-233.

Anschutz, P., Jorissen, F.J., Chaillou, G., Abu-Zied, R., Fontanier, C., 2002. Recent turbidite deposition in the eastern Atlantic: early diagenesis and biotic recovery. Journal of Marine Research, 60: 835-854.

Bazylinski, D.A., Frankel, R.B., 2004. Magnetosome formation in prokaryotes. Nature Reviews Microbiology, 2: 217.

Berelson, W.M. et al., 2019. Santa Barbara Basin flood layers: impact on sediment diagenesis. From the Mountains to the Abyss: The California Borderland as an Archive of Southern California Geologic Evolution, 110. Society for Sedimentary Geology.

Berelson, W.M. et al., 2005. Anaerobic diagenesis of silica and carbon in continental margin sediments: Discrete zones of TCO2 production. Geochimica et Cosmochimica Acta, 69(19): 4611-4629.

Berner, R.A., 1981. A new geochemical classification of sedimentary environments. Journal of Sedimentary Petrology, 51(2): 359-365.

Boudreau, B.P., 1984. On the equivalence of nonlocal and radial-diffusion models for porewater irrigation. Journal of Marine Research, 42(3): 731-735.

Bryant, R.N. et al., 2019. Sulfur isotope analysis of microcrystalline iron sulfides using secondary ion mass spectrometry imaging: Extracting local paleo-environmental information from modern and ancient sediments. Rapid Commun Mass Spectrom, 33(5): 491-502.

Calvert, S.E., Pedersen, T., 1996. Sedimentary geochemistry of manganese- Implications for the environment of formation of manganiferous black shales. Economic Geology, 91: 26-47.

Calvert, S.E., Pedersen, T.F., 2007. Elemental Proxies for Palaeoclimatic and Palaeoceanographic Variability in Marine Sediments: Interpretation and Application, Developments in Marine Geology, pp. 567-644.

Canfield, D.E., 1989. Reactive iron in marine sediments. Geochimica et Cosmochimica Acta, 53(3): 619-632.

Canfield, D.E., Berner, R.A., 1987. Dissolution and pyritization of magnetite in anoxic marine sediments. Geochimica et Cosmochimica Acta, 51(3): 645-659.

Canfield, D.E., Poulton, S.W., Narbonne, G.M., 2007. Late-Neoproterozoic deep-ocean oxygenation and the rise of animal life. Science, 315(5808): 92-94.

Canfield, D.E., Raiswell, R., Bottrell, S., 1992. The reactivity of sedimentary iron minerals toward sulfide. American Journal of Science, 292(9): 659-683.

Canfield, D.E., Raiswell, R., Westrich, J.T., Reaves, C.M., Berner, R.A., 1986. The use of chromium reduction in the anlysis of reduced inorganic sulfur in sediments and shales. Chemical Geology, 54(1986): 149-155.

Carvallo, C., Özdemir, Ö., Dunlop, D.J., 2004. First-order reversal curve (FORC) diagrams of elongated single-domain grains at high and low temperatures. Journal of Geophysical Research: Solid Earth, 109(B4).

Chaillou, G., Schäfer, J., Blanc, G., Anschutz, P., 2008. Mobility of Mo, U, As, and Sb within modern turbidites. Marine Geology, 254(3-4): 171-179.

Chang, L., Heslop, D., Roberts, A.P., Rey, D., Mohamed, K.J., 2016a. Discrimination of biogenic and detrital magnetite through a double Verwey transition temperature. Journal of Geophysical Research: Solid Earth, 121: 3-14.

Chang, L. et al., 2016b. Widespread occurrence of silicate-hosted magnetic mineral inclusions in marine sediments and their contribution to paleomagnetic recording. Journal of Geophysical Research: Solid Earth, 121: 8415-8431.

Chang, L. et al., 2009. Low-temperature magnetic properties of greigite (Fe3S4). Geochemistry, Geophysics, Geosystems, 10(1).

Chang, L. et al., 2013. Low-temperature magnetic properties of pelagic carbonates: Oxidation of biogenic magnetite and identification of magnetosome chains. Journal of Geophysical Research: Solid Earth, 118: 6049-6065.

Chang, S.-B.R., Kirschvink, J.L., 1989. Magnetofossils, the magnetization of sediments and the evolution of magnetite biomineralization. Annual Review of Earth and Planetary Sciences, 17: 169-195.

Cheng, M. et al., 2016. Marine Mo biogeochemistry in the context of dynamically euxinic mid-depth waters: A case study of the lower Cambrian Niutitang shales, South China. Geochimica et Cosmochimica Acta, 183: 79-93.

Clarkson, M.O., Poulton, S.W., Guilbaud, R., Wood, R.A., 2014. Assessing the utility of Fe/Al and Fe-speciation to record water column redox conditions in carbonate-rich sediments. Chemical Geology, 382: 111-122.

Crusius, J., Calvert, S., Pedersen, T., Sage, D., 1996. Rhenium and molybdenum enrichments in sediments as indicators of oxic, suboxic and sulfidic conditions of deposition. Earth and Planetary Science Letters, 145: 65-78.

Crusius, J., Thomson, J., 2000. Comparative behavior of authigenic Re, U, and Mo during reoxidation and subsequent long-term burial in marine sediments. Geochimica et Cosmochimica Acta, 64(13): 2233-2242.

Day, R., Fuller, M., Schmidt, V.A., 1977. Hysteresis properties of titanomagnetites: Grain-size and compositional dependence. Physics of the Earth and Planetary Interiors, 13: 260-267.

Deflandre, B., Mucci, A., Gagné, J.-P., Guignard, C., Sundby, B., 2002. Early diagenetic processes in coastal marine sediments disturbed by a catastrophic sedimentation event. Geochimica et Cosmochimica Acta, 66(14): 2547-2558.

Degens, E.T., Stoffers, P., Golubic, S., Dickman, M.D., 1978. Varve chronology: estimated rates of sedimentation in the Black Sea deep basin, pp. 499-508.

Dekkers, M.J., 1989a. Magnetic Properties of Natural Goethite—II. TRM Behaviour During Thermal and Alternating Field Demagnetization and Low-Temperature Treatment. Geophysical Journal International, 97(2): 341-355.

Dekkers, M.J., 1989b. Magnetic properties of natural pyrrhotite. II. High- and low-temperature behaviour of Jrs and TRM as function of grain size. Physics of the Earth and Planetary Interiors, 57: 266-283.

Du, X., Hendy, I., Schimmelmann, A., 2018. A 9000-year flood history for Southern California: A revised stratigraphy of varved sediments in Santa Barbara Basin. Marine Geology, 397: 29-42.

Dunlop, D.J., 2002. Theory and application of the Day plot (Mrs/Ms versus Hcr/Hc) 1. Theoretical curves and tests using titanomagnetite data. Journal of Geophysical Research, 107(B3).

Egli, R., 2013. VARIFORC: An optimized protocol for calculating non-regular first-order reversal curve (FORC) diagrams. Global and Planetary Change, 110: 302-320.

Egli, R., Chen, A.P., Winklhofer, M., Kodama, K.P., Horng, C.-S., 2010. Detection of noninteracting single domain particles using first-order reversal curve diagrams. Geochemistry, Geophysics, Geosystems, 11(1): 1-22.

Emiroğlu, S., Rey, D., Petersen, N., 2004. Magnetic properties of sediment in the Ría de Arousa (Spain): dissolution of iron oxides and formation of iron sulphides. Physics and Chemistry of the Earth, Parts A/B/C, 29(13-14): 947-959.

Erickson, B.E., Helz, G.R., 2000. Molybdenum(VI) speciation in sulfidic waters: stability and lability of thiomolybdates. Geochimica et Cosmochimica Acta, 64(7): 1149-1158.

Frederichs, T., von Dobeneck, T., Bleil, U., Dekkers, M.J., 2003. Towards the identification of siderite, rhodochrosite, and vivianite in sediments by their low-temperature magnetic properties. Physics and Chemistry of the Earth, 28: 669-679.

Goldhaber, M.B. et al., 1977. Sulfate reduction, diffusion, and bioturbation in Long Island Sound sediments; report of the FOAM Group. American Journal of Science, 277(3): 193-237.

Hardisty, D.S. et al., 2018. An evaluation of sedimentary molybdenum and iron as proxies for pore fluid paleoredox conditions. American Journal of Science, 318(5): 527-556.

Harrison, B.K., Zhang, H., Berelson, W., Orphan, V.J., 2009. Variations in archaeal and bacterial diversity associated with the sulfate-methane transition zone in continental margin sediments (Santa Barbara Basin, California). Appl Environ Microbiol, 75(6): 1487-99.

Harrison, R.J., Feinberg, J.M., 2008. An improved algorithm for calculating first-orderreversal curve distributions using locally weighted regression smoothing. Geochemistry, Geophysics, Geosystems, 9(5): 1-11.

Harrison, R.J., Lascu, I., 2014. FORCulator: A micromagnetic tool for simulating first-order reversal curve diagrams. Geochemistry, Geophysics, Geosystems, 15(12): 4671-4691.

Helz, G.R., Bura-Nakić, E., Mikac, N., Ciglenečki, I., 2011. New model for molybdenum behavior in euxinic waters. Chemical Geology, 284(3-4): 323-332.

Helz, G.R., Dolor, M.K., 2012. What regulates rhenium deposition in euxinic basins? Chemical Geology, 304-305: 131-141.

Helz, G.R. et al., 1996. Mechanism of molybdenum removal from the sea and its concentration in black shales: EXAFS evidence. Geochimica et Cosmochimica Acta, 60(19): 3631-3642.

Hendy, I.L., Napier, T.J., Schimmelmann, A., 2015. From extreme rainfall to drought: 250 years of annually resolved sediment deposition in Santa Barbara Basin, California. Quaternary International, 387: 3-12.

Hendy, I.L., Pedersen, T.F., 2005. Is pore water oxygen content decoupled from productivity on the California Margin? Trace element results from Ocean Drilling Program Hole 1017E, San Lucia slope, California. Paleoceanography, 20(4): 1-12.

Hensen, C. et al., 2003. Control of sulfate pore-water profiles by sedimentary events and the significance of anaerobic oxidation of methane for the burial of sulfur in marine sediments. Geochimica et Cosmochimica Acta, 67(14): 2631-2647.

Horng, C.-S., Roberts, A.P., 2018. The Low-Temperature Besnus Magnetic Transition: Signals Due to Monoclinic and Hexagonal Pyrrhotite. Geochemistry, Geophysics, Geosystems, 19(9): 3364-3375.

Hunt, C.P., Moskowitz, B.M., Banerjee, S.K., 1995. Magnetic properties of rocks and minerals. In: Ahrens, T.J. (Ed.), Rock Physics & Phase Relations: A Handbook of Physical Constants. American Geophysical Union, Washington, D. C., pp. 189-204.

Jackson, M., Solheid, P., 2010. On the quantitative analysis and evaluation of magnetic hysteresis data. Geochemistry, Geophysics, Geosystems, 11(Q04Z15).

Kaplan, I.R., Emery, K.O., Rittenberg, S.C., 1963. The distribution and isotopic abundance of sulphur in recent marine sediments off southern California. Geochimica et Cosmochimica Acta, 27(4): 297-331.

Karlin, R., 1990a. Magnetic mineral diagenesis in suboxic sediments at Bettis Site W-N, NE Pacific Ocean. Journal of Geophysical Research: Solid Earth, 95(B4): 4421-4436.

Karlin, R., 1990b. Magnetite diagenesis in marine sediments from the Oregon continental margin. Journal of Geophysical Research: Solid Earth, 95(B4): 4405-4419.

Kawamura, N., Ishikawa, N., Torii, M., 2012. Diagenetic alteration of magnetic minerals in Labrador Seasediments (IODP Sites U1305, U1306, and U1307). Geochemistry, Geophysics, Geosystems, 13(8): 1-16.

Komada, T. et al., 2016. Organic matter cycling across the sulfate-methane transition zone of the Santa Barbara Basin, California Borderland. Geochimica et Cosmochimica Acta, 176: 259-278.

Kopp, R.E., Kirschvink, J.L., 2008. The identification and biogeochemical interpretation of fossil magnetotactic bacteria. Earth-Science Reviews, 86(1-4): 42-61.

Kuwabara, J.S., Geen, A.V., Mccorkle, D.C., Bernhard, J.M., 1999. Dissolved sulfide distributions in the water column and sediment pore waters of the Santa Barbara Basin. Geochimica et Cosmochimica Acta, 63(15): 2199-2209.

Leslie, B.W., Hammond, D.E., Berelson, W.M., Lund, S.P., 1990. Diagenesis in anoxic sediments from the California continental borderland and its influence on iron, sulfur, and magnetite behavior. Journal of Geophysical Research, 95(B4): 4453.

Li, C. et al., 2010. A stratified redox model for the Ediacaran ocean. Science, 328(5974): 80-83.

Li, C. et al., 2015. Marine redox conditions in the middle Proterozoic ocean and isotopic constraints on authigenic carbonate formation- Insights from the Chuanlinggou Formation, Yanshan Basin, North China. Geochimica et Cosmochimica Acta, 150(2015): 90-105.

Liu, Q. et al., 2012. Environmental magnetism: Principles and applications. Reviews of Geophysics, 50(4).

Liu, Q., Roberts, A.P., Torrent, J., Horng, C.-S., Larrasoaña, J.C., 2007. What do the HIRM and S-ratio really measure in environmental magnetism? Geochemistry, Geophysics, Geosystems, 8(9): 1-10.

Liu, Q. et al., 2006. Characteristic low-temperature magnetic properties of aluminous goethite [α-(Fe, Al)OOH] explained. Journal of Geophysical Research: Solid Earth, 111(B12).

Lyons, T.W., Reinhard, C.T., Planavsky, N.J., 2014. The rise of oxygen in Earth's early ocean and atmosphere. Nature, 506(7488): 307-15.

Lyons, T.W., Severmann, S., 2006. A critical look at iron paleoredox proxies: New insights from modern euxinic marine basins. Geochimica et Cosmochimica Acta, 70(23): 5698-5722.

Madison, A.S., Tebo, B.M., Mucci, A., Sundby, B., Luther, G.W.I., 2013. Abundant porewater Mn(III) is a major component of the sedimentary redox system. Science, 341(6148): 875-878.

März, C., Hoffmann, J., Bleil, U., de Lange, G.J., Kasten, S., 2008a. Diagenetic changes of magnetic and geochemical signals by anaerobic methane oxidation in sediments of the Zambezi deep-sea fan (SW Indian Ocean). Marine Geology, 255(3-4): 118-130.

März, C. et al., 2008b. Redox sensitivity of P cycling during marine black shale formation-Dynamics of sulfidic and anoxic, non-sulfidic bottom waters. Geochimica et Cosmochimica Acta, 72(2008): 3703-3717.

McKay, J., Pedersen, T., Mucci, A., 2007. Sedimentary redox conditions in continental margin sediments (N.E. Pacific) — Influence on the accumulation of redox-sensitive trace metals. Chemical Geology, 238(3-4): 180-196.

McKay, J.L., Pedersen, T.F., 2014. Geochemical response to pulsed sedimentation: Implications for the use of Mo as a paleo-proxy. Chemical Geology, 382: 83-94.

McManus, J., Berelson, W.M., Klinkhammer, G.P., Hammond, D.E., Holm, C., 2005. Authigenic uranium: Relationship to oxygen penetration depth and organic carbon rain. Geochimica et Cosmochimica Acta, 69(1): 95-108.

McManus, J. et al., 2006. Molybdenum and uranium geochemistry in continental margin sediments: Paleoproxy potential. Geochimica et Cosmochimica Acta, 70(18): 4643-4662.

Meyers, S.R., 2007. Production and preservation of organic matter: The significance of iron. Paleoceanography, 22(4): 1-16.

Middelburg, J.J., 1991. Organic carbon, sulphur, and iron in recent semi-euxinic sediments of Kau Bay, Indonesia. Geochimica et Cosmochimica Acta, 55(3): 815-828.

Middelburg, J.J., De Lange, G.J., Van Der Sloot, H.A., Van Emburg, P.R., Sophiah, S., 1988. Particulate manganese and iron framboids in Kau Bay, Halmahera (eastern Indonesia). Marine Chemistry, 23(3): 353-364.

Morford, J.L., Emerson, S.R., 1999. The geochemistry of redox sensitive trace metals in sediments. Geochimica et Cosmochimica Acta, 63(11/12): 1735-1750.

Mucci, A., 2004. The behavior of mixed Ca–Mn carbonates in water and seawater: controls of manganese concentrations in marine porewaters. Aquatic Geochemistry, 10(1-2): 139-169.

Mucci, A., Boudreau, B., Guignard, C., 2003. Diagenetic mobility of trace elements in sediments covered by a flash flood deposit: Mn, Fe and As. Applied Geochemistry, 18(7): 1011-1026.

Myhre, S.E., Kroeker, K.J., Hill, T.M., Roopnarine, P., Kennett, J.P., 2017. Community benthic paleoecology from high-resolution climate records: Mollusca and foraminifera in post-glacial environments of the California margin. Quaternary Science Reviews, 155: 179-197.

Otero, X.L., Huerta-Diaz, M.A., Macías, F., 2003. Influence of a turbidite deposit on the extent of pyritization of iron, manganese and trace metals in sediments from the Guaymas Basin, Gulf of California (Mexico). Applied Geochemistry, 18(8): 1149-1163.

Özdemir, Ö., Banerjee, S.K., 1984. High temperature stability of maghemite (γ-Fe2O3). Geophysical Research Letters, 11(3): 161-164.

Özdemir, Ö., Dunlop, D.J., 1996. Thermoremanence and Néel temperature of goethite. Geophysical Research Letters, 23(9): 921-924.

Özdemir, Ö., Dunlop, D.J., 2010. Hallmarks of maghemitization in low-temperature remanence cycling of partially oxidized magnetite nanoparticles. Journal of Geophysical Research, 115(B02101).

Passier, H.F., Dekkers, M.J., de Lange, G.J., 2001. Magnetic properties and geochemistry of the active oxidation front and the youngest sapropel in the eastern Mediterranean Sea. Geophysical Journal International, 145(3): 604-614.

Peterson, L.C. et al., 2000. Late Quaternary stratigraphy and sedimentation at Site 1002, Cariaco Basin (Venezuela).

Pike, C.R., Roberts, A.P., Verosub, K.L., 1999. Characterizing interactions in fine magnetic particle systems using first order reversal curves. Journal of Applied Physics, 85(9): 6660-6667.

Poulton, S.W., Canfield, D.E., 2005. Development of a sequential extraction procedure for iron: implications for iron partitioning in continentally derived particulates. Chemical Geology, 214(3-4): 209-221.

Poulton, S.W., Canfield, D.E., 2011. Ferruginous conditions: a dominant feature of the ocean through Earth's history. Elements, 7: 107-112.

Poulton, S.W. et al., 2015. A continental-weathering control on orbitally driven redox-nutrient cycling during Cretaceous Oceanic Anoxic Event 2. Geology, 43(11): 963-966.

Poulton, S.W., Krom, M.D., Raiswell, R., 2004. A revised scheme for the reactivity of iron (oxyhydr)oxide minerals towards dissolved sulfide. Geochimica et Cosmochimica Acta, 68(18): 3703-3715.

Poulton, S.W., Raiswell, R., 2002. The low-temperature geochemical cycle of iron: from continental fluxes to marine sediment deposition. American Journal of Science, 302(9): 774-805.

Poulton, S.W., Raiswell, R., 2005. Chemical and physical characteristics of iron oxides in riverine and glacial meltwater sediments. Chemical Geology, 218(3-4): 203-221.

Raiswell, R., Anderson, T.F., 2005. Reactive iron enrichment in sediments deposited beneath euxinic bottom waters: constraints on supply by shelf recycling. In: McDonald, I., Boyce, A.J., Butler, I.B., Herrington, R.J., Polya, D.A. (Eds.), Mineral Deposits and Earth Evolution. Geological Society of London, London, pp. 179-194.

Raiswell, R., Canfield, D.E., 1998. Sources of iron for pyrite formation in marine sediments. American Journal of Science, 298(3): 219-245.

Raiswell, R., Canfield, D.E., 2012. Geochemical Perspectives: The Iron Biogeochemical Cycle Past and Present, 1.

Raiswell, R. et al., 2018. The iron paleoredox proxies: A guide to the pitfalls, problems and proper practice. American Journal of Science, 318: 491-526.

Raiswell, R. et al., 2008. Turbidite depositional influences on the diagenesis of Beecher's Trilobite Bed and the Hunsrück Slate; sites of soft tissue pyritization. American Journal of Science, 308(2): 105-129.

Raven, M.R., Sessions, A.L., Fischer, W.W., Adkins, J.F., 2016. Sedimentary pyrite δ34S differs from porewater sulfide in Santa Barbara Basin: Proposed role of organic sulfur. Geochimica et Cosmochimica Acta, 186: 120-134.

Reimers, C.E., Lange, C., Tabak, M., Bernhard, J., 1990. Seasonal spillover and varve formation in the Santa Barbara Basin, California. Limnology and Oceanography, 35(7): 1577-1585.

Reimers, C.E., Ruttenberg, K.C., Canfield, D.E., Christiansen, M.B., Martin, J.B., 1996. Porewater pH and authigenic phases formed in the uppermost sediments of Santa Barbara Basin. Geochimica et Cosmochimica Acta, 60(21): 4037-4057.

Reinhard, C.T., Raiswell, R., Scott, C., Anbar, A.D., Lyons, T.W., 2009. A late Archean sulfidic sea stimulated by early oxidative weathering of the continents. Science, 326(5953): 713-6.

Rickard, D., Morse, J.W., 2005. Acid volatile sulfide (AVS). Marine Chemistry, 97(3-4): 141-197.

Roberts, A.P., 2015. Magnetic mineral diagenesis. Earth-Science Reviews, 151(2015): 1-47.

Roberts, A.P. et al., 2017. Resolving the Origin of Pseudo-Single Domain Magnetic Behavior. Journal of Geophysical Research: Solid Earth, 122(12): 9534-9558.

Roberts, A.P., Chang, L., Heslop, D., Florindo, F., Larrasoaña, J.C., 2012. Searching for single domain magnetite in the “pseudo-single-domain”sedimentary haystack: implications of biogenic magnetitepreservation for sediment magnetism and relative paleointensity determinations. Journal of Geophysical Research, 117(B08104).

Roberts, A.P., Chang, L., Rowan, C.J., Horng, C.-S., Florindo, F., 2011. Magnetic properties of sedimentary greigite (Fe3S4): An update. Reviews of Geophysics, 49(1).

Roberts, A.P., Heslop, D., Zhao, X., Pike, C.R., 2014. Understanding fine magnetic particle systems through use of first-order reversal curve diagrams. Reviews of Geophysics, 52: 557-602.

Roberts, A.P. et al., 2006. Characterization of hematite (α-Fe2O3), goethite (α-FeOOH), greigite (Fe3S4), and pyrrhotite (Fe7S8) using first-order reversal curve diagrams. Journal of Geophysical Research, 111(B12).

Roberts, A.P., Pike, C.R., Verosub, K.L., 2000. First-order reversal curve diagrams: A new tool for characterizing the magnetic properties of natural samples. Journal of Geophysical Research, 105(B12): 28461-28475.

Roberts, A.P., Tauxe, L., Heslop, D., Zhao, X., Jiang, Z., 2018. A Critical Appraisal of the "Day" Diagram. Journal of Geophysical Research: Solid Earth.

Roberts, A.P., Turner, G.M., 1993. Diagenetic formation of ferrimagnetic iron sulphide minerals in rapidly deposited marine sediments, South Island, New Zealand. Earth and Planetary Science Letters, 115: 257-273.

Robinson, S.G., Sahota, J.T.S., 2000. Rock-magnetic characterization of early, redoxomorphic diagenesis in turbiditic sediments from the Madeira Abyssal Plain. Sedimentology, 47(2): 367-394.

Robinson, S.G., Sahota, J.T.S., Oldfield, F., 2000. Early diagenesis in North Atlantic abyssal plain sediments characterized by rock-magnetic and geochemical indices. Marine Geology, 163(1): 77-107.

Rowan, C.J., Roberts, A.P., Broadbent, T., 2009. Reductive diagenesis, magnetite dissolution, greigite growth and paleomagnetic smoothing in marine sediments: A new view. Earth and Planetary Science Letters, 277(1-2): 223-235.

Schimmelmann, A., 2011. The "coffin lid" effect: flood layers and turbidites in Santa Barbara Basin affect diagenesis of organic matter in underlying varved sediment. In: Besonen, M.R. (Editor), Second Workshop of the PAGES Varves Working Group, Corpus Christi, Texas, USA, pp. 83-86.

Schimmelmann, A., Kastner, M., 1993. Evolutionary changes over the last 1000 years of reduced sulfur phases and organic carbon in varved sediments of the Santa Barbara Basin, California. Geochimica et Cosmochimica Acta, 57(67-78).

Schimmelmann, A. et al., 1992. Extreme climatic conditions recorded in Santa Barbara Basin laminated sediments: the 1835–1840 Macoma event. Marine Geology, 106(1992): 279-299.

Schimmelmann, A., Lange, C.B., Berger, W.H., 1990. Climatically controlled marker layers in Santa Barbara Basin sediments and fine-scale core-to-core correlation. Limnology and Oceanography, 35(1): 165-173.

Scholz, F., McManus, J., Mix, A.C., Hensen, C., Schneider, R.R., 2014. The impact of ocean deoxygenation on iron release from continental margin sediments. Nature Geoscience, 7(6): 433-437.

Schwertmann, U., 2008. Iron oxides. In: Chesworth, W. (Editor), Encyclopedia of soil science. Springer, Dordrecht, pp. 353-369.

Scott, C. et al., 2008. Tracing the stepwise oxygenation of the Proterozoic ocean. Nature, 452(7186): 456-9.

Severmann, S., Lyons, T.W., Anbar, A.D., MacManus, J., Gordon, G.W., 2008. Modern iron isotope perspective on the benthic iron shuttle and the redox evolution of ancient oceans. Geology, 36(6): 487-490.

Shiller, A.M., Gieskes, J.M., Brian Price, N., 1985. Particulate iron and manganese in the Santa Barbara Basin, California. Geochimica et Cosmochimica Acta, 49(5): 1239-1249.

Smirnov, A.V., Tarduno, J.A., 2000. Low-temperature magnetic properties of pelagic sediments (Ocean Drilling Program Site 805C): tracers of maghemitization and magnetic mineral reduction. Journal of Geophysical Research, 105(B7): 16457-16471.

Soutar, A., Crill, P.A., 1977. Sedimentation and climatic patterns in the Santa Barbara Basin during the 19th and 20th centuries. Geological Society of America Bulletin, 88(8): 1161-1172.

Stolz, J.F., Chang, S.-B.R., Kirschvink, J.L., 1986. Magnetotactic bacteria and single-domain magnetite in hemipelagic sediments. Nature, 321: 849-851.

Tessin, A., Sheldon, N.D., Hendy, I., Chappaz, A., 2016. Iron limitation in the Western Interior Seaway during the Late Cretaceous OAE3 and its role in phosphorus recycling and enhanced organic matter preservation. Earth and Planetary Science Letters, 449(2016): 135-144.

Tribovillard, N., Algeo, T.J., Baudin, F., Riboulleau, A., 2012. Analysis of marine environmental conditions based onmolybdenum–uranium covariation—Applications to Mesozoic paleoceanography. Chemical Geology, 324-325: 46-58.

Tribovillard, N., Algeo, T.J., Lyons, T., Riboulleau, A., 2006. Trace metals as paleoredox and paleoproductivity proxies: An update. Chemical Geology, 232(1-2): 12-32.

van der Zee, C., Roberts, D.R., Rancourt, D.G., Slomp, C.P., 2003. Nanogoethite is the dominant reactive oxyhydroxide phase in lake and marine sediments. Geology, 31(11): 993-996.

Vorlicek, T.P., Chappaz, A., Groskreutz, L.M., Young, N., Lyons, T.W., 2015. A new analytical approach to determining Mo and Re speciation in sulfidic waters. Chemical Geology, 403: 52-57.

Vorlicek, T.P., Kahn, M.D., Kasuya, Y., Helz, G.R., 2004. Capture of molybdenum in pyrite-forming sediments: role of ligand-induced reduction by polysulfides. Geochimica et Cosmochimica Acta, 68(3): 547-556.

Wang, Y., Hendy, I., Napier, T.J., 2017. Climate and Anthropogenic Controls of Coastal Deoxygenation on Interannual to Centennial Timescales. Geophysical Research Letters, 44(22): 11528–11536.

Warrick, J.A., Farnsworth, K.L., 2009a. Dispersal of river sediment in the Southern California Bight. 454: 53-67.

Warrick, J.A., Farnsworth, K.L., 2009b. Sources of sediment to the coastal waters of the Southern California Bight. The Geological Society of America Special Paper, 454: 39-52.

Wijsman, J.W.M., Middelburg, J.J., Heip, C.H.R., 2001. Reactive iron in Black Sea Sediments: implications for iron cycling. Marine Geology, 172(2001): 167-180.

Yücel, M., Luther, G.W., Moore, W.S., 2010. Earthquake-induced turbidite deposition as a previously unrecognized sink for hydrogen sulfide in the Black Sea sediments. Marine Chemistry, 121(1-4): 176-186.

Zheng, Y., Anderson, R.F., Geen, A.V., James, K., 2000. Authigenic molybdenum formation in marine sediments: A link to pore water sulfide in the Santa Barbara Basin. Geochimica et Cosmochimica Acta, 64(24): 4165-4178.

Chapter 4

Climate and Anthropogenic Controls of Coastal Deoxygenation on Interannual to Centennial Timescales [2]

4.1 Abstract

Understanding dissolved oxygen variability in the ocean is limited by the short duration of direct measurements, however sedimentary oxidation-reduction reactions can provide context for modern observations. Here we use bulk sediment redox-sensitive metal enrichment factors (Mo_{EF}, $Re_{EF,}$ and U_{EF}) and scanning X-ray fluorescence (XRF) records to examine annual-scale sedimentary oxygen concentrations in the Santa Barbara Basin from the Industrial Revolution (AD ~1850) to present. Enrichments are linked to measured bottom water oxygen concentrations after 1986. We reveal gradual intensification of the coastal oxygen minimum zone (OMZ) on the southern California margin coinciding the 20th century anthropogenic warming trend that leads to reduced oxygen solubility and greater stratification. High-frequency interannual oscillations become more prominent over the last three decades. These are attributed to local 'flushing events' triggered by the transition from El Niño to La Niña conditions, which further amplify changes in the extratropical southern Californian OMZ.

4.2 Introduction

As a critical component in marine environments, dissolved oxygen (DO) strongly modulates both metabolic and geochemical processes (Keeling et al., 2010). Reduced DO in the water column results in loss of biodiversity and sublethal stresses on surviving organisms (e.g., forced migration and reduction of habitats), especially in coastal marine ecosystems already impacted by pre-existing low-O_2 stresses (Bopp et al., 2002; Deutsch et al., 2014; Rabalais et al., 2002; Vaquer-Sunyer and Duarte, 2008). In a warming ocean, declining O_2 in OMZs is attributed

[2] Published under the citation: Wang, Y., Hendy, I., Napier, T.J., 2017. Climate and Anthropogenic Controls of Coastal Deoxygenation on Interannual to Centennial Timescales. Geophysical Research Letters, 44(22): 11528–11536.

to lower gas solubility in the surface ocean and increased stratification, which reduces subsurface O_2 supply (Keeling and Garcia, 2002). Primary productivity also plays a role as organic matter remineralization consumes significant O_2 in the ocean interior, and thus upwelling-induced high primary productivity regions often intersect with coastal OMZs. Human activities contribute to oxygen minimum zone (OMZ) expansion through anthropogenic climate change and eutrophication (Deutsch et al., 2014; Diaz and Rosenberg, 2008). Nutrient-rich river discharge causes eutrophication, further stimulating phytoplankton growth, resulting in greater organic carbon flux and consequent O_2 loss. However, advection of oxygenated water into coastal OMZs replenishes stagnant, low-O_2 waters, counteracting eutrophication. Although ocean time series (McClatchie et al., 2010; Whitney et al., 2007) and repeated hydrological surveys (Bograd et al., 2008; Stramma et al., 2008) demonstrate statistically significant declines in water column DO, these measurements are limited by sparse sampling and short time series (< 50 years).

Pre-instrumental OMZ changes are often reconstructed using sedimentary geochemical proxies, as DO controls redox-sensitive elemental concentrations in sediments during organic matter remineralization (Calvert and Pedersen, 2007; Scholz et al., 2014). Following depletion of oxygen, sulfate eventually becomes the dominant electron acceptor in remineralization, resulting in accumulation of HS^- and facilitating redox-sensitive metal precipitation (Canfield and Thamdrup, 2009). Here we use redox metal enrichment factors ($metal_{EF}$) over local lithogenic background to track changes in the reducing environment of sediment porewaters (see Methods). Both Re and U have a negligible lithogenic background and are conservative in oxygenated waters, but are reduced to insoluble precipitates and enriched in sediments under low O_2 conditions (Crusius et al., 1996; Tribovillard et al., 2006). In contrast, authigenic Mo precipitation proceeds only in the presence of free HS^- when O_2 concentrations are negligible, and thus indicates a strongly reducing environment (Crusius et al., 1996). As Re is preferentially scavenged under less reducing conditions, Re/Mo ratios are used to indicate changing redox conditions at the time of sediment deposition (Crusius et al., 1996). Sedimentary Re/Mo decreases when porewaters shift from slightly- to strongly-reducing sulfidic environments (free HS^- present).

As a near-shore basin in the southern California Bight, the Santa Barbara Basin (SBB) provides an ideal sedimentary archive for high-resolution reconstruction of the pre-instrumental OMZ from both climatic and anthropogenic perspectives. Measurements by the California

Cooperative Oceanic and Fisheries Investigations (CalCOFI) indicate persistent low-oxygen concentrations (typically < 20 μmol/kg) in the bottom water of central SBB. This low oxygen environment is inhospitable for most benthic mega- and macrofauna (notably burrowing organisms) except the sediment surface-dwelling gastropod *Alia permodesta* (Bernhard et al., 2000; Bernhard et al., 2003; Myhre et al., 2017), preserving the seasonally distinct varved laminations for high-resolution reconstructions (Schimmelmann et al., 1990). With a sill depth of ~450 m to the west, bottom water in the basin is either supplied from the California Undercurrent (CUC) (Bograd et al., 2008; Lynn and Simpson, 1990; Nam et al., 2015) or 'flushing events' - uplifted cold intermediate water (Auad et al., 2003) that flush SBB when dense subsurface waters displace more buoyant water in the basin (Bograd, 2002). Furthermore, due to its proximity to densely populated southern California, high-resolution sediment records in the SBB also make it possible to investigate abrupt OMZ responses to anthropogenic impacts.

Although extremely low oxygen concentrations in SBB are in part enhanced by silled bathymetry (Moffitt et al., 2014), SBB still provides an model for near-shore basins in the Southern California Bight (e.g., Santa Monica Basin and San Pedro Basin) and physically connected to Baja California (eastern tropical northern Pacific, ETNP) via the CUC (Deutsch et al., 2014; Kienast et al., 2002). Here we reconstruct the long-term and interannual OMZ responses to the global change since the Industrial Revolution in SBB sediments to understand processes controlling southern Californian OMZ variability, and to improve predictions of OMZ responses to human activities (Fig. 4-1). The core site has also been monitored quarterly by the CalCOFI since 1985. This provides direct measurements of bottom water properties for ~30 years and a unique linkage between the sedimentary record and water column observations.

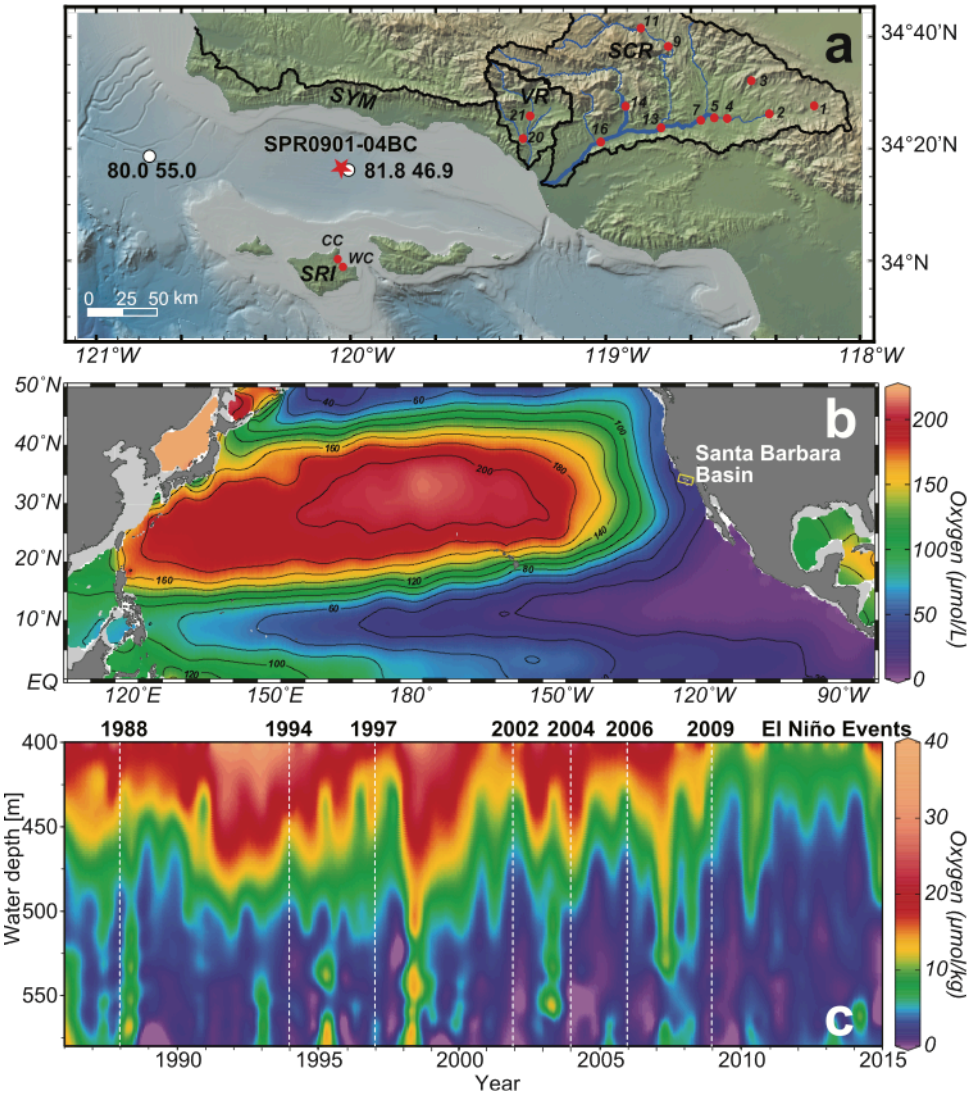

Figure 4-1 Study area and oxygen time series. (a) Map of the Santa Barbara Basin (SBB). The red star denotes the core site of SPR0901-04BC while the two white circles represent the CalCOFI stations (81.8 46.9 [34°16'29.64"N, 120°1'30"W] and 80.0 55.0 [34°19'N, 120°48'10.8"W]). River catchments are outlined in black. Main stems of selected rivers are indicated by thick blue lines: Santa Clara River (SCR), Ventura River (VR), Santa Ynez Mountain (SYM), and Santa Rosa Island (SRI). Lithogenic background sample sites are shown in red circles. Bathymetry is from Global Multi-Resolution Topography version 2.6 (Ryan et al., 2009). (b) Color shaded contour map shows the oxygen concentration (μmol/L) at 400 m water depth. SBB is denoted with a yellow box. Data are from the World Ocean Atlas 2013 on a 1° longitude×1° latitude grid; (c) Intermediate-depth O_2 concentration time series (μmol/kg) from 1985 to 2015 at the center of SBB, indicating highly variable oxygen concentrations. Selected El Niño events are highlighted with white dashed lines. Data are obtained from CalCOFI station 81.8 46.9. Maps and profiles are generated from Ocean Data View (Schlitzer, 2000).

4.3 Materials and Methods

The 67-cm box core SPR0901-04BC (34°16.895'N, 120°02.489'W, 588 m water depth) was recovered from SBB in January 2009 (Figs. 4-1 and B-1). The basin is bounded by narrow sills to the west and east, with a depth of 475 m and 230 m, respectively (Figs. 4-1 and B-1). SBB sediments are well-dated by radiometric methods and sediment fabric observations through ~40 years of frequent coring expeditions(Hendy et al., 2015). The sediment age model is based

upon well-established varve counts (Schimmelmann et al., 1990) and correlations to previously dated SBB cores using the same distinctive sedimentary fabric, notably varves associated with strong El Niño events in 1941, 1957, 1983, and 1997 CE, two gray layers at 1761 and 1861-1862 CE, the turbidite layer at 1812 CE, and the *Macoma* bivalve layer at 1841 CE (Schimmelmann et al., 1992). Ages were then assigned to other samples based on the age model described above (Hendy et al., 2015).

The core was scanned using an X-ray fluorescence (XRF) core scanner (Cox Analytical Instruments) at the Large Lakes Observatory, University of Minnesota, Duluth. The scanner was operated at 200-µm resolution with an 8-second scan time using a Cr X-ray tube with a voltage of 30 kV and a current at 15 mA. The output results were recorded as counts per 8 seconds and are semi-quantitative (Croudace et al., 2006; Hendy et al., 2015). Elemental XRF counts were normalized to Cr coherent scattering to isolate fluorescence intensity change from instrumental factors (for instance, tube aging) that may affect the primary beam intensity (Croudace et al., 2006). Ti, a conservative element that is well-resolved by scanning XRF was employed as a normalizing element for terrigenous input (Croudace et al., 2006), to isolate the authigenic redox signal from siliciclastic input. Sulfur counts were normalized to Cl, which is known to be conservative and representative of sea salts, to eliminate the influence of porewater salinity (Ziegler et al., 2008).

For quantitative analyses, core SPR0901-04BC was sampled at continuous 1 cm intervals (~2 – 7 years) in spring 2013 to generate bulk samples (Hendy et al., 2015). The samples were freeze-dried and ground to < 75 µm. 3 – 5 g of each powdered sample was sent to ALS Laboratories in Vancouver, Canada. The bulk samples were digested using nitric, perchloric, hydrofluoric, and hydrochloric cocktail. Quantitative analyses of major, minor and trace elements were conducted with inductively coupled plasma (ICP)-mass spectrometry and ICP-atomic emission spectroscopy (ICP-AES). Standard measurement errors for lab standards GBM908-10 and MRGeo08 are listed in Table B-1.

Enrichment factors for redox-sensitive elements are calculated from measured sample concentrations and the regional lithogenic background value of SBB terrigenous sediment sources using the following equation (Turekian and Wedepohl, 1961):

$$EF_i = \frac{(Element_i / Al)_{sample}}{(Element_i / Al)_{background}} \qquad \text{(Eq. 4-1)}$$

The mean background values of three sediment sources (Santa Clara River, Ventura River and the Channel Islands) were used to obtain a representative background lithogenic value for SBB sediments (for sample sites see Figs. 4-1 and B-2; Table B-3). The weighted average value was calculated using a proportional sediment flux contribution of 0.78, 0.07 and 0.15 for the Santa Clara River, Ventura River and the Channel Islands, respectively (Warrick and Farnsworth, 2009).

To relate sedimentary redox proxies to bottom water observations, we used quarterly sampled bottom water nutrients and physical property data by CalCOFI from 1986 to 2015 at Station 81.8 46.9 (center of the basin, 34°16'29.64"N, 120°1'30"W at 557 – 578 m water depth), and station 80.0 55.0 (western sill depth, 34°19'N, 120°48'10.8"W at 500 m water depth) (Fig. 4-1 and Fig B-1). Dissolved oxygen was determined using Winkler titrations (Carpenter, 1965), but this method was replaced by auto-titration measuring UV absorption of tri-iodide ion in 2003. Nutrients were measured with a colorimetrical method on automated analyzers (Gordon et al., 1993). Detailed methods and data processing protocols can be found at www.calcofi.org.

ENSO phases are quantified by SST anomalies obtained from the Niño 3.4 Index (from NOAA, monthly SST from 5°N – 5°S and 170° – 120°W) after removing the mean value from 1951 – 2000. The CalCOFI bottom water temperature record sampled at 3-month intervals was interpolated to generate the same temporal resolution for correlation with monthly Niño 3.4 anomalies between 1986 and 2015 (n = 349). Cross-correlation shows maximum correlation coefficient with 2 – 3 month lag at 95% confidence level (see Appendix B, Fig. B-3). Here we use a response time of 3 months in relating ENSO perturbation to OMZ oscillations to account for the longer lag experienced by subsurface upwelling sourced water as opposed to pycnocline depth anomalies (Jacox et al., 2015).

4.4 Sedimentary oxygen reconstruction since the Industrial Revolution

Core SPR0901-04BC is a mostly laminated sequence except for the two identified gray layers (1761 – 1762 and 1861 flood) and one olive layer associated with the 1812 Santa Barbara earthquake (Hendy et al., 2015). It exhibits both long-term (centennial) evolution of reducing porewater conditions associated with regional warming trends (Barron et al., 2013; Field et al., 2006), and abrupt porewater responses to anthropogenic perturbations. Additionally, a high sedimentation rate (~2 – 3 mm/y) and seasonally distinct laminations allow for identification of interannual climate variability superimposed on the long-time (~150 year) OMZ evolution.

Before AD 1811, sedimentary laminations in the core demonstrate insufficient porewater O_2 for macrofauna. At ~1840 *Macoma* bivalve shells were found preserved *in situ* (Schimmelmann et al., 1992). These bivalves are intolerant of hypoxia (< 65 μmol/kg) (Coan, 2000; Myhre et al., 2017), indicating a relatively well-oxygenated benthic environment existed for < 3 years. Less reducing sedimentary conditions at this time may have been attributed to the abrupt deposition of a seismically triggered turbidite in 1812 (Borrero et al., 2001). A pulse of metal oxides introduced into the deep basin, especially reactive Fe hydroxides, could have provided oxidants for free sulfides in bottom water. However, this interval also coincides with locally depressed sea surface temperatures (SSTs) associated with the end of the Little Ice Age (Briffa et al., 1998; Pak et al., 2016). Higher gas solubility and reduced water column stratification during early 19th century cooling may have led to redistribution of vertical zonation of ecosystems to allow benthic oxygenated ecosystems as O_2 increased on the margin (Moffitt et al., 2015). Our results cannot distinguish between these two possible scenarios, which additionally do not preclude each other. Suffocation of *Macoma* in ~1845 is supported by declining Re/Mo values and concomitant increasing Mo_{EF} (Figs. 4-2a and c), suggesting a return to low-oxygen conditions (Schimmelmann et al., 1992).

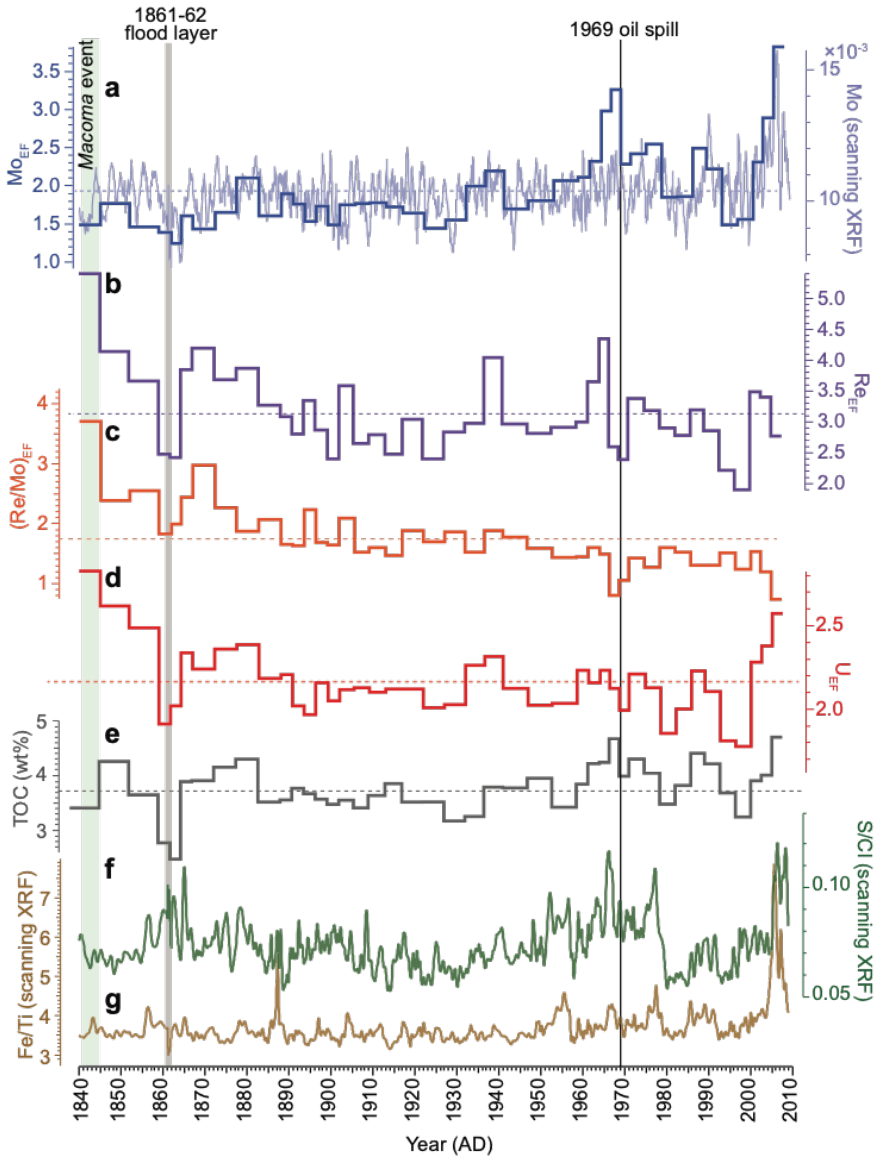

Figure 4-2 Enrichment factors (EFs) of redox proxies and average values for the last 170 years: (a) Mo_{EF} (thick blue line), the average value of Mo_{EF} (blue dashed line), and 20-pt moving average of scanning XRF Mo normalized to Cr coherent scattering (thin blue line); (b) Re_{EF} (thick purple line) and average value (purple dashed line); (c) Re_{EF}/Mo_{EF} ratio (thick orange line) and average value (orange dashed line); (d) U_{EF} (thick red line) and average value (red dashed line); (e) TOC (wt. %, thick gray line) and mean value (gray dashed line)(Hendy et al., 2015); (f-g) The 20-pt moving average of scanning XRF Fe/Ti (brown line) and S/Cl (green line); The *Macoma* bivalve layer (green shading), 1861 – 62 flood layer (gray bar), and 1969 oil spill event (black line) are indicated.

The 1861 – 62 flood (~0.7 cm gray layer, Hendy et al. (2015)) brought a pulse of oxygenated sediments into the basin that partly obscure the long-term trend towards more reducing porewater conditions (Fig. 4-2). However, from 1870 to ~1950 the average Mo_{EF} increased from 1.46 ± 0.12 (95% confidence level, prior to 1870) to 1.73 ± 0.08 with a concurrent Re/Mo decline from 2.55 ± 0.47 to 1.77 ± 0.09, as Re_{EF} decreased from 3.73 ± 0.76 to 3.04 ± 0.18 and U_{EF} from 2.35 ± 0.24 to 2.13 ± 0.05 (Figs. 4-2a to d). This redox shift was

decoupled from the sedimentary total organic carbon (TOC) concentrations, which remained mostly below average (~3.74 wt%) during this interval (Fig. 4-2e). Thus factors other than O_2 consumption by organic matter remineralization must have played a role in changing porewater redox chemistry. This long-term shift coincided with a rise in regional SSTs, as indicated by dinoflagellate cyst, foraminifera, coccolithophore, diatom and silicoflagellate census data (Barron et al., 2013; Bringué et al., 2014; De Bernardi et al., 2008; Field et al., 2006; Grelaud et al., 2009). Dinoflagellate taxa from SBB sediments suggest both warming SSTs and relaxation of upwelling conditions as early as the 1900s (Bringué et al., 2014). Diatoms also indicate 20th century warming, as assemblages shift toward larger diatom species around the 1940s (Barron et al., 2013). Anthropogenic 20th century warming could have led to a deeper thermocline and more intense stratification, reducing the O_2 supply to subsurface waters and providing a mechanism for the long-term shift toward more reducing conditions in the basin (Di Lorenzo et al., 2005; Keeling and Garcia, 2002).

The sedimentary record also reveals the role of anthropogenic impacts on rapidly altering porewater redox chemistry, as indicated by sharp spikes in Mo_{EF} and a dramatic Re/Mo decline after 1950 and notably at 1969 (Fig. 4-2). These abrupt changes are clearly identified in the high-resolution Fe/Ti and S/Cl scanning XRF records. The sudden increase of sedimentary O_2 demand in 1969 may be associated with a well blowout in the Santa Barbara Channel that released ~420,0000 gallons of crude oil following ~40 years of metal enriched drill oil discharge into SBB (Foster et al., 1971). A demand for porewater O_2 during the degradation of spilled hydrocarbon in this interval could have produced a dramatic shift toward more reducing porewater conditions. Similar sedimentary responses towards more reducing environments have also been observed in the Gulf of Mexico within the following two years after the *Deepwater Horizon* blowout in 2010 (Hastings et al., 2016), further addressing the role of anthropogenic perturbations on interannual oxygenation shifts in coastal areas.

After the 1970s, S/Cl and Fe/Ti records, in addition to redox sensitive metals, exhibit coincident oscillations (Fig. 4-2). Redox sensitive metal EFs, Mo in particular, become more coherent with sedimentary TOC content (correlation coefficient of 0.83, n = 12, after 1969 compared to 0.66, n = 25, between 1870 – 1969), suggesting organic matter remineralization controlled porewater redox changes that lead to rapid scavenging of redox elements near the sediment-water interface (Algeo and Lyons, 2006).

4.5 Water column observations and the sedimentary redox record

Comparison of independent, quarterly-sampled CalCOFI water chemistry time series to sub-annually sampled sedimentary scanning XRF records of redox-sensitive metals demonstrate annual-scale coherence from 1986 to 2010 (corresponding to ~7 cm depth in the sediment record). Nitrite spikes recorded (~4 and 7 µmol/kg nitrite) in the summers of 2004 and 2005 were produced by denitrification in the local water column supported by concurrent decline of bottom water nitrate concentrations in the basin (Fig. 4-3c). Denitrification may have aggravated nitrogen loss in the water column and sharply altered the redox potential to facilitate redox metal precipitation. Coincident peaks in the subannually resolved scanning XRF Mo and Fe/Ti counts (Figs. 4-3a and b) confirm redox mineral preservation near the sediment-water interface that can be linked to highly active biogeochemical nutrient cycling in the water column. Thus, sedimentary redox proxies are closely associated with water column oxygenation conditions, highlighting the validity of applying downcore records to reconstruct water column chemistry. Furthermore, scanning XRF records have the potential to capture annually resolved redox changes.

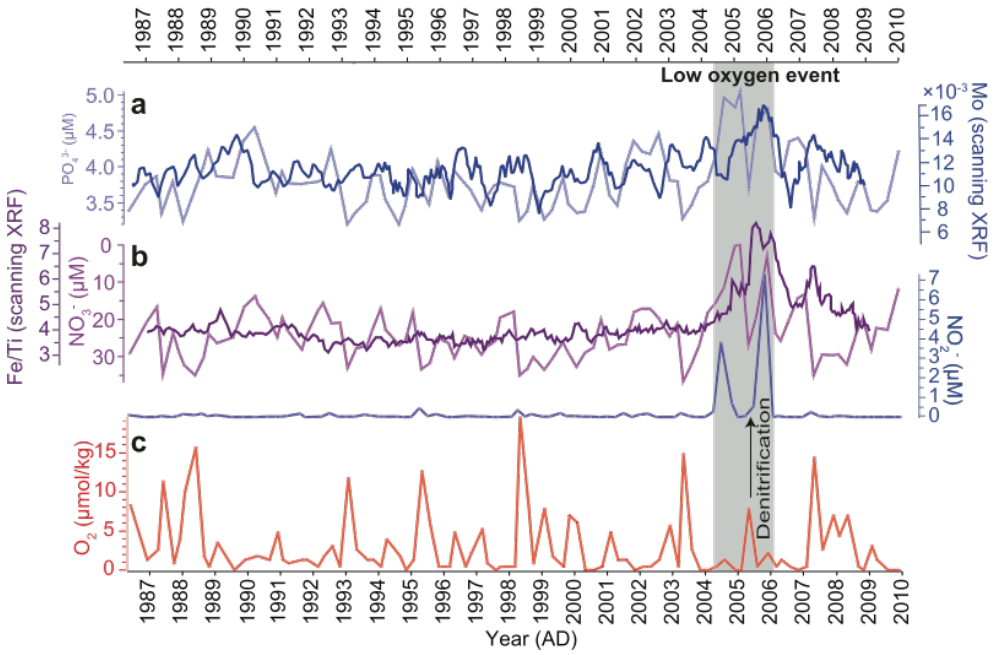

Figure 4-3 Bottom water properties of Santa Barbara Basin (SBB) and redox proxies. (a) Bottom water phosphate (µmol/L, thick light blue line) and the 5-pt moving average of normalized scanning XRF Mo (thin blue line) normalized to Cr coherent scattering; (b) Nitrate (µmol/L, light purple line), 5-point moving average of Fe/Ti (dark purple line), and nitrite (µmol/L, light blue line); (c) Dissolved oxygen of bottom water (µmol/kg, red line). Water chemistry and temperature data are obtained from California Cooperative Oceanic Fisheries Investigations (CalCOFI). The low oxygen event is indicated by gray shading.

4.6 Interannual dissolved oxygen concentrations and ENSO variability

Observed high frequency variability in redox metal concentrations suggests that other mechanisms beyond the centennial temperature-driven O_2 saturation may be important to DO concentrations. Both SBB sediment geochemistry and direct water column measurements display O_2 variability on an annual scale (Figs. 4-3 and 4-4) that can be attributed to interannual climate variability. Fig.4 demonstrates a tight linkage between ENSO variability and bottom water oxygen replenishment since 1986, notably through aforementioned 'flushing events' that control interannual bottom water O_2 concentrations and consequently impact the redox potential of sediment porewaters. When a 3-month lag is applied to the bottom water temperature and DO measurements relative to the Niño 3.4 temperature anomaly record, a significant correspondence (cross correlation r = 0.33, 95% confidence level, see Supporting Information) is produced (Fig. 4-4). Rapid bottom water temperature decreases typically correspond to DO increases, suggesting external input of dense, cold and oxygenated water by flushing events. During El Niño years, bottom waters are typically anomalously warm (with a ~3 month response time). The concurrently depressed thermocline, weakened upwelling with shallower source water depth (Jacox et al., 2015), and the stronger CUC (Lynn and Bograd, 2002) contribute to a stagnant water column in SBB (lower frequency of flushing events, Fig. 4-4). With the transition from El Niño to La Niña conditions, invigorated upwelling flushes colder and more oxygenated intermediate water into the basin. Although flushing events are able to replenish water column O_2 instantaneously, SBB is only temporarily ventilated because subsequent remineralization of sinking organic matter quickly consumes the newly replenished O_2 in the bottom water (Fig. 4-4). Therefore, ENSO variability currently plays a role in rapidly switching the basin between the two oxygenation states (ventilated or stagnant) within several months. This highly oscillatory bottom water chemistry has contributed to the significant variability in porewater redox conditions over the past several decades. These results suggest short duration OMZ shifts can be predicted using ENSO indices providing several months of lead-time to assess potential ecological and environmental impacts on local ecosystems.

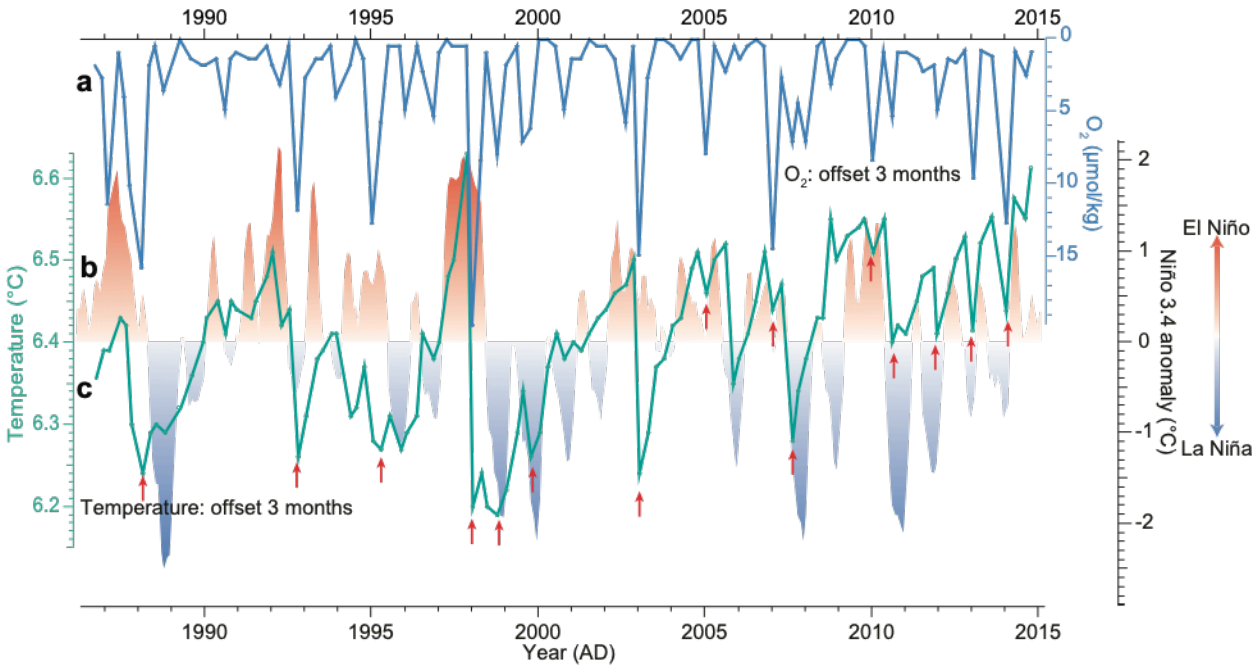

Figure 4-4 Relationship between bottom water temperature, oxygen concentration and ENSO variability. (a) Dissolved oxygen of bottom water (blue line, µmol/kg) at station 81.8 46.9 (water depths between 557 – 578 m used; data offset of 3 months applied); (b) Bottom water temperature at the same station denoted as the green line (°C, data offset of 3 months applied); (c) Red (El Niño) and blue (La Niña) shading represent Niño 3.4 anomalies as indicators of ENSO variability. Red arrows indicate flushing events that correspondent to abrupt water temperature decreases.

4.7 Conclusions

This high-resolution sediment archive extends dissolved oxygen (DO) instrumental measurements back in time and provides a unique insight into long-term evolution of the southern Californian coastal oxygen minimum zone (OMZ) since the Industrial Revolution (~1850). Enrichment of redox-sensitive metals in Santa Barbara Basin (SBB) sediments demonstrate aggravated reducing porewater environments that may result from the OMZ intensification through time. This centennial deoxygenation is attributed to the warming of the North Pacific Ocean as primary productivity is shown to decouple from observed OMZ evolution. The 1969 oil spill in SBB is also recorded as a regional anthropogenic driven OMZ perturbation. Furthermore, interannual DO variability within the long-term deoxygenation trend is observed in both bottom water observations and the subannual scanning XRF elemental composition of sediments. 'Flushing event' frequency of SBB bottom waters is associated with interannual climate (ENSO) variability, which switches the basin between a stagnant and ventilated water column, further amplifying the OMZ variability.

4.8 Acknowledgments

This work is supported by the National Science Foundation under grant number OCE-1304327 awarded to I.H.; Y.W. and T.J.N. acknowledge support from the Rackham Graduate School of the University of Michigan. We would like to thank crews and scientists in CalCOFI for collecting high-quality data for decades and making it accessible to the public. CalCOFI data were freely obtained from http://calcofi.org/data.html. Other data are included as tables in the Appendix B.

4.9 References

Algeo, T.J., Lyons, T.W., 2006. Mo-total organic carbon covariation in modern anoxic marine environments: Implications for analysis of paleoredox and paleohydrographic conditions. Paleoceanography, 21(1): 1-23.

Auad, G., Kennett, J.P., Miller, A.J., 2003. North Pacific Intermediate Water response to a modern climate warming shift. Journal of Geophysical Research, 108(C11): 1-13.

Barron, J.A., Bukry, D., Field, D.B., Finney, B., 2013. Response of diatoms and silicoflagellates to climate change and warming in the California Current during the past 250 years and the recent rise of the toxic diatom Pseudo-nitzschia australis. Quaternary International, 310: 140-154.

Bernhard, J.M., Buck, K.R., Farmer, M.A., Bowser, S.S., 2000. The Santa Barbara Basin is a symbiosis oasis. Nature, 403: 77-80.

Bernhard, J.M., Visscher, P.T., Bowser, S.S., 2003. Submillimeter life positions of bacteria, protists, and metazoans in laminated sediments of the Santa Barbara Basin. Limnology and Oceanography, 48(2): 813-828.

Bograd, S.J., 2002. Bottom water renewal in the Santa Barbara Basin. Journal of Geophysical Research, 107(C12).

Bograd, S.J. et al., 2008. Oxygen declines and the shoaling of the hypoxic boundary in the California Current. Geophysical Research Letters, 35(12): 1-6.

Bopp, L., Le Quéré, C., Heimann, M., Manning, A.C., Monfray, P., 2002. Climate-induced oceanic oxygen fluxes: Implications for the contemporary carbon budget. Global Biogeochemical Cycles, 16(2): 1-13.

Borrero, J.C., Dolan, J.F., Synolakis, C.E., 2001. Tsunamis within the Eastern Santa Barbara Channel. Geophysical Research Letters, 28(4): 643-646.

Briffa, K.R., Jones, P.D., Schwelngruber, F.H., Osborn, T.J., 1998. Influence of volcanic eruptions on Northern Hemisphere summer temperature over the past 600 years. Nature, 393: 450-455.

Bringué, M., Pospelova, V., Field, D.B., 2014. High resolution sedimentary record of dinoflagellate cysts reflects decadal variability and 20th century warming in the Santa Barbara Basin. Quaternary Science Reviews, 105: 86-101.

Calvert, S.E., Pedersen, T.F., 2007. Elemental Proxies for Palaeoclimatic and Palaeoceanographic Variability in Marine Sediments: Interpretation and Application, Developments in Marine Geology, pp. 567-644.

Canfield, D.E., Thamdrup, B., 2009. Towards a consistent classification scheme for geochemical environments, or, why we wish the term 'suboxic' would go away. Geobiology, 7(4): 385-92.

Carpenter, J.H., 1965. The Chesapeake Bay Institute Technique for the Winkler dissolved oxygen method. Limnology and Oceanography, 10(1): 141-143.

Coan, E.V., 2000. The eastern Pacific Recent species of the bivalve genus Gari (Tellinoidea: Psammobiidae), with notes on western Atlantic and fossil taxa. Malacologia, 42(1-2): 1-29.

Croudace, I.W., Rindby, A., Rothwell, R.G., 2006. ITRAX: description and evaluation of a new multi-function X-ray core scanner. Geological Society, London, Special Publications, 267(1): 51-63.

Crusius, J., Calvert, S., Pedersen, T., Sage, D., 1996. Rhenium and molybdenum enrichments in sediments as indicators of oxic, suboxic and sulfidic conditions of deposition. Earth and Planetary Science Letters, 145: 65-78.

De Bernardi, B., Ziveri, P., Erba, E., Thunell, R.C., 2008. Calcareous phytoplankton response to the half century of interannual climatic variability in Santa Barbara Basin (California). Paleoceanography, 23(2): 1-13.

Deutsch, C. et al., 2014. Centennial changes in North Pacific anoxia linked to tropical trade winds. Science, 345(6197): 665-668.

Di Lorenzo, E., Miller, A.J., Schneider, N., McWilliams, J.C., 2005. The Warming of the California Current System- Dynamics and Ecosystem Implications. Journal of Physical Oceanography, 35: 336-362.

Diaz, R.J., Rosenberg, R., 2008. Spreading dead zones and consequences for marine ecosystems. Science, 321(5891): 926-9.

Field, D., Baumgartner, T.R., Charles, C.D., Ferrelra-Bartrina, V., Ohman, M.D., 2006. Planktonic foraminifera of the California Current reflect 20th-century warming. Science, 311: 63-66.

Foster, M., Charters, A.C., Neushul, M., 1971. The Santa Barbara oil spill Part 1: initial quantities and distribution of pollutant crude oil. Environmental Pollution, 2: 97-113.

Gordon, L.I., Jennings, J.C.J., Ross, A.A., Krest, J.M., 1993. A Suggested Protocol for Continuous Flow Automated Analysis of Seawater Nutrients in the WOCE Hydrographic Program and the Joint Global Ocean Fluxes Study, WOCE Hydrographic Program Office.

Grelaud, M., Schimmelmann, A., Beaufort, L., 2009. Coccolithophore response to climate and surface hydrography in the Santa Barbara Basin, California, AD 1917-2004. Biogeosciences, 6: 2025-2039.

Hastings, D.W. et al., 2016. Changes in sediment redox conditions following the BP DWH blowout event. Deep Sea Research Part II: Topical Studies in Oceanography, 129: 167-178.

Hendy, I.L., Napier, T.J., Schimmelmann, A., 2015. From extreme rainfall to drought: 250 years of annually resolved sediment deposition in Santa Barbara Basin, California. Quaternary International, 387: 3-12.

Jacox, M.G., Fiechter, J., Moore, A.M., Edwards, C.A., 2015. ENSO and the California Current coastal upwelling response. Journal of Geophysical Research: Oceans, 120: 1691-1702.

Keeling, R.E., Garcia, H.E., 2002. The change in oceanic O2 inventory associated with recent global warming. Proceedings of the National Academy of Sciences of the United States of America, 99(12): 7848-7853.

Keeling, R.E., Kortzinger, A., Gruber, N., 2010. Ocean deoxygenation in a warming world. Ann Rev Mar Sci, 2: 199-229.

Kienast, S.S., Calvert, S.E., Pedersen, T.F., 2002. Nitrogen isotope and productivity variations along the northeast Pacific margin over the last 120 kyr: Surface and subsurface paleoceanography. Paleoceanography, 17(4): 7-1-7-17.

Lynn, R.J., Bograd, S.J., 2002. Dynamic evolution of the 1997–1999 El Niño–La Niña cycle in the southern California Current System. Progress in Oceanography, 54: 59-75.

Lynn, R.J., Simpson, J.J., 1990. The flow of the undercurrent over the continental borderland off southern California. Journal of Geophysical Research, 95(C8): 12995-13008.

McClatchie, S., Goericke, R., Cosgrove, R., Auad, G., Vetter, R., 2010. Oxygen in the Southern California Bight-Multidecadal trends and implications for demersal fisheries. Geophysical Research Letters, 37(L19602): 1-5.

Moffitt, S.E., Hill, T.M., Ohkushi, K., Kennett, J.P., Behl, R.J., 2014. Vertical oxygen minimum zone oscillations since 20 ka in Santa Barbara Basin: A benthic foraminiferal community perspective. Paleoceanography, 29(1): 44-57.

Moffitt, S.E., Hill, T.M., Roopnarine, P.D., Kennett, J.P., 2015. Response of seafloor ecosystems to abrupt global climate change. Proc Natl Acad Sci U S A, 112(15): 4684-9.

Myhre, S.E., Kroeker, K.J., Hill, T.M., Roopnarine, P., Kennett, J.P., 2017. Community benthic paleoecology from high-resolution climate records: Mollusca and foraminifera in post-glacial environments of the California margin. Quaternary Science Reviews, 155: 179-197.

Nam, S., Takeshita, Y., Frieder, C.A., Martz, T., Ballard, J., 2015. Seasonal advection of Pacific Equatorial Water alters oxygen and pH in the Southern California Bight. Journal of Geophysical Research: Oceans, 120(5387-5399).

Pak, D.K., Hendy, I.L., Weaver, J.C., Schimmelmann, A., Clayman, L., 2016. Foraminiferal proxy response to ocean temperature variability and acidification over the last 150 years in the Santa Barbara Basin (California). Quaternary International.

Rabalais, N.N., Turner, R.E., Wiseman, W.J., 2002. Gulf of Mexico Hypoxia, A.K.A. "The Dead Zone". Annual Review of Ecology and Systematics, 33(1): 235-263.

Ryan, W.B.F. et al., 2009. Global Multi-Resolution Topography synthesis. Geochemistry, Geophysics, Geosystems, 10(3): 1-9.

Schimmelmann, A. et al., 1992. Extreme climatic conditions recorded in Santa Barbara Basin laminated sediments: the 1835–1840 Macoma event. Marine Geology, 106(1992): 279-299.

Schimmelmann, A., Lange, C.B., Berger, W.H., 1990. Climatically controlled marker layers in Santa Barbara Basin sediments and fine-scale core-to-core correlation. Limnology and Oceanography, 35(1): 165-173.

Schlitzer, R., 2000. Electronic atlas of WOCE hydrographic and tracer data now available. Eos, Transactions American Geophysical Union, 81(5): 45-45.

Scholz, F., McManus, J., Mix, A.C., Hensen, C., Schneider, R.R., 2014. The impact of ocean deoxygenation on iron release from continental margin sediments. Nature Geoscience, 7(6): 433-437.

Stramma, L., Johnson, G.C., Sprintall, G.C., Mohrholz, V., 2008. Expanding Oxygen-Minimum Zones in the Tropical Oceans. Science, 320(5876): 655-658.

Tribovillard, N., Algeo, T.J., Lyons, T., Riboulleau, A., 2006. Trace metals as paleoredox and paleoproductivity proxies: An update. Chemical Geology, 232(1-2): 12-32.

Turekian, K., Wedepohl, K.H., 1961. Distribution of the Elements in Some Major Units of the Earth's Crust. Geological Society of America Bulletin, 72: 175-192.

Vaquer-Sunyer, R., Duarte, C.M., 2008. Thresholds of hypoxia for marine biodiversity. Proceedings of the National Academy of Sciences of the United States of America, 105(40): 15452-15457.

Warrick, J.A., Farnsworth, K.L., 2009. Sources of sediment to the coastal waters of the Southern California Bight. The Geological Society of America Special Paper, 454: 39-52.

Whitney, F.A., Freeland, H.J., Robert, M., 2007. Persistently declining oxygen levels in the interior waters of the eastern subarctic Pacific. Progress in Oceanography, 75(2): 179-199.

Ziegler, M., Jilbert, T., de Lange, G.J., Lourens, L.J., Reichart, G.-J., 2008. Bromine counts from XRF scanning as an estimate of the marine organic carbon content of sediment cores. Geochemistry, Geophysics, Geosystems, 9(5): 1-6.

Chapter 5

Local and Remote Forcing of Denitrification in the Northeast Pacific for the Last 2000 Years[3]

5.1 Abstract

Sedimentary $\delta^{15}N$ ($\delta^{15}N_{sed}$) has been widely applied as a proxy for water-column denitrification. When combined with additional productivity proxies, it provides insights into the driving forces behind long-term changes in water column oxygenation. High-resolution (~2 years) $\delta^{15}N_{sed}$ and productivity proxy records (total organic carbon [TOC], Si/Ti and Ca/Ti) from Santa Barbara Basin, California were generated from a well-dated Kasten core (SPR0901-03KC). These records reveal the relationship between Southern California upwelling and oxygenation over the past 2000 years.

Inconsistencies between Si/Ti (coastal upwelling proxy) and TOC (total export productivity proxy) suggest wind-curl upwelling influenced Southern California primary productivity, especially during intervals of weak coastal upwelling. Coherence between $\delta^{15}N_{sed}$, TOC, and drought indicators supports a local control of $\delta^{15}N_{sed}$ by atmospheric circulation, as persistent Northerly Winds associated with an intensified North Pacific High pressure cell lead to enhanced coastal upwelling. In the northeast Pacific, $\delta^{15}N_{sed}$ is used as a water mass tracer of denitrification signals transported north from the Eastern Tropical North Pacific (ETNP) via the California Undercurrent. A 1200-year $\delta^{15}N_{sed}$ record from the Pescadero slope, Gulf of California lies between denitrifying subsurface waters in the ETNP and Southern California. During the Medieval Climate Anomaly, coherence between Pescadero and SBB $\delta^{15}N_{sed}$ indicates connections between ETNP and Southern California on centennial time scales. Yet an out-of-phase relationship occurred when the Aleutian Low was anomalously strong during the Little Ice Age. We suggest intensified nutrient-rich subarctic water advection might have transported high-

[3] Published under the citation: Wang, Y., Hendy, I.L., Thunell, R., 2019. Local and Remote Forcing of Denitrification in the Northeast Pacific for the Last 2,000 Years. Paleoceanography and Paleoclimatology, 34: 1517-1533.

^{15}N nitrate into Southern California when the California Undercurrent and ETNP denitrification weakened.

5.2 Introduction

Highly active biogeochemical processes in oxygen minimum zones (OMZs) play a significant role in global nutrient cycling through their impact on nitrogen (N) cycles. In the three largest OMZs (eastern tropical North Pacific, eastern tropical South Pacific, and the Arabian Sea), water-column denitrification and anammox (anaerobic ammonium oxidation) observed at ~200-800 m (Brandes et al., 1998) account for almost a half of the total oceanic N loss (Ganeshram et al., 2002; Ganeshram et al., 1995). Thus, OMZs cast control on global nutrients through the fixed N inventory and ocean nutrient limitation, contributing to the regulation of CO_2 levels (Altabet, 2006b; Altabet and François, 1994; Deutsch et al., 2004; Ganeshram et al., 2002; Kienast et al., 2002). OMZs are anticipated to expand in a warming world due to reduced gas solubility and intensified stratification of the water column, yet the brevity of O_2 concentration observations in these OMZs (< 50 years) makes separating long-term (multidecadal to centennial) natural oceanic variability from anthropogenic influences difficult.

OMZ intensity controls water-column denitrification, as nitrate becomes the favorable electron acceptor after dissolved O_2 is depleted in microbe-regulated organic carbon remineralization. $\delta^{15}N$ is widely accepted as a proxy for water-column denitrification (Altabet et al., 1995; Altabet et al., 1999a; Thunell et al., 2004). Preferential removal of ^{14}N by denitrification progressively enriches ^{15}N in the remaining subsurface nitrate pool, which is then advected throughout the ocean. When this $\delta^{15}N$-enriched nitrate is upwelled into the photic zone and incorporated in particulate organic carbon that is exported to the sea floor, the subsurface $\delta^{15}N$ signal is preserved in the sediments, leading to elevated sedimentary $\delta^{15}N$ (Altabet, 2006b; Altabet and François, 1994; Deutsch et al., 2004; Ganeshram et al., 2002; Kienast et al., 2002). When O_2 supplies are reduced (e.g. due to lower solubility in a warmer climate) and/or O_2 consumption increases (e.g. due to greater availability of organic carbon for remineralization), sedimentary $\delta^{15}N$ increases alongside intensified water-column denitrification. To use $\delta^{15}N$ as an indicator of O_2 concentration, complete nitrate utilization in the photic zone must occur and $\delta^{15}N$ cannot be compromised during sedimentary diagenesis (Prokopenko et al., 2006; Thunell et al., 2004). Incomplete nitrate consumption in the photic zone, however, leaves a high $\delta^{15}N_{nitrate}$ signature due to preferential uptake of ^{14}N in photosynthesis, complicating sedimentary $\delta^{15}N$

interpretations (Altabet and François, 1994). The relative contribution of different N sources may also alter $\delta^{15}N$ of the fixed N pool and sedimentary $\delta^{15}N$ records (Fig. 5-1). Although oceanic N is usually sourced from N fixation ($\delta^{15}N$ = -2 – 0‰), atmospheric deposition ($\delta^{15}N \approx$ -2‰), and terrestrial input ($\delta^{15}N \approx$ 4‰) (Altabet, 2006b; Sigman et al., 2009a), increasing anthropogenic atmospheric deposition can decrease surface water $\delta^{15}N$ (Ren et al., 2017), and $\delta^{15}N$-depleted terrestrial inorganic carbon input can bias sedimentary $\delta^{15}N$ towards lower values (Kienast et al., 2005). Additionally, remotely advected water masses with different $\delta^{15}N$ signatures supply extra N to the photic zone in upwelling regions (e.g., Southern California margin; Liu and Kaplan (1989)), transmitting unique $\delta^{15}N$ signatures to sediments.

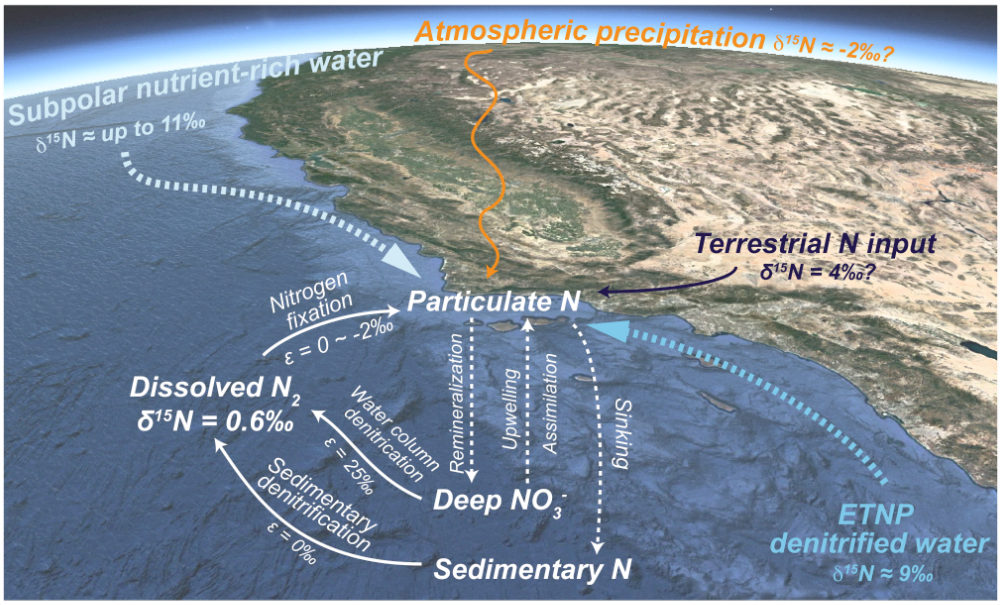

Figure 5-1 The nitrogen cycle in Southern California. Nitrogen inputs include dissolved N_2 via N fixation, atmospheric precipitation, terrestrial input, and remotely advected water masses (subpolar nutrient-rich waters and Eastern Tropical North Pacific [ETNP] dentrified waters shown in blue dashed arrows). Nitrogen outputs include water column and sedimentary denitrification. Internal cycling (e.g., remineralization, assimilation) is denoted with white dashed arrows. Kinetic fractionation effects (ε) and isotopic values for major N sources and transformation pathways are labeled.

Previous studies have shown that >1‰ $\delta^{15}N$ shifts in the Arabian Sea and the east tropical north Pacific (ETNP) occurred between glacial and interglacial, as OMZs contracted during cool intervals and expanded as climate warmed (Altabet et al., 1995; Ganeshram et al., 1995; Pride et al., 1999). Although $\delta^{15}N$ is assumed to be relatively stable in the late Holocene (Altabet, 2006a), several millennial-scale $\delta^{15}N$ records have shown linkages between OMZ variability and the Intertropical Convergence Zone (ITCZ) migration (Agnihotri et al., 2008; Salvatteci et al., 2014). A more southerly ITCZ position associated with centennial/millennial-

scale Northern Hemisphere (NH) cooling coincides with lower surface productivity and reduced denitrification off Peru (Agnihotri et al., 2008), supporting an oceanic OMZ response to climate forcing via large-scale atmospheric circulation.

A 2000-year high-resolution (~2 years) $\delta^{15}N_{sed}$ record from the well-dated Kasten core SPR0901-03KC (34°16.99'N, 120°2.408'W; 586 m depth) in the Santa Barbara Basin (SBB), Southern California was generated to explore long-term natural variability of $\delta^{15}N$ in response to water-column oxygenation and/or N flux changes. Paired total organic carbon (TOC) and the scanning X-ray fluorescence (XRF) elemental analyses constrain the impacts of regional productivity and terrestrial N input on sedimentary $\delta^{15}N$. These records show coherence between $\delta^{15}N_{sed}$, export productivity, and local precipitation to reveal a local control of the Southern California denitrification. The SBB $\delta^{15}N_{sed}$ was also compared to the 1200-year $\delta^{15}N_{sed}$ record from the Pescadero slope, Gulf of California (Tems et al., 2016), and the Mt. Logan ice core record (Osterberg et al., 2014) to investigate the coherence of northeast Pacific $\delta^{15}N$ variability in response to larger-scale (regional or global) processes (e.g., tropical and extra-tropical forcing). We will demonstrate competing influences of high-$\delta^{15}N$ saline water from the ETNP OMZ and oxygenated fresh water from the subarctic ocean following multidecadal to centennial-scale climate change.

5.3 Background

The Santa Barbara Basin (SBB) is a semi-closed basin located on the Southern California margin. Sedimentation in SBB is associated with annual couplets formed by alternation of biogenic-rich (light laminae under the X-ray radiography) and siliciclastic-rich sediments (dark laminae under the X-ray radiography). The lithogenic component accounts for ~70-80% of SBB sediments (Thunell et al., 1995) and is delivered to the basin via rivers draining the Western Transverse Ranges (Hendy et al., 2015). Under California's Mediterranean climate, the North Pacific High (NPH) weakens and is displaced equatorward in winter, allowing a strengthened Aleutian Low (AL) to steer precipitation toward Southern California, driving increased river runoff and silicilastic sedimentation (Checkley and Barth, 2009; Warrick and Farnsworth, 2009a).

In spring and summer, the NPH strengthens and migrates poleward, resulting in strong east-west pressure gradients that drive northerly upwelling-favorable alongshore winds, generating strong coastal upwelling (Checkley and Barth, 2009; Chelton, 1981). Nutrient-rich subsurface water upwells along the coast, producing spring-summer plankton blooms. In

addition to coastal upwelling that is typically restricted within 5 – 30 km along the coast (Checkley and Barth, 2009), offshore upwelling (up to 200 km) also plays a role in generating the high productivity observed in SBB. In the Southern California Current System (CCS), negative wind-curl in the North Pacific subtropical gyre is balanced by the positive wind-stress curl near-shore (Checkley and Barth, 2009; Pickett, 2003; Rykaczewski and Checkley, 2008). Upwelling driven by the positive wind-curl usually has much lower velocities (0.1 – 0.2 m/d vs. 10 – 20 m/d for coastal upwelling) (Pickett, 2003). However, the volume transport of wind-curl upwelling is significant due to greater areal extent (Chelton et al., 2007; Jacox et al., 2014; Münchow, 2000). Together, coastal upwelling and wind-curl upwelling in SBB result in the annual formation of biogenic-rich sediment layers during times of NPH dominance. Finally, low O_2 bottom water (< 20 μmol/kg) preserves varves formed by the seasonal shift between biogenic and silicilastic sedimentation (Hendy et al., 2015; Schimmelmann et al., 1992; Schimmelmann et al., 1990), while high sedimentation rates (~1 mm/y) minimize sedimentary diagenesis, such that SBB sediments retain the original subsurface $\delta^{15}N$ signal (Prokopenko et al., 2006).

SBB waters are affected by the equatorward California Current (CC) and poleward California Undercurrent (CUC) (Fig. 5-2). As a part of the North Pacific Gyre, the CC originates in the bifurcation of the North Pacific Current (NPC) (Checkley and Barth, 2009). Occupying the upper 500 m and strongest at the surface, the CC transports cold, fresh, and oxygenated water from the subpolar region (Checkley and Barth, 2009; Hickey, 1978). CC strength is connected to large-scale gyral circulation and atmospheric forcing (strength of the Trade Winds/Westerlies). When the NPC is stable, CC transport is generally anti-correlated with Alaska Current strength (Rykaczewski and Checkley, 2008). However, when the NPC intensifies, both CC and Alaska Current transport increase, while when the NPC weakens, transport decreases (Cummins and Freeland, 2007). Most observed low-frequency CC variability is associated with NPC transport changes (Cummins and Freeland, 2007). Satellite altimetry reveals in-phase NPC strength and Ekman pumping variations in the subpolar and subtropical gyres (Cummins and Freeland, 2007), further linking CCS strength to gyral circulation behavior. Finally, where the NPC bifurcates on the North America margin affects SBB water properties, as a poleward displacement leads to transport of fresher, nutrient-rich water from the subpolar gyre into the CCS (Freeland and Cummins, 2005; Sydeman et al., 2011).

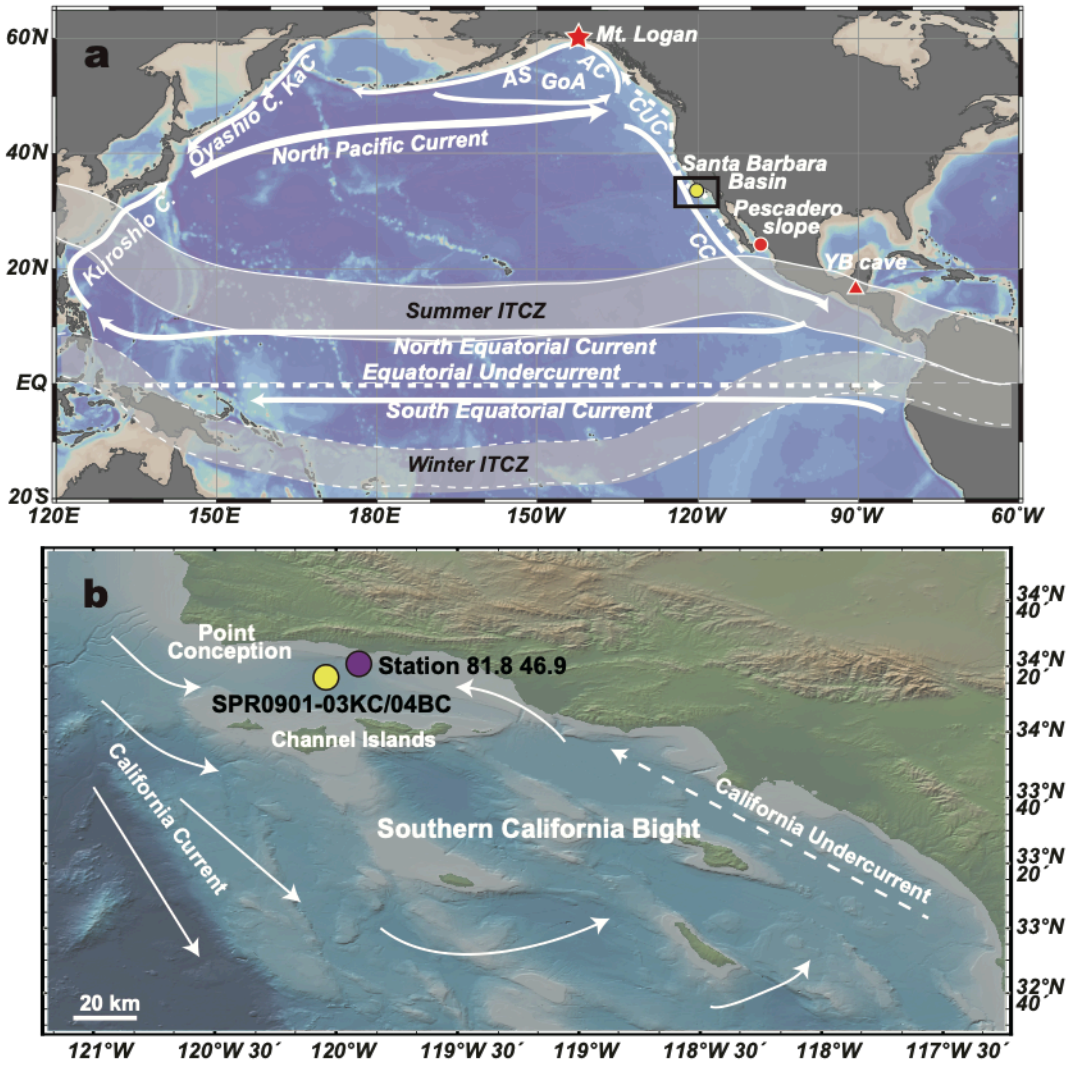

Figure 5-2 Core locations. a. Yellow circle: Core SPR0901-03KC (34°16.99'N, 120°2.408'W; 586 m depth) from the Santa Barbara Basin (SBB); red circle: Pescadero Slope core location from Tems et al. (2016). Red star: ice core location from Mt. Logan (Osterberg et al., 2014); red triangle: the YOK-I speleothem record from Belize (Kennett et al., 2012). Summer and winter ITCZ positions are indicated in white belts bound by solid and dashed lines, respectively. Ocean currents are shown in white arrows. KaC: Kamchatka Current; Oyashio C: Oyashio Current; KuC: Kuroshio Current; CC: California Current; CUC: California Undercurrent; GoA: Gulf of Alaska; AC: Alaska Current; AS: Alaska Stream. b. Southern California Bight map corresponding to the black rectangle in a. The cores SPR0901-03KC and SPR0901-04BC (34°16.895'N, 120°2.489'W, 588 m water depth) are shown in the yellow circles. The CalCOFI Station 81.8 46.9 is represented by the purple circle, and the circulation pattern is modified from Hickey (1992). The base maps are generated from the Ocean data View in (a) and the GeoMapApp (http://www.geomapapp.org, Ryan et al. (2009)), respectively.

CUC is a subsurface poleward flow with a core depth of ~200 – 300 m occupying the nearshore region (within 25 – 40 km off the shelf break), which advects warm, salty, and low-oxygen water from the ETNP up the coast of North America (Hickey, 1978). Nutrient-rich CUC waters are upwelled to the surface along the coast, supporting biological productivity in the southern CCS (Hickey, 1978; McClatchie et al., 2016). Bi-annual CUC intensification is

observed in June and December (Chelton, 1984; Lynn and Simpson, 1987) and was linked to local processes (upwelling-enhanced subsurface flow in spring-summer and the strong Southern California Eddies in winter) (Connolly et al., 2014; Hickey, 1978). Recent studies, however, indicate that coastal-trapped Kelvin waves control CUC intensity, which propagate a sea level signal from the equator, providing a further connection between the southern CCS and the Tropics (Gómez-Valdivia et al., 2015; Gómez-Valdivia et al., 2017).

5.4 Methods

Core SPR0901-03KC was scanned using an ITRAX X-ray fluorescence (XRF) core scanner (Cox Analytical Instruments) at the Large Lakes Observatory, University of Minnesota, Duluth. The scanner was equipped with a Cr X-ray tube and was operated at 200-μm resolution with an 8-second scan time at 30 kV and 15 mA. The output data are recorded as counts per 8 seconds and are semi-quantitative (Croudace et al., 2006; Hendy et al., 2015). A split of SPR0901-03KC was sampled continuously at 2-mm interval (~2 years per sample). Individual samples were freeze-dried and ground to produce bulk samples for $\delta^{15}N$ and TOC measurements. Bulk sedimentary $\delta^{15}N$ was measured on a Euro Elemental Analyzer interfaced to a GV Isoprime continuous flow isotope-ratio mass spectrometer (IRMS) at University of South Carolina on unacidified samples. $\delta^{15}N$ is defined as $[(^{15}N/^{14}N_{sample})/(^{15}N/^{14}N_{standard})-1]\times1000$ with the standard of atmospheric N_2. The reference standards used for data normalization were N-1 ($\delta^{15}N$ = 0.4‰), N-2 ($\delta^{15}N$ = 20.41‰), N-3 ($\delta^{15}N$ = 4.7‰), and USGS-40 ($\delta^{15}N$ = -4.52‰). For TOC measurements, ~250 mg aliquots were acidified to remove carbonate with 10 mL 5% HCl on a 50 °C hotplate for three times. Acidified samples were oven-dried at 65 °C for at least 48 hrs and then ground for TOC measurements. Eight to 12 mg of acidified samples were loaded into tin capsules and measured on a Costech ECS 4010 Elemental Analyzer at University of Michigan. Acetanilide (C = 71.09 wt. %) and atropine (C = 70.56 wt.%) were used as standards, and the standard deviation of repeated measurements was within 2%. Flood and turbidite layers were removed from the geochemical time series as they do not reflect background marine sedimentation and siliciclastic sediment input causes significant dilution (Hendy et al., 2013).

The age model of SPR0901-03KC was constructed by correlation with nearby cores. Forty nine mixed planktonic foraminifera accelerator mass spectrometry (AMS) ^{14}C dates (Du et al., 2018; Hendy et al., 2013) from SPR0901-06KC (34°16.914'N, 120°02.419'W, 591 m water depth) were mapped on the master core SPR0901-03KC using sediment fabric characteristics.

Varve counted dates of marker layers (e.g., gray layers at 1861 – 62 CE and 1761 CE, the *Macoma* layer at 1841 CE, and a turbidite layer at 1811 CE) were used instead of ^{14}C to constrain the past 300 years (Hendy et al., 2015; Schimmelmann et al., 1992). Instantaneous packets of sediments produced by floods and turbidites were removed from the core depths. An age-depth model for 03KC scanning XRF records was then generated using Bacon 2.2 (Blaauw and Christen, 2011; Du et al., 2018), where ^{14}C ages were converted to calendar ages using the Marine13 calibration curves (Reimer et al., 2013) with variable reservoir ages from Hendy et al. (2013). This age model was then applied to the suite of SBB cores using 31 tie points including known turbidites, flood layers, and 12 visually distinct additional marker horizons determined by distinguishable core fabric differences (e.g., varve color and thicknesses).

Geochemical data were interpolated to obtain evenly spaced time series (sampling resolution of 2.28 years after interpolation) prior to statistical analyses. Cross-wavelet analysis was used to calculate squared wavelet coherence and phase differences on a time-frequency plane to reveal regional coherence between individual time series (Grinsted et al., 2004; Torrence and Compo, 1997) . All wavelet coherence is calculated using the analytical Morlet wavelet (central frequency $\omega_0 = 6$) in MATLAB.

5.5 Results

Bulk sedimentary $\delta^{15}N$ in the core SPR0901-03KC varies between 6.78‰ and 8.33‰ with a mean value of 7.74‰ (Fig. 5-3b). There is no long-term trend through the record; however, several low- $\delta^{15}N_{sed}$ intervals occur, including ~1000 – 1100 CE during the Medieval Climate Anomaly (MCA) and 1460 – 1750 CE during the Little Ice Age (LIA). $\delta^{15}N$ values decline from ~1800 to the core top (~1900 CE).

Bulk TOC concentrations are low at the base of the core (from 170 BCE to 0) with a minimum value of 2.63 wt.% (Fig. 5-3c), and generally increase toward the core top, varying between 4.89 wt.% and 3.77 wt.% (excluding instantaneous depositional events). TOC concentrations are not statistically significant different between cooler (e.g., Dark Age Cold Period at 400 – 765 CE [Helama et al., 2017] and LIA) and warmer climate intervals (e.g., MCA), yet they have a statistically significant correlation with $\delta^{15}N$ ($r = 0.0760$, $p<0.05$). Despite overall coherence, the positive correlation disappears between 950 – 1550 CE and after 1800s. The elemental, isotopic, and organic geochemical composition of organic carbon in SBB indicates marine sources with significant contributions from terrestrial organic carbon, notably in

flood sediments (Sarno et al., 2019). Background SBB sediment $\delta^{13}C$ values of -21.75‰ support a marine source, as terrestrial contributions (primarily from the Santa Clara River (Warrick and Farnsworth, 2009b) are characterized by bedload sediment $\delta^{13}C$ values of -28.15‰ (Meyers, 1997; Sarno et al., 2019).

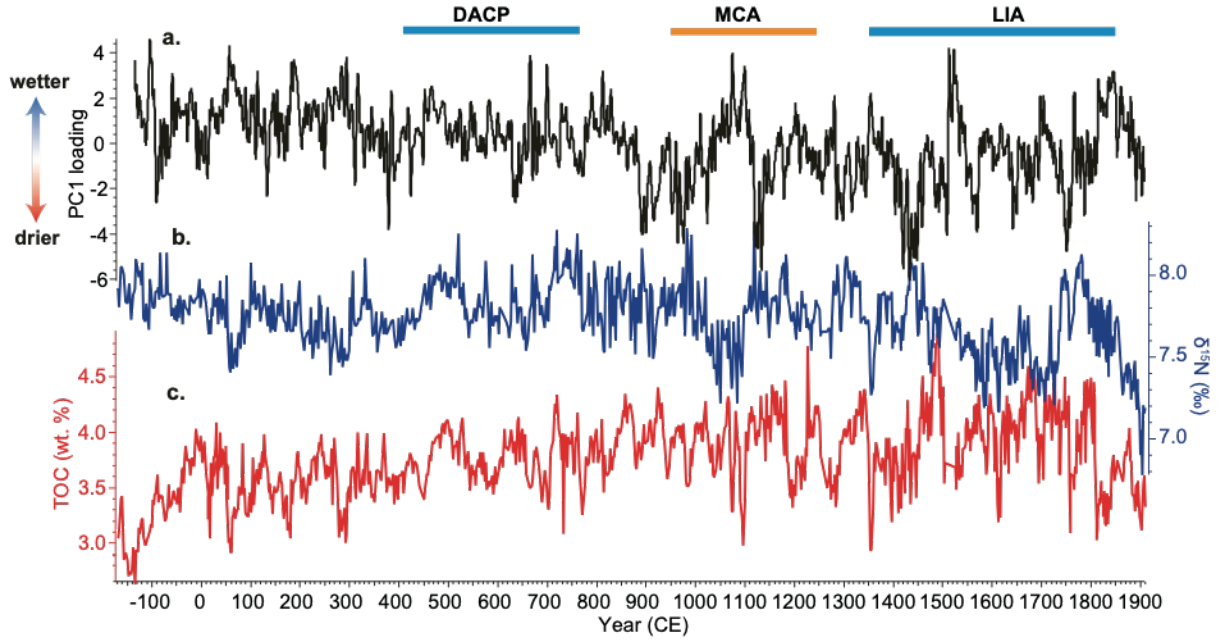

Figure 5-3 Local influences on $\delta^{15}N_{sed}$ in the Santa Barbara Basin. (a) The first principal component (PC1) of the scanning XRF elemental data for SPR0901-03KC (black line) used as a proxy for siliciclastic sediment derived from river runoff (Heusser et al., 2015). Higher PC1 indicates wetter conditions while low PC1 indicates drought; (b-c) $\delta^{15}N_{sed}$ (‰) (blue line) and TOC (wt. %) (red line) records from SPR0901-03KC, respectively. Blue bars indicate cool intervals: Dark Age Cold Period (DACP) and Little Ice Age (LIA). Red bars indicate warm intervals: Medieval Climate Anomaly (MCA). All instantaneous depositional events (flood and turbidite layers) have been removed.

The first principal component (PC1) of the scanning XRF elements in SPR0901-02KC has been used as a proxy for lithogenic sediment delivery to SBB by river runoff, with higher PC1 corresponding to wetter intervals (Fig. 5-3a) (Heusser et al., 2015). PC1 is anti-correlated with TOC ($r = -0.4004$, $p < 0.0001$), and has a statistically significant negative correlation with $\delta^{15}N_{sed}$ ($r = -0.1617$, $p < 0.001$). Stronger coherence between PC1 and $\delta^{15}N_{sed}$ is observed during wetter intervals (50 – 100 CE, 950 – 1130 CE, 1530 – 1700 CE), whereas the correlation is lost during drier periods (770 – 1000 CE). This negative correlation also disappears after ~1800 as $\delta^{15}N_{sed}$ decreases monotonically (Fig. 5-3a and b).

Scanning XRF elemental records of Ca/Ti and Si/Ti are used here as proxies for inorganic carbon (Hendy et al., 2015) and biogenic silica (Brown et al., 2007), respectively. Ca/Ti varies on a decadal to centennial time scale but no longer-term trend is observed. Several low biogenic silica periods are observed in the Si/Ti record, including 450 – 890, 1000 – 1100,

1150 – 1260, 1310 – ~1370, and 1520 – 1650 CE (Fig. 5-4e). These intervals correspond to intervals of low upwelling silicoflagellate (*Distephanus speculum*) and diatom (*Rhizosolenia spp*.) abundance (Barron et al. (2015), Fig. 5-4d). A significant positive correlation is found between Ca/Ti and TOC ($r = 0.3532$, $p < 0.001$). High Si/Ti (high biogenic silica) generally coincides with increased TOC (e.g., ~1100 – 1170 CE and ~870 – 1000 CE, Fig. 5-4). Yet a weak anti-correlation is observed between TOC and Si/Ti ($r = -0.0941$, $p < 0.05$), notably between 570 – 970, 1000 – 1100, 1150 – 1270, and 1320 – 1370 CE.

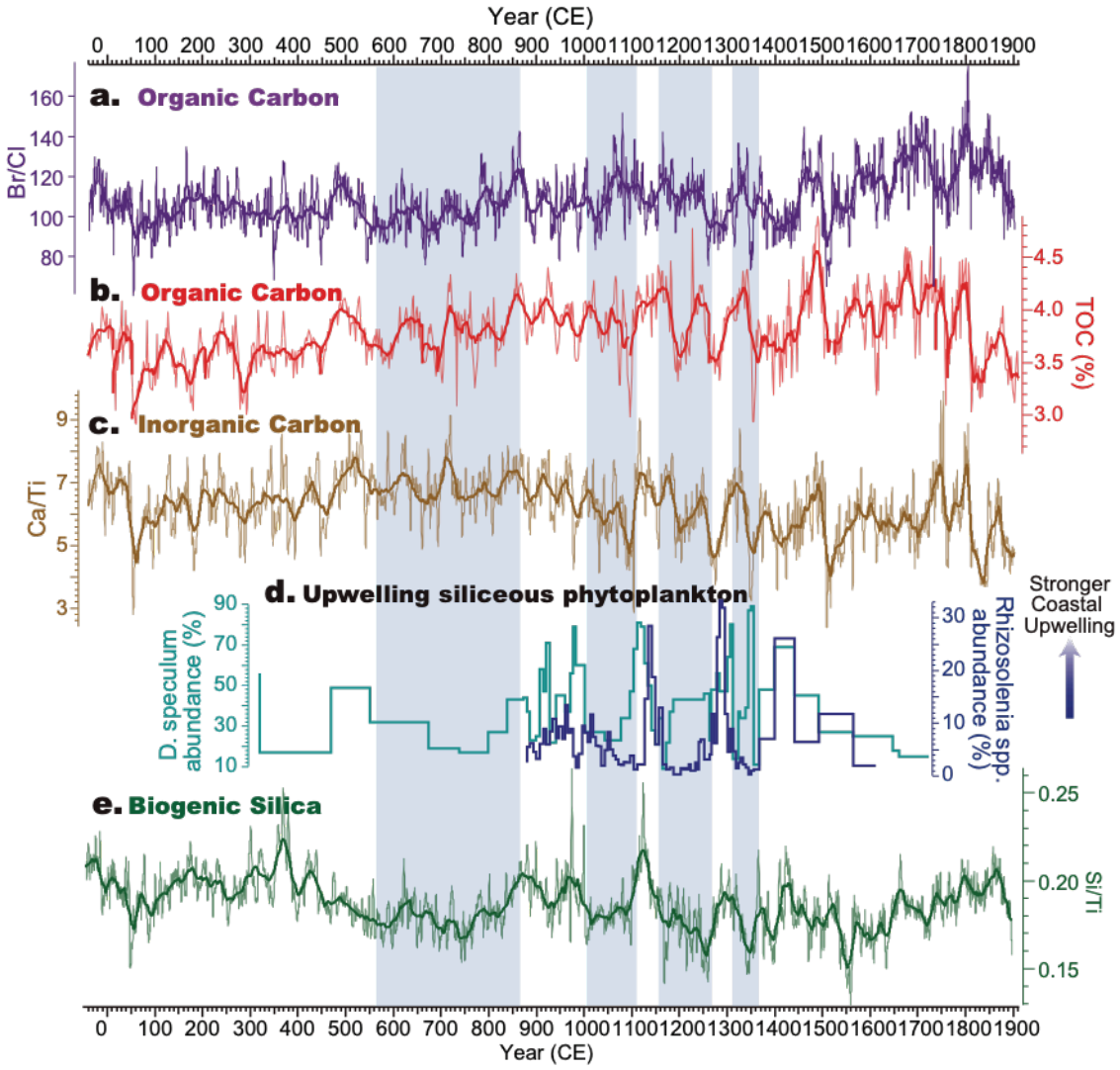

Figure 5-4 Productivity proxies. (a) Scanning XRF Br/Cl (proxy for organic carbon, thin purple line). Thick purple line represents the 101-point running mean; (b) TOC (wt. %) (thin red line) with 11-point running mean (thick red line); (c) scanning XRF of Ca/Ti (thin brown line) with the 101-point running mean (thick brown line); (d) upwelling diatoms and silicoflagellates from Barron et al. (2015); The teal and blue line represent the relative abundance of *Distephanus speculum* and *Rhizosolenia* spp., respectively; (e) proxy for biogenic silica, Si/Ti, from scanning XRF (thin green line) with the 101-point running mean (thick green line). Blue shaded rectangles indicate intervals of low coastal upwelling indicated from upwelling diatom and silicoflagellate abundance in (d).

5.6 Discussions

5.6.1 Export productivity proxies and upwelling

In Southern California, upwelling (coastal and wind-curl) brings subsurface high-nutrient denitrified waters to the euphotic zone to support export productivity. Water-column denitrification (increasing $\delta^{15}N$) is subsequently intensified by increased export productivity when organic carbon remineralization uses nitrate as the electron acceptor in low-O_2 waters. Export productivity and upwelling variability thus need to be reconstructed using biogenic sediments (e.g., TOC, biogenic carbonate and silica) to understand local water-column denitrification.

TOC is commonly employed as a proxy for carbon export from the upper ocean. An overall increase of TOC (~1 wt. %) occurs over the last two millennia, indicating a general increase in export productivity, with significant variability on centennial timescales (Fig. 5-3c). However, the bulk sediment TOC concentration could subject to sedimentary diagenesis, causing the record to deviate from carbon export. In high-sedimentation rate settings (>0.03 cm/y, Canfield (1994)), OC could continue to decompose downcore via anaerobic pathways in reducing porewaters, leading to lower sedimentary TOC (Canfield et al., 1993). Additionally, higher TOC values (enhanced OC preservation) could occur beneath instantaneous depositional events (e.g., flood and turbidite layers) that reduce O_2 penetration and aerobic OC degradation (i.e., the 'coffin-lid' effect, Schimmelmann (2011)).

To exclude the fore-mentioned complexities, an independent export productivity indicator is needed to account for likely diagenetic processes affecting TOC records. Inorganic carbon determined by scanning XRF Ca/Ti is a productivity proxy representing biogenic carbonate production (primarily foraminifera and coccolithophores, Fig. 5-4c). In SBB, well-preserved inorganic carbon is unaffected by sedimentary anaerobic OC degradation and/or enhanced OC preservation, and thus provides an independent measure of export productivity that can be compared to TOC. Ca/Ti and TOC are generally coherent on decadal to centennial timescales. This statistically significant correlation ($r = 0.3532$, $p < 0.01$) suggests TOC preservation below instantaneous deposition events was not enhanced, nor were there significant changes in TOC anaerobic decomposition downcore. Thus, sedimentary TOC is likely primarily recording export productivity in SBB.

Additionally, biogenic silica (largely produced by diatoms and silicoflagellates) is another major contributor to export productivity, especially during coastal upwelling events. Scanning XRF Si/Ti is used here as a proxy for biogenic silica, with the expectation that higher Si/Ti corresponds to enhanced export productivity. Coherent TOC and Si/Ti maxima are observed (e.g., 1130 and 1300 CE), yet negative correlations between Si/Ti and TOC are shown during intervals of low Si/Ti, during which TOC remains relatively stable (Fig. 5-4b and e). Anti-correlations between TOC and biogenic silica have also been recorded in the Gulf of California, where biogenic silica is the primary biogenic sediment component (Pichevin et al., 2012; Thunell, 1998b). Previous studies have related this inverse relationship to either Fe limitation (Firme et al., 2003) and/or enhanced silica preservation during strong coastal upwelling events due to silica supersaturation in porewaters (Pichevin et al., 2012). However, SBB sediments are dominated by lithogenic input (50 – 80%), with much lower biogenic silica contributions (~15% – 20% in SBB vs. up to ~75% during upwelling in the Guaymas Basin, Gulf of California) (Thunell, 1998a; Thunell, 1998b). Thus, SBB porewaters are always undersaturated for silica, as indicated by the absence of weakly silicified species (Barron et al., 2015; Reimers et al., 1990). Iron limitation due to upwelled Fe-depleted waters and/or low riverine input usually occurs along narrow shelf areas (e.g., the northern and central California coast) (Bruland et al., 2001; Firme et al., 2003). However, relatively high dissolved Fe (dFe) concentrations (>1 nM) have been observed at the surface in SBB with increasing dFe in depth (up to ~30 nM at 560 m), arguing against reduced organic carbon production because of Fe limitation (John et al., 2012; King and Barbeau, 2011). Therefore, the lack of TOC and biogenic silica correspondence in SBB requires another explanation.

In the Gulf of California, negative correlations between biogenic silica and TOC usually happen during intervals associated with strong coastal upwelling (Pichevin et al., 2012) In SBB, however, negative relationships are more prominent during weak biogenic silica production intervals indicated by the low abundance of coastal upwelling diatom (*Rhizosolenia* spp.) and silicoflagellate species (*Distephanus speculum*) (Fig. 5-4d) (Barron et al., 2015). Despite undersaturated porewaters leading to biogenic silica dissolution, Si/Ti shows consistent variability with independently measured upwelling diatoms and silicoflagellates. Sedimentary Si/Ti increases when *Rhizosolenia* spp. and *Distephanus speculum* become abundant at 1110 – 1160, 1270 – 1310, and 1370 – 1490 CE, supporting the interpretation of intensified coastal

upwelling (Fig. 5-4d) (Barron et al., 2015). Low Si/Ti is coincident with a scarcity of these upwelling species during 570 – 870, 1000 – 1100, 1155 – 1265, and 1310 – 1370 CE, suggesting weakened coastal upwelling. Si/Ti thus appears to be an indicator of coastal upwelling but not necessarily export productivity, and can be decoupled from TOC when coastal upwelling is weak.

Nevertheless, anti-correlations between Si/Ti and TOC contradicts sediment trap studies in SBB, where export particulate organic carbon (POC) is positively correlated with opal fluxes on an annual basis (Thunell et al., 2007). This may relate to the limitation of the short duration sediment trap study. Weak coastal upwelling in the paleoproductivity record is sustained on decadal to centennial timescales, such that this observed low-frequency variability might be associated with processes that have not yet been observed in the annual trap data.

When biogenic silica indicates weak coastal upwelling, Ca/Ti and TOC support normal to increased productivity (e.g., 1000 – 1100 and 1310 – 1370 CE, Fig. 5-4b, c, and e), indicating that nutrients are being supplied by processes other than coastal upwelling. Discrepancies between high foraminifera production and biogenic silica were also observed in the northern CCS during the Last Glacial Maximum, and were attributed to increased wind-curl upwelling (Ortiz et al., 1997). Coastal upwelling is usually associated with high nutrient delivery due to high vertical velocity and a shoaling of the nearshore nutricline (Rykaczewski and Checkley, 2008; Taylor et al., 2015a), producing diatom blooms (high Si/Ti) and physically larger plankton. In the southern CCS, modeled total upwelling transport (including both coastal and wind-curl upwelling), however, is not significantly correlated with the coastal upwelling index calculated from atmospheric sea level pressure (Bakun, 1973). Rather, the nearshore high primary productivity band contains both coastal (< 50 km) and wind-curl upwelling nutrient contributions (50-200 km) (Jacox et al., 2014).

The contribution of wind-curl upwelling is difficult to reconstruct, as the bloom-forming taxa associated with strong coastal upwelling events (e.g., upwelling diatoms that favor high nutrient environments) can overprint physically smaller planktonic taxa that dominate offshore and more oligotrophic environments associated with slow and broad wind-curl upwelling (Ortiz et al., 1995). Yet, the importance of wind-curl upwelling on southern CCS planktic biomass is widely reported. Wind-stress modeling shows strong wind-curl upwelling transport adjacent to coastal promontories (e.g., Point Conception) (Pickett, 2003) — a prediction corroborated by wind stress and upwelling rate observations (Enriquez and Friehe, 1995). The biological

significance of wind-curl upwelling has been observed in seasonal offshore (100 km) zooplankton abundances (Chelton et al., 1982). Chlorophyll *a* concentrations (proxy for primary productivity) are significantly correlated with the wind-curl upwelling but not the coastal upwelling rate, and corroborate the active role of curl-driven upwelling in Southern California primary productivity (Rykaczewski and Checkley, 2008). Wind-curl upwelling could thus be an important driver of export productivity in SBB over the last 2000 years, such that intervals of weaker coastal upwelling (low Si/Ti) may have been offset by greater wind curl upwelling to maintain stable/high export productivity (TOC and inorganic carbon) (Fig. 5-4).

5.6.2 Santa Barbara Basin $\delta^{15}N$ history over the past 2000 years

Use of $\delta^{15}N_{sed}$ as a proxy for water column denitrification requires both complete nitrate utilization and the absence of sedimentary diagenesis. Diagenetic isotopic alteration of $\delta^{15}N$ should be negligible in SBB as high sedimentation rates and low-oxygen bottom waters only allow a small fraction of aerobic OC decomposition before burial (Altabet et al., 1999b; Prokopenko et al., 2006). A minimal (< 0.5‰) offset between the sediment trap $\delta^{15}N$ time series and down-core $\delta^{15}N_{sed}$ records supports this premise (Davis et al., 2019). Preservation of the original $\delta^{15}N$ of sinking OC thus allows water-column denitrification reconstructions from the $\delta^{15}N_{sed}$ record in SBB. Resolution of our record (~2 years), however, is insufficient to resolve O_2 entrainment/solubility shifts induced by seasonal wind-driven mixing/upwelling oscillations. Our $\delta^{15}N_{sed}$ record, therefore, can only reveal water-column $\delta^{15}N$ variability averaged over decadal or longer timescales.

Despite an ~1 wt.% increase of TOC over the last 2000 years (Fig. 5-3c), relatively invariant $\delta^{15}N_{sed}$ values (varying within ~1‰) indicate a general stability of water-column oxygenation and/or $\delta^{15}N$ input from different N sources. Exceptions to this stability occurred, however. Sustained low $\delta^{15}N_{sed}$ values during ~1100 – 1300, 1460 – 1750 CE, and after 1800s (>1‰ decline), suggesting the presence of more oxygenated waters or increasing $\delta^{15}N$-depleted N inputs (Fig. 5-3b). The post-1800s decreasing $\delta^{15}N_{sed}$ trend has also been observed in the Santa Monica Basin and in the ETNP, where it has been associated with decreasing trade wind strength, reduced equatorial upwelling, and ETNP OMZ contraction (Davis et al., 2019; Deutsch et al., 2014). The stability of the $\delta^{15}N_{sed}$ record suggests that denitrification appears insensitive to SST change during the warm (MCA) and cold periods (Dark Age Cold Period [DACP] or LIA) in the late Holocene (Fig. 5-3; PAGES 2k Consortium (2013)). This may be related to limited Northern

Hemisphere mean SST variability (typically < 1 °C for LIA, Moberg et al. (2005)), resulting in a gas solubility change (~ 5 μmol/kg given 1 °C SST change at 16 °C) that was insufficient to impact O_2 concentrations and thus denitrification.

Low $\delta^{15}N_{sed}$ intervals (~1100 – 1300 CE, 1460 – 1750 CE) are usually coincident with high values of the first principle component of the scanning XRF elements (PC1; Fig. 5-3, r = -0.1617, p < 0.001), which have been associated with greater Southern California rainfall (Hendy et al., 2015; Heusser et al., 2015). This anti-correlation may be related to changes in N source between wet and dry climates as enhanced clay-bound N delivery adds $\delta^{15}N$-depleted ammonium (~2 – 4‰; Schubert and Calvert (2001); Sigman et al. (2009b)) that may substitute for K^+ in illite clay structures (Kienast et al., 2005; Müller, 1977; Schubert and Calvert, 2001). Yet the TOC-TN plot (Fig. 5-5) shows a negative intercept, indicating that the contribution from terrestrial clay-bound N is negligible.

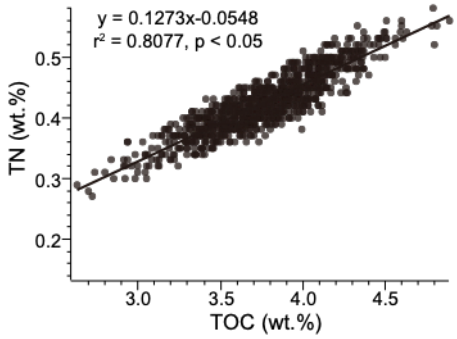

Figure 5-5 Cross plot of TOC (wt. %) and TN (wt. %) from SPR0901-03KC. Black line represents linear relationship from the least-square regression.

More likely, the relationship between rainfall (PC1) and $\delta^{15}N_{sed}$ is indirect via the North Pacific High (NPH), and related to export productivity. The positive correlation between bulk sedimentary TOC (export productivity proxy) and $\delta^{15}N_{sed}$ (r = 0.0760, p < 0.05) indicates a general productivity control on water-column denitrification, with enhanced OC export increasing O_2 demand and thus denitrification. The negative correlation between TOC and PC1 (r = -0.4004, p < 0.001) further suggests an inverse relationship between export productivity and local precipitation that is controlled by the NPH. A stronger and/or more persistent NPH enhances alongshore northerly winds, which induce stronger coastal upwelling and the upward advection of $\delta^{15}N$-rich subsurface waters to support higher export productivity (higher TOC, Fig. 5-3). Simultaneously, this persistent high-pressure over western North America reduces rainfall in Southern California and lowers PC1, leading to a negative correlation between PC1 and TOC

(Hendy et al., 2015; Heusser et al., 2015). Despite the overall local productivity control on $\delta^{15}N_{sed}$ via the NPH, TOC, $\delta^{15}N_{sed}$ and PC1 still show discrepancies (notably in 750 – 1250 and 1700 – 1900 CE), indicating that remote processes/teleconnections must have also played a role.

5.6.3 Teleconnections to tropical and high-latitude forcing

Inconsistencies between $\delta^{15}N_{sed}$ and local NPH control on export productivity (TOC) and precipitation (PC1) require an alternative explanation involving remotely advected $\delta^{15}N$ signals via ocean currents. Currents transport nitrate with unique $\delta^{15}N$ signatures from remote water sources. The nitrate is subsequently incorporated into sinking particulate N and preserved in sediments (Fig. 5-2), and thus $\delta^{15}N_{sed}$ can be used as a water mass tracer to track N contribution changes from different sources. In Southern California, water mass properties are primarily controlled by two competing water mass influences: high-$\delta^{15}N$, warm, saline (spicy) waters from the East Tropical North Pacific (ETNP) OMZ transported by the California Undercurrent (CUC), as well as nutrient-rich, cold, and fresh subarctic waters advected by the California Current (CC) (Kienast et al., 2002; Liu and Kaplan, 1989) (Fig. 5-2). To investigate impacts of remote water mass advection, the Mt. Logan in Yukon Territory (a high-latitude site) and the Pescadero Slope in the Gulf of California (a tropical site) are used as potential regions communicating with the Southern California OMZ (Fig. 5-1). The 1200-year $\delta^{15}N_{sed}$ record from the Pescadero Slope serves as an end member for ETNP $\delta^{15}N$-rich spicy water, as the site is located at the northern edge of the ETNP OMZ and records water-column denitrification in the ETNP (Tems et al., 2016). The competing subpolar end member is represented by the 1200-year North Pacific Index (NPI) reconstruction from the Mt. Logan ice core (Osterberg et al., 2014). Sodium ion concentrations in the Mt. Logan ice core are interpreted as an indicator of the North Pacific sea level pressure and winter Aleutian Low (AL) intensity (Osterberg et al., 2014). Thus, we use the ice core record to link the atmospheric forcing (AL intensity) with the oceanic responses (Ekman pumping and North Pacific Current variability) (Ishi and Hanawa, 2005) that result in subarctic water transport into the CCS. Here the focus is on decadal to centennial timescales, as the data resolution (~2-3 years for $\delta^{15}N$) is insufficient to resolve interannual variability.

5.6.3.1 Equatorial water influences and atmospheric forcing

Spicy and high-$\delta^{15}N$ waters from ETNP could be advected to Southern California via CUC to elevate $\delta^{15}N_{sed}$ in SBB. A positive correlation between $\delta^{15}N$ from a SBB box core (SPR0901-04BC, 34º 16.895'N, 120º 02.489'W, 588 m water depth) and measured salinity at the

core of CUC (σ_θ = 26.4 – 26.5, Gay and Chereskin (2009)) from the CalCOFI station 81.8 46.9 (center of SBB, 34°16′29.64"N, 120°1′30"W) during the last 50 years supports this assertion (Fig. 5-6).

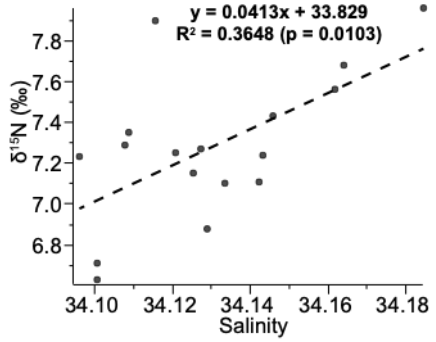

Figure 5-6 Cross plot of $\delta^{15}N_{sed}$ of the SBB core SPR0901-04BC (34° 16.895'N, 120° 02.489'W, 588 m water depth) and mean annual salinity of σ_θ = 26.4 – 26.5 from the CalCOFI Station 81.8 46.9 (34°16'29.64" N, 120°1'30" W). The black dashed line shows the least-square regression.

Water-column denitrification ($\delta^{15}N$) in ETNP has been associated with tropical climate through Trade Wind strength (Deutsch et al., 2014). Weak easterly Trade Winds reduce upwelling and lower export productivity, leading to ETNP OMZ contraction that subsequently reduces $\delta^{15}N$. The strength of Trade Winds is related to ITCZ migration in response to inter-hemispheric temperature differences. A southward shift of the ITCZ with extratropical cooling in the Northern Hemisphere (NH) relative to the Southern Hemisphere (SH) is usually accompanied by intensified northeast Trades in the NH and weakened southeast Trades in the SH (Broccoli et al., 2006; Chiang and Bitz, 2005; Haug et al., 2001; Jacobel et al., 2016; McGee et al., 2018; Meehl et al., 2008; Schneider et al., 2014). Because the ITCZ primarily resides in the NH (Philander et al., 1996; Xie, 1994), a southward ITCZ shift weakens the easterly Trades at the equator, deepening the thermocline and reducing upwelling in the Eastern Equatorial Pacific (Costa et al., 2017; Koutavas and Lynch-Stieglitz, 2004).

The linkage between ITCZ migration and ETNP $\delta^{15}N$ is further demonstrated by the relationship between Pescadero Slope $\delta^{15}N_{sed}$ values and a $\delta^{18}O$ speleothem record (YOK-I) from Belize that is sited on the northern edge of the ITCZ (Kennett et al., 2012). From 1850 to 2004, YOK-I $\delta^{18}O$ values significantly correlate with Pescadero $\delta^{15}N$ values (Fig. 5-7, $r = -0.5494$, $p < 0.001$). The observed southward displacement of ITCZ since ~1850 (Hwang et al., 2013; Ridley et al., 2015; Rotstayn and Lohmann, 2002) could have slackened east Trades and weakened upwelling at the equator, reducing export productivity and decreasing Pescadero $\delta^{15}N_{sed}$ (a record that represents ETNP $\delta^{15}N$). Cross-wavelet coherence between the two records further indicates

significant anti-phase coherence on decadal (~1100 – 1300 CE) to centennial timescales (Fig. 5-8e), supporting a persistent linkage between ETNP $\delta^{15}N$ and the ITCZ over the past 1200 years (Fig. 5-8).

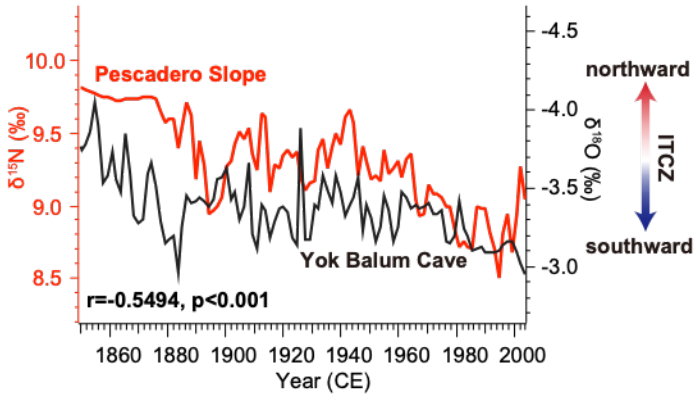

Figure 5-7 Comparison of $\delta^{15}N_{sed}$ of the Pescadero Basin (red line) with $\delta^{18}O$ of the Yok Balum Cave (YOK-I, black line, Kennett et al. (2012)) showing a statistically negative correlation ($r = -0.5494$, $p < 0.001$).

The SBB and Pescadero $\delta^{15}N_{sed}$ records are usually in-phase on decadal to centennial timescales during the MCA (e.g., 980 – 1120 CE, Fig. 5-8b and c). Thus the ITCZ position increased Southern California (SBB) $\delta^{15}N$ through the advection of denitrified ETNP waters in the region via the CUC during the warm Northern Hemisphere climate interval. However, this relationship collapses between ~1320 – 1450 and 1670 – 1880 CE (Fig. 5-8). The anti-phase correlation in 1320 – 1450 CE could be attributed to ^{14}C dating uncertainties producing a 20 – 30 year offset between the two records. Yet the out-of-phase pattern during 1670 – 1840 CE (1720 – 1840 CE in particular) cannot be explained by age model offsets given its duration of centuries. Coincident with NH cooling during the Maunder (1645 – 1715 CE) and Dalton (1790 – 1820 CE) solar minimum, the 1670 – 1840 CE interval stands out as a period of equatorward ITCZ migration (YOK-I $\delta^{18}O$; Kennett et al. (2012)) where the weakened ETNP OMZ resulted in low Pescadero $\delta^{15}N_{sed}$ values (Tems et al., 2016) (Fig. 5-8c and d), while SBB $\delta^{15}N_{sed}$ values increased (Fig. 5-8b).

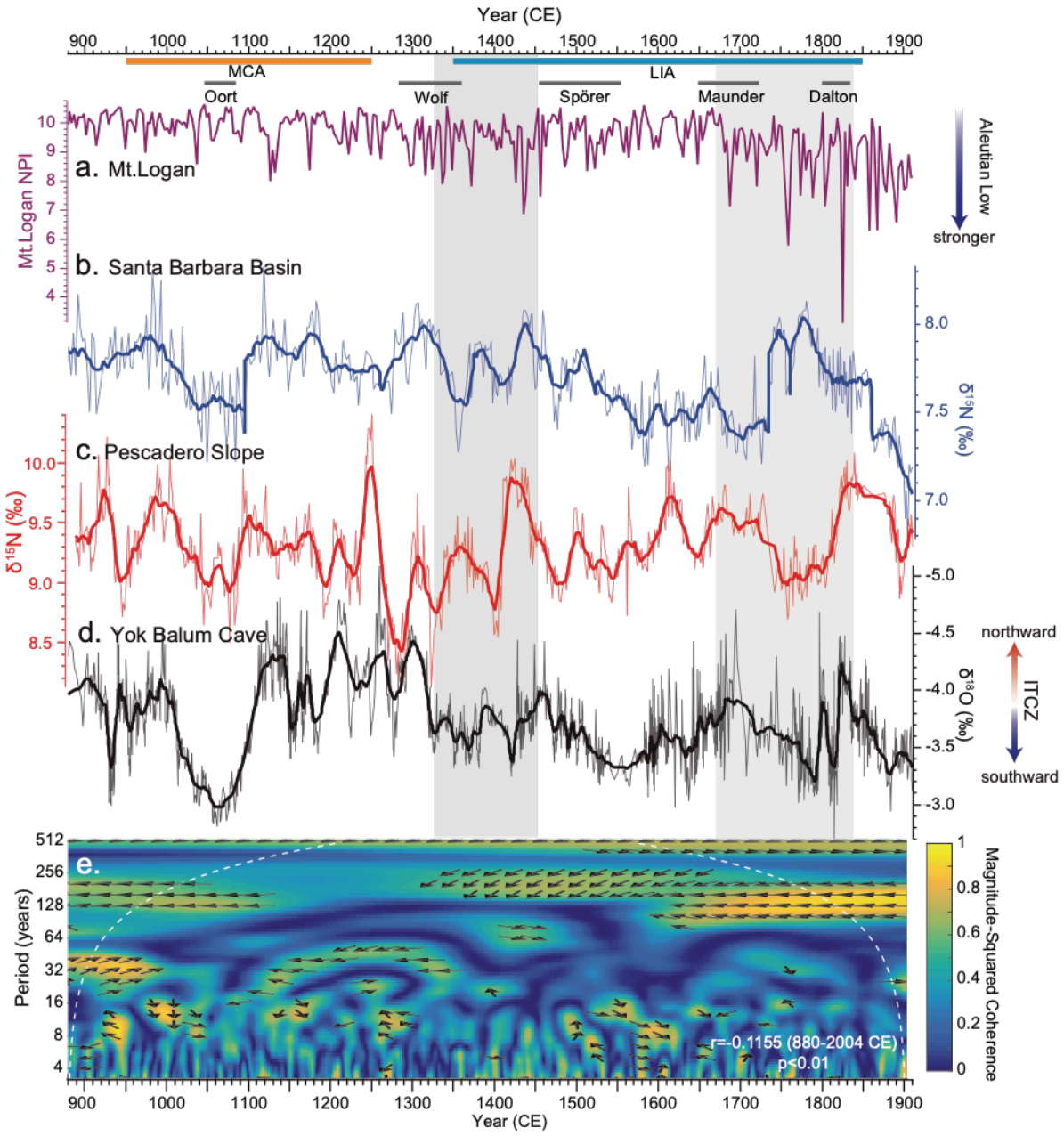

Figure 5-8 $\delta^{15}N$ regional comparison with North Pacific teleconnections. (a) Mt. Logan North Pacific Index proxy record (purple line, Osterberg et al. (2014)). Lower values indicate stronger winter Aleutian Low; (b) $\delta^{15}N_{sed}$ from SBB core SPR0901-03KC with the thick purple line showing the 11-point running mean to highlight multidecadal variability; (c) $\delta^{15}N_{sed}$ of the Pescadero Basin (Tems et al., 2016) with the thick red line denoting 11-point running mean; (d) YOK-I speleothem $\delta^{18}O$ as a proxy for ITCZ migration (Kennett et al., 2012). The 41-point running mean is shown in the black solid line. (e) Cross-wavelet coherence between $\delta^{18}O$ in (d) and Pescadero $\delta^{15}N_{sed}$ in (c). Arrows show phase differences between the two records when the magnitude-squared coherence is above 0.5 (> 95% significance). Arrows pointing left indicate anti-phase correlations at that frequency. The Medieval Climate Anomaly (MCA) and the Little Ice Age (LIA) are shown in orange and blue shaded bars, respectively. Grand solar minima are indicated with gray bars. Rectangles shaded in gray show time intervals where SBB and Pescadero $\delta^{15}N_{sed}$ records are not correlated.

As Pescadero $\delta^{15}N_{sed}$ values are always higher than those in SBB, this out-of-phase pattern reduces the $\delta^{15}N$ difference between the two sites. One explanation could be enhanced

poleward transport of ETNP waters to Southern California. However, an equatorward ITCZ displacement would have led to similar equatorward migration of the NPH and AL (Christoforou and Hameed, 1997; Lechleitner et al., 2017), suppressing coastal upwelling in Southern California while enhancing upwelling in the Gulf of California (Barron and Bukry, 2007; Pérez-Cruz, 2017). Reduced the sea surface height at the southern boundary of CCS would decrease poleward CUC flow, producing a $\delta^{15}N$ result opposite to the one observed (Connolly et al., 2014; Taylor et al., 2015b). Another possibility is that during this interval of weak Southern California (SBB) and ETNP (Pescadero Slope) water mass communication, subarctic water influences became more prominent to produce the discrepancy between 1670 and 1840 CE.

5.6.3.2 Subarctic water transport and atmospheric forcing

Nutrient-rich subarctic water transported via CC is associated with the latitudinal position and intensity of the North Pacific Current (NPC) (Cummins and Freeland, 2007; Di Lorenzo et al., 2008; Freeland and Cummins, 2005; Sydeman et al., 2011). The CC intensifies following increased NPC transport (Cummins and Freeland, 2007; Douglass et al., 2006). Serving as the boundary between the Gulf of Alaska and northeast Pacific subtropical gyre, the strength of NPC is closely linked with in-phase variations of Ekman pumping in both gyres, and directly responds to atmospheric forcing (Cummins and Freeland, 2007). This co-variability of subpolar and subtropical gyres is similar to the North Pacific Gyre Oscillation (NPGO) proposed by Di Lorenzo et al. (2008), which has been used to explain nutrient variability in CCS. As no NPGO reconstruction is available for the last two millennia, the Mt. Logan ice core North Pacific Index (NPI) reconstruction is used instead as an indicator of winter AL intensity and thus is associated with Ekman pumping in the Gulf of Alaska (GoA) (Osterberg et al., 2014).

When the connection between Southern California (SBB) and ETNP (Pescadero Slope) was weak between 1670 – 1840 CE, an intensified winter AL suggested by the ice core record (Fig. 5-8a) (Osterberg et al., 2014) could have resulted in anomalous cyclonic wind stress curl and stronger Ekman upwelling in GoA. Stronger wind stress curl would in turn lead to intensified southward transport of subarctic water into the NPC and subsequently the CCS (Freeland, 2003; Murphree et al., 2003). A similar anomalous southward intrusion of subarctic waters to CCS was observed in the 2002 summer, when the subarctic anomaly extended more than 1500 km along the US west coast, to at least 33°N (Bograd and Lynn, 2003; Huyer, 2003; Strub and James, 2003). Due to incomplete nitrate utilization in the subarctic ocean, nitrate $\delta^{15}N$

in the GoA photic zone is also elevated (up to 11‰ at the surface, Casciotti et al. (2002)). Increasing advection of nutrient-rich and high $\delta^{15}N$ subarctic water would then serve as another source of high-$\delta^{15}N$ nitrate for surface SBB waters. The observed correspondence between intensified AL and increased SBB $\delta^{15}N_{sed}$ thus indicates a stronger connection with the subarctic waters when the tropical influences weakened during the Little Ice Age (1670 – 1840 CE, Fig. 5-8).

5.7 Conclusions

Marine dissolved oxygen concentrations play an important role in biogeochemical cycles and can be impacted by climate changes. The high-resolution 2000-year sedimentary $\delta^{15}N$ ($\delta^{15}N_{sed}$) record from Santa Barbara Basin (SBB) reveals natural variability of Southern California water column oxygenation and highlights competition between tropical and subarctic water masses as surface ocean currents respond to climate forcing. Proxies for siliceous plankton bloom events (diatom and silicoflagellate populations, and scanning XRF Si/Ti) and export productivity (TOC) suggests that coastal upwelling and export productivity are not always in phase. This incoherence indicates a potential role for wind-curl upwelling in driving SBB primary productivity, especially during intervals of weak coastal upwelling. The correspondence of $\delta^{15}N_{sed}$ to export productivity (TOC) and local precipitation (PC1) indicates that an intensified and/or persistent North Pacific High (NPH) pressure cell was associated with enhanced export productivity during drought intervals.

Comparison with the Pescadero slope $\delta^{15}N_{sed}$ record in the Gulf of California (Tems et al., 2016) supports subsurface tropical water influences on the surface waters of the Southern California Bight. The Pescadero $\delta^{15}N_{sed}$ record suggests that Eastern Tropical North Pacific (ETNP) denitrification was associated with Intertropical Convergence Zone migration on multidecadal to centennial timescales and supports the stronger tropical water transport into Southern California during the Medieval Climate Anomaly. An out-of-phase relationship between the Pescadero and SBB $\delta^{15}N_{sed}$ records during the Little Ice Age (1670 – 1840 CE) occurred during an interval of anomalous intensified Aleutian Low activity (Osterberg et al., 2014). During this interval we suggest that an intensified North Pacific Current advected more subarctic water into the California Current System. Enhanced advection of nutrient-rich subarctic waters might have introduced high-$\delta^{15}N$ nitrate to SBB, resulting in elevated SBB $\delta^{15}N_{sed}$ values while $\delta^{15}N_{sed}$ decreased at the Pescadero site.

The observed natural variability of water-column denitrification is associated with both local (export productivity shifts controlled by NPH) and remote water mass influences related to large-scale atmospheric forcing, and thus addresses regional teleconnections within the California Current System. A warming climate might lead to a strong, MCA-like connection between the Southern California margin and ETNP, with weaker influences from subpolar regions. Such natural oscillations would continue to be embedded in future climate change with anthropogenic forcing, which will further complicate predictions of future ocean deoxygenation.

5.8 Acknowledgments

This work is supported by the National Science Foundation under grant number OCE-1304327 awarded to I.H.; Y.W. acknowledges support from the Rackham Graduate School of the University of Michigan and the Scott Turner Award. We thank Eric Tappa, Alexander Postmaa, and Madeline Parks for lab assistance.

5.9 References

Agnihotri, R., Altabet, M.A., Herbert, T.D., Tierney, J.E., 2008. Subdecadally resolved paleoceanography of the Peru margin during the last two millennia. Geochemistry, Geophysics, Geosystems, 9(5).

Altabet, M., 2006a. Constraints on oceanic N balance/imbalance from sedimentary 15N records. Biogeosciences Discussions, 3(4): 1121-1155.

Altabet, M.A., 2006b. Isotopic Tracers of the Marine Nitrogen Cycle: Present and Past. The Handbook of Environmental Chemistry, 2N: 251-293.

Altabet, M.A., François, R., 1994. Sedimentary nitrogen isotopic ratio as a recorder for surface nitrate utilization. Global Biogeochemical Cycles, 8(1): 103-116.

Altabet, M.A., Francois, R., Murray, D.W., Prell, W.L., 1995. Climate-related variations in denitrification in the Arabian Sea from sediment 15N/14N ratios. Nature, 373: 506-509.

Altabet, M.A., Murray, D.W., Prell, W.L., 1999a. Climatically linked oscillations in Arabian Sea denitrification over the past 1 m.y.: Implications for the marine N cycle. Paleoceanography, 14(6): 732-743.

Altabet, M.A. et al., 1999b. The nitrogen isotope biogeochemistry of sinking particles from the margin of the Eastern North Pacific. Deep Sea Research I, 46(1999): 655-679.

Bakun, A., 1973. Coastal upwelling indices, west coast of North America, 1946-71, NOAA, Seattle.

Barron, J.A., Bukry, D., 2007. Development of the California Current during the past 12,000 yr based on diatoms and silicoflagellates. Palaeogeography, Palaeoclimatology, Palaeoecology, 248(3-4): 313-338.

Barron, J.A., Bukry, D., Hendy, I.L., 2015. High-resolution paleoclimatology of the Santa Barbara Basin during the Medieval Climate Anomaly and early Little Ice Age based on diatom and silicoflagellate assemblages in Kasten core SPR0901-02KC. Quaternary International, 387: 13-22.

Blaauw, M., Christen, J.A., 2011. Flexible paleoclimate age-depth models using an autoregressive gamma process. Bayesian Analysis, 6(3): 457-474.

Bograd, S.J., Lynn, R.J., 2003. Anomalous subarctic influence in the southern California Current during 2002. Geophysical Research Letters, 30(15).

Brandes, J.A., Devol, A.H., Yoshinari, T., Jayakumar, D.A., Naqvi, S.W.A., 1998. Isotopic composition of nitrate in the central Arabian Sea and eastern tropical North Pacific: a tracer for mixing and nitrogen cycles. Limnology and Oceanography, 43(7): 1680-1689.

Broccoli, A.J., Dahl, K.A., Stouffer, R.J., 2006. Response of the ITCZ to Northern Hemisphere cooling. Geophysical Research Letters, 33(1).

Brown, E.T., Johnson, T.C., Scholz, C.A., Cohen, A.S., King, J.W., 2007. Abrupt change in tropical African climate linked to the bipolar seesaw over the past 55,000 years. Geophysical Research Letters, 34(20).

Bruland, K.W., Rue, E.L., Smith, G.J., 2001. Iron and macronutrients in California coastal upwelling regimes: Implications for diatom blooms. Limnology and Oceanography, 46(7): 1661-1674.

Canfield, D.E., 1994. Factors influencing organic carbon preservation in marine sediments. Chemical Geology, 114(3-4): 315-329.

Canfield, D.E., Thamdrup, B., Hansen, J.W., 1993. The anaerobic degradation of organic matter in Danish coastal sediments: iron reduction, manganese reduction, and sulfate reduction. Geochimica et Cosmochimica Acta, 57(16): 3867-3883.

Casciotti, K.L., Sigman, D.M., Hastings, M.G., Böhlke, J.K., Hilkert, A., 2002. Measurement of the oxygen isotopic composition of nitrate in seawater and freshwater using the denitrifier method. Analytical Chemistry, 74(19): 4905-4912.

Checkley, D.M., Barth, J.A., 2009. Patterns and processes in the California Current System. Progress in Oceanography, 83(1-4): 49-64.

Chelton, D.B., 1981. Interannual variability of the California Current - physical factors.

Chelton, D.B., 1984. Seasonal variability of alongshore geostrophic velocity off central California. Journal of Geophysical Research, 89(C3): 3473.

Chelton, D.B., Bernal, P.A., McGowan, J.A., 1982. Large-scale interannual physical and biological interaction in the California Current. Journal of Marine Research, 40: 1095-1125.

Chelton, D.B., Schlax, M.G., Samelson, R.M., 2007. Summertime Coupling between Sea Surface Temperature and Wind Stress in the California Current System. Journal of Physical Oceanography, 37(3): 495-517.

Chiang, J.C.H., Bitz, C.M., 2005. Influence of high latitude ice cover on the marine Intertropical Convergence Zone. Climate Dynamics, 25(5): 477-496.

Christoforou, P., Hameed, S., 1997. Solar cycle and the Pacific 'centers of action'. Geophysical Research Letters, 24(3): 293-296.

Connolly, T.P., Hickey, B.M., Shulman, I., Thomson, R.E., 2014. Coastal Trapped Waves, Alongshore Pressure Gradients, and the California Undercurrent*. Journal of Physical Oceanography, 44(1): 319-342.

Costa, K.M. et al., 2017. Productivity patterns in the equatorial Pacific over the last 30,000 years. Global Biogeochemical Cycles, 31(5): 850-865.

Croudace, I.W., Rindby, A., Rothwell, R.G., 2006. ITRAX: description and evaluation of a new multi-function X-ray core scanner. Geological Society, London, Special Publications, 267(1): 51-63.

Cummins, P.F., Freeland, H.J., 2007. Variability of the North Pacific Current and its bifurcation. Progress in Oceanography, 75(2): 253-265.

Davis, C.V. et al., 2019. Ongoing increase in Eastern Tropical North Pacific denitrification as interpreted through Santa Barbara Basin sedimentary δ15N record. Paleoceanography and Paleoclimatology(Same issue).

Deutsch, C. et al., 2014. Centennial changes in North Pacific anoxia linked to tropical trade winds. Science, 345(6197): 665-668.

Deutsch, C., Sigman, D.M., Thunell, R.C., Meckler, A.N., Haug, G.H., 2004. Isotopic constraints on glacial/interglacial changes in the oceanic nitrogen budget. Global Biogeochemical Cycles, 18(4).

Di Lorenzo, E. et al., 2008. North Pacific Gyre Oscillation links ocean climate and ecosystem change. Geophysical Research Letters, 35(8).

Douglass, E., Roemmich, D., Stammer, D., 2006. Interannual variability in northeast Pacific circulation. Journal of Geophysical Research, 111(C4).

Du, X., Hendy, I., Schimmelmann, A., 2018. A 9000-year flood history for Southern California: A revised stratigraphy of varved sediments in Santa Barbara Basin. Marine Geology, 397: 29-42.

Enriquez, A.G., Friehe, C.A., 1995. Effects of wind stress and wind stress curl variability on coastal upwelling. Journal of Physical Oceanography, 25: 1651-1671.

Firme, G.F., Rue, E.L., Weeks, D.A., Bruland, K.W., Hutchins, D.A., 2003. Spatial and temporal variability in phytoplankton iron limitation along the California coast and consequences for Si, N, and C biogeochemistry. Global Biogeochemical Cycles, 17(1).

Freeland, H.J., 2003. Cold halocline in the northern California Current: An invasion of subarctic water. Geophysical Research Letters, 30(3).

Freeland, H.J., Cummins, P.F., 2005. Argo: A new tool for environmental monitoring and assessment of the world's oceans, an example from the N.E. Pacific. Progress in Oceanography, 64(1): 31-44.

Ganeshram, R.S., Pedersen, T.F., Calvert, S.E., François, R., 2002. Reduced nitrogen fixation in the glacial ocean inferred from changes in marine nitrogen and phosphorus inventories. Nature, 415: 156-159.

Ganeshram, R.S., Pedersen, T.F., Calvert, S.E., Murra, J.W., 1995. Large changes in oceanic nutrient inventories from glacial to interglacial periods. Nature, 376: 755-758.

Gay, P.S., Chereskin, T.K., 2009. Mean structure and seasonal variability of the poleward undercurrent off southern California. Journal of Geophysical Research, 114(C2).

Gómez-Valdivia, F., Parés-Sierra, A., Flores-Morales, A.L., 2015. The Mexican Coastal Current: A subsurface seasonal bridge that connects the tropical and subtropical Northeastern Pacific. Continental Shelf Research, 110: 100-107.

Gómez-Valdivia, F., Parés-Sierra, A., Laura Flores-Morales, A., 2017. Semiannual variability of the California Undercurrent along the Southern California Current System: A tropical generated phenomenon. Journal of Geophysical Research: Oceans, 122(2): 1574-1589.

Grinsted, A., Moore, J.C., Jevrejeva, S., 2004. Application of the cross wavelet transform and wavelet coherence to geophysical time series. Nonlinear Processes in Geophysics(11): 561-566.

Haug, G.H., Hughen, K.A., Sigman, D.M., Peterson, L.C., Röhl, U., 2001. Southward migration of the intertropical convergence zone through the Holocene. Science, 293(5533): 1304-1308.

Helama, S., Jones, P.D., Briffa, K.R., 2017. Dark Ages Cold Period: A literature review and directions for future research. The Holocene, 27(10): 1600-1606.

Hendy, I.L., Dunn, L., Schimmelmann, A., Pak, D.K., 2013. Resolving varve and radiocarbon chronology differences during the last 2000 years in the Santa Barbara Basin sedimentary record, California. Quaternary International, 310: 155-168.

Hendy, I.L., Napier, T.J., Schimmelmann, A., 2015. From extreme rainfall to drought: 250 years of annually resolved sediment deposition in Santa Barbara Basin, California. Quaternary International, 387: 3-12.

Heusser, L.E., Hendy, I.L., Barron, J.A., 2015. Vegetation response to southern California drought during the Medieval Climate Anomaly and early Little Ice Age (AD 800–1600). Quaternary International, 387: 23-35.

Hickey, B.M., 1978. The California current system—hypotheses and facts. Progress in Oceanography, 8(4): 191-279.

Hickey, B.M., 1992. Circulation over the Santa Monica-San Pedro Basin and Shelf. Progress in Oceanography, 30: 37-115.

Huyer, A., 2003. Preface to special section on enhanced Subarctic influence in the California Current, 2002. Geophysical Research Letters, 30(15).

Hwang, Y.-T., Frierson, D.M.W., Kang, S.M., 2013. Anthropogenic sulfate aerosol and the southward shift of tropical precipitation in the late 20th century. Geophysical Research Letters, 40(11): 2845-2850.

Ishi, Y., Hanawa, K., 2005. Large-scale variabilities of wintertime wind stress curl field in the North Pacific and their relation to atmospheric teleconnection patterns. Geophysical Research Letters, 32(10).

Jacobel, A.W., McManus, J.F., Anderson, R.F., Winckler, G., 2016. Large deglacial shifts of the Pacific Intertropical Convergence Zone. Nat Commun, 7: 10449.

Jacox, M.G., Moore, A.M., Edwards, C.A., Fiechter, J., 2014. Spatially resolved upwelling in the California Current System and its connections to climate variability. Geophysical Research Letters, 41(9): 3189-3196.

John, S.G., Mendez, J., Moffett, J., Adkins, J., 2012. The flux of iron and iron isotopes from San Pedro Basin sediments. Geochimica et Cosmochimica Acta, 93: 14-29.

Kennett, D.J. et al., 2012. Development and disintegration of Maya political systems in response to climate change. Science, 338(6108): 788-91.

Kienast, M. et al., 2005. On the sedimentological origin of down-core variations of bulk sedimentary nitrogen isotope ratios. Paleoceanography, 20(2): 1-13.

Kienast, S.S., Calvert, S.E., Pedersen, T.F., 2002. Nitrogen isotope and productivity variations along the northeast Pacific margin over the last 120 kyr: Surface and subsurface paleoceanography. Paleoceanography, 17(4): 7-1-7-17.

King, A.L., Barbeau, K.A., 2011. Dissolved iron and macronutrient distributions in the southern California Current System. Journal of Geophysical Research, 116(C3).

Koutavas, A., Lynch-Stieglitz, J., 2004. Variability of the Marine ITCZ over the Eastern Pacific during the Past 30,000 Years. In: Diaz, H.F., Bradley, R.S. (Eds.), The Hadley Circulation: Present, Past and Future. Advances in Global Change Research. Springer, Dordrecht, pp. 347-369.

Lechleitner, F.A. et al., 2017. Tropical rainfall over the last two millennia: evidence for a low-latitude hydrologic seesaw. Sci Rep, 7: 45809.

Liu, K.-K., Kaplan, I.R., 1989. The eastern tropical Pacific as a source of 15N-enriched nitrate in seawater off southern California. Limnology and Oceanography, 34(5): 820-830.

Lynn, R.J., Simpson, J.J., 1987. The California Current System: The Seasonal Variability of its Physical Characteristics. Journal of Geophysical Research, 92(12): 12947-19966.

McClatchie, S. et al., 2016. The influence of Pacific Equatorial Water on fish diversity in the southern California Current System. Journal of Geophysical Research: Oceans, 121(8): 6121-6136.

McGee, D. et al., 2018. Hemispherically asymmetric trade wind changes as signatures of past ITCZ shifts. Quaternary Science Reviews, 180: 214-228.

Meehl, G.A., Arblaster, J.M., Branstator, G., van Loon, H., 2008. A Coupled Air–Sea Response Mechanism to Solar Forcing in the Pacific Region. Journal of Climate, 21(12): 2883-2897.

Meyers, P.A., 1997. Organic geochemical proxies of paleoceanographic, paleolimnologic, and paleoclimatic processes. Organic Geochemistry, 27(5/6): 213-250.

Moberg, A., Sonechkin, D.M., Holmgren, K., M., D.N., Karlén, W., 2005. Highly variable Northern Hemisphere temperatures reconstructed from low- and high-resolution proxy data. Nature, 433(7026): 613-617.

Müller, P.J., 1977. C/N ratios in Pacific deep-sea sediments: effect of inorganic ammonium and organic nitrogen compounds sorbed by clays. Geochimica et Cosmochimica Acta, 41(6): 765-776.

Münchow, A., 2000. Wind stress curl forcing of the coastal ocean near Point Conception, California. Journal of Physical Oceanography, 30: 1265-1280.

Murphree, T., Bograd, S.J., Schwing, F.B., Ford, B., 2003. Large scale atmosphere-ocean anomalies in the northeast Pacific during 2002. Geophysical Research Letters, 30(15).

Ortiz, J., Mix, A., Hostetler, S., Kashgarian, M., 1997. The California Current of the Last Glacial Maximum: Reconstruction at 42°N based on multiple proxies. Paleoceanography, 12(2): 191-205.

Ortiz, J.D., Mix, A.C., Collier, R.W., 1995. Environmental control of living symbiotic and asymbiotic foraminifera of the California Current. Paleoceanography, 10(6): 987-1009.

Osterberg, E.C. et al., 2014. Mount Logan ice core record of tropical and solar influences on Aleutian Low variability: 500–1998 A.D. Journal of Geophysical Research: Atmospheres, 119(19): 11189-11204.

PAGES 2k Consortium, 2013. Continental-scale temperature variability during the past two millennia. Nature Geoscience, 6(5): 339-346.

Pérez-Cruz, L., 2017. Hydrological changes and paleoproductivity in the Gulf of California during middle and late Holocene and their relationship with ITCZ and North American Monsoon variability. Quaternary Research, 79(02): 138-151.

Philander, S.G.H., Gu, D., Lambert, G., Li, T., 1996. Why the ITCZ is mostly north of the equator. Journal of Climate, 9: 2958-2972.

Pichevin, L. et al., 2012. Silicic acid biogeochemistry in the Gulf of California: Insights from sedimentary Si isotopes. Paleoceanography, 27(2).

Pickett, M.H., 2003. Ekman transport and pumping in the California Current based on the U.S. Navy's high-resolution atmospheric model (COAMPS). Journal of Geophysical Research, 108(C10).

Pride, C. et al., 1999. Nitrogen isotopic variations in the Gulf of California since the Last Deglaciation: Response to global climate change. Paleoceanography, 14(3): 397-409.

Prokopenko, M. et al., 2006. Nitrogen cycling in the sediments of Santa Barbara basin and Eastern Subtropical North Pacific: Nitrogen isotopes, diagenesis and possible chemosymbiosis between two lithotrophs (Thioploca and Anammox)—"riding on a glider". Earth and Planetary Science Letters, 242(1-2): 186-204.

Reimer, P.J. et al., 2013. IntCal13 and Marine13 radiocarbon age calibration curves 0–50,000 years cal BP. Radiocarbon, 55(4): 1869-1887.

Reimers, C.E., Lange, C., Tabak, M., Bernhard, J., 1990. Seasonal spillover and varve formation in the Santa Barbara Basin, California. Limnology and Oceanography, 35(7): 1577-1585.

Ren, H. et al., 2017. 21st-century rise in anthropogenic nitrogen deposition on a remote coral reef. Science, 356(6339): 749-752.

Ridley, H.E. et al., 2015. Aerosol forcing of the position of the intertropical convergence zone since ad 1550. Nature Geoscience, 8(3): 195-200.

Rotstayn, L.D., Lohmann, U., 2002. Tropical Rainfall Trends and the indirect aerosol effect. Journal of Climate, 15: 2103-2116.

Ryan, W.B.F. et al., 2009. Global Multi-Resolution Topography synthesis. Geochemistry, Geophysics, Geosystems, 10(3): 1-9.

Rykaczewski, R.R., Checkley, D.M., Jr., 2008. Influence of ocean winds on the pelagic ecosystem in upwelling regions. Proc Natl Acad Sci U S A, 105(6): 1965-70.

Salvatteci, R. et al., 2014. The response of the Peruvian Upwelling Ecosystem to centennial-scale global change during the last two millennia. Climate of the Past, 10(2): 715-731.

Sarno, C.T. et al., 2019. The impacts of flood, drought, and turbidites on organic carbon burial over the past 2000 years in the Santa Barbara Basin, California. Paleoceanography and Paleoclimatology(same issue).

Schimmelmann, A., 2011. The "coffin lid" effect: flood layers and turbidites in Santa Barbara Basin affect diagenesis of organic matter in underlying varved sediment. In: Besonen, M.R. (Editor), Second Workshop of the PAGES Varves Working Group, Corpus Christi, Texas, USA, pp. 83-86.

Schimmelmann, A. et al., 1992. Extreme climatic conditions recorded in Santa Barbara Basin laminated sediments: the 1835–1840 Macoma event. Marine Geology, 106(1992): 279-299.

Schimmelmann, A., Lange, C.B., Berger, W.H., 1990. Climatically controlled marker layers in Santa Barbara Basin sediments and fine-scale core-to-core correlation. Limnology and Oceanography, 35(1): 165-173.

Schneider, T., Bischoff, T., Haug, G.H., 2014. Migrations and dynamics of the intertropical convergence zone. Nature, 513(7516): 45-53.

Schubert, C.J., Calvert, S.E., 2001. Nitrogen and carbon isotopic composition of marine and terrestrial organic matter in Arctic Ocean sediments: implications for nutrient utilization and organic matter composition. Deep Sea Research I, 48(3): 789-810.

Sigman, D.M., Karsh, K.L., Casciotti, K.L., 2009a. Nitrogen Isotopes in the Ocean, Encyclopedia of Ocean Sciences (Second Edition). Academic Press, Oxford, pp. 40-54.

Sigman, D.M., Karsh, K.L., Casciotti, K.L., 2009b. Ocean process tracers: nitrogen isotopes in the ocean.

Strub, P.T., James, C., 2003. Altimeter estimates of anomalous transports into the northern California Current during 2000-2002. Geophysical Research Letters, 30(15).

Sydeman, W.J. et al., 2011. Does positioning of the North Pacific Current affect downstream ecosystem productivity? Geophysical Research Letters, 38(12): 1-6.

Taylor, A.G., Landry, M.R., Selph, K.E., Wokuluk, J.J., 2015a. Temporal and spatial patterns of microbial community biomass and composition in the Southern California Current Ecosystem. Deep Sea Research Part II: Topical Studies in Oceanography, 112: 117-128.

Taylor, M.A., Hendy, I.L., Pak, D.K., 2015b. The California Current System as a transmitter of millennial scale climate change on the northeastern Pacific margin from 10 to 50 ka. Paleoceanography, 30(9): 1168-1182.

Tems, C.E. et al., 2016. Decadal to centennial fluctuations in the intensity of the eastern tropical North Pacific oxygen minimum zone during the last 1200 years. Paleoceanography, 31(8): 1138-1151.

Thunell, R., Benitez-Nelson, C., Varela, R., Astor, Y., Muller-Karger, F., 2007. Particulate organic carbon fluxes along upwelling-dominated continental margins: Rates and mechanisms. Global Biogeochemical Cycles, 21(1).

Thunell, R.C., 1998a. Particle fluxes in a coastal upwelling zone: sediment trap results from Santa Barbara Basin, California. Deep Sea Research Part II: Topical Studies in Oceanography, 45(8): 1863-1884.

Thunell, R.C., 1998b. Seasonal and annual variability in particle fluxes in the Gulf of California: A response to climate forcing. Deep Sea Research Part I: Oceanographic Research Papers, 45(12): 2059-2083.

Thunell, R.C., Sigman, D.M., Muller-Karger, F., Astor, Y., Varela, R., 2004. Nitrogen isotope dynamics of the Cariaco Basin, Venezuela. Global Biogeochemical Cycles, 18(3): 1-13.

Thunell, R.C., Tappa, E.J., Andersen, D.M., 1995. Sediment fluxes and varve formation in Santa Barbara Basin, offshore California. Geology, 23(12): 1083-1086.

Torrence, C., Compo, G.P., 1997. A practical guide to wavelet analysis. Bulletin of the American Meteorological Society, 79(1): 61-78.

Warrick, J.A., Farnsworth, K.L., 2009a. Dispersal of river sediment in the Southern California Bight. 454: 53-67.

Warrick, J.A., Farnsworth, K.L., 2009b. Sources of sediment to the coastal waters of the Southern California Bight. The Geological Society of America Special Paper, 454: 39-52.

Xie, S.-P., 1994. Oceanic response to the wind forcing associated with the Intertropical Convergence Zone in the northern hemisphere. Journal of Geophysical Research, 99(C10): 20393.

Chapter 6

Large Natural Variability of the Southern California Oxygen Minimum Zone Revealed During the Common Era

6.1 Abstract

Despite recent observations of aggravated oceanic deoxygenation due to the ongoing warming trend, much remains unknown on the natural processes driving dissolved oxygen (DO) variability. The duration (~60 years) of current instrumental records is insufficient to resolve multidecadal to centennial-scale natural DO variability. Here we present a suite of redox-sensitive trace metal records from the Santa Barbara Basin (SBB), which allow us to reconstruct decadal to millennial variations of a coastal oxygen minimum zone (OMZ) on the Southern California Margin at a resolution of 4 to 9 years over the Common Era (CE, last 2000 years). DO concentrations mostly vary as expected during the climate changes of the CE, with more oxygenated conditions during the cooling in early Little Ice Age (LIA, 1250 – 1500 CE). The most reducing conditions (940 – 1050 and 1100 – 1160 CE) occurred during the warm Medieval Climate Anomaly (MCA), as suggested by the highest metal enrichments of the record. Both OMZ intensification and relaxation are rapid. The reconstructed MCA intensification rates are 1 – 2 orders of magnitude faster than changes occurring in the 20th century, highlighting that natural OMZ oscillations can occur more rapidly than anticipated in the instrumental record.

However, in contrast to the expected DO response to climate, low-oxygen conditions also occur between ~1550 – 1750 CE coinciding with the coldest interval of the LIA. In the absence of changes in local export productivity and upwelling, a more distal cause is indicated in the reduction of intermediate water ventilation. Evidence from proxy reconstructions and the Last Millennium Reanalysis (LMR) project suggests that a weaker/westward Aleutian Low (AL) and weakened Siberian High (SH) generated prevailing easterlies and weakened wind stress over the Sea of Okhotsk. This change in wind direction and speed reduced sea ice formation in the Sea of

Okhotsk and thus brine rejection, thereby limiting a major contributor to North Pacific Intermediate Water (NPIW) formation in the North Pacific. The LMR also reveals a positive Arctic Dipole (AD) anomaly during 1550 – 1750 CE that may have led to the high-latitude atmospheric responses (weakened SH and westward AL). Thus, we suggest that NPIW ventilation is sensitive to large-scale atmospheric forcing and more nuanced NPIW ventilation responses to climate change requires additional scrutiny to better understand natural OMZ variability. More high-resolution proxy reconstructions, however, are still required to constrain the remote atmospheric forcing on basin-scale oxygen variations.

6.2 Introduction

The potential of ocean deoxygenation since the 1950s has increasingly drawn attention as aggravated dissolved oxygen (DO) decline and oxygen minimum zone (OMZ) expansion are observed in both open-ocean and coastal waters (Breitburg et al., 2018; Diaz and Rosenberg, 2008; Keeling et al., 2010; Schmidtko et al., 2017). As oxygen is a fundamental constraint for marine productivity, biodiversity, and important biogeochemical processes, understanding the dynamics of oceanic DO and the driving mechanisms are essential for regional/global-scale DO predictions and investigating the subsequent impacts on ecosystems that are increasingly constrained by anthropogenic influences.

DO change can be caused by either O_2 supply or consumption changes. Observed DO deficiencies since the mid 20th century have been attributed to anthropogenic global warming that reduces O_2 supply by decreasing O_2 solubility in surface waters and increases water column stratification that prevents mixing of O_2 into subsurface waters (Bopp et al., 2013; Breitburg et al., 2018; Stramma et al., 2010). O_2 consumption is also associated with primary productivity through organic carbon respiration. The current warming trend may enhance O_2 consumption via increasing respiration rates, further aggravating deoxygenation (Carstensen et al., 2014). In addition to O_2 supply from surface waters, O_2 advection through intermediate water masses provides another control on subsurface water oxygenation. This mechanism directly relates to exchange with the atmosphere at the intermediate water formation sites and/or water mass aging owing to respiration along the circulation path. The complex nature of DO responses and short duration (~60 years) of observational records make it challenging to quantify longer term (centennial to millennial) internal/forced DO variability and the underlying drivers. High-resolution paleo-reconstructions from marine archives are thus especially valuable for improving

our understanding of oceanic DO responses to natural climate forcing on sub-decadal to centennial timescales, providing new constraints for future model projections that incorporate both anthropogenic and natural variability.

Geochemical proxies (e.g., redox-sensitive trace metals) are often used to reconstruct oxygenation as redox-sensitive metal preservation is associated with sedimentary redox conditions controlled by DO concentrations (Calvert and Pedersen, 2007). Here we use authigenic enrichments of redox-sensitive metals (e.g., Mo, Re, and Cd) with respect to the lithogenic background to reconstruct past oxygenation. Rhenium has an extremely low crustal concentration (~0.3 – 0.7 ppb, Colodner et al. (1993)) and thus shows the greatest enrichments among the redox-sensitive trace metals with well-understood geochemical behaviors (Crusius et al., 1996). In oxygenated conditions Re exists as conservative ReO_4^-, whereas Re is readily reduced to authigenic Re(IV) oxides/sulfides and preserved in sediments under low-oxygen conditions (Crusius et al., 1996; Tribovillard et al., 2006). Molybdenum primarily exists in the form of conservative molybdate (MoO_4^{2-}) despite scavenging by Mn (oxyhydr)oxides via absorption in oxic waters (Scott et al., 2008) and complexation with dissolved organic carbon (Tessin et al., 2018; Wagner et al., 2017). When free sulfide (HS^-) is present in the ambient waters because of O_2 depletion from organic carbon respiration, conservative MoO_4^{2-} is reduced to thiomolybdates ($MoO_xS_{4-x}^{2-}$) that are readily scavenged into sediments with ambient HS^- (Erickson and Helz, 2000). Thus, Mo can be used as an indicator of strongly reducing conditions (i.e., sulfidic environments with HS^- presence) provided that coeval Re enrichments are observed (Calvert and Pedersen, 2007; Tribovillard et al., 2006; Zheng et al., 2000). As authigenic Re and Mo are preserved under different redox potential, Re/Mo ratio can be further considered to distinguish low-oxygen from sulfidic environments. High Re enrichments and Re/Mo ratios together would indicate low-oxygen (no free sulfide present) environments, whereas high Re and Mo enrichments along with close to seawater Re/Mo values (0.4 mmol/mol) would indicate more reducing conditions (Crusius et al., 1996). Unlike Re and Mo, cadmium only has one oxidation state (Cd(II)) and shows a nutrient-like profile in the water column (Boyle, 1988; Morford, 1999; Rosenthal et al., 1995). Cd is mainly released to ambient waters via organic carbon degradation and can be preserved as insoluble CdS at the presence of low-level free sulfide in suboxic sediments (Gobeil et al., 1997; Rosenthal et al., 1995). Cd can be used as a proxy for low-oxygen and strongly reducing (sulfidic) conditions with additional information on organic carbon export

to the sediments (Hendy and Pedersen, 2005; Rosenthal et al., 1995). Although excess Ba (or biogenic Ba, Ba fraction that is not terrigenous) has been widely used as a productivity indicator (Paytan and Griffith, 2007), marine barite ($BaSO_4$) that precipitates in the water column following organic matter degradation can be dissolved in the sulfidic porewaters, leading to depletion of sedimentary Ba (Griffith and Paytan, 2012; Hendy, 2010; McManus et al., 1998; Torres et al., 1996; Von Breymann et al., 1992). Excess Ba in the sulfidic porewaters could thus be used to indicate relatively oxygenated environments that reduce barite dissolution. A suite of redox-sensitive metals would thus allow a more comprehensive redox reconstruction that spans a broader range of oxygenation variability.

A 2000-year high-resolution (4 – 9 years) redox-sensitive trace metal record (SPR0901-03KC, 34°16.990′N, 120°2.408′W; 586 m depth) from the Santa Barbara Basin (SBB), California, was generated to constrain natural oxygenation oscillations on sub-decadal to millennial timescales in Southern California. It thus provides an opportunity of comparing the magnitude and frequency of natural Southern California OMZ variability to the anthropogenic influences suggested from the post-Industrial Revolution record, which allows us to investigate naturally driven oxygenation responses to Common Era (CE) climatic change (Fig. 6-1b). We paired the redox elemental record with productivity proxies (e.g., total organic carbon) to reveal the local control of Southern California oxygenation. The remote oxygenation influences from intermediate water ventilation and associated atmospheric forcing are then investigated by comparing with other CE proxy records at high latitudes, as well as the reconstructed climatology from the Last Millennium Reanalysis to reveal the possible physical mechanisms leading to ventilation variability.

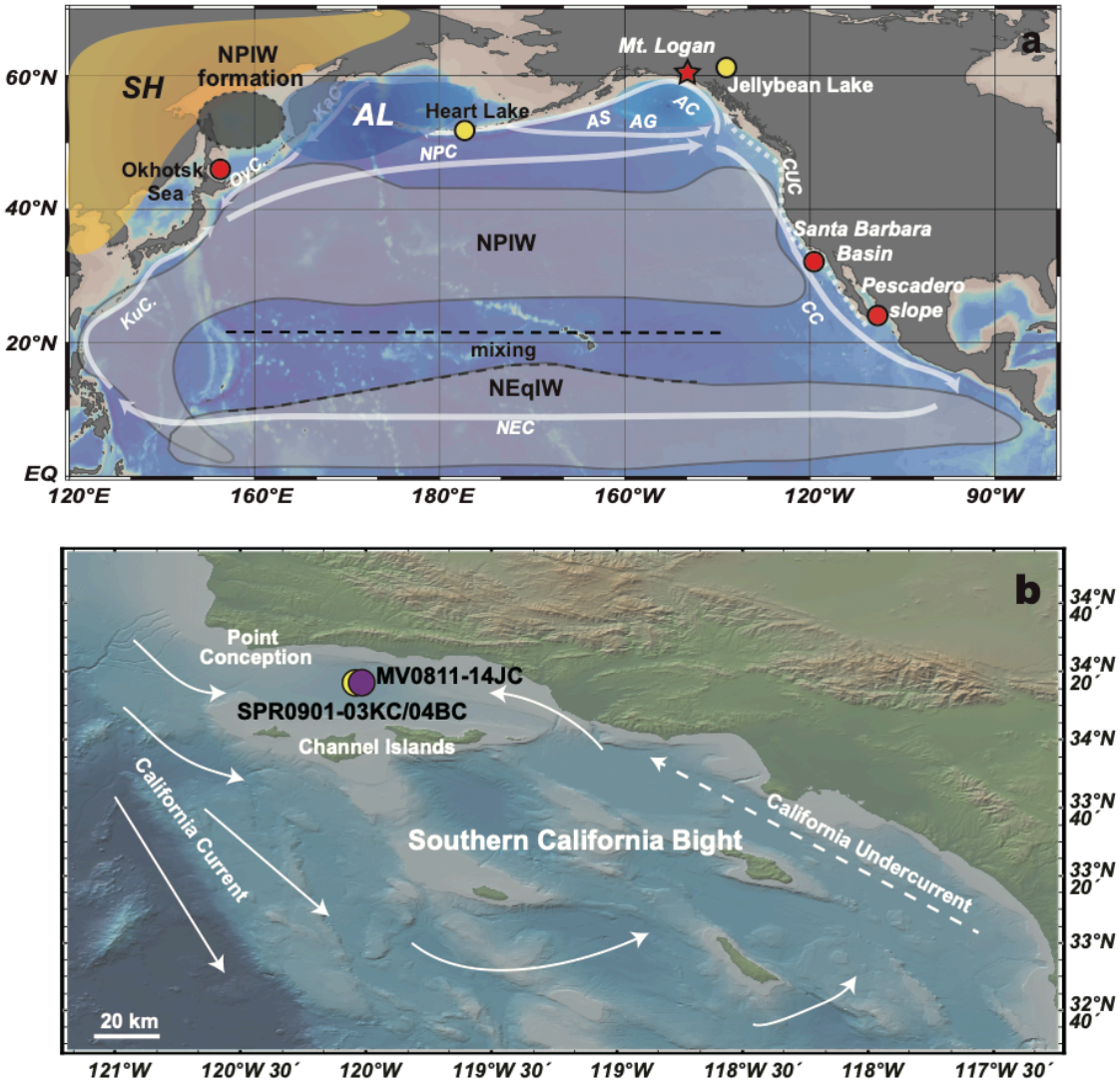

Figure 6-1 Core locations and circulation patterns. (a) Relative position of a westward/weakened Aleution Low (AL) and Siberian High (SH). Red circles: Santa Barbara Basin core SPR0901-03KC, Pescadero Slope core location from Tems et al. (2016), and Sea of Okhotsk core site from Itaki (2004). Yellow circles: the Jellybean lake site from Anderson et al. (2005) and the Heart Lake site from Bailey et al. (2018). Red star: the ice core location from Mount Logan (Osterberg et al., 2014). Intermediate water masses (light gray shading) and the North Pacific Intermediate Water formation regions (dark gray shading with the dashed outline) are adapted from Bostock et al. (2010); Bostock et al. (2013); Talley (2008). Ocean currents are shown in white arrows. KaC: Kamchatka Current; OyC.: Oyashio Current; KuC.: Kuroshio Current; NEC: North Equatorial Current; CC: California Current; CUC: California Undercurrent; GoA: Gulf of Alaska; AC: Alaska Current; AS: Alaska Stream. NPIW: North Pacific Intermediate Water; NEqPIW: North Equatorial Pacific Intermediate Water; (b) The SBB map with ocean circulations. The cores SPR0901-03KC and SPR0901-04BC are shown in the yellow circle. The core MV0811-14JC is represented by the purple circle, and the circulation pattern is modified from Hickey (1992). The base maps are generated from the Ocean data View in (a) and the GeoMapApp (http://www.geomapapp.org, Ryan et al., 2009), respectively.

6.3 Background

The SBB is a semi-closed basin on the Southern California margin with a 475-m sill connecting the basin to the open ocean. An oxygen minimum zone (OMZ) is present in the SBB below the sill depth associated with high upwelling-driven export productivity and basin

bathymetry (Checkley and Barth, 2009; Moffitt et al., 2014). SBB bottom waters have low (suboxic) to non-detectable oxygen (anoxic) concentrations (typically <20 μmol/kg), which suppress mega/macrofaunal activity and enable annually laminated sediment preservation. SBB is connected to the broad Southern California OMZ as the basin is actively ventilated by OMZ waters entering the basin over the western sill during the 'flushing events', during which better oxygenated and dense intermediate waters displace the bottom water in the basin (Bograd, 2002; Goericke et al., 2015). SBB can thus serve as a model for coastal basins in the Southern California bight, providing information on natural variability in Southern California OMZ.

Intermediate water masses ventilating the southern California OMZ include cold and well oxygenated North Pacific Intermediate Water (NPIW), as well as the warm and low oxygen Equatorial Pacific Intermediate Water (EqPIW). As the densest water mass formed in the North Pacific, NPIW (potential density σ_θ = 26.7~26.9 kg m^{-3}, 300 – 800 m water depth, Reid (1965); You (2003)) forms in the Mixed Water Region between the Kuroshio Extension and the Oyashio Fronts (Miyao and Ishikawa, 2003; Talley, 1993; Yasuda, 1997; You, 2003). NPIW primarily ventilates in the Sea of Okhotsk (Fig. 6-1a), where coastal polynya development due to winter sea ice brine injection on the northern and northwestern shelf leads to well-oxygenated dense shelf water (DSW) formation (Shcherbina et al., 2004a; Shcherbina et al., 2004b; Talley, 1993; Watanabe and Wakatsuchi, 1998). The Gulf of Alaska may be an additional NPIW source region in winter but its contribution is minor (~10%) and restricted to upper NPIW (You et al., 2000; You et al., 2003).

NPIW ventilation induced by Sea of Okhotsk ice formation is closely associated with atmospheric circulation (e.g., position and intensity of the Aleutian Low [AL] and Siberian High [SH]) that determines both wind direction and stress (Kimura, 2004; Martin et al., 1998; Parkinson, 1990; Tachibana et al., 1996). Increased sea ice brine rejection (ventilation) usually corresponds to strong offshore (northerly/northwesterly) winds under deepened AL centered in the northeastern Pacific and/or intensified SH in the far-east Asia (Parkinson, 1990; Tachibana et al., 1996), because the strong offshore winds facilitate polynya production in the sea leading to intermediate water formation. Westward/weakened AL and SH that lead to easterlies and reduced wind stress, on the contrary, are usually linked with milder sea ice conditions and less ventilation in the Sea of Okhotsk (Fig. 6-1a).

EqPIW, an intermediate water mass from tropics, is a mixture of heavily modified Antarctica Intermediate Water (AAIW) and upwelled Pacific Deep Water forming in the western equatorial Pacific (Bostock et al., 2010). EqPIW is then transported towards the eastern equatorial Pacific (EEP) via the Equatorial Undercurrent, where DO in the EqPIW is further consumed due to high primary productivity driven by extensive equatorial upwelling. This low-O_2 subsurface water mass is then advected north to the Southern California via the California Undercurrent (CUC) (Fig. 6-1).

6.4 Methods

6.4.1 Geochemical measurements and enrichment factors

The kasten core SPR0901-03KC has a well-constrained age model. The published age model from a companion core SPR0901-06KC (Du et al., 2018; Hendy et al., 2013) was generated from 49 mixed planktonic foraminiferal ^{14}C dates converted to calendar ages using the Marine13 calibration curve (Reimer et al., 2013) and varying reservoir ages from Hendy et al. (2013). The past 300 years was dated by varve counting (Hendy et al., 2015; Schimmelmann et al., 1992). An age-depth model was then generated for 06KC using Bacon 2.2 (Du et al., 2018) using these data. The 03KC age model was then generated by mapping the 06KC age-depth model onto 03KC with 31 tie points based on the core fabric (e.g., turbidites, flood layers, and visually distinct varve marker horizons) (Wang et al, 2019).

A split of 03KC was sampled continuously at a 2-mm interval (~2 years per sample). All samples were freeze-dried and ground to generate bulk samples and selected samples were analyzed for major, minor, and trace element concentrations. Instantaneous depositional events (i.e., flood and turbidite layers) were avoided in the sample selection, as not being representative of marine sedimentation processes in the SBB. The intervals from 1350 – 1850 CE and 950 – 1150 CE were specifically targeted with 4 mm sampling (~4 year resolution) to investigate the oxygenation variability responding to major climatic changes during the CE. Other intervals were selected at 8 mm (~8 year) resolution. Detailed method description and validation can be found in the Chapter 2 and the summarized methodology is presented here. ~10 – 15 mg of sample was weighed (~300 samples in total) and was digested with trace metal grade HCl, HNO_3, and HF in 10 mL Teflon vessels using a CEM MARS 6 microwave digestion system. The digested sample was split into 3 aliquots for Re/Mo, Cd, and Al/Ba analyses on the Thermo

iCAP Q inductively coupled plasma mass spectrometer (ICP-MS) and the Thermo Element 2 ICP-MS in the Michigan Elemental Analysis Lab (MEAL) at the University of Michigan. Both the aliquots for Re/Mo and Al/Ba were measured on the Thermo iCAP Q ICP-MS in the kinetic energy discrimination (KED) mode, using the external standard calibration method and bracketing standards for drift correction. Cd was measured using the isotope dilution technique, where an ^{111}Cd-enriched spike was added to the sample prior to digestion. Digested Cd aliquots were passed through an AG 1-X8 anion exchange column to remove spectral interferences and were determined using the low-resolution mode on the Thermo Element 2 ICP-MS in MEAL by monitoring ^{111}Cd and ^{113}Cd. MESS-3, PACS-2, and HISS-1 sediment reference materials were used throughout the sample analyses. The relative standard deviation (RSD) for each sample was < 10% (usually < 5%) on the Thermo iCAP Q, and was < 2% (usually < 1%) on the Thermo Element 2 ICP-MS.

Redox-sensitive trace metal concentrations were normalized to Al to calculate enrichment factors ($Metal_{EF}$) (Eq. 6-1) with respect to the lithogenic background from Wang et al. (2017):

$$Metal_{EF} = \frac{(Metal / Al)_{sample}}{(Metal / Al)_{background}} \qquad \text{(Eq. 6-1)}$$

The lithogenic background was derived from the elemental concentrations of suspended bedload samples from the Santa Clara River, the Ventura River, and the Santa Rosa Islands (Napier et al., 2019), which were then weighted based on the respective sediment transport flux into the SBB (Warrick and Farnsworth, 2009). Barium was corrected for the detrital input ($Ba_{excess} = Ba_{sample} - (Ba/Al)_{background} \times Al_{sample}$ with the background from Wang et al. (2017)).

6.4.2 Last Millennium Reanalysis (LMR)

The Last Millennium Reanalysis project applies an ensemble data assimilation approach (DA), which incorporates information from proxy reconstructions into model simulated data that serve as prior expectations (Hakim et al., 2016; Tardif et al., 2019). The prior ensemble in each Monte Carlo realization was drawn from 100 random years in the Community Climate System Model version 4 (CCSM4) Last Millennium simulation (Tardif et al., 2019; Taylor et al., 2011). The proxy database used is the most extensive high-quality temperature-sensitive records currently available (PAGES 2k Consortium, 2017). Regression-based proxy system models (PSM) for different proxy categories (e.g., tree ring width, coral δ^{18}O) were applied to estimate

the assimilated proxy values from the prior climate variables (e.g., temperature from model simulations), and an ensemble Kalman filter was used to update the prior ensemble (Hakim et al., 2016; Steiger et al., 2014; Tardif et al., 2019). A cut-off length scale of 25000 km was applied with covariance localization in order to avoid spurious covariance with remote records (Hamill et al., 2001). The annual data product is presented on a 2°×2° grid and each variable contains 13 LMR Monte Carlo reconstructions. The grand mean was validated against gridded instrumental analyses (Tardif et al., 2019).

Ventilation of the intermediate water masses is affected by both thermal (surface heat loss) and haline (precipitation/evaporation, runoff, and sea ice formation/melting) causes of buoyancy gain/loss. As no sea ice and runoff information is available in the reanalysis product, a quantitative calculation and decomposition of thermal- and haline-driven density fluxes is not applicable. However, other climate variables can qualitatively evaluate contributions of the two components. Sea surface temperature (SST) and precipitation anomalies were used to assess the impacts of buoyancy change due to heat loss. Sea ice formation was assessed using sea level pressure (SLP), 500 hPa geopotential height, and 2-m air temperature anomalies that determine atmospheric circulation changes. All climate variables were converted to anomalies with respect to the pre-1850 mean for comparison.

6.5 Results

6.5.1 Geochemical measurements

All redox-sensitive trace metals are continuously enriched relative to the lithogenic background throughout the core SPR0901-03KC. Re_{EF} and Mo_{EF} show similar variations ($r = 0.59$, $p < 0.05$) but there is no long-term trend through the CE. Peak enrichments of Re and Mo generally occur between 540 – 800 CE, 910 – 1100 CE, and ~1600 – 1750 CE (Figs. 6-2c and d). Relative low Re and Mo enrichments occurred between 200 – 540, 790 – 880, and 1160 – 1550 CE. Re_{EF} varies between 1.70 (142 BCE) and 7.40 (1640 CE) with an average of 3.75, whereas Mo_{EF} ranges from 1.53 (15 CE) and 11.64 (986 CE) with a mean value of 3.42 (Fig. 6-2). Cd_{EF} show similar enrichment patterns with Re and Mo except Cd_{EF} shows a sharp peak at ~1750 CE, rather than a broad peak for ~1550 – 1750 CE. When Re_{EF} and Mo_{EF} values were lower than average, high Cd_{EF} and highly variable Cd_{EF} were observed during 820 – 940 CE and 200 – 500 CE, respectively. Ba_{excess} through the CE is mostly below the concentration of catchment bedload

sediments draining into SBB (Napier et al., 2019). Two exceptions are observed; A sharp peak at 1087 CE, which corresponds to a local minimum of Cd_{EF}, Re_{EF}, and Mo_{EF} (Fig. 6-2) and a broad peak between ~1250 and 1500 CE, coeval with relatively low redox-sensitive $Metal_{EF}$ intervals. Ba_{excess} mostly shows negative values except a broad peak during 1240 – 1510 CE and a sharp peak at ~1090 CE. Before 1090 CE Ba_{excess} shows a decreasing trend towards the bottom of the core, and a similar oscillatory decline of Ba_{excess} is recorded after 1510 CE (Fig. 6-2).

The $(Re/Mo)_{EF}$ ratio (mean value of 1.18) is mostly above the seawater enrichment value (0.74, suggests quantitative Mo removal from the ambient waters provided with reducing conditions evidenced from enriched Re), except for 110 BCE, 55 CE, 287 CE, 986 CE, and 1758 CE. The highest Mo enrichment between 970 – ~1010 CE leads to the lowest $(Re/Mo)_{EF}$ of 0.36 throughout the record, which is much lower than the seawater value. However, the remaining low $(Re/Mo)_{EF}$ values correspond to low Re and Mo enrichments and therefore are not significant. The highest $(Re/Mo)_{EF}$ occurs at 1738 CE where both Re_{EF} and Mo_{EF} were relatively low (much lower than average) in the core (Fig. 6-2).

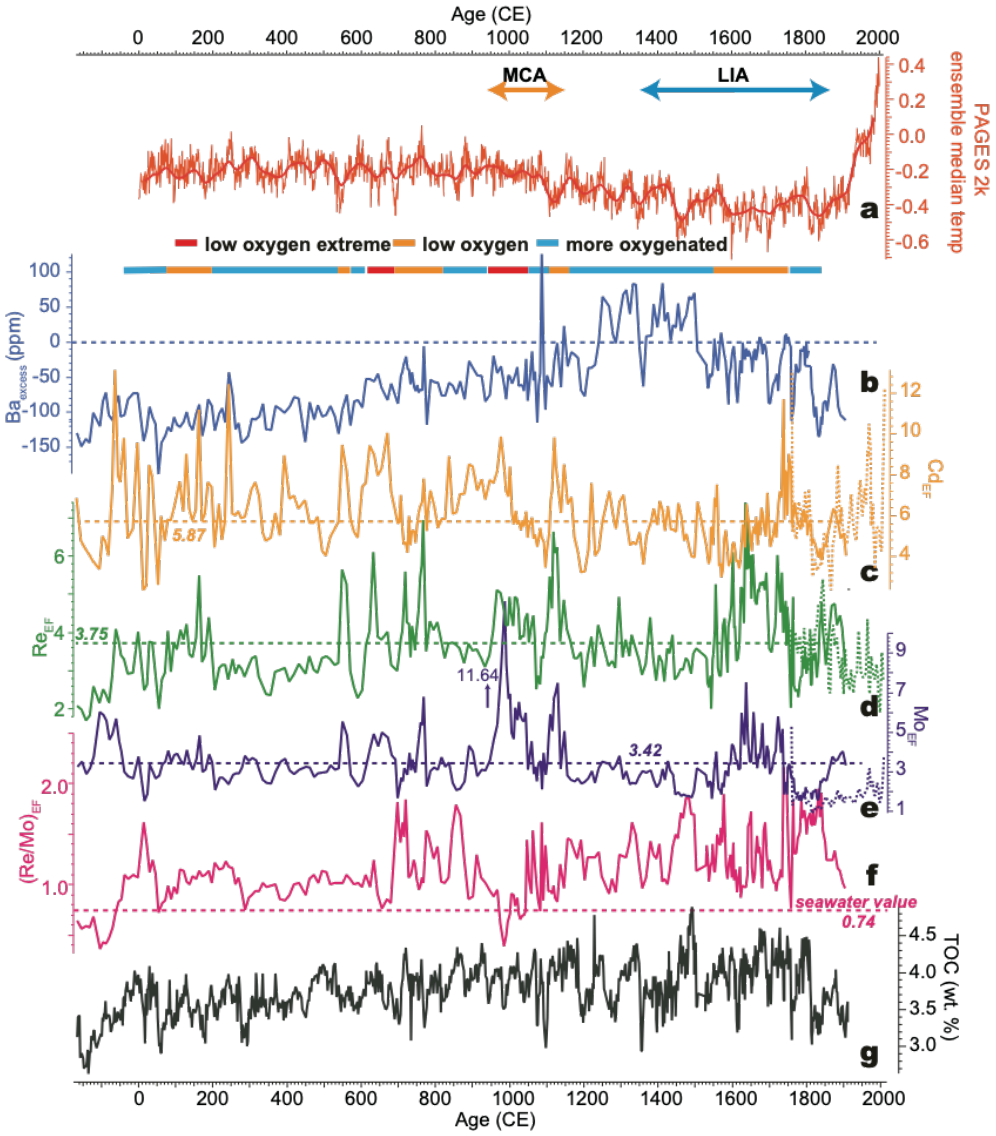

Figure 6-2 Common Era oxygenation variability from metal enrichments and local controls. (a) Model ensemble median for mean annual air temperature reconstruction from Neukom et al. (2019); (b) Ba excess from SPR0901-03KC shown in a blue solid curve; (c-e) enrichment factors for Cd (yellow), Re (green), and Mo (purple) for SPR0901-03KC are show solid curves, whereas dashed curves show respective $Metal_{EF}$ from SPR0901-04BC. The horizontal dashed lines represent the mean values; (f) the magenta solid and dashed curves represent Re/Mo enrichments for 03KC and 04BC, respectively. The horizontal dashed line shows the seawater value of 0.74. (g) Total organic carbon for core SPR0901-03KC from Wang et al. (2019). Warm and cold climatic events in the Common Era are denoted in orange and blue arrows, respectively. MCA: Medieval Climate Anomaly; LIA: Little Ice Age. Blue, orange, and red bars at the bottom show 'more oxygenated', 'low oxygen', and 'low oxygen extreme' intervals.

6.5.2 LMR results

A broad region of 50 – 65°N and 135 – 170°E was chosen to generate time series of spatially averaged climate variables in the Sea of Okhotsk to investigate site specific responses to CE climate change (Fig. 6-3). SSTs were relatively stable during the past 2000 years as the grand mean varies within the range of ±0.3°C, except for a sharp decline of -0.6 °C at 1600 CE (Fig. 6-

3b). Despite the relative stable SST in the Sea of Okhotsk, the positive SLP anomalies were observed during 900 – 1300 CE, while negative SLP frequently occurred after 1300 CE. No SLP anomaly in the grand mean values is shown in the LMR before 900 CE, which might be associated with the sparse records extending to the first millennium (Fig. 6-3).

The interval of 1550 – 1750 CE was targeted in the LMR following the sedimentary Mo and Re enrichments in the SBB record to better understand the forcing mechanism of this interval of redox-sensitive trace metals. A dipole pattern over the high-latitudes is indicated in the 1550 – 1750 CE SLP anomaly (Fig. 6-3c). Negative SLP anomalies were found over the northern Europe, Siberia, Barents Sea, Sea of Okhotsk, Japan Sea, and the Gulf of Alaska, whereas positive SLP anomalies were prevalent over the Greenland and Canadian Arctic Archipelago. Similarly, negative 500 hPa geopotential height anomalies prevailed over the Gulf of Alaska, Siberia, northern Europe and the Sea of Okhotsk, with a slightly positive anomaly over central Pacific and the northwest America (Fig. C-1). Precipitation rates, however, only show minor anomalies over the Okhotsk Sea region during 1550 – 1750 CE (Fig. C-2).

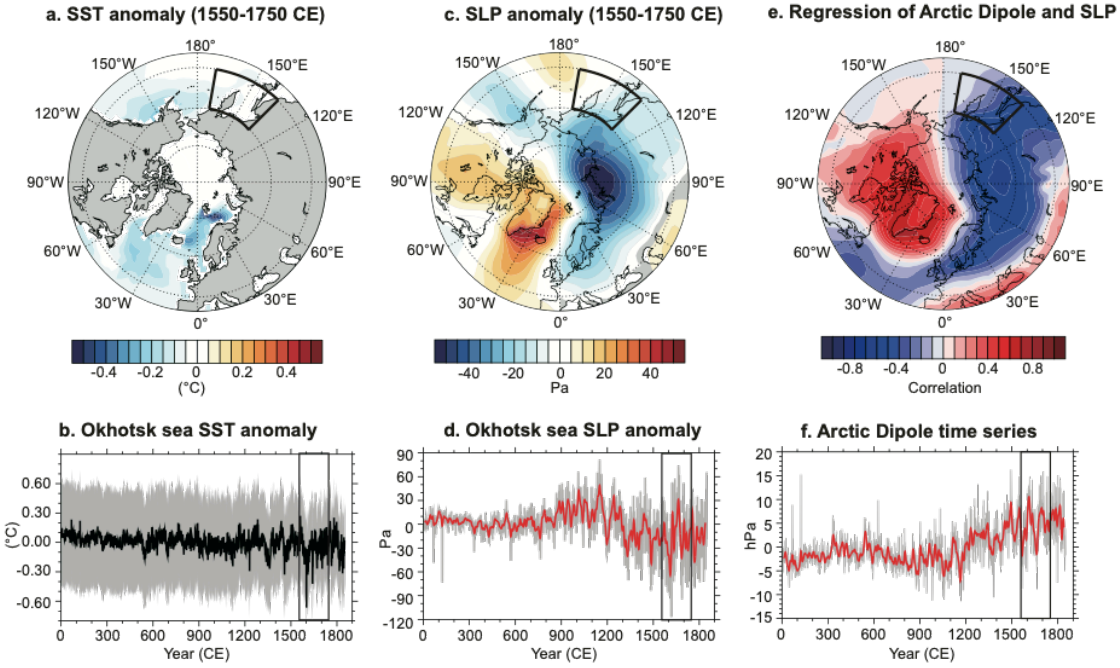

Figure 6-3 Last Millennium Reanalysis results. (a and c) Sea surface temperature (SST) and sea level pressure (SLP) anomaly during 1550 – 1750 CE with respect to 0 – 1850 CE average, respectively; (b) Area weighted SST anomaly time series with respect to 0–1850 CE over the Sea of Okhotsk (50 – 65°N, 135 – 170°E, outlined as the blank fan); The grand mean of 13 Monte Carlo simulations in the LMR is shown in the black curve while the model spread is shown in gray curve. (d) Area weighted SLP anomaly time series with respect to 0 – 1850 CE over the Sea of Okhotsk; the red curve shows 20-year Lanczos bandpass filtered data and grand mean is shown in the gray curve; (e) regression map between the Arctic Dipole pattern derived from LMR and SLP anomaly with respect to 0 – 1850 CE; (f) Arctic Dipole time series with the red curve representing 20-year Lanczos bandpass filtered data and the gray curve showing the grand mean. The 1550 – 1750 CE interval is outlined in the black rectangle in (b), (d), and (f).

To further understand the dipole SLP pattern observed over the high latitudes, annual mean climate indices relevant to high-latitude atmospheric circulation (e.g., the Arctic Dipole index [AD]) from the reanalysis product and were used for field correlation with climate variables that reveal regional responses to atmospheric forcing. The AD is defined as the 2nd empirical orthogonal function (EOF) of winter SLP anomaly north of 70°N (Wang et al., 2009; Wu et al., 2006). A positive AD corresponds to positive SLP anomaly over the Canadian Arctic Archipelago and Greenland, with a negative SLP anomaly over Kara/Leptev Sea close to Siberia (Wang et al., 2009; Wu et al., 2006; Zhang, 2015). The simulated annually resolved AD anomaly (EOF2 of annual SLP anomaly, 14.5% of the total variance) showed a similar pattern with the observed AD patterns (EOF2 of winter [DJF] SLP anomaly, 13% of the total variance) from the NCEP/NCAR reanalysis (1948 to present) (Fig. C-3).

6.6 Discussions

6.6.1 Redox control on sedimentary Ba preservation

Ba_{EF} is often used as a productivity indicator for sediments dominated by biogenic input and with minimal terrestrial influences (Eagle et al., 2003). Ba precipitates as barite ($BaSO_4$) on falling particles in the water column and then buried if porewaters are oxygenated (Bishop, 1988; Dymond et al., 1992; Ganeshram et al., 2003; Gingele et al., 1999; McManus et al., 1994; Paytan and Griffith, 2007). Although stable in oxygenated environments, authigenic barite ($BaSO_4$) can be dissolved to release as free Ba^{2+} in porewaters where sulfate reduction occurs as sulfate serves as an electron acceptor in organic carbon (OC) decay (Griffith and Paytan, 2012; Hendy, 2010; McManus et al., 1998; Torres et al., 1996; Von Breymann et al., 1992), compromising the original productivity signal in the Ba_{excess} record. Depleted oxygen and sulfate reduction occurs within the top several millimeters in the central SBB porewaters, and free HS^- usually accumulates within 5 cm below the sediment-water interface (SWI) (Kuwabara et al., 1999; Raven et al., 2016; Reimers et al., 1996), Thus, typically authigenic barite is dissolved in the SBB porewaters, releasing free Ba^{2+} to the ambient waters. However, Ba shows a statistically significant correlation ($r = 0.57$, $p < 0.05$) with previously published total organic carbon (TOC) in 03KC, a robust export productivity proxy in this core (Wang et al., 2019). High frequency variability in Ba_{excess} can thus be explained by export productivity in SBB even though sedimentary Ba remobilization occurred under sulfate reduction. However, the broad increase in

Ba_{excess} between 1250 and 1550 CE above the lithogenic background corresponds to low $Metal_{EF}$ (Fig. 6-2b), suggesting this interval was associated with increased barite preservation under relatively more oxygenated conditions.

Maximum Ba_{excess} values occur at 1090 CE, corresponding to a local minimum of redox-sensitive $Metal_{EF}$. It is possible that this peak is a response to an abrupt oxygenation interval in SBB. However, barite dissolution increases below this peak as evidenced by a decreasing Ba_{excess} trend downcore. The peak at 1090 CE also resides in the sulfate depletion zone range (~100 – 150 cm below the SWI) (Berelson et al., 2005; Harrison et al., 2009; Reimers et al., 1996). Thus, this peak may be diagenetic barite generated by Ba^{2+} diffusing up from the sulfate-depletion zone below and SO_4^{2-} diffusing down from the upper core (Hendy, 2010). Intensive barite dissolution in the sulfate-depletion zone leads to high Ba^{2+} in porewaters, which would migrate upwards into the sulfate-bearing zone and re-precipitate to form barite immediately above the sulfate depletion zone (Torres et al., 1996; Von Breymann et al., 1992); however, as Ba_{excess} is depleted above 1090 CE, this peak likely stopped migrating at 1100 CE. Diagenetic barite peaks have been widely reported in continental margin records but it usually occurs in more deeply buried sediments as porewaters are more oxygenated than in SBB (Hendy, 2010; McManus et al., 1998; Riedinger et al., 2006; Torres et al., 1996).

6.6.2 Common Era variability of Southern California oxygenation in the Holocene context

The combination of oxygenated (Ba_{excess}), low-oxygen indicators (Cd_{EF} and Re_{EF}), sulfidic proxies (Mo_{EF}, and $(Re/Mo)_{EF}$) allows for assessment of the OMZ intensity. Lower than average enrichments of both low-oxygen and sulfidic indicators along with Ba enrichments would suggest relatively 'oxygenated' conditions. The combination of elevated redox metal enrichments (Cd_{EF}, Re_{EF}, and Mo_{EF}) and lower than the seawater value of $(Re/Mo)_{EF}$ implies extreme reducing environments (i.e., 'low oxygen extreme' with free sulfide presence).

There is a broad correspondence between the climatic events and oxygen concentrations, such as the OMZ expansion during MCA and the OMZ contraction during the early LIA. The most oxygenated interval occurred during 1250 – 1500 CE (early LIA), when persistently low $Metal_{EF}$ coincided with positive Ba_{excess}, suggesting that this interval had sufficient oxygen to preserve barite. Low-oxygen intervals (e.g., 70 – 200, 540 – 570, 690 – 820, 1110 – 1160, and 1550 – 1750 CE) were relatively short in duration (multiple decades), with the longest event (1550 – 1750 CE) lasting for ~200 years. Intensified deoxygenation after the Industrial

Revolution, which appears to be linked with anthropogenic warming since the 20th century was shown in SPR0901-04BC by a gradual increase of Mo_{EF} (mean value of 1.99 ± 0.09, 1SE) and concurrent decrease of $(Re/Mo)_{EF}$ (mean value of 1.61±0.07, 1SE) since ~1870 (Wang et al., 2017). The Common Era record from 03KC shows significantly higher enrichments for Mo (mean value of 3.42 vs. 1.99 for 04BC) and overall much lower $(Re/Mo)_{EF}$ (mean value of 1.18 vs. 1.61), suggesting that the post-Industrial Revolution OMZ intensification has not yet exceeded the envelope of reconstructed natural OMZ variations. The average $Metal_{EF}$ in the Common Era was even higher (Mo_{EF} of 3.42 ± 0.08 vs. 2.54 ± 0.16 [1SE], Fig. 6-2d) than the early-mid Holocene values in the core 14JC (Wang and Hendy, accepted). The abrupt Mo_{EF} peaks between 980 – 1120 CE (11.24 and 7.51, respectively) represent the greatest enrichment during the Holocene. $Metal_{EF}$ peaks thus argue for much larger magnitude of OMZ variability forced by natural processes that are not yet observed/recorded from modern instrumental records.

Mo_{EF} can also provide a qualitative estimate of OMZ intensification and relaxation rate. Although sedimentary Mo enrichments can be associated with shuttle effects of Fe/Mn oxides and organic matter, we can exclude the shuttle effect from Chapter 3, and the lack of correspondence of Mo_{EF} and total organic carbon (Wang et al., 2019) makes productivity control on Mo preservation less likely. SBB bottom waters are always bathed by low-oxygen bottom waters that facilitate Re and Cd enrichments, while Mo enrichments indicate a more sulfidic environment with lethal effects on benthic macro/mega-organisms. The magnitude and frequency of Mo variability was revealed by calculating a downcore Mo_{EF} rate of change (ΔMo_{EF}/year) from the derivative between the adjacent data points. Uneven sampling of the core (denser sampling in the MCA and LIA) may have smoothed out high-frequency OMZ oscillations for intervals with lower sampling frequencies, thus a 5-point Mo_{EF} moving average, which suppresses high-frequency oscillations and highlights multidecadal variability was used. Each interval has at least 5 data points to allow determination of OMZ expansion/relaxation rates using a linear least-square regression (Fig. 6-4a). Eight intervals of OMZ intensification and six intervals of OMZ relaxation were identified (Fig. 6-4b). A number of intervals — 520 – 780, 920 – 1160, and 1480 – 1840 CE — show rapid OMZ oscillations with ΔMo_{EF}/year amplitude exceeding 1 standard deviation (Fig. 6-4c), suggesting that high-frequency and large magnitude of OMZ oscillations are not uncommon and occurred sporadically during the past 2000 years.

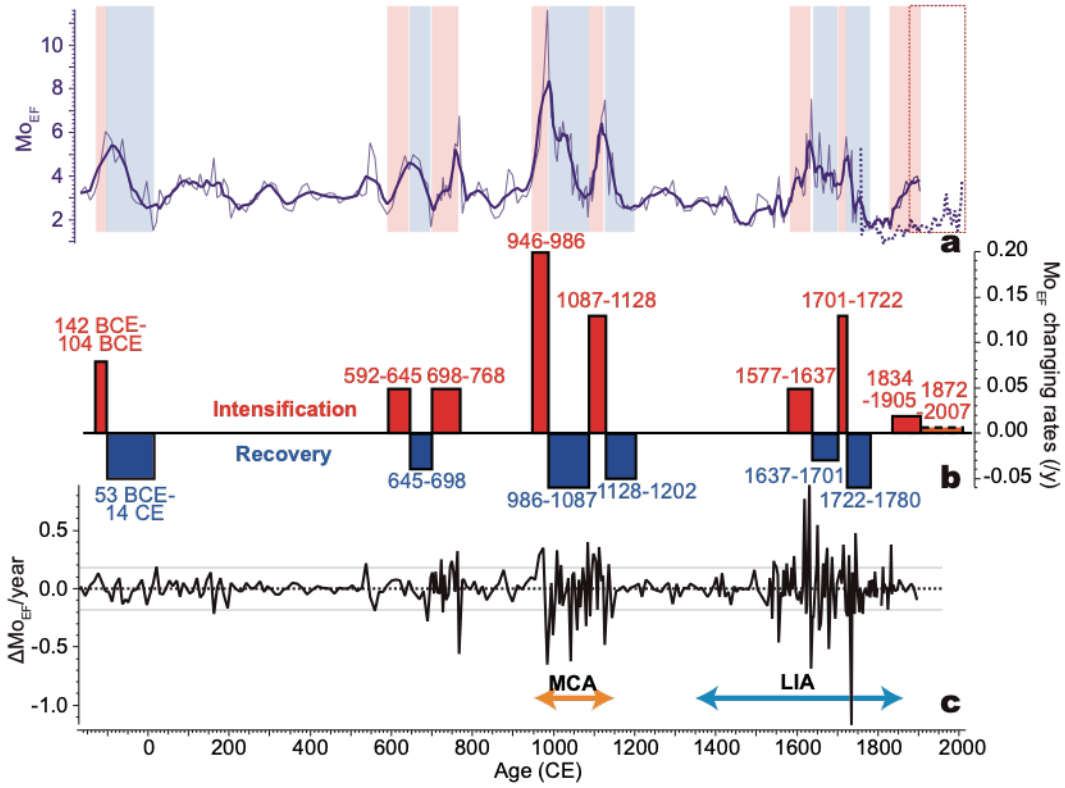

Figure 6-4 Oxygen minimum zone intensification and recovery rates. (a) Mo_{EF} from SPR0901-03KC in the thin solid purple curve with the 5-point running mean shown in a thick solid purple line. The purple dashed curve shows Mo_{EF} from the post-Industrial core SPR0901-04BC. Identified oxygen minimum zone intensification and relaxation intervals are denoted as red and blue bars, respectively. The selected 04BC interval for OMZ intensification rate calculation is denoted by a dashed rectangle. (b) Calculated OMZ intensification/recovery rates based on the least-square linear regression of Mo_{EF} during the intervals identified in (a). Ages of the identified intervals are labeled. The OMZ intensification rate of 04BC is outlined in the dashed line. (c) Changing rates of Mo_{EF} between the two adjacent points. The two horizontal solid lines represent the 1SD envelope. Orange and blue arrows at the bottom show warm and cold climatic events in the Common Era, respectively.

The calculated OMZ expansion rates are comparable or faster than the relaxation rates but the timescale of both processes can be as short as several decades. OMZ expansion rates during the Common Era were orders of magnitude higher than the recent expansion of the 20th century (e.g., 0.20/year for 946 – 986 CE vs. 0.0073/year for 1870 – 2007 CE) (Wang et al., 2017), suggesting that the recent OMZ expansion is not unprecedented regarding both rates and magnitude (Fig. 6-4). The current deoxygenation trend seen in instrumental observations may thus be significantly exacerbated if overlaid by synergistic natural OMZ variability. More high-resolution Common Era reconstructions in other coastal OMZs are needed to better constrain sensitivity of oxygenation to natural climate change.

6.6.3 Controlling mechanism of Southern California OMZ

Reduced DO in subsurface waters can be caused by increased export productivity in the

overlying water column and remote water mass influences lowering DO (e.g., ventilation shifts in the intermediate water formation regions and/or increasing influences of low-O_2 subsurface water masses). Export productivity can draw down DO in the water column and porewaters via organic matter decay. Export productivity is reconstructed from TOC, which is closely associated with the presence of upwelling in SBB (Wang et al., 2019). No statistically significant correlation was found between Cd_{EF} or Mo_{EF} and TOC, indicating that export productivity was not the primary control of reducing conditions in the basin over the past 2000 years. However, productivity control is likely to result in the most reducing conditions in SBB during the warmer MCA (940 – 1050 and 1100 – 1160 CE) suggested from foraminifera assemblages (e.g., low abundance of *Neogloboquadrina pachyderma* in MCA (Fisler and Hendy, 2008), as the higher abudance of upwelling diatoms, silicoflagellates (Barron et al., 2015), and anchovies (Skrivanek and Hendy, 2015) indicates strong coastal upwelling that may have contributed to the intensified OMZ. More oxygenated environments persisted during relatively cool intervals recorded in the basin during the early LIA (1250 – 1500 CE) (Fisler and Hendy, 2008). This association might suggest a relationship between cool climate conditions and well ventilated conditions in the basin as has been observed between glacial and interglacial cycles in the Southern California OMZ (Cartapanis et al., 2011; Hendy and Pedersen, 2005; Ivanochko and Pedersen, 2004).

However, low oxygen intervals also occurred between 620 – 690 and 1550 – 1750 CE. During the 1550 – 1750 CE in particular, the global air temperature reconstructions indicate a ~0.4 °C cool anomaly with respect to the 1916 – 1995 CE average (Neukom et al., 2019), making it the coldest interval of the Common Era (Fig. 6-2b). The late LIA low-oxygen interval would thus seem to contradict with expected relationship between cool climate and greater ventilation of Southern California OMZ that has been well established between glacial-interglacial intervals (Behl and Kennett, 1996; Cannariato and Kennett, 1999; Hendy and Pedersen, 2005). No major productivity event was associated with the two low-oxygen intervals (Barron et al., 2015), and there is no statistically significant TOC difference between the more oxygenated intervals prior to and after the two low-oxygen intervals (Fig. 6-2). In the absence of evidence for local oxygen consumption, influences from the remote water mass must thus have played a role.

Intensified Southern California OMZ driven by remote water mass influences could be associated with less oxygenated EqPIW at the tropics, increased advection of reducing EqPIW

sourced from the Equatorial Pacific, and/or reduced ventilation of NPIW in the NE Pacific. We can assess EqPIW oxygenation and its advection to the Southern California margin using the bulk sediment $\delta^{15}N$, which has been widely applied as a proxy for water column denitrification. Denitrification occurs when nitrate is used as an electron acceptor in the organic carbon decay under low-oxygen conditions (Altabet et al., 1995; Altabet et al., 1999; Thunell et al., 2004). Preferential removal of light ^{14}N by denitrification leaves enriched ^{15}N in the subsurface waters that can be upwelled to the photic zone and incorporated into newly formed particulate OC (Altabet, 2006; Altabet and François, 1994; Ganeshram et al., 2002; Kienast et al., 2002). Elevated $\delta^{15}N$ signal is then preserved in the sediments following OC burial. Thus, higher sedimentary $\delta^{15}N$ would indicate intensified water-column denitrification in response to lower oxygen.

A bulk sediment $\delta^{15}N$ ($\delta^{15}N_{sed}$) record from the Pescadero Slope, Gulf of California (PESC-GC3, 24°16.759'N, 108°11.700'W, 620 m water depth, Fig. 6-1a) located in the Eastern Tropical North Pacific (ETNP) OMZ reflects EqPIW DO variability (Tems et al., 2016), whereas $\delta^{15}N_{sed}$ values in SBB is shown to reflect ETNP denitrified water influences on the Southern California OMZ if a coherence with the Pescadero record is observed (Wang et al., 2019). The greater than 7.8‰ $\delta^{15}N_{sed}$ values in SBB were coincident with Mo and Re enrichments (e.g., 520 – 800 and 950 – 1150 CE, Fig. 6-5a), supporting the possible presence of denitrified water – except during 1550 – 1750 CE (Wang et al., 2019). During the 950 – 1150 CE in particular, the Pescadero $\delta^{15}N_{sed}$ shows increased $\delta^{15}N$ (> 9.5‰), consistent with redox-sensitive metal enrichments in SBB (Fig. 6-5b). Together, the two high-resolution $\delta^{15}N$ records support the intensification of the ETNP OMZ during MCA, suggesting EqPIW contained less O_2 during intervals when the SBB bottom water O_2 decreased. However, the denitrified EqPIW influences on the SBB bottom waters seem to be weakened/diminished as the climate transitioned to the LIA. Despite coincident variability with the SBB $\delta^{15}N$, the most variable and least depleted interval of Pescadero $\delta^{15}N$ (1250 – 1500 CE) occurred when SBB bottom water appear most oxygenated based on the positive Ba_{excess} (Fig. 6-2b) and lowest redox-sensitive metal enrichments (Figs. 6-5c and d). During 1550 – 1750 CE, the relatively high Pescadero Slope $\delta^{15}N$ values indicating intensified ETNP OMZ disagree with the low $\delta^{15}N$ in SBB; it thus appears that low-O_2 EqPIW is not the primary driver for the sustained low-oxygen conditions during the coolest interval of the late LIA.

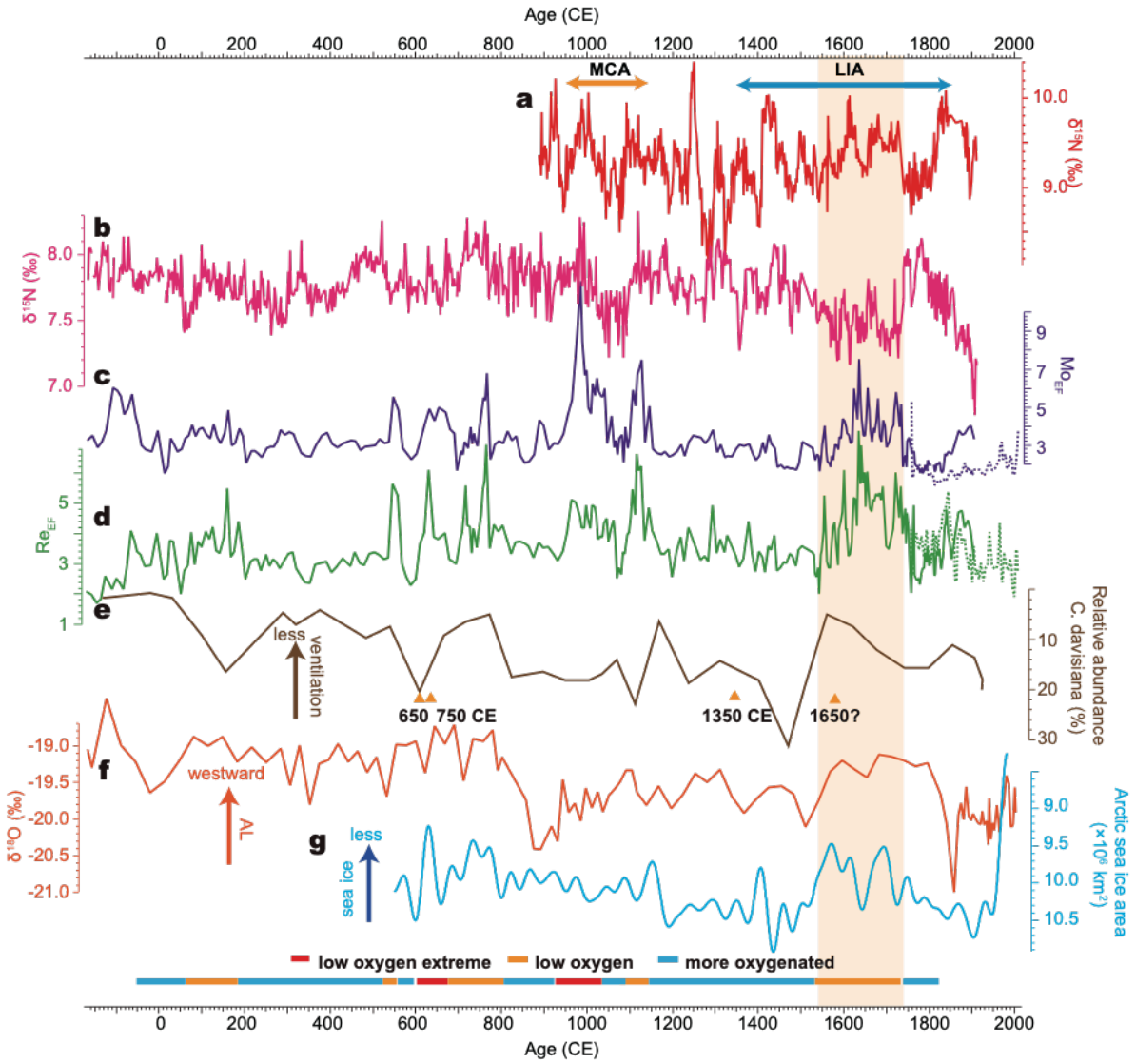

Figure 6-5 Regional comparison of high-latitude ventilation and sea ice proxies. (a) Bulk sedimentary $\delta^{15}N$ from the Pescadero slope (Tems et al., 2016). (b) Bulk sedimentary $\delta^{15}N$ from the SBB (Wang et al., 2019). (c and d) Enrichment factors of Mo (purple) and Re (green) for core SPR0901-03KC in solid lines, repectively. Dash lines are respective enrichment factors from SPR0901-04BC. (e) Relative abundance of *Cycladophora Davisiana* (ventilation indicator) in the Sea of Okhotsk (Itaki, 2004); (f) Lake sediment carbonate $\delta^{18}O$ in the Jellybean Lake (Anderson et al., 2005); (g) Pan-Arctic compilation Arctic sea ice area reconstructions (Kinnard et al., 2011). Blue and red arrows represent cold and warm climatic events, respectively. Blue, orange, and red bars denote intervals with different oxygenation labeled in the figure.

Changes in the ventilation of NPIW may be another possible cause of the anomalous low O_2 bottom water in SBB between 1550 – 1750 CE. NPIW advects from the northwest Pacific, where it is ventilated from the Sea of Okhotsk via intermediate water formation due to heat- or salinity-driven buoyancy loss of the surface water. As simulated SST from the Last Millennium Reanalysis (LMR) only showed minor changes (<0.1 °C except at 1600 CE, Fig. 3) and precipitation rates were relatively stable during 1550 – 1750 CE (Fig. C-2), it is likely that sea

ice should play a role in NPIW ventilation. Sea-ice driven changes in NPIW ventilation can be assessed using a Sea of Okhotsk ice reconstruction (GH01-1011, 44°35.50'N, 144°26.10'E, 1348 m in water depth, Fig. 6-1a) as sea ice brine rejection increases the density of surface waters and causes them to sink. Sea ice extent is based on the abundance of *Cycladophora davisiana* (Fig. 6-5f), a glacial radiolarian species dwelling at ~200 – 500 m depth in the Sea of Okhotsk (Itaki, 2004; Okazaki et al., 2006). At present, *C. davisiana* are only abundant in the Sea of Okhotsk as they are highly adapted to seasonal sea-ice covered environments (Nimmergut and Abelmann, 2002; Okazaki et al., 2006). Regionally, reduced *C. davisiana* production has either been associated with less stratified water column with shortened particulate OC (POC) residence time and/or reduced production of cold and well-ventilated Dense Shelf Water (DSW, a precursor of NPIW; Okazaki et al. (2006)).

Reduced sea ice formation should be the cause of decreased *C. davisiana* abundance between 1550 – 1700 CE instead of the relaxed water column stratification. Although the reconstructed global surface air temperature anomaly was the lowest of the CE during this interval (PAGES 2k Consortium, 2017), the Sea of Okhotsk SST remained stable or even slightly warmer. A SST reconstruction based on diatom assemblages in Southwestern Okhotsk Sea indicates warm water advection from the Japan Sea due to the abundance of open water warm species (e.g., *Thalassionema nitzschioides* and *Neodenticula seminae*) (Shimada et al., 2004). Reduced sea ice in the Sea of Okhotsk is also supported by reduced sea ice-related diatom species (e.g., *Bacterosira fragiles* and *Fragilariopsis cylindrus*) (Koizumi et al., 2003; Shimada et al., 2004). Thus, other mechanisms other than temperature must have played a role in reducing Sea of Okhotsk sea ice formation during the cool interval in the late LIA.

6.6.4 Impacts of atmospheric forcing on intermediate water ventilation

The relative position and intensity of the Aleutian Low (AL) and Siberian High (SH) control the wind stress and wind direction over the Sea of Okhotsk, as prevailing northerly or northwesterly winds produce polynyas along the northern shelf of the Sea of Okhotsk by moving sea ice away from the coast. Polynyas further facilitates dense water formation on the shelf through exposure of open water to subzero air temperatures and surface winds resulting in more heat loss and sea ice brine rejection (Martin et al., 1998). Reduced sea ice extent is associated with reduced wind stress caused by weakened AL/SH and prevailing easterly winds suppressing polynya formation (Parkinson, 1990; Tachibana et al., 1996). Despite the overall reduced surface

air temperature from the PAGES 2k reconstruction, multiple proxy records have shown westward/weakened AL during the LIA. The relatively enriched sedimentary calcite oxygen isotope record ($\delta^{18}O_{Ca}$) from the Jellybean Lake, Yukon Territory has been linked with a weaker and/or westward AL (Fig. 6-5g) (Anderson et al., 2005). This observation has also been corroborated by more enriched diatom $\delta^{18}O$ during 1550 – 1700 CE from the Heart Lake, Aleutian Islands (Bailey et al., 2018) and the reduced Na^+ deposition during 1400 – 1700 CE via sea salt aerosol from the ice core record in the Mt. Logan, Yukon Territory and Denali (Osterberg et al., 2014; Osterberg et al., 2017).

To reveal the large-scale atmospheric patterns that may have led to reduced sea ice cover and intermediate water ventilation in the Sea of Okhotsk, we compare proxy records with the LMR derived climate variables. Comparison with the LMR overcomes the disadvantage of sparse proxy networks by interpreting the atmospheric dynamics in a simulated climate history. The 1550 – 1750 SLP anomaly shows a high latitude dipole pattern with positive anomalies in central North Pacific and negative anomalies over the Gulf of Alaska and the Sea of Okhotsk, suggesting a possibly weaker/westward centered AL (Fig. 6-3c). Reduced SLP is also demonstrated from the field-averaged SLP time series over the Sea of Okhotsk (50 – 65°N, 135 – 170°E, Fig. 6-6d), implying a westward AL that may introduce easterlies over the Sea of Okhotsk suppressing polynya formation. Negative SLP and 500 hPa geopotential height anomalies over the Siberia further indicates a weakened SH that contributes to reduce the wind stress over the Sea of Okhotsk (Figs. 6-3 and C-1). The westward and weakened AL along with a weaker SH is therefore consistent with the proxy-based AL and Sea of Okhotsk sea ice reconstructions.

Additionally, the SLP dipole pattern closely resembles a simulated positive Arctic Dipole (AD) pattern (Figs. 6-3e and f, $p < 0.05$). Strong southerly winds generated under a positive AD anomaly (Fig. 6-3f) could advect warm air from Pacific and intensified Pacific inflow to the Arctic via the Bering Strait (Wang et al., 2009; Woodgate, 2018; Wu et al., 2006). The increased heat transport from subarctic Pacific and transpolar drift of sea ice could then lead to decreasing Arctic ice cover (Wang et al., 2009; Zhang et al., 2008; Zhang, 2015). A sustained positive AD pattern during the 1550 – 1750 CE from LMR could generate coherent high-latitude atmospheric responses (e.g., weakened SH, Fig. 6-3) and thus sea ice responses in LIA (Fig. 6-5), despite the reconstructed colder surface air temperature (PAGES 2k Consortium, 2017). The sea ice

responses (e.g., in the Sea of Okhotsk) driven by atmospheric forcing (e.g., positive AD, weakened AL and SH) could then affect intermediate water ventilation that would propagate through the North Pacific basin.

6.7 Conclusions

Observed ocean deoxygenation since the 1950s has initiated discussion on the natural variability of OMZ strength and extent. The magnitude of natural variability (either externally forced or internal) relative to the current deoxygenation trend caused by the anthropogenic warming (Stramma et al., 2010) provides valuable information for future model predictions and assessment of local ecological responses to oxygen oscillations. Due to the short duration of the instrumental records (~60 years), multidecadal to centennial-scale variations in dissolved oxygen (DO) concentrations remain unknown. A new Common Era redox-sensitive metal enrichment record (SPR0901-03KC) from the Santa Barbara Basin (SBB) allows us to reconstruct variations of a coastal oxygen minimum zone (OMZ) on the Southern California Margin and investigate drivers of natural OMZ shifts on a 4 – 9 year resolution. Multiple intervals of rapid OMZ intensification have been identified, with the most severe low-oxygen conditions occurring during the Medieval Climate Anomaly (MCA, 940 – 1050 and 1100 – 1160 CE). The intensified Southern California OMZ during MCA is the most reducing interval of the entire Holocene, relative to the metal enrichments observed in core MV0811-14JC spanning the interval 9 – 2 ka (Chapter 7) and SPR0901-04BC covering the post-Industrial Revolution period. The new record indicates that both OMZ intensification and relaxation can be rapid occurring within decades (on one to two orders of magnitude faster than the post-Industrial). Thus, the magnitude and rate of OMZ response to either internal or naturally forced variability has yet to be revealed in the instrumental records. An overall correspondence between OMZ variability and the climatic events suggests climate perturbations play a role in natural DO concentration variations. Persistent observations on marine oxygenation and additional high-resolution DO reconstructions are thus required to better constrain this natural variability.

Despite the overall correspondence between OMZ shifts and climatic events in the Common Era, the interval from 1550 – 1750 CE during the late LIA stand outs as an interval when low DO bottom waters bathed SBB when the climate was cool. The lack of correlation between local export productivity and bottom water oxygenation indicates the influence of advected intermediate water masses. We suggest that the low bottom water DO was associated

with reduced NPIW ventilation caused by suppressed Sea of Okhotsk ice formation (Itaki, 2004). A comparison of proxies and the Last Millennium Reanalysis (LMR) indicates that a weaker/westward Aleutian Low with weakened Siberian High could have produced prevailing easterlies over the Sea of Okhotsk, reducing sea ice production and NPIW ventilation. The LMR-revealed atmospheric forcing pattern is also consistent with a positive Arctic Dipole anomaly that may have led to high-latitude atmospheric responses (weakened SH and westward AL) during 1550 – 1750 CE. The natural oxygen variability in the OMZ on the Southern California margin could thus be sensitive to large-scale atmospheric forcing. The less ventilated NPIW during the late LIA suggests that intermediate ventilation is not a simple response of climate change observed during the glacial cycles (more ventilation during cold intervals yet less ventilation in warm climate). We thus highlight the natural OMZ variability driven by subtle ventilation changes in the mid-depth North Pacific in response to climate change, which may have been overlooked during the glacial cycles, adding another layer of complexity of future DO projections under the anthropogenic impacts.

6.8 Acknowledgements

This work is supported by the National Science Foundation under grant number OCE-1304327 awarded to I.H.; Y.W. acknowledges support from the Rackham Graduate School of the University of Michigan and the Scott Turner Award. We thank Angela Dial for lab assistance.

6.9 References

Altabet, M., 2006. Constraints on oceanic N balance/imbalance from sedimentary ^{15}N records. Biogeosciences Discussions, 3(4): 1121-1155.

Altabet, M.A., François, R., 1994. Sedimentary nitrogen isotopic ratio as a recorder for surface nitrate utilization. Global Biogeochemical Cycles, 8(1): 103-116.

Altabet, M.A., Francois, R., Murray, D.W., Prell, W.L., 1995. Climate-related variations in denitrification in the Arabian Sea from sediment 15N/14N ratios. Nature, 373: 506-509.

Altabet, M.A. et al., 1999. The nitrogen isotope biogeochemistry of sinking particles from the margin of the Eastern North Pacific. Deep Sea Research I, 46(1999): 655-679.

Anderson, L., Abbott, M.B., Finney, B.P., Burns, S.J., 2005. Regional atmospheric circulation change in the North Pacific during the Holocene inferred from lacustrine carbonate oxygen isotopes, Yukon Territory, Canada. Quaternary Research, 64(01): 21-35.

Bailey, H.L. et al., 2018. Holocene atmospheric circulation in the central North Pacific: A new terrestrial diatom and δ18O dataset from the Aleutian Islands. Quaternary Science Reviews, 194: 27-38.

Barron, J.A., Bukry, D., Hendy, I.L., 2015. High-resolution paleoclimatology of the Santa Barbara Basin during the Medieval Climate Anomaly and early Little Ice Age based on diatom and silicoflagellate assemblages in Kasten core SPR0901-02KC. Quaternary International, 387: 13-22.

Behl, R.J., Kennett, J.P., 1996. Brief interstadial events in the Santa Barbara basin, NE Pacific, during the past 60 kyr. Nature, 379(6562): 243-246.

Berelson, W.M. et al., 2005. Anaerobic diagenesis of silica and carbon in continental margin sediments: Discrete zones of TCO2 production. Geochimica et Cosmochimica Acta, 69(19): 4611-4629.

Bishop, J.K.B., 1988. The barite-opal-organic carbon association in oceanic particulate matter. Nature, 332(6162): 341-343.

Bograd, S.J., 2002. Bottom water renewal in the Santa Barbara Basin. Journal of Geophysical Research, 107(C12).

Bopp, L. et al., 2013. Multiple stressors of ocean ecosystems in the 21st century: projections with CMIP5 models. Biogeosciences, 10(10): 6225-6245.

Bostock, H.C., Opdyke, B.N., Williams, M.J.M., 2010. Characterising the intermediate depth waters of the Pacific Ocean using δ13C and other geochemical tracers. Deep Sea Research Part I: Oceanographic Research Papers, 57(7): 847-859.

Boyle, E.A., 1988. Cadmium: Chemical tracer of deepwater paleoceanography. Paleoceanography, 3(4): 471-489.

Breitburg, D. et al., 2018. Declining oxygen in the global ocean and coastal waters. Science, 359(6371).

Calvert, S.E., Pedersen, T.F., 2007. Elemental Proxies for Palaeoclimatic and Palaeoceanographic Variability in Marine Sediments: Interpretation and Application, Developments in Marine Geology, pp. 567-644.

Cannariato, K.G., Kennett, J.P., 1999. Climatically related millennial-scale fluctuations in strength of California margin oxygen-minimum zone during the past 60 k.y. Geology, 27(11): 975-978.

Carstensen, J., Andersen, J.H., Gustafsson, B.G., Conley, D.J., 2014. Deoxygenation of the Baltic Sea during the last century. Proc Natl Acad Sci U S A, 111(15): 5628-33.

Cartapanis, O., Tachikawa, K., Bard, E., 2011. Northeastern Pacific oxygen minimum zone variability over the past 70 kyr: Impact of biological production and oceanic ventilation. Paleoceanography, 26(4): 1-17.

Checkley, D.M., Barth, J.A., 2009. Patterns and processes in the California Current System. Progress in Oceanography, 83(1-4): 49-64.

Colodner, D. et al., 1993. The geochemical cycle of rhenium: a reconnaissance. Earth and Planetary Science Letters, 117: 205-221.

Crusius, J., Calvert, S., Pedersen, T., Sage, D., 1996. Rhenium and molybdenum enrichments in sediments as indicators of oxic, suboxic and sulfidic conditions of deposition. Earth and Planetary Science Letters, 145: 65-78.

Diaz, R.J., Rosenberg, R., 2008. Spreading dead zones and consequences for marine ecosystems. Science, 321(5891): 926-9.

Du, X., Hendy, I., Schimmelmann, A., 2018. A 9000-year flood history for Southern California: A revised stratigraphy of varved sediments in Santa Barbara Basin. Marine Geology, 397: 29-42.

Dymond, J., Suess, E., Lyle, M., 1992. Barium in Deep-Sea Sediment: A Geochemical Proxy for Paleoproductivity. Paleoceanography, 7(2): 163-181.

Eagle, M., Paytan, A., Arrigo, K.R., van Dijken, G., Murray, R.W., 2003. A comparison between excess barium and barite as indicators of carbon export. Paleoceanography, 18(1).

Erickson, B.E., Helz, G.R., 2000. Molybdenum(VI) speciation in sulfidic waters: stability and lability of thiomolybdates. Geochimica et Cosmochimica Acta, 64(7): 1149-1158.

Fisler, J., Hendy, I.L., 2008. California Current System response to late Holocene climate cooling in southern California. Geophysical Research Letters, 35(9).

Ganeshram, R.S., François, R., Commeau, J., Brown-Leger, S.L., 2003. An experimental investigation of barite formation in seawater. Geochimica et Cosmochimica Acta, 67(14): 2599-2605.

Ganeshram, R.S., Pedersen, T.F., Calvert, S.E., François, R., 2002. Reduced nitrogen fixation in the glacial ocean inferred from changes in marine nitrogen and phosphorus inventories. Nature, 415: 156-159.

Gingele, F.X., Zabel, M., Kasten, S., Bonn, W.J., Nürnberg, C.C., 1999. Biogenic Barium as a Proxy for Paleoproductivity: Methods and Limitations of Application. In: Fischer, G., Wefer, G. (Eds.), Use of Proxies in Paleoceanography: Examples from the South Atlantic. Springer Berlin Heidelberg, Berlin, Heidelberg, pp. 345-364.

Gobeil, C., Macdonald, R.W., Sundby, B., 1997. Diagenetic separation of cadmium and manganese in suboxic continental margin sediments. Geochimica et Cosmochimica Acta, 61(21): 4647-4654.

Goericke, R., Bograd, S.J., Grundle, D.S., 2015. Denitrification and flushing of the Santa Barbara Basin bottom waters. Deep Sea Research Part II: Topical Studies in Oceanography, 112: 53-60.

Griffith, E.M., Paytan, A., 2012. Barite in the ocean - occurrence, geochemistry and palaeoceanographic applications. Sedimentology, 59(6): 1817-1835.

Hakim, G.J. et al., 2016. The last millennium climate reanalysis project: Framework and first results. Journal of Geophysical Research: Atmospheres, 121(12): 6745-6764.

Hamill, T.M., Whitaker, J.S., Snyder, C., 2001. Distance-Dependent Filtering of Background Error Covariance Estimates in an Ensemble Kalman Filter. Monthly Weather Review, 129(11): 2776-2790.

Harrison, B.K., Zhang, H., Berelson, W., Orphan, V.J., 2009. Variations in archaeal and bacterial diversity associated with the sulfate-methane transition zone in continental margin sediments (Santa Barbara Basin, California). Appl Environ Microbiol, 75(6): 1487-99.

Hendy, I.L., 2010. Diagenetic behavior of barite in a coastal upwelling setting. Paleoceanography, 25(4): n/a-n/a.

Hendy, I.L., Dunn, L., Schimmelmann, A., Pak, D.K., 2013. Resolving varve and radiocarbon chronology differences during the last 2000 years in the Santa Barbara Basin sedimentary record, California. Quaternary International, 310: 155-168.

Hendy, I.L., Napier, T.J., Schimmelmann, A., 2015. From extreme rainfall to drought: 250 years of annually resolved sediment deposition in Santa Barbara Basin, California. Quaternary International, 387: 3-12.

Hendy, I.L., Pedersen, T.F., 2005. Is pore water oxygen content decoupled from productivity on the California Margin? Trace element results from Ocean Drilling Program Hole 1017E, San Lucia slope, California. Paleoceanography, 20(4): 1-12.

Itaki, T., 2004. Middle to late Holocene changes of the Okhotsk Sea Intermediate Water and their relation to atmospheric circulation. Geophysical Research Letters, 31(24).

Ivanochko, T.S., Pedersen, T.F., 2004. Determining the influences of Late Quaternary ventilation and productivity variations on Santa Barbara Basin sedimentary oxygenation: a multi-proxy approach. Quaternary Science Reviews, 23(3-4): 467-480.

Keeling, R.E., Kortzinger, A., Gruber, N., 2010. Ocean deoxygenation in a warming world. Ann Rev Mar Sci, 2: 199-229.

Kienast, S.S., Calvert, S.E., Pedersen, T.F., 2002. Nitrogen isotope and productivity variations along the northeast Pacific margin over the last 120 kyr: Surface and subsurface paleoceanography. Paleoceanography, 17(4): 7-1-7-17.

Kimura, N., 2004. Increase and decrease of sea ice area in the Sea of Okhotsk: Ice production in coastal polynyas and dynamic thickening in convergence zones. Journal of Geophysical Research, 109(C9).

Kinnard, C. et al., 2011. Reconstructed changes in Arctic sea ice over the past 1,450 years. Nature, 479(7374): 509-12.

Koizumi, I., Shiga, K., Irino, T., Ikehara, M., 2003. Diatom record of the late Holocene in the Okhotsk Sea. Marine Micropaleontology, 49(1): 139-156.

Kuwabara, J.S., Geen, A.V., Mccorkle, D.C., Bernhard, J.M., 1999. Dissolved sulfide distributions in the water column and sediment pore waters of the Santa Barbara Basin. Geochimica et Cosmochimica Acta, 63(15): 2199-2209.

Martin, S., Drucker, R., Yamashita, K., 1998. The production of ice and dense shelf water in the Okhotsk Sea polynyas. Journal of Geophysical Research: Oceans, 103(C12): 27771-27782.

McManus, J. et al., 1998. Geochemistry of barium in marine sediments: implications for its use as a paleoproxy. Geochimica et Cosmochimica Acta, 62(21): 3453-3473.

McManus, J., Berelson, W.M., Klinkhammer, G.P., Kilgore, T.E., Hammond, D.E., 1994. Remobilization of barium in continental margin sediments. Geochimica et Cosmochimica Acta, 58(22): 4899-4907.

Miyao, T., Ishikawa, K., 2003. Formation, distribution and volume transport of the North Pacific Intermediate Water studied by repeat hydrographic observations. Journal of Oceanography, 59(6): 905-919.

Moffitt, S.E., Hill, T.M., Ohkushi, K., Kennett, J.P., Behl, R.J., 2014. Vertical oxygen minimum zone oscillations since 20 ka in Santa Barbara Basin: A benthic foraminiferal community perspective. Paleoceanography, 29(1): 44-57.

Morford, J.L., 1999. The geochemistry of redox-sensitive trace metals, University of Washington.

Napier, T.J., Hendy, I.L., Fahnestock, M.F., Bryce, J.G., 2019. Provenance of detrital sediments in Santa Barbara Basin, California, USA: Changes in source contributions between the Last Glacial Maximum and Holocene. GSA Bulletin.

Neukom, R. et al., 2019. Consistent multidecadal variability in global temperature reconstructions and simulations over the Common Era. Nature Geoscience, 12(8): 643-649.

Nimmergut, A., Abelmann, A., 2002. Spatial and seasonal changes of radiolarian standing stocks in the Sea of Okhotsk. Deep Sea Research Part I: Oceanographic Research Papers, 49(3): 463-493.

Okazaki, Y. et al., 2006. Cycladophora davisiana (Radiolaria) in the Okhotsk Sea: a key for reconstructing glacial ocean conditions. Journal of Oceanography, 62: 639-648.

Osterberg, E.C. et al., 2014. Mount Logan ice core record of tropical and solar influences on Aleutian Low variability: 500–1998 A.D. Journal of Geophysical Research: Atmospheres, 119(19): 11189-11204.

Osterberg, E.C. et al., 2017. The 1200 year composite ice core record of Aleutian Low intensification. Geophysical Research Letters, 44(14): 7447-7454.

PAGE 2k Consortium, 2017. A global multiproxy database for temperature reconstructions of the Common Era. Sci Data, 4: 170088.

Parkinson, C.L., 1990. The Impact of the Siberian High and Aleutian Low on the Sea-Ice Cover of the Sea of Okhotsk. Annals of Glaciology, 14: 226-229.

Paytan, A., Griffith, E.M., 2007. Marine barite: Recorder of variations in ocean export productivity. Deep Sea Research Part II: Topical Studies in Oceanography, 54(5-7): 687-705.

Raven, M.R., Sessions, A.L., Fischer, W.W., Adkins, J.F., 2016. Sedimentary pyrite δ34S differs from porewater sulfide in Santa Barbara Basin: Proposed role of organic sulfur. Geochimica et Cosmochimica Acta, 186: 120-134.

Reid, J.L., 1965. Intermediate waters of the Pacific Ocean. Johns Hopkins Oceanography Studies, 5: 1-96.

Reimer, P.J. et al., 2013. IntCal13 and Marine13 radiocarbon age calibration curves 0–50,000 years cal BP. Radiocarbon, 55(4): 1869-1887.

Reimers, C.E., Ruttenberg, K.C., Canfield, D.E., Christiansen, M.B., Martin, J.B., 1996. Porewater pH and authigenic phases formed in the uppermost sediments of the Santa Barbara Basin. Geochimica et Cosmochimica Acta, 60(21): 4037-4057.

Riedinger, N., Kasten, S., Gröger, J., Franke, C., Pfeifer, K., 2006. Active and buried authigenic barite fronts in sediments from the Eastern Cape Basin. Earth and Planetary Science Letters, 241(3-4): 876-887.

Rosenthal, Y., Lam, P., Boyle, E.A., Thomson, J., 1995. Authigenic cadmium enrichments in suboxic sediments: Precipitation and postdepositional mobility. Earth and Planetary Science Letters, 132(1): 99-111.

Schimmelmann, A. et al., 1992. Extreme climatic conditions recorded in Santa Barbara Basin laminated sediments: the 1835–1840 Macoma event. Marine Geology, 106(1992): 279-299.

Schmidtko, S., Stramma, L., Visbeck, M., 2017. Decline in global oceanic oxygen content during the past five decades. Nature, 542(7641): 335-339.

Scott, C. et al., 2008. Tracing the stepwise oxygenation of the Proterozoic ocean. Nature, 452(7186): 456-9.

Shcherbina, A.Y., Talley, L.D., Rudnick, D.L., 2004a. Dense water formation on the northwestern shelf of the Okhotsk Sea: 1. Direct observations of brine rejection. Journal of Geophysical Research: Oceans, 109(C9).

Shcherbina, A.Y., Talley, L.D., Rudnick, D.L., 2004b. Dense water formation on the northwestern shelf of the Okhotsk Sea: 2. Quantifying the transports. Journal of Geophysical Research: Oceans, 109(C9).

Shimada, C., Ikehara, K., Tanimura, Y., Hasegawa, S., 2004. Millennial-scale variability of Holocene hydrography in the southwestern Okhotsk Sea: diatom evidence. The Holocene, 14(5): 641-650.

Skrivanek, A., Hendy, I.L., 2015. A 500 year climate catch: Pelagic fish scales and paleoproductivity in the Santa Barbara Basin from the Medieval Climate Anomaly to the Little Ice Age (AD 1000–1500). Quaternary International, 387: 36-45.

Steiger, N.J., Hakim, G.J., Steig, E.J., Battisti, D.S., Roe, G.H., 2014. Assimilation of Time-Averaged Pseudoproxies for Climate Reconstruction. Journal of Climate, 27(1): 426-441.

Stramma, L., Schmidtko, S., Levin, L.A., Johnson, G.C., 2010. Ocean oxygen minima expansions and their biological impacts. Deep Sea Research Part I: Oceanographic Research Papers, 57(4): 587-595.

Tachibana, Y., Honda, M., Takeuchi, K., 1996. The Abrupt Decrease of the Sea Ice over the Southern Part of the Sea of Okhotsk in 1989 and Its Relation to the Recent Weakening of the Aleutian Low. Journal of the Meteorological Society of Japan. Ser. II, 74(4): 579-584.

Talley, L.D., 1993. Distribution and formation of North Pacific Intermediate Water. Journal of Geophysical Oceanography, 23: 517-537.

Tardif, R. et al., 2019. Last Millennium Reanalysis with an expanded proxy database and seasonal proxy modeling. Climate of the Past, 15(4): 1251-1273.

Taylor, K.E., Stouffer, R.J., Meehl, G.A., 2011. An Overview of CMIP5 and the Experiment Design. Bulletin of the American Meteorological Society, 93(4): 485-498.

Tems, C.E. et al., 2016. Decadal to centennial fluctuations in the intensity of the eastern tropical North Pacific oxygen minimum zone during the last 1200 years. Paleoceanography, 31(8): 1138-1151.

Tessin, A., Chappaz, A., Hendy, I., Sheldon, N., 2018. Molybdenum speciation as a paleo-redox proxy: A case study from Late Cretaceous Western Interior Seaway black shales. Geology, 47(1): 59-62.

Thunell, R.C., Sigman, D.M., Muller-Karger, F., Astor, Y., Varela, R., 2004. Nitrogen isotope dynamics of the Cariaco Basin, Venezuela. Global Biogeochemical Cycles, 18(3): 1-13.

Torres, M.E., Brumsack, H.J., Bohrmann, G., Emeis, K.C., 1996. Barite fronts in continental margin sediments: a new look at barium remobilization in the zone of sulfate reduction and formation of heavy barites in diagenetic fronts. Chemical Geology, 127(1): 125-139.

Tribovillard, N., Algeo, T.J., Lyons, T., Riboulleau, A., 2006. Trace metals as paleoredox and paleoproductivity proxies: An update. Chemical Geology, 232(1-2): 12-32.

Von Breymann, M.T., Emeis, K.-C., Suess, E., 1992. Water depth and diagenetic constraints on the use of barium as a palaeoproductivity indicator. Geological Society, London, Special Publications, 64(1): 273.

Wagner, M., Chappaz, A., Lyons, T.W., 2017. Molybdenum speciation and burial pathway in weakly sulfidic environments: Insights from XAFS. Geochimica et Cosmochimica Acta, 206: 18-29.

Wang, J. et al., 2009. Is the Dipole Anomaly a major driver to record lows in Arctic summer sea ice extent? Geophysical Research Letters, 36(5).

Wang, Y., Hendy, I., Napier, T.J., 2017. Climate and Anthropogenic Controls of Coastal Deoxygenation on Interannual to Centennial Timescales. Geophysical Research Letters, 44(22): 11528–11536.

Wang, Y., Hendy, I.L., Thunell, R., 2019. Local and Remote Forcing of Denitrification in the Northeast Pacific for the Last 2,000 Years. Paleoceanography and Paleoclimatology.

Warrick, J.A., Farnsworth, K.L., 2009. Sources of sediment to the coastal waters of the Southern California Bight. The Geological Society of America Special Paper, 454: 39-52.

Watanabe, T., Wakatsuchi, M., 1998. Formation of 26.8–26.9 σθ water in the Kuril Basin of the Sea of Okhotsk as a possible origin of North Pacific Intermediate Water. Journal of Geophysical Research: Oceans, 103(C2): 2849-2865.

Woodgate, R.A., 2018. Increases in the Pacific inflow to the Arctic from 1990 to 2015, and insights into seasonal trends and driving mechanisms from year-round Bering Strait mooring data. Progress in Oceanography, 160: 124-154.

Wu, B., Wang, J., Walsh, J.E., 2006. Dipole Anomaly in the Winter Arctic Atmosphere and Its Association with Sea Ice Motion. Journal of Climate, 19(2): 210-225.

Yasuda, I., 1997. The origin of the North Pacific Intermediate Water. Journal of Geophysical Research, 102(C1): 893.

You, Y., 2003. The pathway and circulation of North Pacific Intermediate Water. Geophysical Research Letters, 30(24).

You, Y. et al., 2000. Roles of the Okhotsk Sea and Gulf of Alaska in forming the North Pacific Intermediate Water. Journal of Geophysical Research, 105(C2): 3253.

You, Y. et al., 2003. Transport of North Pacific Intermediate Water across Japanese WOCE sections. Journal of Geophysical Research, 108(C6).

Zhang, J., Lindsay, R., Steele, M., Schweiger, A., 2008. What drove the dramatic retreat of arctic sea ice during summer 2007? Geophysical Research Letters, 35(11).

Zhang, R., 2015. Mechanisms for low-frequency variability of summer Arctic sea ice extent. Proc Natl Acad Sci U S A, 112(15): 4570-5.

Zheng, Y., Anderson, R.F., Geen, A.V., James, K., 2000. Authigenic molybdenum formation in marine sediments: A link to pore water sulfide in the Santa Barbara Basin. Geochimica et Cosmochimica Acta, 64(24): 4165-4178.

Chapter 7

Expansion of the Southern California Oxygen Minimum Zone During the Early- to Mid-Holocene Due to Reduced Ventilation of the Northeast Pacific[4]

7.1 Abstract

Oceanic deoxygenation observed since the 1950s has drawn increasing concern as dissolved oxygen (DO) regulates marine biodiversity and biogeochemical cycles. Yet the DO time series from direct instrumental measurements is insufficiently long (several decades) to constrain the centennial to millennial variability. Here we present redox-sensitive metal (Re, U, and Mo) records from Santa Barbara Basin (SBB), California to reconstruct subsurface DO through the Holocene. Significantly higher authigenic metal fluxes and coherent benthic foraminifera faunal responses along a published depth transect reveal vertical expansion and intensification of the Southern California oxygen minimum zone (OMZ) prior to ~6 ka. Comparison with post-Industrial trace metal records suggests low-oxygen conditions were more extreme during early to mid-Holocene (MH), highlighting the magnitude of OMZ variability in the absence of anthropogenic influences.

Inconsistencies between authigenic metal fluxes and local oxygen control indicate a remote weakening of the North Pacific Intermediate Water (NPIW) formation prior to the MH. Reduced ventilation of the mid-depth North Pacific is supported by state-of-the-art Earth system model simulations with realistic MH (6 ka) forcing, highlighting the importance of brine rejection during sea ice formation in changing the buoyancy of NPIW and its basin-wide influences on North Pacific OMZ. Evidence from Holocene marine/lake records and model simulations further suggests a southward Intertropical Convergence Zone (ITCZ) migration and a consequent deepening of the Aleutian Low (AL) towards late Holocene, which favors more sea

[4] Wang, Y., Hendy, I.L., Zhu, J., 2020. Expansion of the Southern California Oxygen Minimum Zone During the Early- to Mid-Holocene Due to Reduced Ventilation of the Northeast Pacific, Quaternary Science Reviews (*accepted)*.

ice brine rejection. Thus, mid-depth ventilation in the North Pacific was closely associated with atmospheric circulation during the Holocene.

7.2 Introduction

Since the 1950s, ocean deoxygenation has been observed in the open ocean and coastal waters via repeated hydrographic measurements (Breitburg et al., 2018; Diaz and Rosenberg, 2008; Keeling et al., 2010; Schmidtko et al., 2017). Oceanic dissolved oxygen (DO) loss can be attributed to either reduction in O_2 supply and/or increase in O_2 consumption. A warming ocean is expected to lower O_2 solubility and increase ocean stratification, reducing DO concentrations in subsurface ocean water (Bopp et al., 2013). Through these processes, the ongoing observed deoxygenation has been attributed to ocean warming in response to anthropogenic greenhouse gas emissions (Breitburg et al., 2018; Stramma et al., 2010). Advection of oxygenated intermediate water masses serves as an important O_2 supply to oxygen minimum zones (OMZs), as DO concentrations directly correspond to rates of subsurface water mass formation and/or water mass modification as subsurface waters circulate around the oceans (Crusius et al., 2004; Lembke-Jene et al., 2017). Between glacial and interglacial climates, intermediate water ventilation could control O_2 concentrations within the North Pacific OMZ (Cartapanis et al., 2011; Ivanochko and Pedersen, 2004; Kennett and Ingram, 1995; Okazaki et al., 2010). During cold climatic intervals (e.g., stadial events during glacial periods), low sea surface temperatures (SST) facilitated brine rejection via sea ice formation and wind-driven mixing in the subarctic Pacific (e.g., the Sea of Okhotsk, the Bering Sea, and the Gulf of Alaska), leading to enhanced intermediate water formation and a better-ventilated North Pacific OMZ (Hendy and Pedersen, 2005; Keigwin, 1998; Kennett and Ingram, 1995; Knudson and Ravelo, 2015). In contrast, during warm climates (e.g., interstadials and the early Holocene), stagnant water columns and reduced sea ice formation weakened intermediate water ventilation in the subarctic Pacific, decreasing DO in the North Pacific OMZ (Lembke-Jene et al., 2018). Simultaneously, enhanced oxygen-depleted intermediate water advection from the tropics during the warm interstadials further reduced mid-depth DO in the Northeast (NE) Pacific (Hendy and Kennett, 2003; Ivanochko and Pedersen, 2004).

O_2 consumption, on the other hand, is dominantly controlled by primary productivity through organic carbon respiration, with low DO corresponding to increased O_2 consumption under high primary productivity. Intensified O_2 consumption near the subsurface water formation

regions can be propagated along the subsurface water circulation path, leading to regionally coherent low-DO conditions. OMZ intensification on the California margin during the Bølling–Allerød – an abrupt warming during the last deglaciation – has been attributed to productivity pulses recorded in the Sea of Okhotsk (Crusius et al., 2004) and throughout the North Pacific (Hendy et al, 2004; Taylor et al, 2017; Chang et al., 2008; McKay et al, 2005). However, the relative contributions of O_2 supply and DO consumption are poorly constrained during the Holocene. Detection of recent OMZ changes using instrumental observations and attribution of solubility and stratification changes to these observations are especially challenging, due to the short duration of records (~60 years). Large glacial-interglacial OMZ changes in the North Pacific imply that there may greater natural variability in DO than in anthropogenically forced responses. If natural DO variability is significant and recurrent, marine biodiversity and biogeochemical cycles may be more robust than previously thought. Alternatively, natural variability may exacerbate the impacts of anthropogenic deoxygenation, placing a greater stress on marine ecosystems than models are predicting. Whether recent anthropogenic deoxygenation is anomalous compared to the entire Holocene should be investigated.

Redox-sensitive metals are often employed as geochemical proxies to reconstruct past DO concentrations because enrichments above the local lithogenic background are directly controlled by redox reactions in the sediments (Calvert and Pedersen, 2007). Here we use authigenic fluxes and enrichments of redox-sensitive metals (Mo, Re, and U) to reconstruct OMZ variability on the California Margin. Re and U have similar redox potentials and are both conservative in oxygenated conditions (as ReO_4^- and $UO_2(CO_3)_2^{2-}$, respectively). Under low DO, Re and U are reduced to form authigenic precipitates (Re(IV) oxides/sulfides and U(IV) precipitates, respectively) and enriched in sediments (Crusius et al., 1996; Tribovillard et al., 2006). As DO is further depleted by oxidant demand, sulfate eventually becomes the favorable electron acceptor in organic carbon remineralization to accumulate free sulfide (HS^-). Authigenic Mo precipitation only proceeds in the presence of free HS^-, such that Mo enrichment indicates a strongly reducing water column (e.g., anoxia) provided with authigenic Re enrichments (Calvert and Pedersen, 2007; Crusius et al., 1996; Tribovillard et al., 2006). Suites of redox-sensitive elements provide more robust reconstructions than single element enrichments as a broader range of oxygenation variation can be assessed.

Here we present a high-resolution (~30 – 80 year resolution) Holocene redox-sensitive trace metal record (MV0811-14JC, 34°16.906'N, 120° 2.162'W, 582 m water depth) from the Santa Barbara Basin (SBB), California, to better constrain natural variability of deoxygenation on centennial to millennial timescales. Low-oxygen bottom waters (~0 – 25 μmol/kg) in the basin suppress mega- and macrofaunal activities, preserving laminated sediments that generate high-resolution paleoceanographic reconstructions. SBB is a semi-closed basin in the Southern California Bight, connecting to the Southern California margin OMZ via a 475-m sill to the west. Bottom waters entering in the basin over the sill during flushing events are either sourced from the low DO waters from the tropics transported via the California Undercurrent (Lynn and Simpson, 1990) or from the uplifted denser and better oxygenated intermediate waters (Bograd, 2002). This new record from the bottom of SBB supplements a Holocene depth transect generated by multiple Southern California cores (ODP Hole 1017E, MV0811-15JC, MD02-2503, MD02-2504, and ODP Hole 893A, Table 7-1) that supports regional coherence of Southern California OMZ variability (Fig. 7-1b). To understand the OMZ variability in our record, we first investigate local export productivity (Br/Cl as a proxy for TOC) to assess O_2 consumption. We next examine the influence of O_2 supply through remote changes in intermediate water mass circulation on mid-depth ocean ventilation using climate simulations with a state-of-the-art Earth system model, the Community Earth System Model 1.2. Model simulations are further compared with Holocene marine/lake records around the Pacific to investigate potential physical causes of changes in intermediate water ventilation.

Table 7-1 Core locations for the Southern California depth transect

Core name	Coordinates	Water depth (m)	References
MV0811-15JC	34°22.2'N, 120°7.8'W	418	Moffitt et al. (2015)
MD02-2504	34°13.998'N, 119°52.08'W	481	Ohkushi et al. (2013)
MD02-2503	34°17.172'N; 120°2.19'W	569	Ohkushi et al. (2013)
ODP Hole 893A	34°17.25'N, 120°2.2'W	575	Behl (1995)
MV0811-14JC	34°16.906'N, 120°2.162'W	582	This study
SPR0901-04BC	34°16.895'N, 120°2.489'W	588	Wang et al. (2017)
ODP Hole 1017E	34°32.10'N, 121°6.43'W	955	Hendy and Pedersen (2005)

7.3 Background

The mid-depth northeast Pacific is dominated by two intermediate water masses (Fig. 7-1a): the more oxygenated North Pacific Intermediate Water (NPIW) from the west subarctic Pacific and the Gulf of Alaska (Talley, 1993; You, 2003; You et al., 2000), and the low-oxygen Equatorial Pacific Intermediate Water (EqPIW) transported via the California Undercurrent.

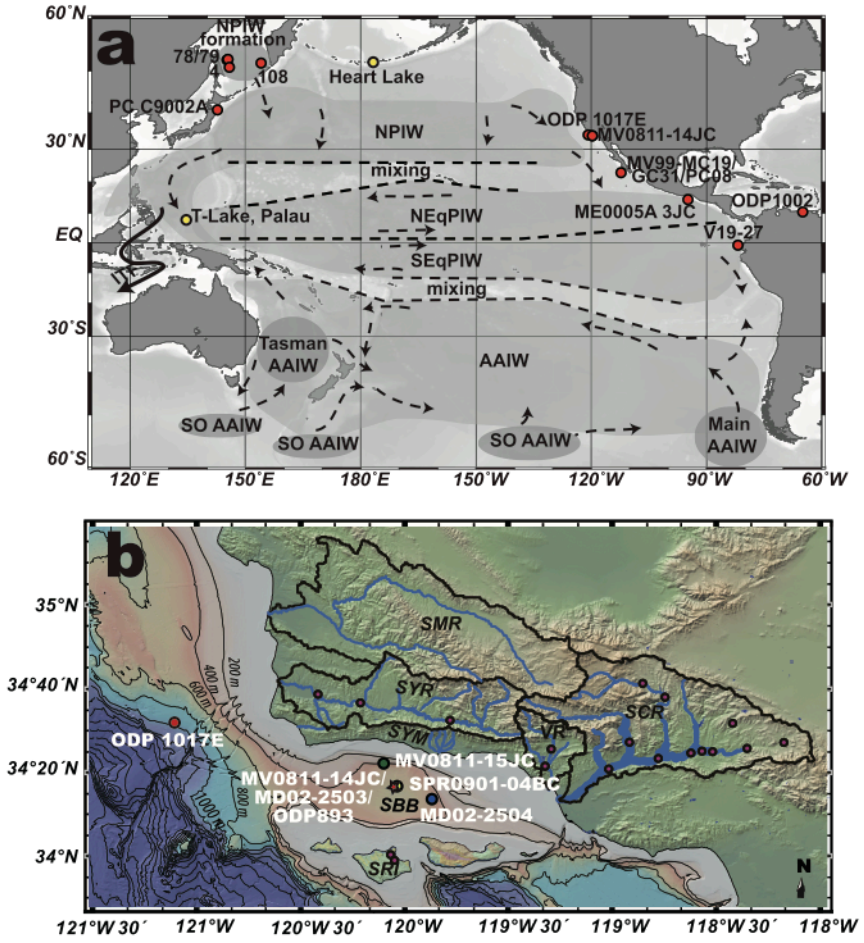

Figure 7-1 Map showing major ocean circulation and relevant paleoclimate records. a) Marine and lake records are shown in red and yellow dots, respectively. Intermediate water masses (light gray shading), formation regions (dark gray shading), water mass boundaries (dashed lines), and possible mixing paths (dashed arrows) are adapted from Bostock et al. (2010); Bostock et al. (2013); and Talley (2008). NPIW: North Pacific Intermediate Water; NEqPIW: North Equatorial Intermediate Water; SEqPIW: South Equatorial Intermediate Water; AAIW: Antarctica Intermediate Water; SO AAIW: Southern Ocean AAIW; ITF: Indonesian Throughflow. b) Map of core locations on the Southern California margin modified from Napier et al. (2019). Rivers are indicated by blue lines and their catchments are outlined with black solid lines, respectively. The red circle denotes the location of the continental slope site (ODP Hole 1017E), and the red star represents the locations of MV0811-14JC, MD02-2503, and ODP Hole 893 (basin bottom sites). SPR0901-04BC, MD02-2504 (sill depth site), and MV0811-15JC (sill depth site) are shown in yellow, blue, and green circles, respectively. SMR: Santa Maria River, SCR: Santa Clara River, VR: Ventura River, SYM: Santa Ynez Mountain, and SRI: Santa Rose Island. The map is generated using GeoMapApp (http://www.geomapapp.org).

7.3.1 North Pacific Intermediate Water (NPIW)

NPIW is currently the densest water mass formed in the North Pacific (Shcherbina et al., 2003), confined by a potential density (σ_θ) from 26.7 – 26.9 kg m^{-3} (corresponding to 300 – 800 m) (Reid, 1965; You, 2003). NPIW can be traced by a salinity minimum (34.0 – 34.3) across the North Pacific that is developed from the Mixed Water Region between the Kuroshio Extension and the Oyashio Fronts (Miyao and Ishikawa, 2003; Talley, 1993; Yasuda, 1997; You, 2003). Here, subarctic Oyashio waters merge with subtropical Kuroshio Extension to generate the

newly formed NPIW, which then flow eastwards across the Pacific Basin (Talley, 1993; Yasuda, 1997). Modern NPIW rarely outcrops in the open North Pacific (Talley, 1993), and thus direct ventilation of current NPIW only occurs in its source regions such as formation of the Okhotsk Sea Intermediate Water (OSIW) (Shcherbina et al., 2004a; Shcherbina et al., 2004b; Talley, 1993; Watanabe and Wakatsuchi, 1998). During glacial climates, however, radiolarian and foraminifera geochemistry evidence suggest that the NPIW could have sourced from the Bering Sea instead of the Sea of Okhotsk (Cook et al., 2005; Kim et al., 2011; Knudson and Ravelo, 2015; Ohkushi et al., 2003). Since the establishment of Holocene subsurface circulation in the North Pacific (9 ka to present), the Sea of Okhotsk has remained the dominant NPIW ventilation source (Ohkushi et al., 2003). The Gulf of Alaska may be an additional NPIW ventilation source, as subpolar water is advected into the subsurface eastern subtropical gyre in winter through the formation of Gulf of Alaska Intermediate Water (GAIW) (You et al., 2000). The GAIW contribution, however, is minor (~10%) compared to OSIW and confined to upper NPIW (You et al., 2000; You et al., 2003).

As the major contributor to NPIW, OSIW has a similar density range (σ_θ = 26.75 – 27.05 kg m^{-3}) and water properties (fresh and oxygenated) as NPIW (Itoh, 2003; Talley, 1993; Watanabe and Wakatsuchi, 1998). OSIW is a mixture of the Dense Shelf Water (DSW) from the Sea of Okhotsk, Western Subarctic Pacific Water (WSAP), and Soya Warm Current (SWC) from the Japan Sea with a mixing ration of ~1:1:0.1 (Itoh, 2003; Yamamoto et al., 2001). The DSW is a cold (<–1°C) and well-oxygenated water mass formed from intense brine rejection during winter sea ice formation in the northern and northwestern coastal polynyas (Itoh, 2003). Formed in the Japan Sea, warm (>6°C) and saline SWC is also oxygen-rich and yet is considered of minor importance for modern OSIW due to its small volume transport compared to DSW and WSAP (Itoh, 2003). WSAP is a warm and saline water mass that mixes with newly formed DSW prior to the OSIW export to Pacific, which flows from the North Pacific into the Sea of Okhotsk (Itoh, 2003).

7.3.2 Equatorial Pacific Intermediate Water (EqPIW)

In the western equatorial Pacific, EqPIW forms from mixing between extensively modified AAIW and upwelled Pacific Deep Water (Bostock et al., 2010). Although AAIW is a distinct oxygen-rich and low-salinity intermediate water mass centered at 27.1 σ_θ (600 – 1300 m, Dickson et al. (2001); Tsuchiya and Talley (1996)), it does not retain these water mass

characteristics after mixing occurs during advection through equatorial circulation. During transport towards the eastern equatorial Pacific (EEP) in the Equatorial Undercurrent, DO is further consumed by high primary productivity under the extensive equatorial upwelling driven by the trade winds (Deustch et al., 2014). As a major ventilation source in the intermediate depth of the Southern Pacific, AAIW plays an important role in the thermohaline circulation (Talley, 2008) and currently stores considerable amounts of CO_2 as a carbon reservoir (Sabine et al., 2004). AAIW primarily forms in the southeast Pacific (Shcherbina et al., 2004a; Tsuchiya and Talley, 1996) and is circulated around the wind-driven subtropical gyre towards the west equatorial Pacific (Bostock et al., 2010; Bostock et al., 2013; Zenk et al., 2005). For Southern California sites in the NE Pacific, direct influences from AAIW are unlikely; Instead, AAIW may indirectly impact NE Pacific intermediate waters through modifying EqPIW. For instance, studies have suggested increasing less-ventilated AAIW influences to EEP during the Last Glacial Maximum may have reduced the EqPIW oxygenation (Bostock et al., 2004; Bostock et al., 2010; Pena et al., 2013).

7.4 Methods

7.4.1 Age Model

The published age model for MV0811-14JC (Du et al., 2018b) is summarized as follows. The age-depth model was generated from 50 mixed planktonic foraminifera ^{14}C ages using the software BACON 2.2 (Blaauw and Christen, 2011). ^{14}C ages were converted to calendar ages using the Marine13 calibration curve (Reimer et al., 2013) with a constant ΔR (regional reservoir age – global mixed-layer ocean reservoir age) of 147 ± 70 yrs (Hendy et al., 2013). Mass accumulation rates (MAR, g cm^{-2} kyr^{-1}) were calculated every 5 cm from the age model generated by BACON 2.2 using the Eq. 7-1:

$$MAR = SR \times (1 - \phi) \times \rho \qquad \text{(Eq. 7-1)}$$

where SR, ϕ, and ρ denote sedimentation rates calculated every 5-cm from the age model, sediment fractional porosity, and gamma density drawn from the Multi-sensor Track measurements, respectively.

7.4.2 Redox-sensitive metal fluxes and enrichment factors

MV0811-14JC (34°16.906'N, 120°2.162'W, 582 m water depth) was scanned at 200-μm resolution on an ITRAX X-ray fluorescence (XRF) core scanner (Cox Analytical Instruments) at

the Large Lakes Observatory, University of Minnesota, Duluth. The scanner is equipped with a Cr X-ray tube to yield higher sensitivity for lighter elements (Croudace et al., 2006), and operated with an 8-second scan time at 30 kV and 15 mA (Hendy et al., 2015).

Discrete 1.5-cm samples from MV0811-14JC were obtained at 5 – 10 cm intervals (~50 – 100 yrs), and were freeze-dried and ground for geochemical analyses at ALS Laboratories in Vancouver, Canada. The bulk samples were digested using a nitric, perchloric, hydrofluoric, and hydrochloric acid cocktail, followed by quantitative analyses of major, minor, and trace elements with inductively coupled plasma (ICP)-mass spectrometry and ICP-atomic emission spectroscopy (ICP-AES). Duplicated lab standard measurements (GBM908-10 and MRGeo08) agree within 5%.

Trace metal data are presented as enrichment factors ($Metal_{EF}$) (Eq. 7-2) and authigenic particulate fluxes (Eq. 7-3), using the lithogenic background from Wang et al. (2017):

$$Metal_{EF} = \frac{(\frac{Metal}{Al})_{sample}}{(\frac{Metal}{Al})_{background}} \qquad \text{(Eq. 7-2)}$$

$$Metal_{auth}fluxes = [Metal_{sample} - \left(\frac{Metal}{Al}\right)_{background} \times Al_{sample}] \times MAR \qquad \text{(Eq. 7-3)}$$

Trace metal diffusive fluxes into sediments are calculated as well to account for sedimentation rate effects on trace metal diffusion and subsequent *in situ* precipitation. Diffusion fluxes are derived from the Fick's Law (Eq. 7-4):

$$F = \phi D_{sed} \frac{\partial [M]}{\partial z} \qquad \text{(Eq. 7-4)}$$

To separate sedimentation rate influences from oxygenation changes, bottom water oxygenation (porewater trace metal concentrations [M]) was kept constant and the diffusion depth (z) varied according to the sedimentation rate changes. This assumption potentially underestimates real diffusion fluxes under more reducing conditions but disentangles impacts of sedimentation rate changes from oxygenation variability. As no porewater measurements are available for this core, previously published porewater profiles of Mo and U were used (Zheng, 1999). The top 2.27 cm and 2.62 cm are chosen respectively (sharpest reduction of Mo and U concentrations near the sediment-water interface) to calculate U and Mo porewater concentration gradients, and the diffusion depths are adjusted accordingly following the porosity (ϕ) at

different depths. Only diffusive fluxes of U and Mo are estimated, as no porewater Re profiles are available in SBB; however, the overall variability should be similar given the assumption of constant bottom water oxygenation. The diffusion coefficient in sediments (D_{sed}) can be estimated from the known diffusion coefficient in seawater (D_{sw}) after correcting the sediment tortuosity (θ^2) from the Eq. 7-5):

$$D_{sed} = \frac{D_{sw}}{\theta^2} \qquad \text{(Eq. 7-5)}$$

The tortuosity values can be estimated from sediment porosity using the following equation (Boudreau, 1997):

$$\theta^2 = 1 - \ln(\phi^2) \qquad \text{(Eq. 7-6)}$$

D_{sw} (at 25°C) of MoO_4^- (9.91×10^{-6} cm^2/s at 25°C) and $UO_2(CO_3)_2^{2-}$ (5.52×10^{-6} cm^2/s at 25 °C) are drawn from Li and Gregory (1974) and Kerisit and Liu (2010), respectively, and have been corrected for dynamic viscosity change at the *in situ* temperature (6 °C) using the Stokes-Einstein Equation described in Li and Gregory (1974). Instantaneous depositional events (turbidites and flood layers) are excluded from data analyses as they do not represent background sedimentation processes (Hendy et al., 2013).

Trace metal data from the ODP Hole 1017E (955 m water depth, Table 7-1) (Hendy and Pedersen, 2005) are reinterpreted as enrichment factors by normalizing to Al concentrations (Tada et al., 2000) and employing a lithogenic background that reflects the river catchments releasing sediment to the site. Located off the Point Conception, ODP site 1017 is dominated by siliciclastic sediments from the Santa Ynez River and the Santa Maria River (Behl et al., 2000). The Santa Ynez and the Santa Maria River account for 65% and 32% of suspended sediment fluxes, respectively; while there is a minor contribution from the Big Sur (Slagel and Griggs, 2008). The elemental composition of Santa Maria River sediments should be similar to the Santa Ynez River sediments due to the similar sedimentary rock units in the catchment (Ludington et al., 2007; Napier et al., 2019). Hence, trace element concentrations from silt-size sediments from three Santa Ynez River catchment samples (Fig. 7-1b) are normalized to Al and averaged to obtain a site-specific lithogenic background (Table D-1) for the ODP Hole 1017E.

Turning points detect when the shift in the mean value of $Metal_{EF}$ is the most significant. This method first treats each datum as a division point that splits the record into two sections. Mean values and deviations from the mean of the two sections are then computed to obtain the

total residual error, and the turning point is determined from the minimum residual in the record (Killick et al., 2012).

7.4.3 Model and experiments

Two simulations were conducted using the Community Earth System Model (CESM) version 1.2 (Hurrell et al., 2013): a preindustrial (PI) and a mid-Holocene (MH). The PI simulation employed a set of boundary conditions from 1850 CE. The MH simulation followed the Paleoclimate Modeling Intercomparison Project (PMIP4) protocol, with altered orbital parameters, greenhouse gas concentrations, and vegetation cover at 6 ka (Otto-Bliesner et al., 2017). Both the PI and MH simulations were run at a horizontal resolution of 1.9 × 2.5° (latitude × longitude) for the atmosphere and land, and a nominal 1° grid for ocean and ice. The simulations were integrated for > 1000 model years for the middle and upper ocean to reach quasi-equilibrium with < 0.01 °C and 0.001 g kg^{-1} change in North Pacific temperature and salinity at the intermediate depth (~ 650 m) for the last 100 years, respectively. The NPIW formation change was identified in the model by calculating the surface density flux (buoyancy forcing) that measures the seawater buoyancy loss/gain associated with freshwater, heat, or salt fluxes with the atmosphere or sea ice (Schmitt et al., 1989). To quantitatively compare the contribution from different processes, the density flux is decomposed into a thermal (heat gain/loss) and a haline component, the latter of which is further separated into precipitation related (evaporation, precipitation, and river runoff) and sea-ice related contributions (freshwater flux from sea ice melting and salt flux from brine rejection).

7.5 Results

7.5.1 Geochemical measurements

Re and U are continuously enriched throughout the Holocene in MV0811-14JC with positive authigenic fluxes (Table D-2). Re_{EF} varies between 1.75 and 8.05 with an average of 3.41, whereas U_{EF} ranges in 1.76 – 4.37 with a mean value of 2.73. Re_{auth} and U_{auth} fluxes show similar variations, with overall higher fluxes prior to ~6 ka (1.7 for Re and 696 cm^{-2} kyr^{-1} for U, respectively) but significantly lower fluxes after the turning point (5.8 ka for Re and 5.4 ka for U) to 0.9 and 405 μg cm^{-2} kyr^{-1}, respectively (Fig. 7-2, Table D-2). Prior to 6 ka, local maxima of authigenic Re occur at 5.9, 7.6, and 8.1 ka, coeval with authigenic U peaks. Authigenic Mo oscillates between depletion and enrichment, and yet a similar transition to low fluxes is still

apparent at 6.1 ka (952 μg cm^{-2} kyr^{-1} prior to the transition vs. 363 μg cm^{-2} kyr^{-1}). Several Mo_{auth} flux local maxima occur at 6.4, 7.4, 8.1, 8.6, and 9 ka with an interval of relatively low enrichments between ~4.1 and 5.1 ka.

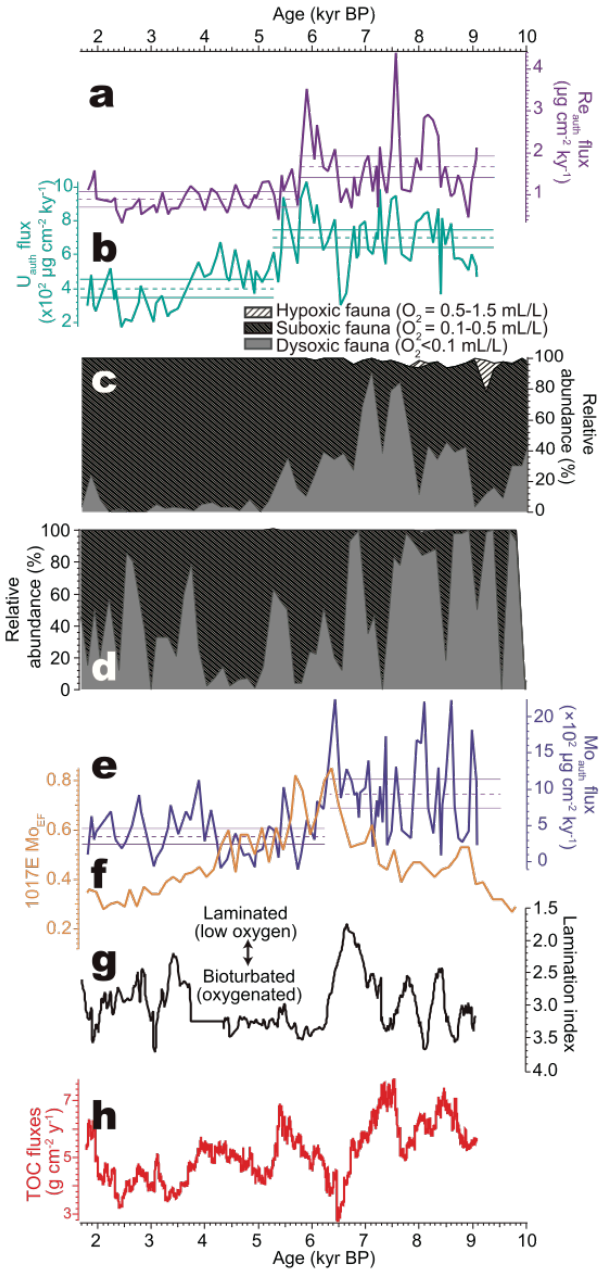

Figure 7-2 Redox conditions on the Southern California margin transect. (a) Authigenic Re (purple line) and (b) U fluxes (green line). Horizontal dashed and solid lines represent the average and 95% confidence intervals. Relative abundance of hypoxic, suboxic, and dysoxic fauna of (c) core MD02-2504 (SBB sill depth site, 481 m water depth) and (d) MD02-2503 (deep SBB site, 569 m water depth) (Ohkushi et al., 2013). (e) Authigenic Mo fluxes from MV0811-14JC (blue line). Horizontal dashed and solid lines represent the average and 95% confidence intervals for the authigenic Mo fluxes. (f) Mo enrichment factors from ODP Hole 1017E (maize line). (g) ODP Hole 893 bioturbation index, where 4 represents bioturbated sediments and 1 represents finely laminated sediments (Behl, 1995). (h) TOC fluxes of MV0811-14JC (red line) calculated from scanning XRF Br/Cl, assuming the linear relationship between TOC and Br/Cl (see Figure S2; Wang et al. (2019)).

Mo_{EF} values in MV0811-14JC, however, oscillate between 0.83 (depletion, 5.72 ka) and 5.92 (enrichment) with an average of 2.13. Re_{EF} shows similar enrichment patterns as Mo_{EF} but with a broader peak during ~6 ka (Figs. 7-4 and D-1). However, higher U_{EF} is sustained before 5.8 ka, after which U_{EF} reveals a persistent decline with a minimum at the core top of 1.8 ka (Figs. 7-4 and D-1, Table D-2).

Mo and U diffusive fluxes range in 37.8 – 344.2 and 5.7 – 51.9 μg cm^{-2} kyr^{-1}, respectively. Mo and U diffusive fluxes were relatively low prior to ~7.0 ka, with maximum fluxes occurring at ~6.5 ka, coincident with the lowest mass accumulation rates (MARs) in the Holocene (Fig. 7-5). Two other localized diffusive flux maxima were recorded at ~5 and ~2.5 ka.

Recalculated published trace metal enrichment factors from the ODP Hole 1017E (Hendy and Pedersen, 2005) show that Re was continuously enriched through the Holocene with enrichment factors of 3.89 to 10.64. U_{EF} oscillates between 0.66 and 1.57 with a mean value of 1.13. Mo, however, is continuously depleted in the core (enrichment factor of 0.23 to 0.85) with a broad Mo_{EF} peak at ~6 ka. U and Re both show low enrichments between ~7.1 and 9.5 ka, while after a turning point at 7.1 ka, Re_{EF} (7.53 after ~7.1 ka vs. 6.34 in the prior interval) and U_{EF} (1.16 after ~7.1 ka vs. 1.04 in the prior interval) oscillate around higher values (Table D-3).

Scanning XRF bromine to chloride ratio (Br/Cl) can be used as a proxy for export productivity, as Br delivered to sediments is associated with marine organic carbon and normalization to Cl accounts for brine salt effects (Ziegler et al., 2008). Although scanning XRF results are considered as semi-quantitative, a statistically significant linear relationship between Br/Cl and total organic carbon (TOC) has been validated from a nearby SBB core (Wang et al., 2019). Organic carbon fluxes are then calculated from scanning XRF Br/Cl and MAR to account for organic carbon dilution by lithogenic components that account for ~70 – 80% of the sediment deposition in SBB (Thunell et al., 1995). TOC flux primarily follows MAR variability with relatively high values before 7 ka but a sharp decline at ~7.3 ka. Despite the highest Br/Cl (export productivity) during 6 – 6.5 ka, TOC MAR indicates the lowest accumulation rates within the core MV0811-14JC (Fig. D-2), indicating the minimum TOC fluxes to the basin sediments at ~6 ka. After a recovery at ~5.4 ka, TOC fluxes remained low between 5 and 2 ka. TOC flux increased after ~2 ka again corresponding to MAR shifts (Fig. D-2).

7.5.2 Reduced MH surface density flux and NPIW ventilation in the model

We chose a broad region of 50 – 65°N and 135 – 170°E to quantify spatially averaged buoyancy forcing in the MH and PI simulations (Fig. 7-3a). The region covers the Sea of Okhotsk and the densest surface water (σ_θ = 26.0 – 26.4 kg m^{-3}) that is likely to sink and form intermediate water masses in the model. We focus on winter months (DJF) in the simulations to diagnose the degree of buoyancy forcing from individual heat and freshwater flux components during changes in NPIW ventilation. Following previous studies (England, 1995; Hall et al., 2007), we use the ideal age in the ocean model to examine the strength of NPIW ventilation, which indicates time elapsed since last contact with the surface ocean. Annual mean ideal age is obtained at a depth of 650 m, which corresponds roughly to an isopycnal-surface of σ_θ = 26.8 kg/m^3, a density surface of core NPIW in South California in the model (Fig. 7-3a). Isopycnal propagation of NPIW across the North Pacific basin following σ_θ = 26.8 kg/m^3 has also been observed from chloroflurocarbon (CFC) concentrations (van Geen et al., 2006).

In the PI simulation, averaged winter buoyancy loss (density increase) in the Sea of Okhotsk region (50 – 65°N, 135 – 170°E) is dominated by the thermal component of heat loss to the atmosphere (Fig. 7-3b), whereas the haline component (freshwater and salt fluxes) plays a secondary role and is only significant along the northern and northwestern margin of the Sea of Okhotsk under the sea ice (Figs. D-3 and D-4). In the MH simulation, sea surface buoyancy increases (density decreases) by ~10%, as a result of the MH climate forcing. ~80% of the MH buoyancy increase can be attributed to the haline component of freshwater flux and brine rejection, with heat flux related processes playing a minor role (Fig. 7-3b). Further calculations suggest that ~60% of the haline buoyancy gain is through the reduction of brine rejection, while the remainder is associated with net precipitation increases (precipitation + river runoff – evaporation). Reduced surface density fluxes are consistent with weakened NPIW ventilation in the simulations, indicated by older ideal ages in the MH simulation (~150 yrs older off Southern California at 650 m depth than in PI, Fig. 7-3c).

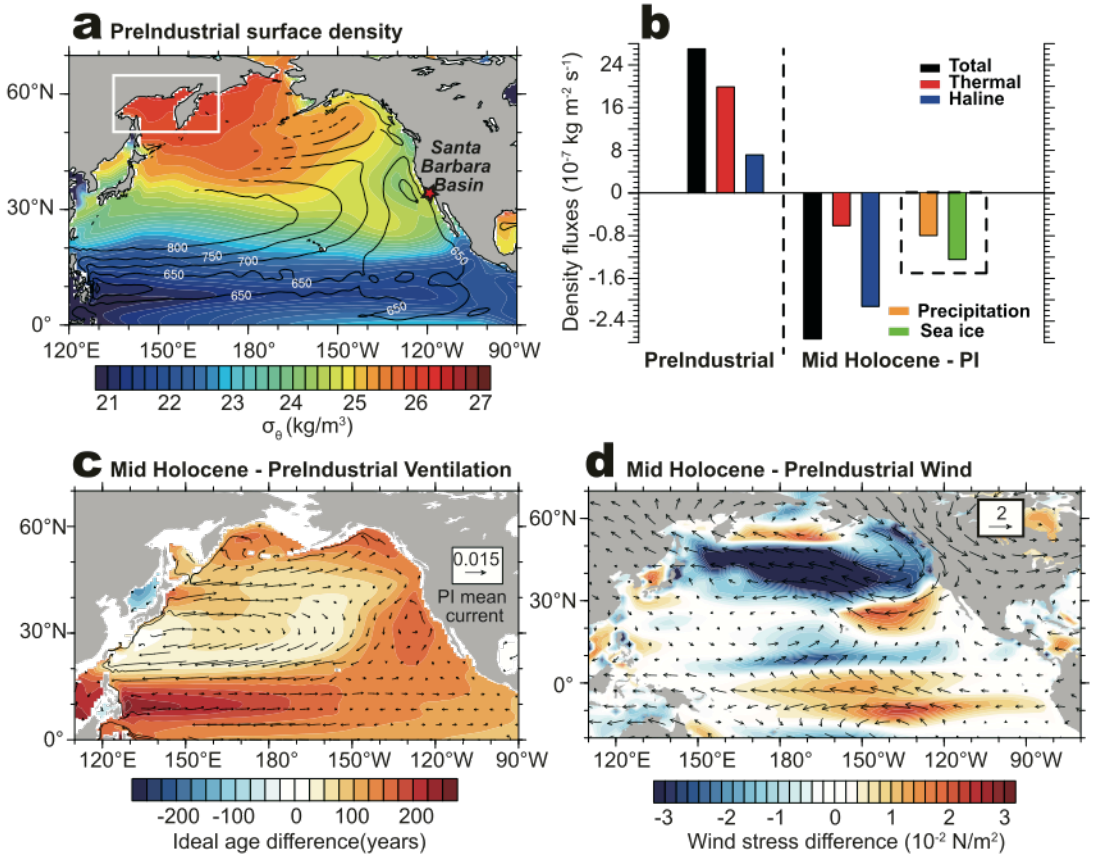

Figure 7-3 Model simulation results. (a) Surface potential density (σ_θ) is shaded in color contours with overlying contours denoting the water depth of σ_θ = 26.8 kg/m^3. Density fluxes are calculated within the white rectangle, while the Santa Barbara Basin is identified by the red star. (b) Surface density flux and its thermal and haline flux components for the pre-Industrial (PI) and mid-Holocene minus PI (MH-PI). Total, thermal, and haline density fluxes are denoted by black, red, and blue bars, respectively. Haline density fluxes can be further decomposed into precipitation and sea ice related processes shown by the orange and green bars, respectively. (c) Ideal age difference between the MH and PI in shaded contours indicating intermediate water ventilation changes, overlain by current vectors at 650 m water depth. (d) Surface wind stress difference between the MH and PI with the overlying 850 hPa wind showing a weakening of the westerlies and strengthening of easterly winds in the northwest Pacific.

7.6 Discussion

7.6.1 Dilution and sedimentation rate effects on trace metal accumulation

Authigenic redox-sensitive metal fluxes and enrichment factors are extensively used as proxies for oxygenation in ambient sedimentary environments (Calvert and Pedersen, 1993; Nameroff et al., 2004; Tribovillard et al., 2006). In addition to the changing redox conditions, trace metal precipitation is also impacted by sedimentation rate changes that may alter bottom water diffusion fluxes and relative sediment compositions (e.g., terrestrial versus biogenic input). Assuming steady-state diagenesis, redox-sensitive metal fluxes are controlled by both diffusion across the sediment-water interface, and irrigation due to physical or biological processes (e.g., irrigated burrows) (Morford et al., 2012; Morford et al., 2009). Irrigation augments diffusive

fluxes by transporting metals in the bottom waters to porewaters, and/or remobilizes accumulated solid-phase metals by introducing more oxygenated waters to porewaters (Aller, 1980; Crusius and Thomson, 2003; Morford et al., 2012). Yet in the SBB sulfidic porewaters, irrigation is of minor importance. Laminated sediments indicate the absence of burrowing fauna, while the observed declining/stable porewater U and Mo concentrations downcore exclude metal addition or remobilization during basin flushing (Zheng et al., 2000; Zheng et al., 2002). Diffusion is thus suggested as the likely primary control of authigenic metal fluxes in SBB sediments.

Based on the Fick's Law (Eq. 7-4), diffusive fluxes depend on porosity and metal concentration gradients (∂[M]/∂z). An assumption of constant bottom water DO concentrations and invariant porewater metal concentrations (∂[M]) is not realistic given the observed variability of bottom water oxygen (Bograd, 2002), but this assumption is needed to separate sediment MAR changes (via changing ∂z) from redox oscillations as the driver of diffusive fluxes and thus authigenic metal fluxes. Low sedimentation rates are expected to reduce MAR following the Equation 1, whereas the metal concentration gradient (∂[M]/∂z) would increase due to decreased ∂z in a given time interval. Thus, by comparing the observed authigenic fluxes with the calculated diffusive fluxes under invariant redox conditions, the impacts of MAR variability on metal precipitation can be evaluated (Fig. 7-5). Coeval peaks of diffusive and authigenic Mo fluxes at ~ 6.5 ka (Fig. 7-5a) indicate that authigenic Mo flux variability could in part be attributed to much lower sediment MAR during this interval. However, there is no coherence between Mo or U authigenic and diffusive fluxes during the early Holocene. Similarly, during the late Holocene, local maxima of calculated Mo and U diffusive fluxes coincide with low authigenic fluxes of both metals (Fig. 7-5). Thus, the sedimentation rate and porosity changes alone are insufficient to generate observed authigenic flux variability (Fig. 7-5b), indicating the role of other processes (e.g., redox condition changes) in producing the observed authigenic metal fluxes.

Changes in the relative contribution of silicilastic input (assessed using bulk sediment Al concentrations) can affect metal enrichments through dilution. Siliciclastic sediments are the dominant contributor (>75%, Thunell (1998)) to basin sediments and therefore drive sedimentation rates. Under low sedimentation rates, decreased siliciclastic Al input would increase the $Metal_{EF}$ ratio under constant bottom water redox conditions (Eq. 7-2), as is observed

by the correspondence between $Metal_{EF}$ peaks and the lowest MAR at ~5.5 – 7.0 ka (Fig. D-1 and Table D-2). Despite the non-linear responses of $Metal_{EF}$ to dilution caused by sedimentation rate shifts, $Metal_{EF}$ and authigenic metal fluxes are still well correlated ($r^2 > 0.8$ for Re and Mo, and $r^2 > 0.6$ for U, $p < 0.01$), suggesting an overall sedimentary redox control on metal enrichments that are ultimately driven by bottom water oxygen concentrations.

7.6.2 The Early to Mid-Holocene Southern California Benthic Environment

Multiple lines of evidence from the bioturbation index (Behl, 1995), microfauna responses (Moffitt et al., 2014; Ohkushi et al., 2003), and geochemical redox proxies suggest that the benthic environment on the Southern California margin OMZ weakened after the mid Holocene (MH). Prior to ~6 ka, significantly higher and more variable authigenic trace metal fluxes are observed from the SBB (Fig. 7-2), suggesting an intensified OMZ in the basin compared to the late Holocene. The highest metal fluxes during this interval generally correspond to the best preserved laminations (low bioturbation index, Fig. 7-2) in the nearby ODP Hole 893A (Fig. 7-1b and Table 7-1) (e.g., 8.3, 7.7, and 6.6 ka, Fig. 7-2f), which supports the exclusion of benthic macrofauna by a low-oxygen environment prior to ~6 ka. Benthic microfauna were also impacted, as dysoxic (dissolved oxygen < 0.1 mL/L or ~4.5 μmol/kg) benthic foraminifera species generally dominate this time interval (despite millennial oscillations) in the nearby core MD02-2503 (569 m water depth, Table 7-1, and Fig. 7-3d) (Ohkushi et al., 2013). Greater dysoxic (O_2 < 0.1 mL/L or ~4.5 μmol/kg) faunal abundance in MD02-2503 is broadly consistent with enhanced authigenic Mo fluxes in MV0811-14JC despite age model differences (Fig. 7-2d). Millennial scale variability continued through the late Holocene when laminated intervals at ~2.7 and 3.4 ka were generally coeval with a return of dysoxic fauna and local maxima of Mo_{auth} fluxes. However, the much lower authigenic Mo flux values after 6 ka indicate a more oxygenated benthic environment compared to the early to mid-Holocene extremes. Higher redox-sensitive trace metal fluxes and dominance of dysoxic fauna are also consistent with the presence of denitrified subsurface water in SBB suggested by higher sedimentary $\delta^{15}N$ values prior to ~7.5 ka at ODP Hole 893A (Emmer and Thunell, 2000).

To evaluate the magnitude of OMZ intensification in the early to mid-Holocene relative to post-Industrial Revolution changes in SBB, the modern OMZ context is assessed using a ~250 year benthic environment reconstruction from a nearby box core (SPR0901-04BC, Fig. 7-1b and Table 7-1) (Wang et al., 2017). Post-Industrial deoxygenation (~1870 – 2007) is indicated by

increasing Mo_{EF} (average of 1.99 ± 0.09 [1 standard error, SE]), Re_{EF} (average of 3.06 ± 0.09 [1SE]), and U_{EF} (average of 2.13 ± 0.02 [1SE]). The early- to mid-Holocene sedimentary $Metal_{EF}$ in MV0811-14JC (e.g., Mo_{EF} of ~2.5 prior to 6 ka) are significantly higher (Fig. 7-4) than the post-Industrial values. Instead, the high SBB metal enrichments during the early- to mid-Holocene argues for a much larger magnitude of OMZ variability than has yet been observed in modern instrumental records.

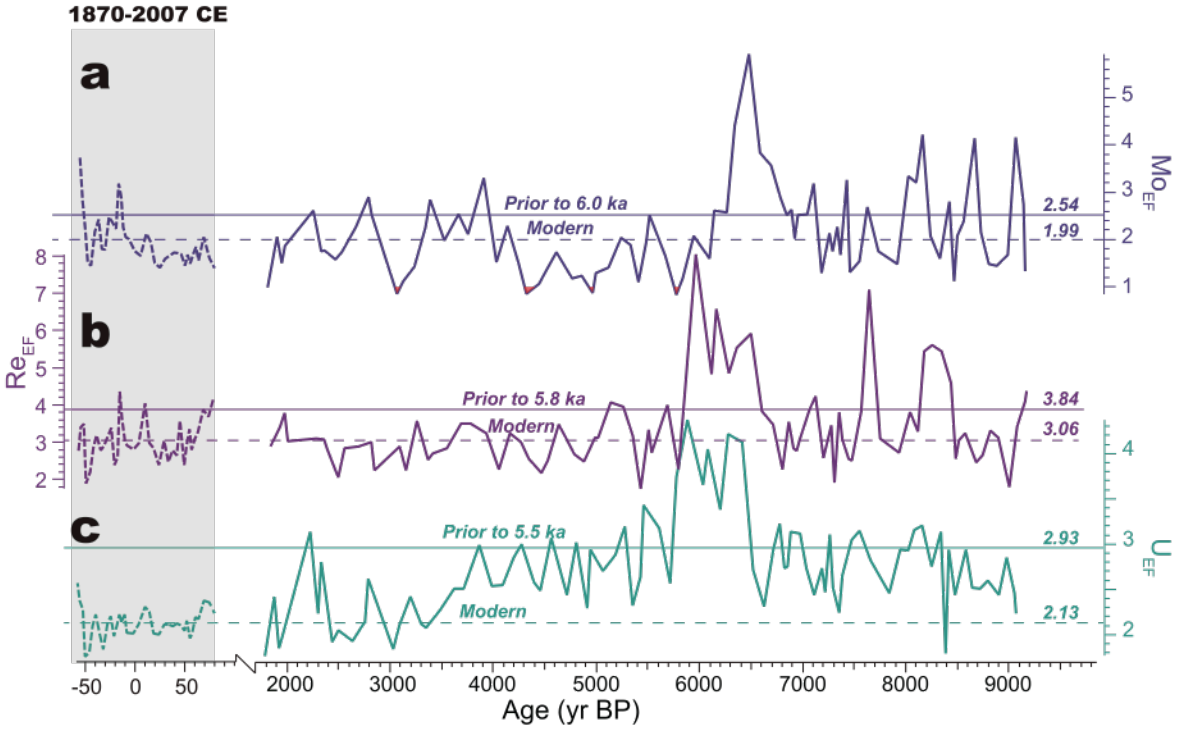

Figure 7-4 Metal enrichment factors and modern comparison. Metal enrichment factors ($Metal_{EF}$) of MV0811-14JC (solid line) compared with the 20th century (SPR0901-04BC, dashed line) shaded in gray in the Santa Barbara Basin (Wang et al., 2017). (a) Mo_{EF} (blue), (b) Re_{EF} (purple), and (c) U_{EF} (teal) records relative to the mean value prior to the respective metal turning point labeled on the figure (horizontal solid line) and after the Industrial Revolution ('Modern', 1870 – 2007 CE, horizontal dashed line). Depleted Mo enrichment factor values (Mo_{EF} < 1) are shaded in red.

Vertical expansion of the Southern California OMZ is observed in benthic assemblages in multiple Southern California archives, in addition to the OMZ intensification suggested by the deepest sited SBB cores prior to 6 ka. A comparison of the published SBB depth transect sites (MV0811-15JC, MD02-2504, MD02-2503, and ODP Hole 893A, Table 7-1, Fig. 7-1b) (Moffitt et al., 2014) with redox-sensitive trace metal records from MV0811-14JC and ODP Hole 1017E (Fig. 7-1b) indicates coherent OMZ responses to DO changes. The deepest SBB sited cores (ODP Hole 893A, MV0811-14JC, and MD02-2503) are located within the core of Southern California OMZ (Fig. 7-1b), but their response to OMZ variability is amplified by the

relationship between high overlying export productivity and the basin flushing events. These sites are connected to the open ocean Southern California OMZ during the 'flushing events', wherein dense and oxygenated intermediate waters enter the basin via the western sill and replenish depleted DO in the deep basin (Reimers et al., 1990). In contrast, the two shallow sites including MV0811-15JC (34°22.2'N, 120°7.8'W; 418 m water depth) and MD02-2504 (34°13.998'N, 119°52.08'W; 481 m) are located above/close to the SBB sill depth of 475 m. These sites intersect with the upper boundary of Southern California OMZ and are unaffected by flushing events. The deeper site (ODP Hole 1017E, 955 m, Table 7-1 and Fig. 7-1b) is located on the continental slope outside of the basin and intersects the lower boundary of the Southern California OMZ (Hendy and Pedersen, 2005).

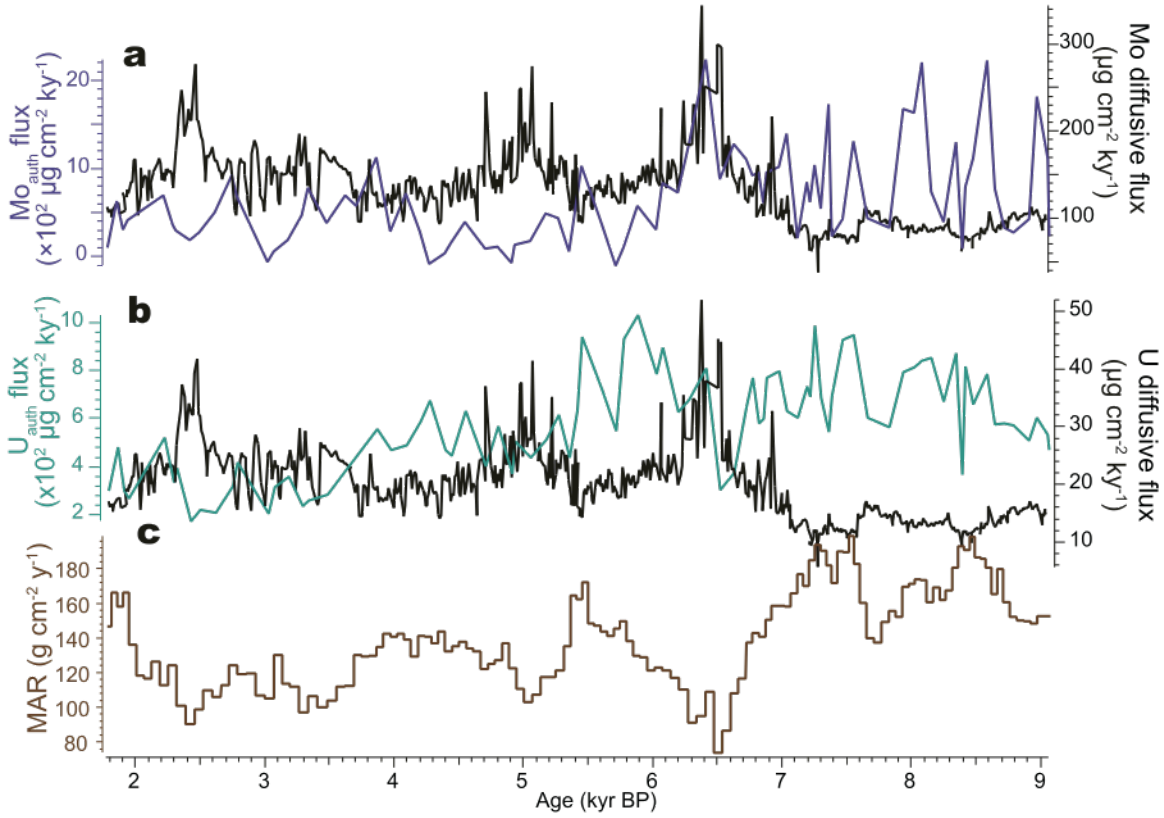

Figure 7-5 Authigenic and diffusive metal fluxes. Comparison between (a) Mo authigenic (purple line) and diffusive fluxes (black line) (b) U authigenic (teal line) and diffusive fluxes (black line); and (c) sediment mass accumulation rates (brown line) in the Santa Barbara Basin (Du et al., 2018b).

Throughout the Holocene, the sill-depth site (MD02-2504, Table 7-1) was generally better oxygenated than the basin floor as suboxic species (DO of 0.1 – 0.5 mL/L or ~4.5 – 23 µmol/kg, Fig. 7-2c) dominate the benthic foraminiferal assemblage (Ohkushi et al., 2013). Yet the trend at this sill-depth site is similar, with lower DO during 6 – 9 ka suggested by a higher

(up to 80% between ~7 and 8 ka) abundance of dysoxic fauna (Fig. 7-2c). The high abundance of hypoxic (DO of 0.5 – 1.5 mL/L or 23 – 67 μmol/kg) foraminifera assemblages between 6 and 9 ka at a nearby site located above the sill (MV0811-15JC, Table 7-1) further corroborates shoaling of the OMZ upper boundary during the early to mid Holocene (Moffitt et al., 2014). A transition to more oxygenated conditions at the sill-depth site after ~5 ka is supported by the increased abundance of suboxic fauna at both shallow sites, corresponding to reduced Re and U authigenic fluxes in the basin floor site (MV0811-14JC) after ~6 ka (Fig. 7-2).

A deeper lower boundary of the Southern California OMZ during the mid-Holocene is suggested by coincident maximum Mo_{EF} values in ODP Hole 1017E (deeper slope site) and authigenic Mo fluxes from MV0811-14JC (basin bottom site) at ~6.5 ka (Figs. 7-2e and f). The accurate age of the Mo_{EF} peak in the ODP Hole 1017E is difficult to determine due to the lack of age control < 8 ka in the core. The core-top age was likely older due to material loss during the core retrieval, such that the broad Mo_{EF} peak at ~6.5 ka may be older. However, the age uncertainty of 1017E does not impact the interpretation of overall expanded Southern California OMZ during the early to mid-Holocene. Taken together, an intensification and expansion of the Southern California OMZ is observed along the California margin vertical transect.

7.6.3 Holocene Northeast Pacific Ocean ventilation variability at intermediate water depths

An intensified OMZ (high authigenic trace metal fluxes) prior to 6 ka could be associated with a number of processes. Enhanced export productivity increases O_2 demand through OC remineralization such that DO in the water columns is drawn down. TOC fluxes are often used to reconstruct export productivity in the water columns (Schoepfer et al., 2015; Wang et al., 2019). Export productivity has shown to play a role in the early Holocene oxygenation (e.g., on the Southern California margin, [Ivanochko and Pedersen (2004); Stott et al. (2000)]) and over the glacial/deglacial timescales (e.g., off the Vancouver Island [Chang et al. (2014); McKay et al. (2005)], Point Conception [Hendy et al. (2004); Taylor et al. (2017)], and on the Alaska margin [Praetorius et al. (2015)]). However, individual peaks and troughs of the TOC fluxes measured on MV0811-14JC are not correlated with authigenic metal fluxes ($Metal_{auth}$) and $Metal_{EF}$ (Fig. 7-2h). Notably, between ~6 – 7 ka, the lowest TOC fluxes of the Holocene coincide with the $Metal_{auth}$ flux maxima. These observations argue against the local export productivity control of basin bottom water oxygenation changes.

Another potential influence on the Southern California OMZ is associated with DO concentrations of intermediate water masses advected into the region. North Pacific OMZs are sensitive to ventilation changes, as indicated from proxy records over glacial cycles (Behl and Kennett, 1996; Cannariato and Kennett, 1999; Hendy and Pedersen, 2005) and ocean modeling (Ito and Deutsch, 2013; Margolskee et al., 2019). Remote water mass oxygenation changes could occur through intermediate water ventilation variability in the source regions (e.g., intermediate water formation rates and local export productivity change at the formation sites) (Crusius et al., 2004) and/or sluggish intermediate water transport, consequently depleting DO in the water columns through the oxidant demand associated with respiration. Thus, intensified Southern California OMZs during the early- to mid-Holocene could be associated with (1) less oxygenated Equatorial Pacific Intermediate Water (EqPIW) advected from the eastern equatorial Pacific (EEP), (2) the shift of intermediate water masses dominating the Southern California margin (from low-oxygen EqPIW before 6 ka to better oxygenated North Pacific Intermediate Water [NPIW]), and/or (3) decreased ventilation of NPIW in the Sea of Okhotsk. To gain insights into intermediate water ventilation shifts, sediment archives retrieved from the intermediate depth (~500 – 1300 m) throughout the North Pacific are compared. These core sites are bathed in the intermediate water masses (NPIW core of 300 – 800 m, EqPIW core of 600 – ~1300 m) (Bostock et al., 2010) where influences of the Pacific Deep Water are of less importance.

We employ a reconstruction of organic matter remineralization in the east equatorial Pacific (V19-27, 0°28.2'S, 82°4.2'W, 1373 m water depth) (Mix et al., 1991) to assess EqPIW O_2 demand in its source region. ^{12}C-enriched organic matter remineralization consumes O_2, and $\delta^{13}C$ values of the ambient waters decreases, leading to low foraminifera $\delta^{13}C$ values (Lynch-Stieglitz and Marchitto, 2014; McCorkle and Keigwin, 1994; Tachikawa and Elderfield, 2002). Unlike the highly variable authigenic trace metal fluxes in SBB during the early to mid Holocene, $\delta^{13}C$ measured on epifaunal benthic foraminifera *Cibicidoides wuellerstorfi* ($\delta^{13}C_{cib}$) in the core V19-27 remained relatively stable ranging between 0.3 – 0.4 ‰ until ~2 ka (Fig. 7-6a), suggesting that EqPIW oxygen demand did not vary through the Holocene (Mix et al., 1991). However, the low resolution of V19-27 might have produced aliasing and led to loss of high-frequency oscillations, and thus we resampled the high-resolution trace metal record (MV0811-14JC) using a similar resolution as V19-27 (Mix et al., 1991) (Fig. D-5). Albeit significantly suppressed, local $Metal_{auth}$ flux maxima in the early Holocene and a transition to lower fluxes

can still be observed, indicating more oxygenated conditions after ~6 ka, in contrast to the invariant $\delta^{13}C_{cib}$ values. Modeling results indicate higher O_2 concentrations in the EEP OMZ at 6 ka should have resulted from greater Equatorial Undercurrent transport of ventilated water from the western Equatorial Pacific (Xu et al., 2015), which is also consistent with our mid-Holocene (MH, 6 ka) simulation. Thus, the relatively invariant (from proxy records) or higher (from model results) oxygen concentrations of EqPIW are unlikely to intensify the Southern California OMZ during the early- to mid-Holocene.

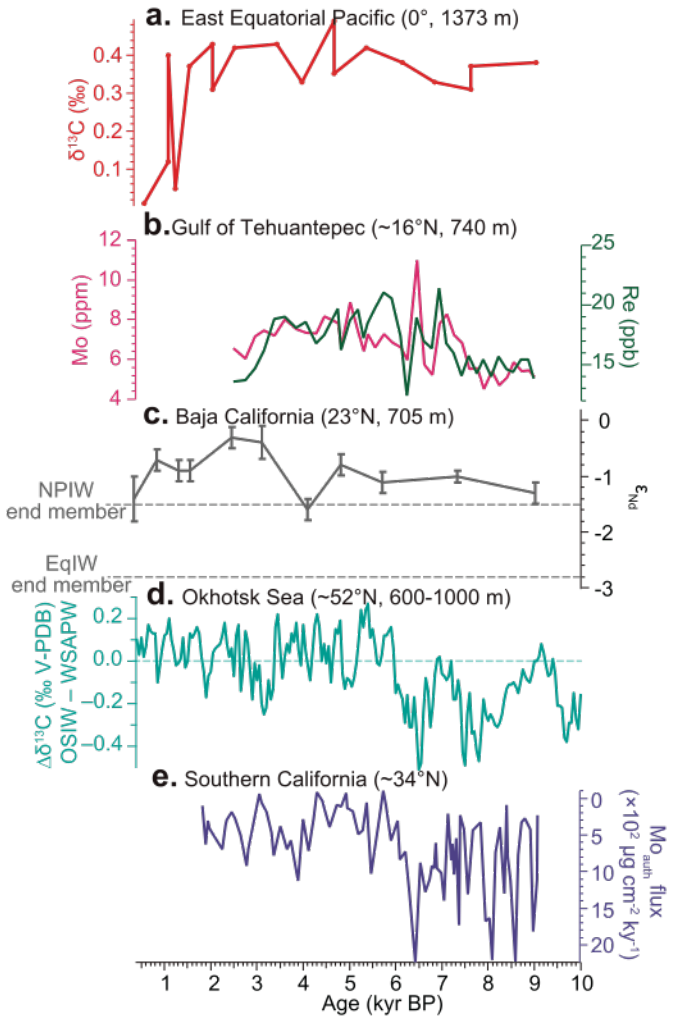

Figure 7-6 Ventilation change in the California Margin relative to changes in possible intermediate water sources. (a) Benthic foraminifera $\delta^{13}C$ (red line) of the core V19-27 from the eastern equatorial Pacific (Mix et al., 1991); (b) Mo (magenta line) and Re (green line) concentrations of the core ME0005A 3JC from the Gulf of Tehuantepec (Hendy and Pedersen, 2006). (c) εNd of fossil fish teeth/debris from the Baja California core MV99-MC19/GC31/PC08 (Basak et al., 2010) with error bars; εNd end member values for the North Pacific Intermediate Water (NPIW, εNd = ~-1.5, minimum estimate) and the Equatorial Pacific Intermediate Water (EqPIW, εNd = ~-2.8) are drawn from Basak et al. (2010) and Lacan and Jeandel (2001). (d) $\Delta\delta^{13}C$ difference (teal line) between Okhotsk Sea Intermediate Water (OSIW) and Western Subarctic Pacific Water (WSAPW) showing ventilation during OSIW formation (Lembke-Jene et al., 2018); The zero $\Delta\delta^{13}C$ difference is shown in the dashed line; (e) authigenic Mo fluxes of MV0811-14JC (590 m; purple line).

The EEP influence on intermediate water masses affecting the Southern California OMZ can be evaluated through a comparison of a trace metal record from the Gulf of Tehuantepec (ME0005A 3JC, 15°39.0'N, 95°16.8'W, 740 m water depth, Fig. 7-1a) with SBB. The Gulf of Tehuantepec record, which lies along the EqPIW transport path up the coast of North America (Hendy and Pedersen, 2006), indicates better oxygenated conditions prior to 7 ka with low Mo and Re concentrations similar to the last glacial. Although trace metal concentrations increase at ~6.5 ka (Fig. 7-6b) similar to SBB authigenic Mo fluxes, concentrations remain high through the mid-Holocene until at least 3 ka. Likewise, only minor EqPIW influences on the Southern California OMZ are suggested by a fish-teeth/debris εNd record from Baja California (MV99-MC19/GC31/PC08, 23°30'N, 111°36'W, 705 m water depth, Fig. 7-1a). The Baja California site was persistently dominated by NPIW during the early to mid-Holocene, as evidenced by > -1.5 εNd values in the record (Fig. 7-6c). Possible aliasing was also evaluated and the transition from high to low $Metal_{auth}$ fluxes remains apparent under low temporal resolution (Mo in particular at ~6 ka, Fig. D-6). Thus, the poor correspondence between EEP and the Southern California paleoceanographic reconstructions does not support EqPIW as the primary ventilation source of the Southern California OMZ during the Holocene.

The DO supply to the subsurface northeast Pacific could also be reduced by decreased ventilation of NPIW during formation at its source. Presently NPIW is directly ventilated via brine rejection during sea ice development in the northwestern Sea of Okhotsk, which subsequently generates Okhotsk Sea Intermediate Water (OSIW) (Talley, 1993). Comparison of OSIW and Western Subarctic Pacific Water (WSAPW) $\delta^{13}C_{cib}$ values prior to 6 ka suggests that newly formed OSIW was much less ventilated/not actively ventilated in early to mid Holocene (Lembke-Jene et al., 2018) (Fig. 7-6d). This observation is consistent with a strengthened Southern California OMZ, as demonstrated by the coeval Mo_{auth} flux maxima of MV0811-14JC (Fig. 7-6e). Weakened ventilation in the Sea of Okhotsk is also supported by the MH simulation, which exhibits a reduced density fluxes at the surface and an increased ideal age at the intermediate depth (Fig. 7-3).

Among the three ventilation sources of OSIW (Dense Shelf Water [DSW], Soya Warm Current [SWC], and Western Subarctic Pacific Water [WSAPW]), SWC water only has minor contributions to OSIW (Itoh, 2003). Younger ^{14}C projection ages indicate that SWC was better ventilated (Rella and Uchida, 2014) in the early Holocene (particularly at ~6.5 ka BP), and thus

was unlikely to be a source of poorly ventilated water. Similarly, the $\delta^{13}C_{cib}$ records for WSAPW showed no significant changes through the Holocene (Lembke-Jene et al., 2018). Thus, only reduced DSW generation in a more stratified Sea of Okhotsk prior to 6 ka remains as a driver to weaken ventilation of OSIW/NPIW. Less DSW formation via decreased sea ice formation in the Sea of Okhotsk at this time is supported by limited ice-rafted debris (Sakamoto et al., 2005). This observation is consistent with reduced surface density fluxes that are primarily associated with decreased sea ice formation/brine rejection in the CESM MH simulation (Fig. 7-3b). Additionally, a stratified Sea of Okhotsk in early Holocene would have depleted the subsurface silicate supply to the photic zone, resulting in primary productivity dominated by coccolithophorids (Okazaki et al., 2006; Seki et al., 2004). Compared to diatom productivity, the much slower sinking rate of coccolithophorid detritus allows for greater organic carbon remineralization and oxygen consumption in the water column, leading to lower oxygen and higher nutrient concentrations in the newly formed NPIW (Gorbarenko et al., 2010; Lembke-Jene et al., 2018; Okazaki et al., 2006). Reduced NPIW formation also leads to a poorly ventilated mid-depth North Pacific, which agrees with the increased ideal age in the CESM MH simulation (Fig. 7-3c). Coupled intensified and expanded OMZ in the northeast Pacific (the southern California margin vertical transect) indicates a basin-wide OMZ shift communicated via NPIW. Thus, both proxy records and climate modeling suggest a potentially vital role of NPIW in regulating oxygen concentrations in the mid-depth Pacific Ocean through the Holocene.

7.6.4 Basin-wide oceanic responses to atmospheric forcing in Holocene

The reduced sea-ice formation and intermediate water ventilation over the NW Pacific in the mid-Holocene are linked to the orbital forcing and the adjustments in atmospheric circulation. During the early to mid Holocene (prior to 6 ka), the perihelion occurred in the boreal summer, intensifying the Northern Hemisphere (NH) solar insolation while weakening the Southern Hemisphere (SH) counterpart (Berger and Loutre, 1991) (Fig. 7-7a). Consequently, the temperature contrast between the NH and SH was greater than present by as much as ~1.2 °C at ~7.2 ka (Marcott et al., 2013)(Fig. 7-7e). This asymmetry in inter-hemispheric temperature led to a northward displaced Intertropical Convergence Zone (ITCZ), supported by increased the rainfall reconstructed from in the Cariaco Basin and Palau (Haug et al., 2001; Sachs et al., 2018)(Figs. 7-7e and f), the wind response in CESM MH simulation (Fig. 7-3d), and other theoretical and modeling studies (Broccoli et al., 2006; Schneider et al., 2014). A weakened NH

Hadley cell shifts the Aleutian Low (AL) northward and causes its intensity to decrease via the Rossby wave response (Trenberth et al., 1998), which is consistent with the positive sea-level pressure anomalies and the anomalous easterly winds near the Bering Sea and Sea of Okhotsk in the MH simulation (Fig. D-7). This wind pattern favors a reduction in sea ice formation (Figs. 7-2b and D-7) and intermediate water ventilation (Figs. 7-2c and 7-8a).

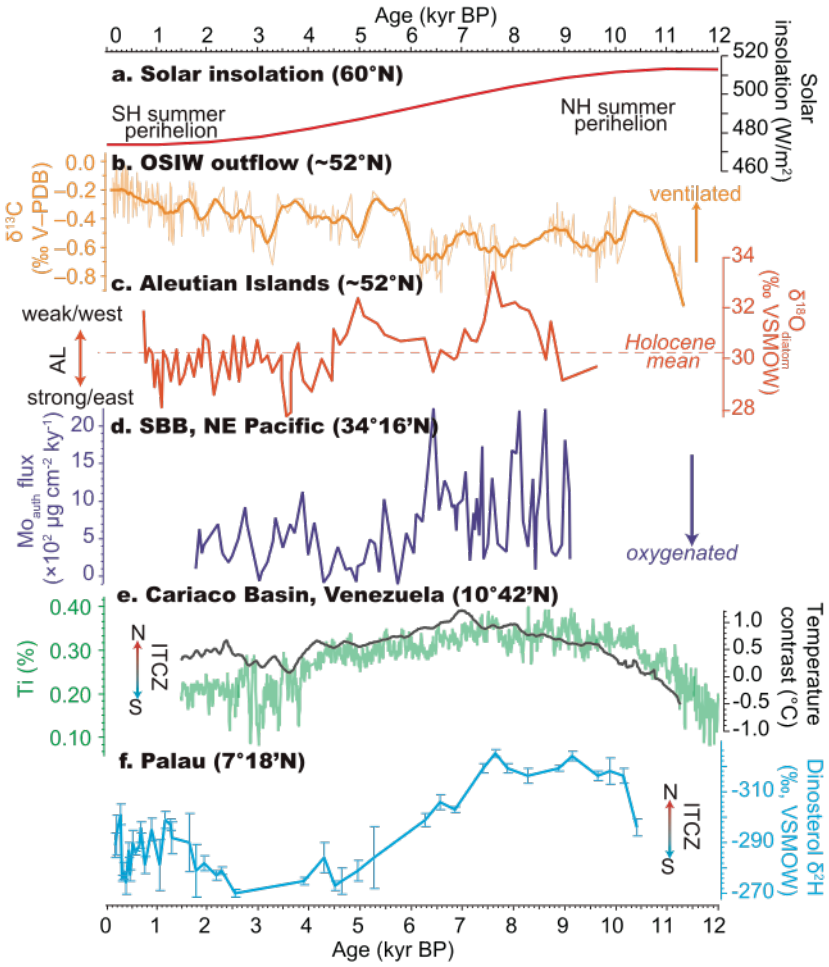

Figure 7-7 Basin-wide comparison of oceanic responses with atmospheric forcing. (a) Boreal summer (June) insolation at 60°N (Berger and Loutre, 1991). (b) $\delta^{13}C$ of OSIW outflow (Lembke-Jene et al., 2018) with a 25 point running mean (thick yellow line). (c) Diatom $\delta^{18}O$ (orange line) of the Heart Lake on the Aleutian Islands, with enriched $\delta^{18}O$ suggesting weak/westward Aleutian Low. The Holocene mean value is indicated by the dashed red line. (d) Authigenic Mo fluxes of MV0811-14JC (purple line) with lower values indicating more oxygenated water column. (e) Scanning XRF Ti counts (teal line) from the Cariaco Basin (ODP Hole 1002) (Haug et al., 2001) and extratropical interhemispheric temperature difference (30 – 60°N vs. 30 – 60°S, black line) (Marcott et al., 2013). Higher Ti counts indicate a northward Intertropical Convergence Zone (ITCZ) displacement; (f) Dinosterol $\delta^{2}H$ record (pale blue line) from T-Lake, Palau, with heavier $\delta^{2}H$ suggesting less precipitation and southward ITCZ migration (Sachs et al., 2018).

NH boreal summer insolation gradually weakened towards the late Holocene (Fig. 7-7a), which results in a southward ITCZ displacement and a deepened AL via the Rossby wave responses. This is observed from a diatom oxygen isotope record ($\delta^{18}O_{diatom}$) from the Aleutian

Islands (Bailey et al., 2018), as $\delta^{18}O_{diatom}$ reflects the moisture source changes that follow storm tracks controlled by pressure systems. After ~5 ka, relatively lower $\delta^{18}O_{diatom}$ indicates enhanced northerly storm tracks under the influence of intensified AL (Bailey et al., 2018)(Fig. 7-7c). A similar transition to intensified and/or eastward AL was observed from the relatively depleted sedimentary calcite $\delta^{18}O$ in the Jellybean Lake, Yukon Territory (Anderson et al., 2005), which is also consistent with CESM model simulated sea-level pressure (Fig. D-7). The intensified AL could have facilitated sea ice formation and NPIW ventilation in the Sea of Okhotsk (Fig. 7-8b). Together, this basin-wide correspondence of atmospheric circulation to solar insolation is linked with intermediate water ventilation changes in the North Pacific, highlighting oceanic responses to climatic forcing via atmospheric teleconnections.

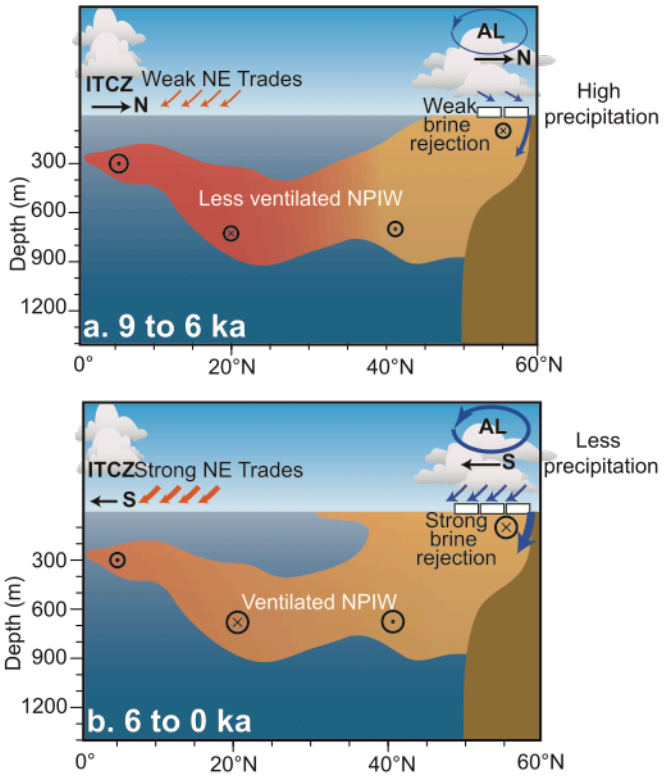

Figure 7-8 A schematic of the atmospheric forcing and oceanic responses during a) the early-mid Holocene (9 to 6 ka) and b) the late Holocene (6 to 0 ka). (a) Prior to 6 ka, a northward positioned ITCZ weakened the AL, creating anomalous easterly winds that reduced sea ice formation and consequently the ventilation of NPIW. (b) After 6 ka, a southward migration of the ITCZ intensified the AL, increasing sea ice formation under dominantly northerly winds. Strong brine rejection contributed to better-ventilated intermediate water. Circles with dots represent current directions toward the reader, while circles with crosses denote current directions into the page.

7.7 Conclusions

Oceanic deoxygenation has been extensively observed since the 1950s (Diaz and Rosenberg, 2008; Stramma et al., 2010). The anthropogenic component of the oceanic

deoxygenation, however, has been difficult to separate from its natural variability due to the short duration of instrumental records. A new Holocene redox-sensitive metal record (MV0811-14JC, 50 – 100 yr sampling resolution) retrieved from the Santa Barbara Basin (SBB) reveals a significantly more reducing water column (higher authigenic fluxes and enrichments of redox-sensitive trace metals) in the early- to mid-Holocene relative to the post-Industrial Revolution average (~1870 – 2007 CE) (Wang et al., 2017). The new trace metal record augments the vertical transect from the sill-depth sites (near or above 475 m, MV0502-2504 and MV0811-15JC) to the open slope site (ODP 1017E, 955 m). The vertical transect indicates that a coherent benthic response to intensified deoxygenation connected to broad variability with the oxygen minimum zone (OMZ) on the California margin (Fig. 7-2). Such extreme low-oxygen conditions in the early Holocene relative to the post-Industrial Revolution highlight the large sensitivity of OMZ responses to climate change in the absence of anthropogenic impacts.

Our results suggest that intensification of the southern California OMZ prior to 6 ka primarily reflects a weakening of NPIW formation, as intermediate water transport rates were relatively invariant during the Holocene (Basak et al., 2010; Du et al., 2018a). Decreased NPIW ventilation is further linked to the sea ice formation in the Sea of Okhotsk (Lembke-Jene et al., 2018), which is corroborated by an increase in the buoyancy forcing in a mid-Holocene simulation using the CESM. A warmer and more stratified Sea of Okhotsk would have suppressed sea ice formation, reduced surface density fluxes, and consequently NPIW ventilation (Lembke-Jene et al., 2018; Okazaki et al., 2006). As the only direct ventilation source in the North Pacific, NPIW ventilation shifts may thus have led to basin-wide coherent responses in oxygenation.

A comparison with model simulations and a basin-wide compilation of proxy records further suggest coherent, orbital-driven responses in the ocean and atmospheric circulations. A comparison of mid-depth ventilation in the North Pacific (NPIW), the intensity and/or position of the Aleutian Low, and the Intertropical Convergence Zone (ITCZ) generally supports a mid-Holocene (~6 – 7 ka) response to decreasing NH boreal summer solar insolation at mid- to high-latitudes. Despite regional heterogeneity, the mid-Holocene transition is characterized by reduced Northern Hemisphere insolation that results in a southward ITCZ shift, as well as an intensified and eastward positioned AL via the Rossby wave responses (Fig. 7-8b). Extratropical cooling and a shift in prevailing winds associated with the AL increased sea ice formation in the

Sea of Okhotsk, and consequently improved the ventilation of the NPIW. Thus, North Pacific subsurface ocean ventilation responses are closely coupled via atmospheric teleconnections throughout the Holocene.

7.8 Acknowledgments

This work is supported by the National Science Foundation under grant number OCE-1304327 (I.H.) and Y.W. acknowledges support from the Rackham Graduate School. We gratefully acknowledge the captain and crew of the R/V Melville, and Co-Chiefs Richard Behl and James Kennett for collection of the core MV0811-14JC.

7.9 References

Aller, R.C., 1980. Quantifying solute distributions in the bioturbated zone of marine sediments by defining an average microenvironment. Geochimica et Cosmochimica Acta, 44(12): 1955-1965.

Anderson, L., Abbott, M.B., Finney, B.P., Burns, S.J., 2005. Regional atmospheric circulation change in the North Pacific during the Holocene inferred from lacustrine carbonate oxygen isotopes, Yukon Territory, Canada. Quaternary Research, 64(01): 21-35.

Bailey, H.L. et al., 2018. Holocene atmospheric circulation in the central North Pacific: A new terrestrial diatom and δ18O dataset from the Aleutian Islands. Quaternary Science Reviews, 194: 27-38.

Basak, C., Martin, E.E., Horikawa, K., Marchitto, T.M., 2010. Southern Ocean source of 14C-depleted carbon in the North Pacific Ocean during the last deglaciation. Nature Geoscience, 3(11): 770-773.

Behl, R.J., 1995. Sedimentary facies and sedimentology on the late Quaternary Santa Barbara Basin, Site 893. Proceedings of the Ocean Drilling Program, Scientific Results, 146: 295.

Behl, R.J., Kennett, J.P., 1996. Brief interstadial events in the Santa Barbara basin, NE Pacific, during the past 60 kyr. Nature, 379(6562): 243-246.

Behl, R.J., Tada, R., Irino, T., 2000. 22. Late Quaternary textural change offshore of Point Conception, Site 1017, central California margin. Proceedings of the Ocean Drilling Program, Scientific Results, 167.

Berger, A., Loutre, M.F., 1991. Insolation values for the climate of the last 10 million years. Quaternary Science Reviews, 10(4): 297-317.

Blaauw, M., Christen, J.A., 2011. Flexible paleoclimate age-depth models using an autoregressive gamma process. Bayesian Analysis, 6(3): 457-474.

Bograd, S.J., 2002. Bottom water renewal in the Santa Barbara Basin. Journal of Geophysical Research, 107(C12).

Bopp, L. et al., 2013. Multiple stressors of ocean ecosystems in the 21st century: projections with CMIP5 models. Biogeosciences, 10(10): 6225-6245.

Bostock, H.C., Opdyke, B.N., Gagan, M.K., Fifield, L.K., 2004. Carbon isotope evidence for changes in Antarctic Intermediate Water circulation and ocean ventilation in the southwest Pacific during the last deglaciation. Paleoceanography, 19(4): n/a-n/a.

Bostock, H.C., Opdyke, B.N., Williams, M.J.M., 2010. Characterising the intermediate depth waters of the Pacific Ocean using δ13C and other geochemical tracers. Deep Sea Research Part I: Oceanographic Research Papers, 57(7): 847-859.

Bostock, H.C., Sutton, P.J., Williams, M.J.M., Opdyke, B.N., 2013. Reviewing the circulation and mixing of Antarctic Intermediate Water in the South Pacific using evidence from geochemical tracers and Argo float trajectories. Deep Sea Research Part I: Oceanographic Research Papers, 73: 84-98.

Boudreau, B.P., 1997. Diagenetic models and their implementation : modelling transport and reactions in aquatic sediments, Berlin ; New York :. Springer, Berlin ; New York :.

Breitburg, D. et al., 2018. Declining oxygen in the global ocean and coastal waters. Science, 359(6371).

Broccoli, A.J., Dahl, K.A., Stouffer, R.J., 2006. Response of the ITCZ to Northern Hemisphere cooling. Geophysical Research Letters, 33(1): n/a-n/a.

Calvert, S.E., Pedersen, T.F., 1993. Geochemistry of Recent oxic and anoxic marine sediments: Implications for the geological record. Marine Geology, 113(1): 67-88.

Calvert, S.E., Pedersen, T.F., 2007. Elemental Proxies for Palaeoclimatic and Palaeoceanographic Variability in Marine Sediments: Interpretation and Application, Developments in Marine Geology, pp. 567-644.

Cannariato, K.G., Kennett, J.P., 1999. Climatically related millennial-scale fluctuations in strength of California margin oxygen-minimum zone during the past 60 k.y. Geology, 27(11): 975-978.

Cartapanis, O., Tachikawa, K., Bard, E., 2011. Northeastern Pacific oxygen minimum zone variability over the past 70 kyr: Impact of biological production and oceanic ventilation. Paleoceanography, 26(4): 1-17.

Chang, A.S., Pedersen, T.F., Hendy, I.L., 2014. Effects of productivity, glaciation, and ventilation on late Quaternary sedimentary redox and trace element accumulation on the Vancouver Island margin, western Canada. Paleoceanography, 29(7): 730-746.

Cook, M.S., Keigwin, L.D., Sancetta, C.A., 2005. The deglacial history of surface and intermediate water of the Bering Sea. Deep Sea Research Part II: Topical Studies in Oceanography, 52(16-18): 2163-2173.

Croudace, I.W., Rindby, A., Rothwell, R.G., 2006. ITRAX: description and evaluation of a new multi-function X-ray core scanner. Geological Society, London, Special Publications, 267(1): 51-63.

Crusius, J., Calvert, S., Pedersen, T., Sage, D., 1996. Rhenium and molybdenum enrichments in sediments as indicators of oxic, suboxic and sulfidic conditions of deposition. Earth and Planetary Science Letters, 145: 65-78.

Crusius, J., Pedersen, T.F., Kienast, S., Keigwin, L., Labeyrie, L., 2004. Influence of northwest Pacific productivity on North Pacific Intermediate Water oxygen concentrations during the Bølling-Ållerød interval (14.7–12.9 ka). Geology, 32(7): 633.

Crusius, J., Thomson, J., 2003. Mobility of authigenic rhenium, silver, and selenium during postdepositional oxidation in marine sediments. Geochimica et Cosmochimica Acta, 67(2): 265-273.

Diaz, R.J., Rosenberg, R., 2008. Spreading dead zones and consequences for marine ecosystems. Science, 321(5891): 926-9.

Dickson, B. et al., 2001. Chapter 7.3 The world during WOCE. In: Siedler, G., Church, J., Gould, J. (Eds.), International Geophysics. Academic Press, pp. 557-583.

Du, J., Haley, B.A., Mix, A.C., Walczak, M.H., Praetorius, S.K., 2018a. Flushing of the deep Pacific Ocean and the deglacial rise of atmospheric CO2 concentrations. Nature Geoscience, 11(10): 749-755.

Du, X., Hendy, I., Schimmelmann, A., 2018b. A 9000-year flood history for Southern California: A revised stratigraphy of varved sediments in Santa Barbara Basin. Marine Geology, 397: 29-42.

Emmer, E., Thunell, R.C., 2000. Nitrogen isotope variations in Santa Barbara Basin sediments: Implications for denitrification in the eastern tropical North Pacific during the last 50,000 years. Paleoceanography, 15(4): 377-387.

England, M.H., 1995. The Age of Water and Ventilation Timescales in a Global Ocean Model. Journal of Physical Oceanography, 25(11): 2756-2777.

Gorbarenko, S.A. et al., 2010. Paleoenvironment changes in the NW Okhotsk Sea for the last 18kyr determined with micropaleontological, geochemical, and lithological data. Deep Sea Research Part I: Oceanographic Research Papers, 57(6): 797-811.

Hall, T.M. et al., 2007. Ventilation Rates Estimated from Tracers in the Presence of Mixing. Journal of Physical Oceanography, 37(11): 2599-2611.

Haug, G.H., Hughen, K.A., Sigman, D.M., Peterson, L.C., Röhl, U., 2001. Southward migration of the intertropical convergence zone through the Holocene. Science, 293(5533): 1304-1308.

Hendy, I.L., Dunn, L., Schimmelmann, A., Pak, D.K., 2013. Resolving varve and radiocarbon chronology differences during the last 2000 years in the Santa Barbara Basin sedimentary record, California. Quaternary International, 310: 155-168.

Hendy, I.L., Kennett, J.P., 2003. Tropical forcing of North Pacific intermediate water distribution during Late Quaternary rapid climate change? Quaternary Science Reviews, 22(5-7): 673-689.

Hendy, I.L., Napier, T.J., Schimmelmann, A., 2015. From extreme rainfall to drought: 250 years of annually resolved sediment deposition in Santa Barbara Basin, California. Quaternary International, 387: 3-12.

Hendy, I.L., Pedersen, T.F., 2005. Is pore water oxygen content decoupled from productivity on the California Margin? Trace element results from Ocean Drilling Program Hole 1017E, San Lucia slope, California. Paleoceanography, 20(4): 1-12.

Hendy, I.L., Pedersen, T.F., 2006. Oxygen minimum zone expansion in the eastern tropical North Pacific during deglaciation. Geophysical Research Letters, 33(20): n/a-n/a.

Hendy, I.L., Pedersen, T.F., Kennett, J.P., Tada, R., 2004. Intermittent existence of a southern Californian upwelling cell during submillennial climate change of the last 60 kyr. Paleoceanography, 19(3): 1-15.

Hurrell, J.W. et al., 2013. The Community Earth System Model: A Framework for Collaborative Research. Bulletin of the American Meteorological Society, 94(9): 1339-1360.

Ito, T., Deutsch, C., 2013. Variability of the oxygen minimum zone in the tropical North Pacific during the late twentieth century. Global Biogeochemical Cycles, 27(4): 1119-1128.

Itoh, M., 2003. Distribution and formation of Okhotsk Sea Intermediate Water: An analysis of isopycnal climatological data. Journal of Geophysical Research, 108(C8).

Ivanochko, T.S., Pedersen, T.F., 2004. Determining the influences of Late Quaternary ventilation and productivity variations on Santa Barbara Basin sedimentary oxygenation: a multi-proxy approach. Quaternary Science Reviews, 23(3-4): 467-480.

Keeling, R.E., Kortzinger, A., Gruber, N., 2010. Ocean deoxygenation in a warming world. Ann Rev Mar Sci, 2: 199-229.

Keigwin, L.D., 1998. Glacial-age hydrography of the far northwest Pacific Ocean. Paleoceanography, 13(4): 323-339.

Kennett, J.P., Ingram, B.L., 1995. A 20,000-year record of ocean circulation and climate change from the Santa Barbara basin. Nature, 377(6549): 510-514.

Kerisit, S., Liu, C., 2010. Molecular simulation of the diffusion of uranyl carbonate species in aqueous solution. Geochimica et Cosmochimica Acta, 74(17): 4937-4952.

Killick, R., Fearnhead, P., Eckley, I.A., 2012. Optimal Detection of Changepoints With a Linear Computational Cost. Journal of the American Statistical Association, 107(500): 1590-1598.

Kim, S., Khim, B.K., Uchida, M., Itaki, T., Tada, R., 2011. Millennial-scale paleoceanographic events and implication for the intermediate-water ventilation in the northern slope area of the Bering Sea during the last 71kyrs. Global and Planetary Change, 79(1): 89-98.

Knudson, K.P., Ravelo, A.C., 2015. North Pacific Intermediate Water circulation enhanced by the closure of the Bering Strait. Paleoceanography, 30(10): 1287-1304.

Lacan, F., Jeandel, C., 2001. Tracing Papua New Guinea imprint on the central Equatorial Pacific Ocean using neodymium isotopic compositions and Rare Earth Element patterns. Earth and Planetary Science Letters, 186(3): 497-512.

Lembke-Jene, L., Tiedemann, R., Nürnberg, D., Gong, X., Lohmann, G., 2018. Rapid shift and millennial-scale variations in Holocene North Pacific Intermediate Water ventilation. Proceedings of the National Academy of Sciences, 115(21): 5365.

Lembke-Jene, L. et al., 2017. Deglacial variability in Okhotsk Sea Intermediate Water ventilation and biogeochemistry: Implications for North Pacific nutrient supply and productivity. Quaternary Science Reviews, 160: 116-137.

Li, Y.-H., Gregory, S., 1974. Diffusion of ions in sea water and in deep-sea sediments. Geochimica et Cosmochimica Acta, 38(5): 703-714.

Ludington, S. et al., 2007. Preliminary integrated geologic map databases for the United States, United States Geological Survey.

Lynch-Stieglitz, J., Marchitto, T.M., 2014. Tracers of Past Ocean Circulation. 435-451.

Lynn, R.J., Simpson, J.J., 1990. The flow of the undercurrent over the continental borderland off southern California. Journal of Geophysical Research, 95(C8): 12995-13008.

Marcott, S.A., Shakun, J.D., Clark, P.U., Mix, A.C., 2013. A Reconstruction of Regional and Global Temperature for the Past 11,300 Years. Science, 339(6124): 1198.

Margolskee, A., Frenzel, H., Emerson, S., Deutsch, C., 2019. Ventilation Pathways for the North Pacific Oxygen Deficient Zone. Global Biogeochemical Cycles, 33(7): 875-890.

McCorkle, D.C., Keigwin, L.D., 1994. Depth profiles of δ13C in bottom water and core top C. wuellerstorfi on the Ontong Java Plateau and Emperor Seamounts. Paleoceanography, 9(2): 197-208.

McKay, J.L., Pedersen, T.F., Southon, J., 2005. Intensification of the oxygen minimum zone in the northeast Pacific off Vancouver Island during the last deglaciation: Ventilation and/or export production? Paleoceanography, 20(4).

Mix, A.C. et al., 1991. Carbon 13 in Pacific Deep and Intermediate Waters, 0-370 ka: Implications for Ocean Circulation and Pleistocene CO2. Paleoceanography, 6(2): 205-226.

Miyao, T., Ishikawa, K., 2003. Formation, distribution and volume transport of the North Pacific Intermediate Water studied by repeat hydrographic observations. Journal of Oceanography, 59(6): 905-919.

Moffitt, S.E., Hill, T.M., Ohkushi, K., Kennett, J.P., Behl, R.J., 2014. Vertical oxygen minimum zone oscillations since 20 ka in Santa Barbara Basin: A benthic foraminiferal community perspective. Paleoceanography, 29(1): 44-57.

Moffitt, S.E., Hill, T.M., Roopnarine, P.D., Kennett, J.P., 2015. Response of seafloor ecosystems to abrupt global climate change. Proc Natl Acad Sci U S A, 112(15): 4684-9.

Morford, J.L., Martin, W.R., Carney, C.M., 2012. Rhenium geochemical cycling: Insights from continental margins. Chemical Geology, 324-325: 73-86.

Morford, J.L., Martin, W.R., François, R., Carney, C.M., 2009. A model for uranium, rhenium, and molybdenum diagenesis in marine sediments based on results from coastal locations. Geochimica et Cosmochimica Acta, 73(10): 2938-2960.

Nameroff, T.J., Calvert, S.E., Murray, J.W., 2004. Glacial-interglacial variability in the eastern tropical North Pacific oxygen minimum zone recorded by redox-sensitive trace metals. Paleoceanography, 19(1): n/a-n/a.

Napier, T.J., Hendy, I.L., Fahnestock, M.F., Bryce, J.G., 2019. Provenance of detrital sediments in Santa Barbara Basin, California, USA: Changes in source contributions between the Last Glacial Maximum and Holocene. GSA Bulletin.

Ohkushi, K. et al., 2013. Quantified intermediate water oxygenation history of the NE Pacific: A new benthic foraminiferal record from Santa Barbara basin. Paleoceanography, 28(3): 453-467.

Ohkushi, K.i., Itaki, T., Nemoto, N., 2003. Last Glacial–Holocene change in intermediate-water ventilation in the Northwestern Pacific. Quaternary Science Reviews, 22(14): 1477-1484.

Okazaki, Y. et al., 2006. Cycladophora davisiana (Radiolaria) in the Okhotsk Sea: a key for reconstructing glacial ocean conditions. Journal of Oceanography, 62: 639-648.

Okazaki, Y. et al., 2010. Deepwater Formation in the North Pacific During the Last Glacial Termination. Science, 329(5988): 200.

Otto-Bliesner, B.L. et al., 2017. The PMIP4 contribution to CMIP6 – Part 2: Two interglacials, scientific objective and experimental design for Holocene and Last Interglacial simulations. Geoscientific Model Development, 10(11): 3979-4003.

Pena, L.D. et al., 2013. Rapid changes in meridional advection of Southern Ocean intermediate waters to the tropical Pacific during the last 30kyr. Earth and Planetary Science Letters, 368: 20-32.

Praetorius, S.K. et al., 2015. North Pacific deglacial hypoxic events linked to abrupt ocean warming. Nature, 527(7578): 362-6.

Reid, J.L., 1965. Intermediate waters of the Pacific Ocean. Johns Hopkins Oceanography Studies, 5: 1-96.

Reimer, P.J. et al., 2013. IntCal13 and Marine13 radiocarbon age calibration curves 0–50,000 years cal BP. Radiocarbon, 55(4): 1869-1887.

Reimers, C.E., Lange, C., Tabak, M., Bernhard, J., 1990. Seasonal spillover and varve formation in the Santa Barbara Basin, California. Limnology and Oceanography, 35(7): 1577-1585.

Rella, S.F., Uchida, M., 2014. A Southern Ocean trigger for Northwest Pacific ventilation during the Holocene? Scientific Reports, 4: 4046.

Sabine, C.L. et al., 2004. The Oceanic Sink for Anthropogenic CO<sub>2</sub&gt. Science, 305(5682): 367.

Sachs, J.P. et al., 2018. Southward Shift of the Pacific ITCZ During the Holocene. Paleoceanography and Paleoclimatology.

Sakamoto, T. et al., 2005. Ice-rafted debris (IRD)-based sea-ice expansion events during the past 100kyrs in the Okhotsk Sea. Deep Sea Research Part II: Topical Studies in Oceanography, 52(16-18): 2275-2301.

Schmidtko, S., Stramma, L., Visbeck, M., 2017. Decline in global oceanic oxygen content during the past five decades. Nature, 542(7641): 335-339.

Schmitt, R.W., Bogden, P.S., Dorman, C.E., 1989. Evaporation Minus Precipitation and Density Fluxes for the North Atlantic. Journal of Physical Oceanography, 19(9): 1208-1221.

Schneider, T., Bischoff, T., Haug, G.H., 2014. Migrations and dynamics of the intertropical convergence zone. Nature, 513(7516): 45-53.

Schoepfer, S.D. et al., 2015. Total organic carbon, organic phosphorus, and biogenic barium fluxes as proxies for paleomarine productivity. Earth-Science Reviews, 149: 23-52.

Seki, O. et al., 2004. Reconstruction of paleoproductivity in the Sea of Okhotsk over the last 30 kyr. Paleoceanography, 19(1): n/a-n/a.

Shcherbina, A.Y., Talley, L.D., Rudnick, D.L., 2003. Direct Observations of North Pacific Ventilation: Brine Rejection in the Okhotsk Sea. Science, 302(5652): 1952.

Shcherbina, A.Y., Talley, L.D., Rudnick, D.L., 2004a. Dense water formation on the northwestern shelf of the Okhotsk Sea: 1. Direct observations of brine rejection. Journal of Geophysical Research: Oceans, 109(C9).

Shcherbina, A.Y., Talley, L.D., Rudnick, D.L., 2004b. Dense water formation on the northwestern shelf of the Okhotsk Sea: 2. Quantifying the transports. Journal of Geophysical Research: Oceans, 109(C9).

Slagel, M.J., Griggs, G.B., 2008. Cumulative Losses of Sand to the California Coast by Dam Impoundment. Journal of Coastal Research, 243: 571-584.

Stott, L.D., Berelson, W., Douglas, R., Gorsline, D., 2000. Increased dissolved oxygen in Pacific intermediate waters due to lower rates of carbon oxidation in sediments. Nature, 407: 367-370.

Stramma, L., Schmidtko, S., Levin, L.A., Johnson, G.C., 2010. Ocean oxygen minima expansions and their biological impacts. Deep Sea Research Part I: Oceanographic Research Papers, 57(4): 587-595.

Tachikawa, K., Elderfield, H., 2002. Microhabitat effects on Cd/Ca and δ13C of benthic foraminifera. Earth and Planetary Science Letters, 202(3): 607-624.

Tada, R., Sato, S., Irino, T., Matsui, H., Kennett, J.P., 2000. 25. Millennial-scale compositional variations in late Quaternary sediments at Site 1017, Southern California. Proceedings of the Ocean Drilling Program: Scientific Results, 167.

Talley, L.D., 1993. Distribution and formation of North Pacific Intermediate Water. Journal of Geophysical Oceanography, 23: 517-537.

Talley, L.D., 2008. Freshwater transport estimates and the global overturning circulation: Shallow, deep and throughflow components. Progress in Oceanography, 78(4): 257-303.

Taylor, M.A., Hendy, I.L., Chappaz, A., 2017. Assessing oxygen depletion in the Northeastern Pacific Ocean during the last deglaciation using I/Ca ratios from multiple benthic foraminiferal species. Paleoceanography, 32(8): 746-762.

Thunell, R.C., 1998. Particle fluxes in a coastal upwelling zone: sediment trap results from Santa Barbara Basin, California. Deep Sea Research Part II: Topical Studies in Oceanography, 45(8): 1863-1884.

Thunell, R.C., Tappa, E.J., Andersen, D.M., 1995. Sediment fluxes and varve formation in Santa Barbara Basin, offshore California. Geology, 23(12): 1083-1086.

Trenberth, K.E. et al., 1998. Progress during TOGA in understanding and modeling global teleconnections associated with tropical sea surface temperatures. Journal of Geophysical Research: Oceans, 103(C7): 14291-14324.

Tribovillard, N., Algeo, T.J., Lyons, T., Riboulleau, A., 2006. Trace metals as paleoredox and paleoproductivity proxies: An update. Chemical Geology, 232(1-2): 12-32.

Tsuchiya, M., Talley, L.D., 1996. Water-property distributions along an eastern Pacific hydrographic section at 135W. Journal of Marine Research, 54(3): 541-564.

van Geen, A., Smethie, W.M., Horneman, A., Lee, H., 2006. Sensitivity of the North Pacific oxygen minimum zone to changes in ocean circulation: A simple model calibrated by chlorofluorocarbons. Journal of Geophysical Research, 111(C10).

Wang, Y., Hendy, I., Napier, T.J., 2017. Climate and Anthropogenic Controls of Coastal Deoxygenation on Interannual to Centennial Timescales. Geophysical Research Letters, 44(22): 11528–11536.

Wang, Y., Hendy, I.L., Thunell, R., 2019. Local and Remote Forcing of Denitrification in the Northeast Pacific for the Last 2,000 Years. Paleoceanography and Paleoclimatology.

Watanabe, T., Wakatsuchi, M., 1998. Formation of 26.8–26.9 σθ water in the Kuril Basin of the Sea of Okhotsk as a possible origin of North Pacific Intermediate Water. Journal of Geophysical Research: Oceans, 103(C2): 2849-2865.

Xu, X., Segschneider, J., Schneider, B., Park, W., Latif, M., 2015. Oxygen minimum zone variations in the tropical Pacific during the Holocene. Geophysical Research Letters, 42(20): 8530-8537.

Yamamoto, M., Tanaka, N., Tsunogai, S., 2001. Okhotsk Sea intermediate water formation deduced from oxygen isotope systematics. Journal of Geophysical Research: Oceans, 106(C12): 31075-31084.

Yasuda, I., 1997. The origin of the North Pacific Intermediate Water. Journal of Geophysical Research, 102(C1): 893.

You, Y., 2003. The pathway and circulation of North Pacific Intermediate Water. Geophysical Research Letters, 30(24).

You, Y. et al., 2000. Roles of the Okhotsk Sea and Gulf of Alaska in forming the North Pacific Intermediate Water. Journal of Geophysical Research, 105(C2): 3253.

You, Y. et al., 2003. Transport of North Pacific Intermediate Water across Japanese WOCE sections. Journal of Geophysical Research, 108(C6).

Zenk, W. et al., 2005. Pathways and variability of the Antarctic Intermediate Water in the western equatorial Pacific Ocean. Progress in Oceanography, 67(1-2): 245-281.

Zheng, Y., 1999. The marine geochemistry of germanium, molybdenum and uranium: The sinks, ProQuest Dissertations Publishing.

Zheng, Y., Anderson, R.F., Geen, A.V., James, K., 2000. Authigenic molybdenum formation in marine sediments: A link to pore water sulfide in the Santa Barbara Basin. Geochimica et Cosmochimica Acta, 64(24): 4165-4178.

Zheng, Y., Anderson, R.F., van Geen, A., Fleisher, M.Q., 2002. Remobilization of authigenic uranium in marine sediments by bioturbation. Geochimica et Cosmochimica Acta, 66(10): 1759-1772.

Ziegler, M., Jilbert, T., de Lange, G.J., Lourens, L.J., Reichart, G.-J., 2008. Bromine counts from XRF scanning as an estimate of the marine organic carbon content of sediment cores. Geochemistry, Geophysics, Geosystems, 9(5).

Chapter 8

Conclusions

8.1 Summary of results and overall conclusions

In Chapter 2, I established the bulk sediment elemental analysis method that allows rapid and simultaneous major, minor, and trace element measurements from one microwave digested sample. The elemental analysis method overcomes the matrix effects and spectral influences by matrix separation using column chemistry and the collision cell prior to the quadrupole inductively coupled plasma mass spectrometry (Q-ICPMS). The multi-element analysis method shows good recovery (80 – 120%, mostly within ~90 – 110%) for 24 certified elements when tested against three sediment reference materials (MESS-3, PACS-2, and HISS-1) and comparable recoveries with published Santa Barbara Basin bulk elemental compositions (difference ≤ 20%, mostly <10%). Better Ag and Cd recoveries were achieved with a simplified column chemistry procedure modified from Prof. Thomas Pedersen Lab (University of Victoria, BC, Canada), which also reduced concentrated acid usage for batch sample processing. This bulk sediment analysis method could thus contribute to future high-resolution elemental reconstructions with rapid and simultaneous data acquisition.

In Chapter 3, I explored sedimentary redox proxy (indicators of ambient water oxygenation) responses (e.g., iron speciation and redox-sensitive trace metals) in the Santa Barbara Basin (SBB), which represents an intermediate environment with low-oxygen bottom waters and sulfidic (HS^- present and no oxygen) porewaters. I presented Fe speciation and magnetism data from a box core (SPR0901-04BC, 34°16.895'N, 120°02.489'W, 588 m water depth) that preserves sediment-water interface (SWI), to investigate how Fe speciation interpretations can be obscured by high sedimentation rates and non-steady-state diagenesis that is triggered by instantaneous depositional events (e.g., flood and turbidite layers). In particular, sedimentary Fe can be remobilized as Fe(II) following the instantaneous depositional events (i.e.,

turbidite or flood layer deposition), and this can lead to post-depositional (diagenetic) Fe sulfide (e.g., pyrite) formation after sulfidic porewater environments are re-established, This newly precipitated Fe sulfide then overprints the original redox signal. However, redox-sensitive trace metal records seem to be unaffected by this post-deposition remobilization as redox-sensitive trace metal enrichments are occurring near the SWI in the basin. Complications shown in this chapter thus highlight the necessity of scrutiny before applying redox proxies to local reconstructions.

In Chapter 4, I used the same box core (SPR0901-04BC) in Chapter 3 to reconstruct the Southern California oxygen minimum zone (OMZ) expansion since the Industrial Revolution. The OMZ gradually expanded after the ~1870s as redox-sensitive trace metals became more enriched. This expansion and intensification of the OMZ has been attributed to the anthropogenic warming trend during the 20th century. The anthropogenic influence on coastal OMZ are also indicated from the extreme low oxygen conditions after the 1969 oil spill off Santa Barbara. Additionally, interannual OMZ variability (waxing and waning) documented by bottom water observations from the California Cooperative Oceanic Fisheries Investigations and variations in the scanning X-ray fluorescence (XRF) Mo counts are attributed to El Niño Southern Oscillation (ENSO) variability. The transition from the El Niño to the La Niña state could have switched the basin from stagnant to ventilated as the flushing events allow the dense and oxygenated bottom water ventilate the SBB.

In Chapter 5, I presented a high resolution (~2 – 4 years) export productivity and denitrification records spanning the Common Era (the last 2,000 years). Through comparison between productivity proxies (total organic carbon, scanning XRF Si/Ti and Ca/Ti) and upwelling-related siliceous plankton assemblages, I observe that coastal upwelling – associated with the alongshore winds driven by the strengthened North Pacific High – is not always in phase with the total export productivity. I therefore suggest that wind-curl upwelling (associated with the positive wind curl off shore) plays an important role in driving SBB primary productivity when coastal upwelling is weak. In addition to providing a record of regional primary productivity, this denitrification record also shows a relationship between the competing tropics and subarctic water mass influences. Stronger connections with subsurface Eastern Tropical North Pacific (ETNP) denitrified waters are observed during the Medieval Climate Anomaly (MCA). However, a greater connection with the subarctic regions associated with the

anomalously deepened Aleutian Low (AL) is suggested during the Little Ice Age (LIA, 1670 – 1840 CE). This connection could have altered $\delta^{15}N_{sed}$ by advecting nutrient-rich subarctic waters via the California Current (CC). This chapter thus addresses the role of remote water mass advection (relevant to large-scale atmospheric forcing) in controlling the nitrogen sources in the California Current System (CCS).

In Chapter 6, I moved away from anthropogenic-forced OMZ shifts on the Southern California margin and focused on the natural OMZ variability on decadal to centennial time scales. The new high resolution (~4 – 9 years) Common Era OMZ reconstruction based on redox-sensitive trace metal enrichments reveals multiple intervals where low-oxygen bottom waters bathed SBB, with the most reducing conditions occurring during the MCA (940 – 1050 and 1100 – 1160 CE). Significantly larger magnitudes of OMZ oscillations based on redox-sensitive metal enrichments were observed during the MCA relative to the post-Industrial Revolution record of Chapter 4. More rapid OMZ intensification during the MCA compared to the post-Industrial was also observed from Mo enrichment intensification rates. Thus, modern observations are not of sufficient duration to fully capture the magnitude and rate of natural OMZ oscillations. Despite relatively oxygenated conditions found during the early LIA (1250 – 1500 CE), a low-oxygen interval is identified during 1550 – 1750 CE, coincident with the coolest air temperature of the Common Era (PAGES 2k Consortium, 2017). Insignificant variance of export productivity suggests a remote ventilation control of the sustained low oxygen conditions. Reduced Sea of Okhotsk ice formation (Itaki, 2004) during ~1550 – 1750 CE, was associated with the prevailing easterlies induced by a westward/weakened AL and Siberian High (SH) over this interval, which is corroborated the Last Millennium Reanalysis (Tardif et al., 2019). The reduced sea ice formation could then lead to less ventilated North Pacific Intermediate Water (NPIW) and subsequent low oxygen conditions on the Southern California margin, despite the coolest conditions in the last 2000 years (~1550 – 1750 CE). It is thus suggested that sea ice formation and the consequent intermediate water ventilation responses to natural climate change in the Common Era is not a simple response to temperature, but ARE also sensitive to large-scale atmospheric forcing that changes wind directions and stress (e.g., positions and locations of AL and SH). This chapter underlines the complex nature of OMZ natural variability associated with large-scale atmospheric circulations.

Chapter 7 presents a Holocene oxygen reconstruction that allows a full Holocene perspective of Southern California OMZ oscillations. Along with other published records that span the depth range of the Southern California OMZ, a consistent OMZ expansion and intensification is suggested during the early- to mid-Holocene. Decoupled responses of authigenic redox-sensitive metal fluxes to export productivity again indicate intermediate water ventilation shifts. The lack of Equatorial Pacific Intermediate Water oxygen variations implies the less ventilated NPIW associated with reduced sea ice formation in the Sea of Okhotsk, as corroborated by Sea of Okhotsk ventilation records (Lembke-Jene et al., 2018) and the state-of-the-art model (Community Earth System Model) simulations in the mid-Holocene. Unlike the Common Era case where the orbital parameter was similar to present, the mid-Holocene orbital configuration features stronger Northern Hemisphere solar insolation that results in a northward displacement of the Intertropical Convergence Zone (ITCZ) and a subsequent weaker and/or westward AL through the Rossby wave responses (Trenberth et al., 1998). This chapter further addresses Southern California OMZ responses to the external natural forcing (e.g., orbital forcing).

8.2 Synthesis

Marine sediment archives can be utilized to reconstruct past oxygen variability beyond the instrumental observations. However, post-depositional alteration (diagenesis) of the original oxygenation signal is likely to obscure the dissolved O_2 reconstructions. In this dissertation, I have discussed the post-depositional diagenetic processes triggered by the instantaneous depositional events (flood and turbidite deposition) in the SBB with implications on the caution needed for oxygenation reconstructions using Fe speciation records. This work thus addresses the importance of multi-proxy oxygen reconstructions and necessity of more research on sedimentary diagenetic processes. In the following studies, I presented a Holocene record of Southern California OMZ and investigated the driving mechanisms on the interannual to millennial timescales, providing high-resolution constraints on the magnitude and the rate of OMZ variations responding to anthropogenic and natural climate change. This work traced the influence of the anthropogenic warming trend on the Southern California OMZ intensification back to 1900s, and revealed the much larger natural variability compared to the pre-Industrial during the past 2000 years. Thus, I highlighted the necessity of more high-resolution studies to reveal the OMZ sensitivity to natural climate change that is not yet fully recovered from

observations. Additionally, this dissertation addresses the role of intermediate water ventilation on OMZ variability and the complex nature of ventilation responses to climate change. This work indicates that intermediate water ventilation is not solely forced by sea surface temperature but is strongly dependent on the atmospheric forcing, and decoupled ventilation responses from climate change could occur (e.g., the low oxygen interval during ~1550 – 1750 CE despite the coolest climate in the Common Era). This nuanced ventilation response could have contributed to a larger magnitude of OMZ variability when overlying with other anthropogenic/natural forcing mechanisms, and thus this work also emphasizes the necessity of better constraints on atmospheric forcing and intermediate water advection in the past oxygen reconstructions and future OMZ projections.

8.3 Future work

This dissertation work has raised a sequence of new research questions about redox proxy development and driving mechanisms of OMZ variability. These future research directions are outlined below.

(1) Given the common occurrences of diagenetic processes, is there a redox proxy that is not affected by certain diagenetic pathways? Results from this thesis have revealed diagenetic overprinting of Fe speciation interpretations, including Fe remobilization due to Fe oxyhydr(oxide) reduction and post-depositional pyrite formation upon deposition of flood and/or turbidite layers. Although not significant in our core records, redox-sensitive trace metal precipitation can also be perturbed by instantaneous depositional events (McKay and Pedersen, 2014; Mucci et al., 2003), and thus it is necessary to develop novel redox proxies that are less affected by these diagenetic processes. Implementation of the new redox proxies would contribute evaluations of diagenetic overprinting and provide additional information on the past oxygenation interpretations.

One candidate is thallium isotopic composition, which has shown to have the potential of tracing Mn oxide burial from the water column (Owens et al., 2017). As the primary sink of Tl, Mn oxide preferentially scavenges heavy Tl isotope to the sediments, leaving unique isotope signatures in response to Mn oxide burial flux shifts (Nielsen et al., 2005; Owens et al., 2017). No Tl fractionation has been observed in other redox-related processes (e.g., diagenetic pyrite formation), and thus a Tl isotope record from the SBB sediments could assist evaluation of diagenetic overprinting for the redox interpretations. As redox applications of Tl isotopes have

only been validated in oxygenated and sulfidic conditions, more modern calibration studies in the intermediate reducing environments (e.g., low-oxygen bottom waters and sulfidic porewaters in SBB) are required to systematically evaluate the use of Tl isotopes as a redox proxy.

(2) *How would anthropogenic input of nitrogen affect nutrient cycling (e.g., nitrogen) off Southern California?* The Common Era denitrification record in Chapter 5 demonstrates a persistent declining trend since 1800s that is decoupled from export productivity and local precipitation on the Southern California margin. Inconsistency between $\delta^{15}N$ and redox-sensitive trace metal enrichments from Chapter 6 indicates that the Southern California OMZ is not the primary driver for $\delta^{15}N$ variability, and thus the nitrogen budget (e.g., source and/or sink) shifts might have played a role. This > 1‰ decline of $\delta^{15}N$ in SBB sediments marks the most significant change during the past 2000 years and shows a regional coherence with Baja California and the Gulf of California sediments until the apparent OMZ intensification after 1970s in SBB (Deutsch et al., 2014; Tems et al., 2016). One possibility is that there was increased nitrate input from atmospheric deposition during ~1800s – 1970s, particularly anthropogenic atmospheric N (AAN), which has a light isotopic composition ($\delta^{15}N$ < -2‰) compared to the $\delta^{15}N$ of oxygenated deep ocean nitrate (> 5‰). Given that the heavily populated Southern California coastal environment may have witnessed drastic increase of AAN since the Industrial Revolution, a regional survey of N cycling is needed. This survey should include terrestrial sedimentary records (e.g., lake archives subject to anthropogenic influences), a monitoring network of atmospheric N deposition by dry and wet deposition sample collection, and a regional AAN model simulation from the land use data. This will be a critical step forward in our understanding of how human activities have affected nitrogen dynamics in the natural environment.

(3) How does the intermediate water ventilation affect the size and strength of OMZs around the North Pacific basin? Results in this thesis have suggested that NPIW plays a central role in controlling Southern California OMZ ventilation over the decadal to centennial timescales, as NPIW production has varied throughout the Holocene in response to atmospheric forcing associated with climate changes (Chapter 6 and 7). We have suggested that NPIW formation is not a simple response to sea surface temperature in a warm/cold climate but is sensitive to large scale atmospheric forcing associated with climate shifts. However, whether NPIW formation and ventilation shifts have basin-wide influences on the mid-depth ventilation is difficult to assess

given the lack of high-resolution Holocene redox records in the North Pacific. Additionally, NPIW formation sites have been suggested to migrate to the Bering Sea instead of the Sea of Okhotsk during the glacial periods (Cook et al., 2005; Ohkushi et al., 2003), which may have shifted the depth and circulation pathway of NPIW and affected mid-depth North Pacific ventilation. Thus, sediment mapping of dissolved oxygen concentrations at water depths between 500 and 1500 m (mid-depth) around the North Pacific basin during the Holocene and the glacial cycles would be constructive to evaluate the NPIW formation rate changes and how NPIW ventilation shifts have affected mid-depth Pacific oxygen concentrations in response to climate variations. In addition to more high-resolution sea ice and DO reconstructions at the NPIW formation regions, future studies focused on NPIW migration along its circulation path will better constrain NPIW modification (due to mixing and organic carbon degradation) and subsequent effects on mid-depth ventilation. In tandem with redox proxies for oxygenation reconstructions, a proxy for deep water circulation such as $^{231}Pa/^{230}Th$ could trace NPIW transport rates. As ^{230}Th has higher removal rate than ^{231}Pa, ^{231}Pa is more likely to escape local scavenging and be transported farther by subsurface water masses (Henderson and Anderson, 2003). Faster intermediate water mass transport would thus lead to a Pa deficit at the formation site but a higher $^{231}Pa/^{230}Th$ at a transport downstream site (McManus et al., 2004). Paired redox and $^{231}Pa/^{230}Th$ reconstructions in the mid-depth North Pacific would then provide valuable insights on the North Pacific circulation and ventilation history, with implications of mid-depth inorganic carbon storage changes in response to climate shifts.

(4) How does OMZ variability (internal/naturally forced) from transient simulations compare with proxy record reconstructions? Chapter 6 and 7 of the thesis reveal significant Southern California OMZ intensification on decadal to centennial timescales due to the naturally forced or internal variability. To date there is no direct model evidence of rapid OMZ intensification/recovery during the Common Era. Given the complex interplay of various controls on OMZ variability, a significant step forward is to perform a transient simulation using the state-of-the-art model with biogeochemistry component included. However, it has been suggested that model simulations are not capable of producing the spatial patterns in modern observations, especially the low-latitude OMZs (Andrews et al., 2013; Bopp et al., 2013). In addition, such model simulations are also computer-intensive. However, if given the computing resources and starting from intermediate complexity ocean, a biogeochemistry model might

provide some insights on the natural internal variations that control O_2 contents in the simulations. The data and model comparison would then improve our understanding of internal and/or externally forced OMZ oscillations.

8.4 References

Andrews, O.D., Bindoff, N.L., Halloran, P.R., Ilyina, T., Le Quéré, C., 2013. Detecting an external influence on recent changes in oceanic oxygen using an optimal fingerprinting method. Biogeosciences, 10(3): 1799-1813.

Bopp, L. et al., 2013. Multiple stressors of ocean ecosystems in the 21st century: projections with CMIP5 models. Biogeosciences, 10(10): 6225-6245.

Cook, M.S., Keigwin, L.D., Sancetta, C.A., 2005. The deglacial history of surface and intermediate water of the Bering Sea. Deep Sea Research Part II: Topical Studies in Oceanography, 52(16-18): 2163-2173.

Deutsch, C. et al., 2014. Centennial changes in North Pacific anoxia linked to tropical trade winds. Science, 345(6197): 665-668.

Henderson, G.M., Anderson, R.F., 2003. The U-series Toolbox for Paleoceanography. Reviews in Mineralogy and Geochemistry, 52(1): 493-531.

Itaki, T., 2004. Middle to late Holocene changes of the Okhotsk Sea Intermediate Water and their relation to atmospheric circulation. Geophysical Research Letters, 31(24).

Lembke-Jene, L., Tiedemann, R., Nürnberg, D., Gong, X., Lohmann, G., 2018. Rapid shift and millennial-scale variations in Holocene North Pacific Intermediate Water ventilation. Proceedings of the National Academy of Sciences, 115(21): 5365.

McKay, J.L., Pedersen, T.F., 2014. Geochemical response to pulsed sedimentation: Implications for the use of Mo as a paleo-proxy. Chemical Geology, 382: 83-94.

McManus, J.F., Francois, R., Gherardi, J.M., Keigwin, L.D., Brown-Leger, S., 2004. Collapse and rapid resumption of Atlantic meridional circulation linked to deglacial climate changes. Nature, 428(6985): 834-837.

Mucci, A., Boudreau, B., Guignard, C., 2003. Diagenetic mobility of trace elements in sediments covered by a flash flood deposit: Mn, Fe and As. Applied Geochemistry, 18(7): 1011-1026.

Nielsen, S.G. et al., 2005. Thallium isotope composition of the upper continental crust and rivers—An investigation of the continental sources of dissolved marine thallium. Geochimica et Cosmochimica Acta, 69(8): 2007-2019.

Ohkushi, K.i., Itaki, T., Nemoto, N., 2003. Last Glacial–Holocene change in intermediate-water ventilation in the Northwestern Pacific. Quaternary Science Reviews, 22(14): 1477-1484.

Owens, J.D., Nielsen, S.G., Horner, T.J., Ostrander, C.M., Peterson, L.C., 2017. Thallium-isotopic compositions of euxinic sediments as a proxy for global manganese-oxide burial. Geochimica et Cosmochimica Acta, 213: 291-307.

PAGES 2k Consortium, 2017. A global multiproxy database for temperature reconstructions of the Common Era. Sci Data, 4: 170088.

Tems, C.E. et al., 2016. Decadal to centennial fluctuations in the intensity of the eastern tropical North Pacific oxygen minimum zone during the last 1200 years. Paleoceanography, 31(8): 1138-1151.

Trenberth, K.E. et al., 1998. Progress during TOGA in understanding and modeling global teleconnections associated with tropical sea surface temperatures. Journal of Geophysical Research: Oceans, 103(C7): 14291-14324.

Appendices

Appendix A: Supplementary Information for Chapter 3

A.1 Methods for magnetic measurements

Freeze-dried samples were loaded into 5.28 cm^3 P1 plastic boxes at the Institute for Rock Magnetism, University of Minnesota. When the sample mass was not sufficient for P1 boxes, gel capsules were used which resulted in lower signal-to-noise ratio of magnetic measurements (11 – 12, 15 – 16, 22 – 23 and 34 – 35 cm). Here we outline the analytical procedures of anhysteretic remanent magnetization (ARM) and low-temperature remanence curve measurements.

A 2G Enterprises superconducting quantum interference device (SQUID) Passthrough Magnetometer in a magnetically shielded laboratory was used to measure ARMs and saturated isothermal remanent magnetizations (SIRMs). The measurement sequence was set as follows:

(1) An ARM was imparted by applying a 100 mT alternating field (AF) demagnetization superimposed by an axial 0.1 mT DC bias field, then measured and progressively AF demagnetized.

(2) A subsequent ARM was imparted by applying a 40 mT alternating field (AF) demagnetization and same DC bias field.

(3) An SIRM was imparted to the discrete samples via treatment of a 1 T direct field in a 2G core pulse magnetizer.

Low-temperature magnetic measurements were made on a quantum design magnetic properties measurement system (MPMS-5S) using the following procedure:

(1) A DC field of 2.5 T was continuously imparted on the sample while it cooled from 300 K to 10 K (field-cooled). The magnetic field was switched off at 10 K and the magnetic remanence was measured as the sample was warmed back up to 300K using a 5 K step, generating the field-cooled remanence curve (FC remanence).

(2) The sample was subsequently cooled in the absence of a magnetic field from room temperature to 10 K, and a 2.5 T low-temperature SIRM (LTSIRM) was imparted on the sample before its remanence was measured every 5 K during warming to 300 K producing the zero-field-cooled remanence (ZFC remanence).

(3) A room temperature SIRM (RTSIRM) was imparted on the sample for ~1 min at 300 K. The specimen was subsequently cooled to 10 K then warmed to 300 K, while measuring the magnetic (zero field) over the entire cooling-warming cycle using a measurement 5 K interval to generate the RTSIRM cooling and warming curves.

A.2 Magnetic measurement interpretations

A.2.1 Down-core profile of bulk-sediment measurements

We subdivided the core into three zones based on down-core variations that are defined by a gradual decrease of stable magnetic minerals, the coercivity of magnetic minerals (concentration-independent), and changes in magnetic grain size.

A.2.1.1 Zone 1 (0-35 cm)

Within the uppermost 35 cm, concentration-dependent parameters (χ, ARM, SIRM) are characterized by relatively high, yet variable values (Figs. 3-2a to c), suggesting high concentrations of stable ferrimagnetic minerals. The average S-ratio (backfield = 300 mT) value of 0.96 (Fig. 3-2h) supports the dominance of low coercivity magnetic minerals, while the HIRM indicates relatively high absolute concentrations of high-coercivity minerals (mean value 1.67×10^{-4} Am^2 kg^{-1}, Fig. 3-2c). Hysteresis loops, however, are mostly pot-bellied and saturate by 700 mT (Fig. A-1), suggesting that the high coercivity magnetic minerals (e.g., hematite and goethite) are only a minor constituent in the samples. ARM40/ARM, SIRM/χ, and ARM/SIRM provide information about magnetic grain sizes (Oldfield and Yu, 1994; Thompson, 1986). These three parameters reach their highest values within Zone 1 ($>\sim0.51$, $>\sim15\times10^{3}$ and $>\sim7\times10^{-2}$, respectively) and are consistent with the clustered Zone 1 samples falling in the 'vortex state' field following Roberts et al. (2018) on the Day plot (Fig. 3-3, Dunlop (2002)).

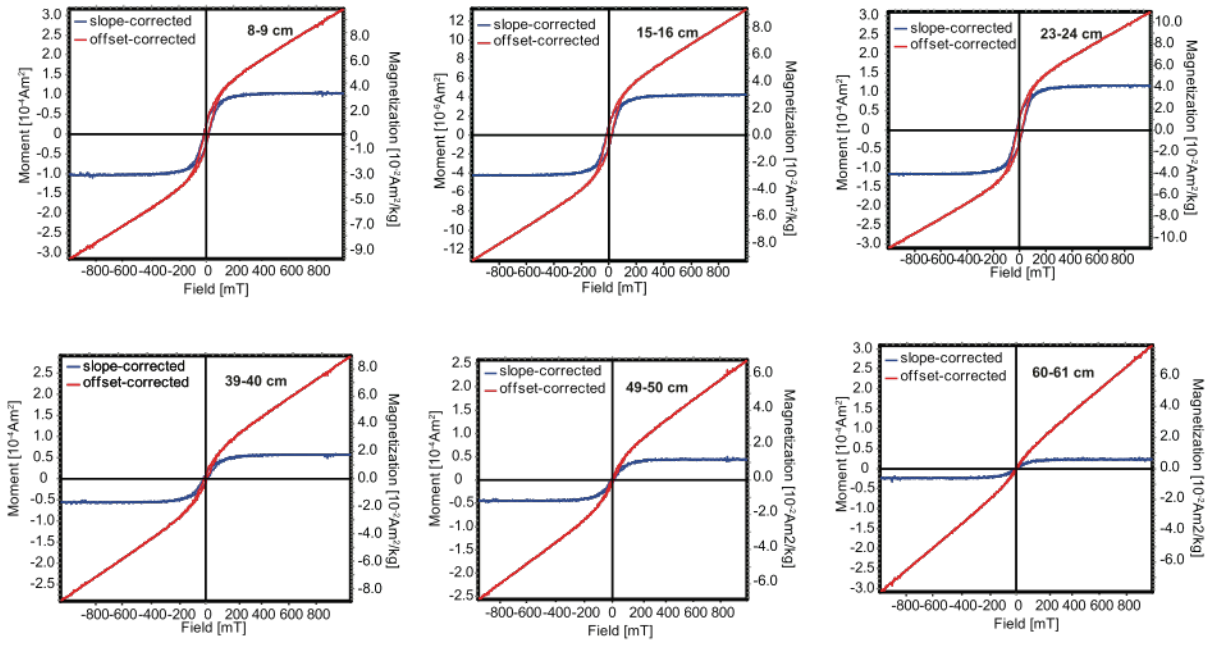

Figure A-1 Hysteresis loops for selected samples in core SPR0901-04BC. Red and blue curves represent hysteresis loops after offset-correction (e.g., Jackson and Solheid (2010)) and paramagnetic slope-correction, respectively. Sample depths are indicated.

This group of samples has the highest B_{cr} (40.78 mT – 53.78 mT) and B_c (17.32 mT – 23.67 mT), consistent with high coercivity minerals. B_{cr}/B_c and M_r/M_s values for Zone 1 primarily fall in narrow ranges (2.02 – 2.71 and 0.24 – 0.28, respectively). Despite the clustered data on the Day plot, selected FORC diagrams (Fig. 3-3) for Zone 1 samples show a 'central ridge' typical for non-interacting single domain (SD) and an expanded vertical distribution consistent with a vortex-state behavior (Egli et al., 2010; Newell, 2005; Roberts et al., 2014). Certain samples (e.g. 15 – 16 cm, Fig. 3-3) reveal a lobe-like morphology akin to interacting SD particles (Harrison and Lascu, 2014). It is noted that this morphology could in part be due to data quality that results in horizontal streaking in the FORC diagrams. Increased smoothing reduces the indentation between the central ridge and the lower lobe, however the horizontal streaking cannot be fully overcome without over-smoothing. Discriminating between vortex-state and interacting SD particles would be somewhat speculative. However, interactive SD behavior could be caused by either dissolution of Fe oxides and subsequent authigenic recrystallization, or collapse of biogenic magnetite chains (e.g., Harrison and Lascu (2014)). Preservation and oxidation of primary phases, including biogenic magnetite, a conclusion of this study, would preclude dissolution and in-situ recrystallization, and thus favor gradual collapse of biogenic magnetite

chains. Alternatively, vortex-state distributions would result from a population of larger grains, and thus reflect a detrital process. This interpretation is consistent with a shift of the B_c peak towards lower-coercivities with depth (~45 mT to ~35 mT in Fig. 3-3), further suggesting increasing grain size within Zone 1. This observation is consistent with the trend observed through Zones 2 and 3 described below.

A.2.1.2 Zone 2 (35 – 56 cm)

This zone features a major transition to much lower magnetic mineral concentrations and a coarser magnetic grain size distribution. Concentration-dependent magnetic parameters (χ, ARM, SIRM) all decrease within this ~20 cm stratigraphic interval, indicating a constant depletion of stable magnetic minerals downcore. Parameters sensitive to stable SD mineral assemblages (ARM) display a greater decline (by 93.1%) (Fig. 3-2b) than magnetic properties (χ and SIRM) that are more sensitive to vortex-state and MD particles (Figs. 3-3a and c, 36.8% and 80.7%, respectively). The mean S-ratio sharply decreases to 0.89 immediately below 35 cm, indicating increased relative contribution of high-coercivity magnetic minerals (hematite or goethite) despite decreases in their absolute concentration observed in the HIRM (Figs. 3-2g). However, the saturation field of hysteresis loops only indicates minor contributions from high-coercivity components. Magnetic grain size indicators (ARM40/ARM, SIRM/χ, and ARM/SIRM) also display sharp declines in this zone (Figs. 3-2d to f), and together point to coarser magnetic grain sizes at depth, which is consistent with the coarsening trend observed on the Day plot (Fig. 3-3). Note, however, that an increase in high coercivity minerals will increase the B_{cr}/B_c ratio, also producing a "coarsening trend" on the Day plot. For these reasons the Day plot should be interpreted with caution when mixtures of Ti-magnetite and hematite are present.

In contrast to the clustered hysteresis parameters observed in Zone 1, hysteresis parameters in Zone 2 are rather scattered on the Day plot, reflecting greater variations in particle grain sizes. Samples have lower but less variable B_{cr} values (37.08 mT – 40.02 mT), while B_c values decrease significantly (4.50 mT – 20.09 mT), resulting in a noticeable shift toward high B_{cr}/B_c values of 8.63 (Fig. 3-3). M_r/M_s values range from 0.04 (55 – 56 cm) to 0.24, and together with B_{cr}/B_c form a trajectory towards coarser vortex-state to MD assemblages according to FORC diagrams (Fig. 3-3).

FORC diagrams further illustrate the down-core mineralogy transition. The closed contours of the FORC data move towards the B_u axis and the high B_c peaks observed in Zone 1 gradually disappear with depth. Near the base of Zone 2 FORC distributions lose closed central contours and are dominated by low-coercivity vortex-state/MD magnetic minerals consistent with the FORC diagrams (Egli et al., 2010; Roberts et al., 2014). It is also noticed that the vertical distribution at $B_c = 0$, indicative of MD behavior, is not entirely contained within the confidence envelopes (e.g., 49 – 50 cm) and thus vortex-state behaviors seem to be still dominant. Additionally, occasional appearance of superparamagnetic (SP) contributions cannot be entirely ruled out from the FORC distributions (e.g., the positive region in negative quadrangle of B_u for 49 – 50 cm).

Zone 2 also features two instantaneous sediment deposition layers, a ~0.7-cm-thick gray layer associated with the 1861 – 1862 flood event (Hendy et al., 2015) and an ~8-cm olive layer attributed to a turbidite induced by the 1812 Santa Barbara earthquake (Napier and Hendy, 2016). Within the gray layer, a slight χ peak and sharp decrease ARM/SIRM indicate an external input of coarse ferrimagnetic minerals although other parameters remain constant (Figs. 3-2a and f). Similarly, the olive layer records a higher and stable χ level and larger magnetic grain sizes suggesting vortex-state/MD ferrimagnetic mineral input (Fig. 3-2). Magnetic mineralogy responses to these deposition events are also visible from L-ratio (Liu et al., 2007). Below 40 cm, a correlation between L-ratio and HIRM is observed (Fig. 3-4, $R^2 = 0.5450$, $n = 16$, $p<0.01$), indicating that coercivity plays a role in controlling HIRM values. The most variable L-ratios coincide with the turbidite layer (ranging from ~0.30 at 50 cm to ~0.49 at 48 cm), confirming instantaneous input of high-coercivity minerals (e.g., hematite) via the turbidite. Additionally, L-ratio declines above and below 48 cm are also observed.

A.2.1.3 Zone 3 (56 – 61 cm)

This stratigraphic interval has the lowest concentrations of magnetic minerals with the highest proportion of high coercivity minerals (Fig. 3-2h). There is no systematic difference in concentration-dependent magnetic parameters from the base of Zone 2, yet coercivity and mineralogical properties are easily distinguished from the samples of Zone 2. Immediately below the zone boundary (59 cm), B_{cr} (36.04 mT – 54.55 mT), B_c (5.91 mT – 20.98 mT), B_{cr}/B_c (2.12 – 6.23), and M_r/M_s (0.09 – 0.16) reverse the trend back toward finer grain sizes (more vortex-state

like behavior) (Fig. 3). The highest B_{cr} in this zone (54.55 mT, 59 – 60 cm) is comparable to the maximum value in Zone 1 (53.78 mT). However, this high value is attributed to vortex-state/MD high-coercivity Fe oxide input on the basis of lower S-ratios.

FORC distribution further suggest mineralogy shifts towards increased contributions from high-coercivity Fe oxides (e.g., hematite), as indicated by extended divergent contours to ~200 mT along the B_c axis, although not entirely contained by the 95% confidence intervals (Fig. 3-3). Additionally, an elongated central feature is present in the FORC distribution up to ~130 mT (60-61 cm), and a return to a finer grain size is shown on the Day plot This looping trend of the Day plot is also reported by (Rowan et al., 2009) in the northern California margin and Oman margin, where the looping trend results from growth of SP greigite to a stable SD range (Rowan et al., 2009). From the FORC distributions, we cannot rule out SP greigite formation, but decreasing S-ratios and ARM/SIRM values in most of Zone 3 (Figs. 3-2f and g) seem to argue against significant contributions from SD greigite. Sample depths in Zone 3 are still above the sulfate-methane transition zone (SMTZ) in SBB (~100 – 160 cmbct, Kuwabara et al. (1999); Raven et al. (2016)), and high sulfide concentrations in porewaters are not conducive for significant preservation of meta-stable species of Fe sulfides (Kao et al., 2004).

Zone 3 also contains a 1.5-cm thick gray layer associated with the 1761 flood (Hendy et al., 2015). In contrast to the previous gray layer, χ, ARM, and SIRM show a sharp decline, suggesting decreasing concentrations of ferrimagnetic minerals. However, magnetic grain size indicators exhibit similar responses with a sharp decline in SIRM/ χ and ARM/SIRM, and thus implicate coarser magnetic grain sizes in the gray layer, which is consistent with the other instantaneous deposition layers in Zone 2 (Figs. 3-2e and f). The L-ratio within Zone 3 also demonstrates a linear relationship with HIRM (Fig. 4, $R^2 = 0.7310$, $n = 6$, $p < 0.05$), suggesting that coercivity exerts a control on HIRM changes, similar to the Zone 2 samples that would indicate a similar massive introduction of high-coercivity minerals by the flood layer. However, Zone 3 samples have a significantly different slope (95% confidence level) from the regression line of Zone 2, and seem to indicate that a 'harder' (higher-coercivity) mineral assemblage is deposited in flood layers compared to the turbidites.

A.2.2 Low temperature measurements

Field-cooling (FC) and zero field-cooling (ZFC) curves show monotonous remanence decay during the warming process to room temperature (Fig. A-2). Generally, FC remanence is

stronger than ZFC but the difference gradually decreases as temperature increases. Siderite is not detected as no sharp decay was observed in FC remanence at its Néel temperature of 37 K (Frederichs et al., 2003), yet the separation of the FC and ZFC curves up to ~250 K together with a modest, but distinct increase of remanence with decreasing temperature in the RTSIRM curves (particularly below T_V) is indicative of goethite presence (Figs. A-2 and A-3) (Liu et al., 2006). Superimposed, a general negative slope of all RTSIRM curves from low to room temperature is consistent with small amount of goethite in the samples.

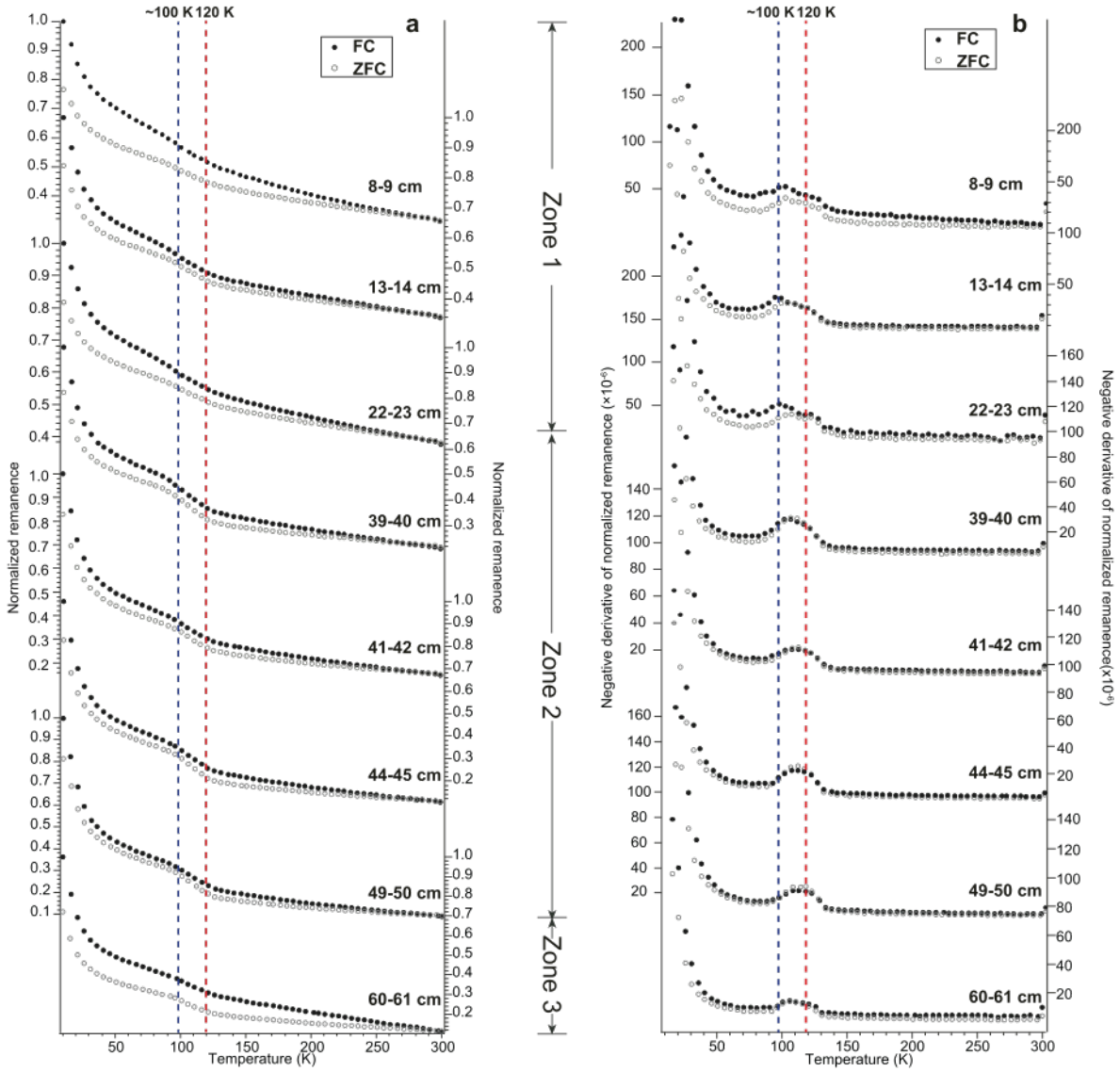

Figure A-2 Field-cooled (FC) and zero-field-cooled (ZFC) treatments of SPR0901-04BC samples. (a) Low-temperature warming curves of remanence after ZFC and FC treatments for selected samples throughout the core. Filled and hollow circles represent FC and ZFC remanence curves, respectively. Remanence is normalized to the low-temperature SIRM after FC treatments on each sample. (b) Corresponding derivatives of the FC and ZFC curves in (a). Sample depths are shown on the figure. The blue and red dashed vertical lines indicate the two T_v peaks at ~100 and 120 K observed in the core, respectively.

A relatively gradual remanence decrease is observed between ~100 K and ~120 K, suggesting a broad Verwey transition (T_v) (Fig. A-2b). The presence of a T_v is also supported by the 120 K peaks in the derivative of the RTSIRM curves between 300 and 10 K upon cooling and warming (Fig. A-3b, Özdemir and Dunlop (2010)).

No sharp remanence increase in RTSIRM upon warming is observed at 30 – 34 K, suggesting that pyrrhotite ($Fe_{1-x}S$, x = 0~0.2) is not a major component in any samples (Dekkers, 1989; Rochette et al., 1990). Although no Morin transition is observed in the RTSIRM cycling curves at ~260 K, hematite is still likely to be present as the transition can be greatly depressed if hematite is fine-grained and/or there are defects in the crystal lattices (de Boer et al., 2001; Dunlop and Özdemir, 1997). RTSIRM cooling curves typically gradual increases at first with a subsequent faster decreases forming a hump-shaped curve that is matched with another humped curve during warming (Chang et al., 2016; Chang et al., 2013; Özdemir and Dunlop, 2010)(Fig. A-3a), indicating maghemitization (oxidation of magnetite) throughout the core (Özdemir and Dunlop, 2010). Along with suppressed Verwey transitions, low-temperature measurements together suggest that maghemite and/or magnetite mixtures are present throughout the core (Özdemir and Dunlop, 2010; Özdemir et al., 1993).

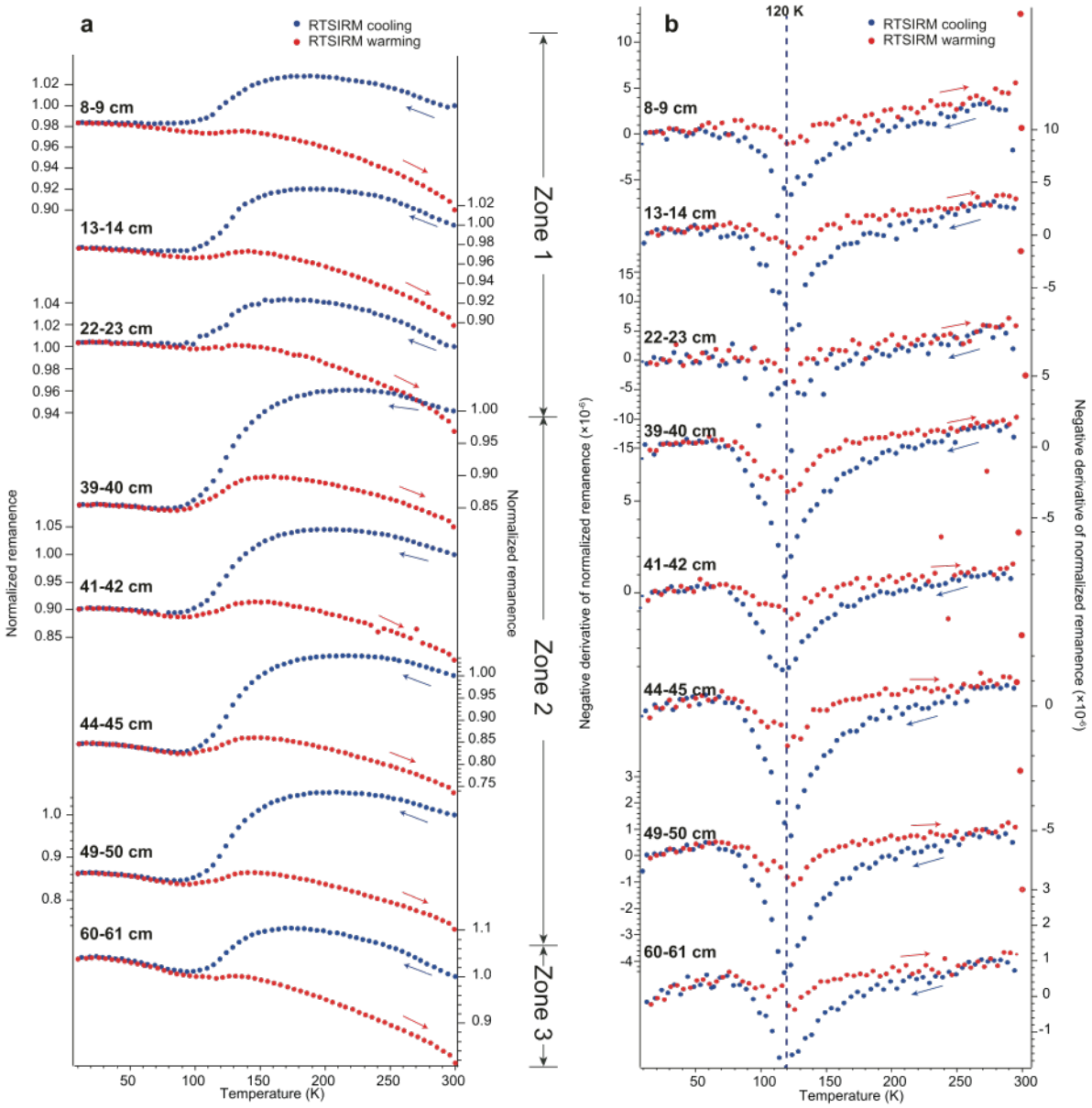

Figure A-3 Low-temperature cycling (LTC) of room temperature SIRM (RTSIRM). (a) Normalized RTSIRM low-temperature cycling curves for selected samples from core SPR0901-04BC. Blue and red circles represent cooling and warming data, respectively. Arrows suggest the direction of temperature scans. Remanence is normalized towards the RTSIRM at the beginning of a cooling cycle. (b) Corresponding derivatives of the LTC curves. Depths are indicated in the figure. The dashed blue line shows T_v at 120 K.

For Zone 1 (0 – 35 cm), first derivatives of FC and ZFC remanence curves have broad peaks between 100 – 120 K, and a double-peak at ~98 K and ~118 K is commonly observed, especially in the FC remanence curves (Fig. A-2b), which suggest that Zone 1 samples contain a significant amount of mixed, oxidized biogenic and inorganic magnetite (Chang et al., 2016),

which is consistent with the 'central ridge' features in FORC distributions for samples of Zone 1 (Fig. A-2).

FC and ZFC remanence curves in Zone 2 and Zone 3 are characterized by a pronounced decrease at around T_v = 120 K, suggesting higher contribution from detrital magnetite than Zone 1 (Chang et al., 2016). Concurrently, first derivatives of the two curves show one broad bell-shaped peak at T_v but no double-peak feature can be observed. Additionally, in the low temperature cooling (LTC) treatment, remanence recovery for samples in Zone 2 and 3 is lower compared to Zone 1, varying from ~0.75 – 0.85 (Fig. A-3a). Irreversible LTC curves and disappearance of peak splitting around T_v suggest dominance of less maghemitized inorganic magnetite in these two zones and larger magnetic grain sizes (Chang et al., 2013).

A.2.3. High temperature measurements

Magnetic susceptibility slightly increases before ~250 °C suggesting formation of magnetite from oxidation of iron sulfides. Susceptibility then gradually increases until a sharp peak appears at ~500 °C, which is indicative of newly created magnetic minerals upon heating. Repeated heating treatments for selected samples show constantly increasing susceptibility in the successive cooling curves, confirming continuous magnetite formation during the heating cycles. At depth, the peak is suppressed and becomes broader, consistent with inversion of maghemite to hematite (~450 °C, e.g., Dunlop and Özdemir (1997)).

A Curie temperature (T_c) at 580 °C in most samples confirms the presence of magnetite, partly due to pyrite/Fe sulfide oxidation when heating in the air (Figs. A-4a and b). Susceptibility values are typically higher during the cooling process, indicating continued formation of magnetite after T_c (Roberts, 1995; Roberts et al., 2011). Repeated heating treatments for selected samples also show constantly increasing susceptibility in the successive cooling curves, which confirms continuous magnetite formation during the heating cycles. Fig. A-4c demonstrates that a higher T_c at ~700 °C should be associated with further oxidation and inversion of maghemite to hematite (Hunt et al., 1995). For some samples from Zone 2 and Zone 3, cooling curves also demonstrate a major increase in susceptibility at ~300 °C (e.g., 44 – 45 cm and 60 – 61 cm), indicating significant generation of pyrrhotite (T_c = 320 °C) from pyrite oxidation (Hunt et al., 1995). Overall, high-temperature treatments confirm widespread Fe sulfides (e.g., pyrite) presence throughout the core.

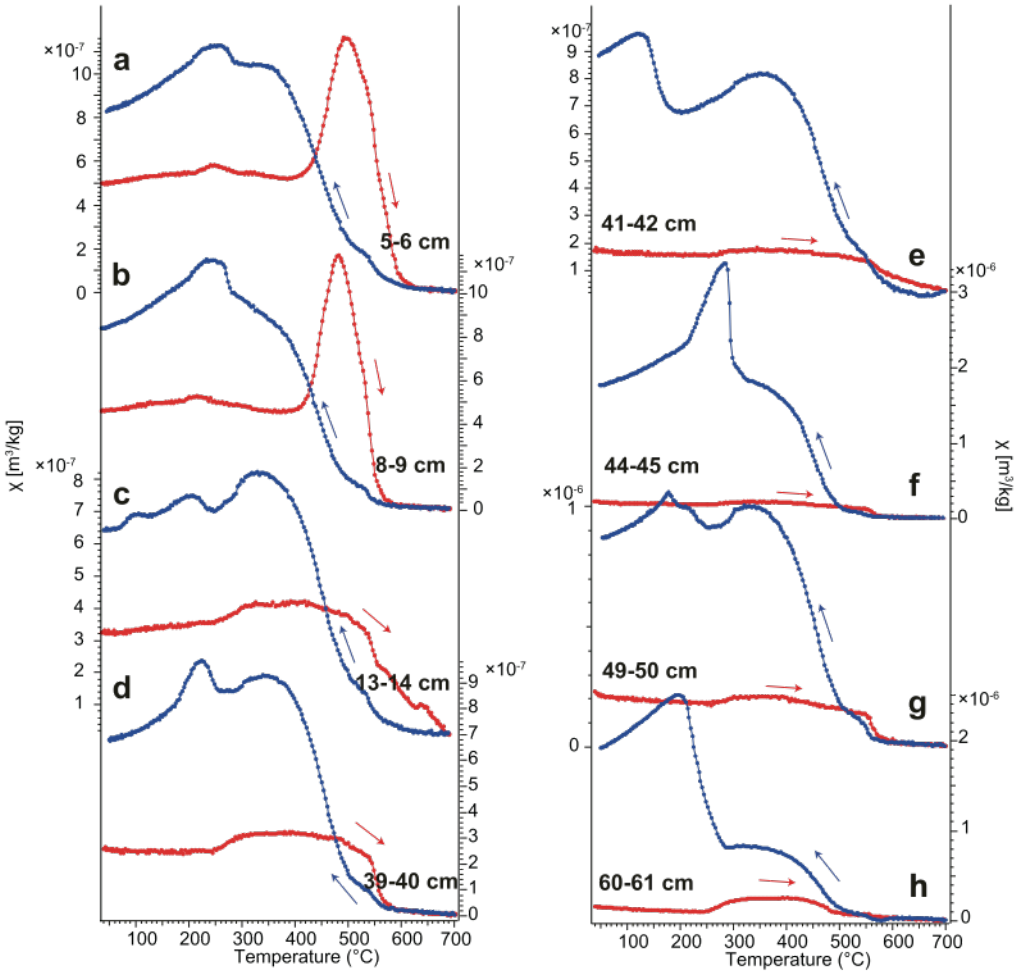

Figure A-4 High-temperature susceptibility curves of SPR0901-4BC samples. Red and blue curves are heating and cooling curves, respectively. Arrows represent the direction of temperature changes and sample depths are indicated.

A.3 Trace metal enrichment factors

Enrichment factors (EF) for redox-sensitive elements for SPR0901-04BC are presented in (Wang et al., 2017) and thus methods for $metal_{EF}$ calculation are only summarized here. Enrichment factors are obtained from measured metal concentrations and the regional lithogenic background values of SBB terrigenous sediment sources using the following equation (Turekian and Wedepohl, 1961):

$$EF_i = \frac{(\frac{Element}{Al})_{sample}}{(\frac{Element}{Al})_{background}} \qquad \text{(Eq. A-1)}$$

The Santa Clara River, Ventura River, and the Channel Islands along the southern basin margin transport sediment into the basin and are used to obtain background metal values for SBB

sediments prior to enrichment (Feleischer, 1972; Marsaglia et al., 1995). Redox-sensitive metal concentrations of fine-grained (<63 μm) stream bed samples (Wang et al., 2017) are used to obtain the mean background lithogenic sediment value for each catchment. The lithogenic background of each redox-sensitive metal is then calculated from the relative sediment flux contribution for each river (78, 7, and 15% for the Santa Clara River, Ventura River and the Channel Islands, respectively) following Warrick et al. (2009).

Table A-1 Comparison of Fe_{dith} with Raven et al. (2016)

Depth (cm, Raven et al. (2016))*	Fe_{dith} (%)	Depth (cm)	Fe_{dith} (%) in this manuscript	Average Fe_{dith} (%) in this manuscript
1-3.5	0.57	2 – 3	0.51	0.51
3.5-6	0.62	3 – 4, 4 – 5, 5 – 6	0.63, 0.66, 0.65	0.65
8.5-11	0.56	8 – 9, 9 – 10, 10 – 11	0.59, 0.72, 0.68	0.66
13.5-16	0.37	13 – 14, 14 – 15	0.36, 0.40	0.38
23.5-26	0.25	23 – 24, 24 – 25, 25 – 26	0.62, 0.44, 0.54	0.53
33.5-36	0.21	33 – 34, 35 – 36	0.60, 0.36	0.48
43.5-46	0.20	43 – 44, 44 – 45, 45 – 46	0.51, 0.29, 0.49	0.43
53.5-56	0.16	53 – 54, 55 – 56	0.31, 0.49	0.40

* We assume the depths are similar as Raven et al. (2016) collected the core material in 2013, 4 years after the SPR0901-04BC were collected. As no core location information was provided in the paper, we assume similar bottom water and porewater environments. Unfortunately, no description of sediments in their core was included in the paper so we do not know if instantaneous depositional events appeared in their core, or the depths of these events, which would have aided core correlation.

A.4 References

Chang, L., Heslop, D., Roberts, A.P., Rey, D., Mohamed, K.J., 2016. Discrimination of biogenic and detrital magnetite through a double Verwey transition temperature. Journal of Geophysical Research: Solid Earth, 121: 3-14.

Chang, L. et al., 2013. Low-temperature magnetic properties of pelagic carbonates: Oxidation of biogenic magnetite and identification of magnetosome chains. Journal of Geophysical Research: Solid Earth, 118: 6049-6065.

de Boer, C.B., Mullender, T.A.T., Dekkers, M.J., 2001. Low-temperature behaviour of haematite- susceptibility andmagnetization increase on cycling through the Morin transition. Geophysical Journal International, 146: 201-216.

Dekkers, M.J., 1989. Magnetic properties of natural pyrrhotite. II. High- and low-temperature behaviour of Jrs and TRM as function of grain size. Physics of the Earth and Planetary Interiors, 57: 266-283.

Dunlop, D.J., 2002. Theory and application of the Day plot (Mrs/Ms versus Hcr/Hc) 1. Theoretical curves and tests using titanomagnetite data. Journal of Geophysical Research, 107(B3).

Dunlop, D.J., Özdemir, Ö., 1997. Rock Magnetism: Fundamentals and Frontiers. Cambridge University Press, New York.

Egli, R., Chen, A.P., Winklhofer, M., Kodama, K.P., Horng, C.-S., 2010. Detection of noninteracting single domain particles using first-order reversal curve diagrams. Geochemistry, Geophysics, Geosystems, 11(1): 1-22.

Feleischer, P., 1972. Mineralogy and Sedimentation history, Santa Barbara Basin, California. Journal of Sedimentary Petrology, 42(1): 49-58.

Frederichs, T., von Dobeneck, T., Bleil, U., Dekkers, M.J., 2003. Towards the identification of siderite, rhodochrosite, and vivianite in sediments by their low-temperature magnetic properties. Physics and Chemistry of the Earth, 28: 669-679.

Harrison, R.J., Lascu, I., 2014. FORCulator: A micromagnetic tool for simulating first-order reversal curve diagrams. Geochemistry, Geophysics, Geosystems, 15(12): 4671-4691.

Hendy, I.L., Napier, T.J., Schimmelmann, A., 2015. From extreme rainfall to drought: 250 years of annually resolved sediment deposition in Santa Barbara Basin, California. Quaternary International, 387: 3-12.

Hunt, C.P., Moskowitz, B.M., Banerjee, S.K., 1995. Magnetic properties of rocks and minerals: a handbook of physical constants, Rock physics and phase relations. American Geophysical Union, pp. 189-204.

Jackson, M., Solheid, P., 2010. On the quantitative analysis and evaluation of magnetic hysteresis data. Geochemistry, Geophysics, Geosystems, 11(Q04Z15).

Kao, S.-J., Horng, C.-S., Roberts, A.P., Liu, K.-K., 2004. Carbon–sulfur–iron relationships in sedimentary rocks from southwestern Taiwan: influence of geochemical environment on greigite and pyrrhotite formation. Chemical Geology, 203(1-2): 153-168.

Kuwabara, J.S., Geen, A.V., Mccorkle, D.C., Bernhard, J.M., 1999. Dissolved sulfide distributions in the water column and sediment pore waters of the Santa Barbara Basin. Geochimica et Cosmochimica Acta, 63(15): 2199-2209.

Liu, Q., Roberts, A.P., Torrent, J., Horng, C.-S., Larrasoaña, J.C., 2007. What do the HIRM and S-ratio really measure in environmental magnetism? Geochemistry, Geophysics, Geosystems, 8(9): 1-10.

Liu, Q. et al., 2006. The characteristic low-temperature magnetic properties of aluminous goethite [α-(Fe, Al)OOH] explained. Journal of Geophysical Research, 111(B12S34).

Marsaglia, K.M., Rimukus, K.C., Behl, R.J., 1995. Provenance of sand deposited in the Santa Barbara Basin at Site 893 during the last 155,000 years. In: Kennett, J.P., Baldauf, J.G., Lyle, M. (Eds.), Proceedings of the Ocean Drilling Program, Scientific Results.

Napier, T.J., Hendy, I.L., 2016. The impact of hydroclimate and dam construction on terrigenous detrital sediment composition in a 250-year Santa Barbara Basin record off southern California. Quaternary International, in press.

Newell, A.J., 2005. High-precision first-order reversal curve (FORC) functions for single-domain ferromagnets with uniaxial anisotropy. Geochemistry, Geophysics, Geosystems, 6(Q05010): 1-14.

Oldfield, F., Yu, L., 1994. The influence of particle size variations on the magnetic properties of sediments from the north-eastern Irish Sea. Sedimentology, 41: 1093-1108.

Özdemir, Ö., Dunlop, D.J., 2010. Hallmarks of maghemitization in low-temperature remanence cycling of partially oxidized magnetite nanoparticles. Journal of Geophysical Research, 115(B02101).

Özdemir, Ö., Dunlop, D.J., Mokowitz, B.M., 1993. The effect of oxidation on the Verwey transition in magnetite. Geophysical Research Letters, 20(16): 1671-1674.

Raven, M.R., Sessions, A.L., Fischer, W.W., Adkins, J.F., 2016. Sedimentary pyrite δ34S differs from porewater sulfide in Santa Barbara Basin: Proposed role of organic sulfur. Geochimica et Cosmochimica Acta, 186: 120-134.

Roberts, A.P., 1995. Magnetic properties of sedimentary greigite (Fe3S4). Earth and Planetary Science Letters, 134: 227-236.

Roberts, A.P., Chang, L., Rowan, C.J., Horng, C.-S., Florindo, F., 2011. Magnetic properties of sedimentary greigite (Fe3S4): An update. Reviews of Geophysics, 49(1).

Roberts, A.P., Heslop, D., Zhao, X., Pike, C.R., 2014. Understanding fine magnetic particle systems through use of first-order reversal curve diagrams. Reviews of Geophysics, 52: 557-602.

Roberts, A.P., Tauxe, L., Heslop, D., Zhao, X., Jiang, Z., 2018. A Critical Appraisal of the "Day" Diagram. Journal of Geophysical Research: Solid Earth.

Rochette, P., Fillion, G., Mattéi, J.-L., Dekkers, M.J., 1990. Magnetic transition at 30-34 Kelvin in pyrrhotite-insight into a widespread occurrence of this mineral in rocks. Earth and Planetary Science Letters, 98: 319-328.

Rowan, C.J., Roberts, A.P., Broadbent, T., 2009. Reductive diagenesis, magnetite dissolution, greigite growth and paleomagnetic smoothing in marine sediments: A new view. Earth and Planetary Science Letters, 277(1-2): 223-235.

Thompson, R., 1986. Environmental Magnetism. Springer Netherlands.

Turekian, K., Wedepohl, K.H., 1961. Distribution of the Elements in Some Major Units of the Earth's Crust. Geological Society of America Bulletin, 72: 175-192.

Wang, Y., Hendy, I., Napier, T.J., 2017. Climate and Anthropogenic Controls of Coastal Deoxygenation on Interannual to Centennial Timescales. Geophysical Research Letters, 44(22): 11528–11536.

Appendix B: Supplementary Information for Chapter 4

B.1 Validity of XRF redox proxy analyses

Scanning XRF provides high-resolution elemental measurements for sediment samples in a rapid and non-destructive manner, which has proved to be particularly promising in complimenting quantitative elemental analyses, as short time-scale variations are usually averaged out in conventional measurements. Correlation analysis suggest statistically significant relationships between ICP-MS/AES measurements and scanning XRF counts at 1% significance level except for S (p-value = 0.0546 for S, n = 61), which may be attributed to attenuation of radiation by the water content in wet core sediments (Dickson et al., 2012; Tjallingii et al., 2007).

Due to the variability in X-ray penetration depth caused by heterogeneous grain sizes and porosity, non-linear responses to elemental variations are expected in sediment cores, especially for light elements like S (Hennekam and de Lange, 2012; Richter et al., 2006). Scanning XRF record Mo seems to miss the enrichment peak at 1969 from the ICP-MS profile caused by the oil spill in the Santa Barbara Channel, which might be associated with its high signal-to-noise ratio. However, it is notable that scanning XRF records for redox sensitive elements not only captured major peaks of ICP-MS/AES analyses, but also exhibit comparable or larger relative shifts compared with ICP-MS/AES records, indicating the scanning XRF records capture the underlying signal despite the high-frequency noise in the Mo and S records (Fig. B-1). Therefore, although a linear relationship between scanning XRF data to ICP-MS/AES analyses is not quantitatively possible, scanning XRF records associated with redox sensitive elements capture highly resolved relative elemental variability, validating their use to increase the temporal resolution of proxy records through time.

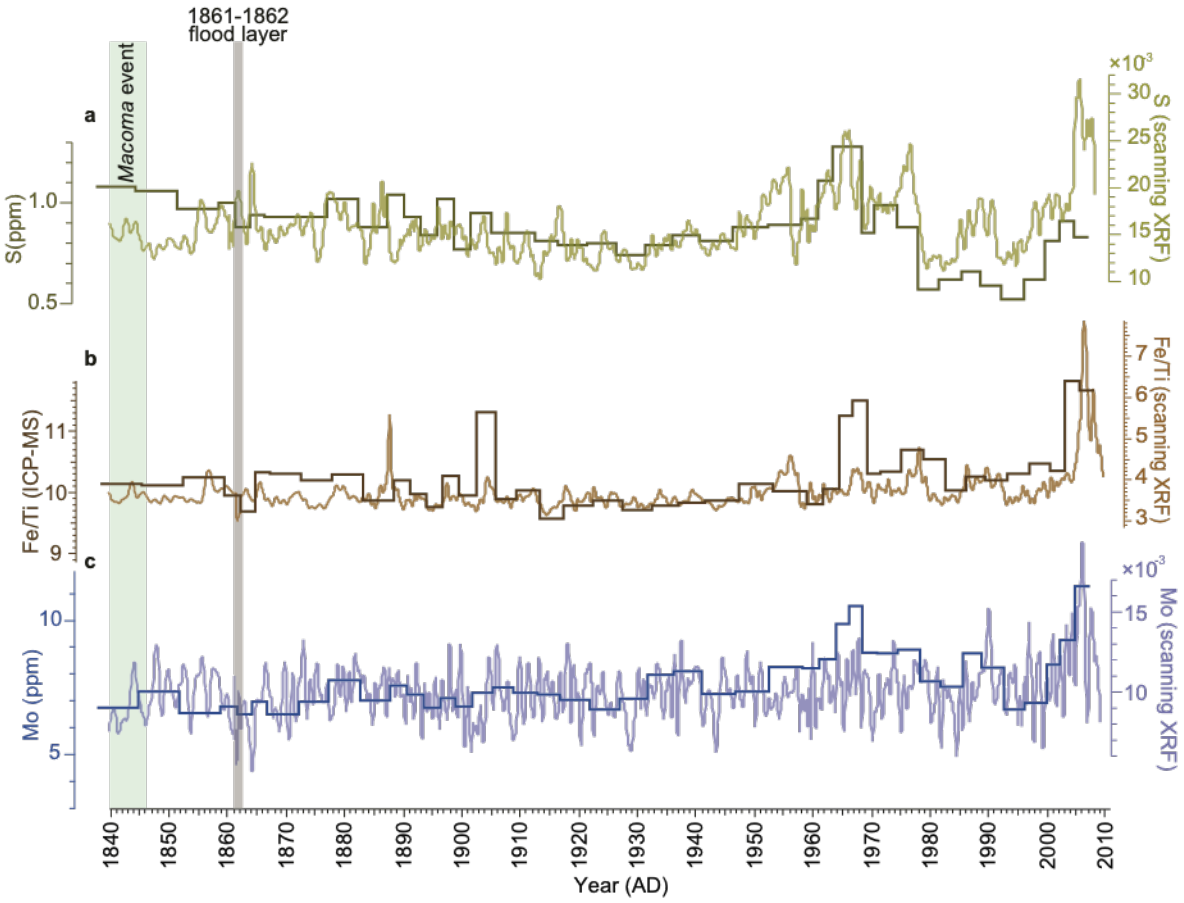

Figure B-1 Comparison between XRF data and bulk sediment elemental concentrations. (a) Sulfur concentration measured by ICP-MS/AES (ppm, thick green line) and the 20-point moving average of the normalized scanning XRF sulfur (thin green line); (b) ICP-MS/AES Fe/Ti (thick brown line) and 20-point moving average of normalized scanning XRF Fe (thin brown line); (c) ICP-MS/AES Mo (ppm, thick blue line) and the 20-pt moving average of normalized scanning XRF Mo (thin blue line); The *Macoma* bivalve layer and the flood layer are represented by green and gray shading, respectively.

B.2 Lithogenic sediment input to the Santa Barbara Basin

Lithogenic sediments in SBB are predominantly delivered by rivers, principally the Santa Clara River and to a lesser extent the Ventura River (Feleischer, 1972; Marsaglia et al., 1995). The Santa Ynez River does not discharge into the basin directly although some sediment is transported into the basin by longshore current and surface circulation (Feleischer, 1972); thus it is not considered as a major sediment source and we did not include Santa Ynez River in the background value (Marsaglia et al., 1995). The Channel Islands along the southern basin margin provide sediment via creeks draining into the basin, and therefore Santa Rosa Island samples are used to represent the Channel Islands background value (Fig. B-2).

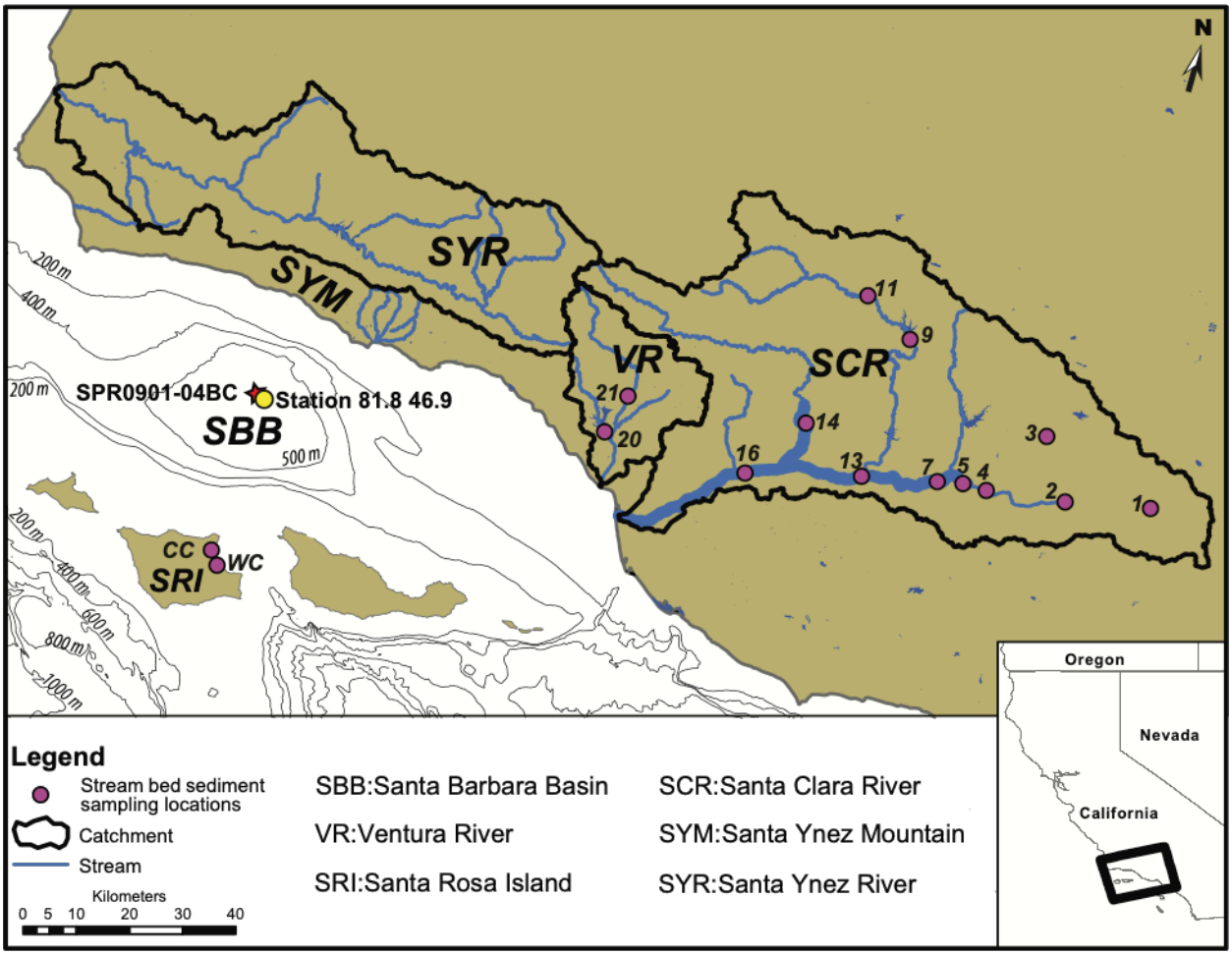

Figure B-2 Map of lithogenic background sampling locations and box core SPR0901-04BC (depicted by the red star). River catchments are outlined in black. Selected rivers are shown by blue lines; main stem of river indicated by thick blue line. Sample sites are shown in purple circles. Bathymetry is from Global Multi-Resolution Topography version 2.6 (Ryan et al., 2009).

All bedload samples were sieved at 63 μm to isolate fine-grained fraction (0 – 63 μm) then powdered for determination of elemental concentrations. This size fraction was used to represent the suspended load that could be deposited in SBB. Sample preparation and standard measurements followed the previously described core sample protocol for ICP-MS/AES analyses.

B.3 Teleconnection between ENSO perturbation and coastal OMZ in Southern California

Oceanic ENSO perturbations from the western tropical Pacific can propagate as equatorial Kelvin waves and move northward along the American coast as coastal trapped waves on the order of months (Frischknecht et al., 2015). Cross correlation between interpolated bottom water temperature and monthly Niño 3.4 anomalies is calculated using the following equation:

$$\rho_{XY}(\tau) = \frac{1}{\sigma_X \sigma_Y} E[(X_t - \mu_X)(Y_{t+\tau} - \mu_Y)] \qquad \text{(Eq. B-1)}$$

τ is the time lag between the two variables. σ and μ stand for standard deviation and mean value of the two variables, respectively.

As we expected positive correlation between Niño 3.4 anomalies and our bottom water temperature record, time lag for maximum cross-correlation coefficient is at ~2 – 3 months (Fig. B-3). Our results fall into the estimated time range (1 – 6 months) required for poleward propagation of the pycnocline depth anomalies into California Current System (CCS) (Chelton and Davis, 1982). Recent model studies also demonstrated 2 – 3 month lag between Ocean Niño Index (ONI) and the upwelling anomalies in the southern California Current System (e.g. depth of the 26.0 kg m^{-3} potential density surface) (Jacox et al., 2015). Therefore, we use a response time of 3 months to account for the longer lag experienced by subsurface upwelling source water as opposed to pycnocline depth anomalies (Jacox et al., 2015).

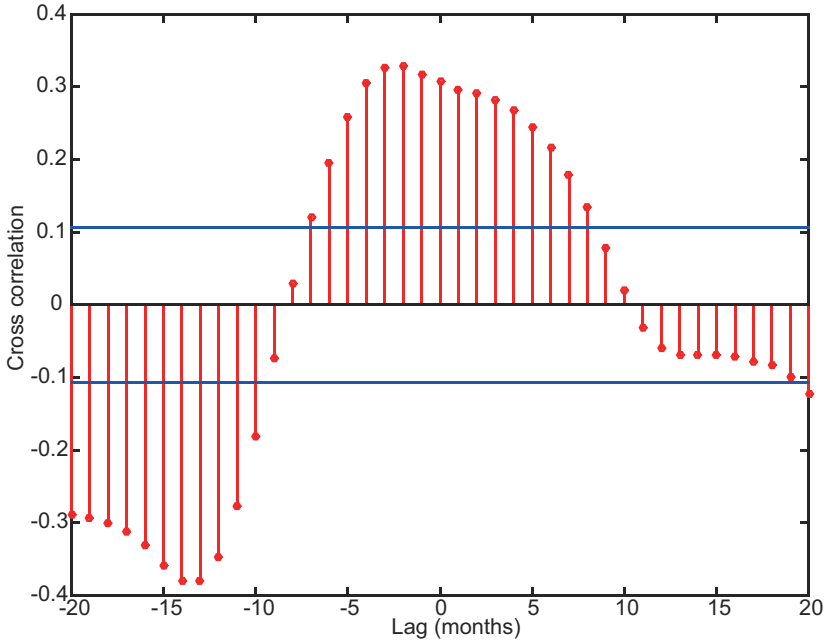

Figure B-3 Cross-correlation between Niño 3.4 anomalies and interpreted bottom water temperature. Negative lags indicate that Niño 3.4 anomalies precede temperature records. Blue lines represent 95% confidence bounds.

Table B-1 Duplicated standards analyzed by ICP-MS/AES and Elemental Analyzer for SPR0901-04BC sediment samples. Data are presented as mean ± 1 standard error.

Elements	GBM908-10 (n = 6)	MRGeo08 (n = 8)	Acetanilide(n = 15)	Atropine(n = 15)
Al (wt.%)	2.97±0.06	4.34±0.06	-	-
Mo (μg g^{-1})	64.15±1.93	14.23±0.20	-	-

Re (μg g^{-1})	0.0028±0.0004	0.0095±0.0004	-	-
U (μg g^{-1})	1.24±0.02	1.06±0.02	-	-
Fe (μg g^{-1})	5.64±0.05	3.98±0.07	-	-
Ti (μg g^{-1})	0.670±0.008	0.501±0.008	-	-
S (wt. %)	0.38±0.01	0.38±0.005		
C (wt. %)	-	-	71.34±0.10	71.25±0.10

Table B-2 Correlation between sediment core data from ICP-MS/AES and scanning XRF.

Elements	**Correlation coefficient**	**p-value (n = 61)**
Fe/Ti	0.6938	5.68×10^{-10}
Mo	0.5625	2.38×10^{-6}
S	0.2474	0.0546

Table B-3 Lithogenic background values for element enrichment factors.

Sediment Source	Sample Name	Location	Sample description	Al (%)	Mo (μg g^{-1})	Re (μg g^{-1})	U (μg g^{-1})
Santa Clara River (SCR)	Loc 1	Santa Clara River	< 63 μm	8.81	1.77	<0.002	1.40
	Loc 2	Santa Clara River	< 63 μm	9.31	8.47	<0.002	0.60
	Loc 3	Bouquet Canyon	< 63 μm	6.93	8.74	<0.002	6.00
	Loc 4	Discovery Park	Bulk	8.92	0.50	<0.002	0.50
	Loc 7	Off CA-126/Newhall Ranch Rd.	< 63 μm	8.07	3.97	<0.002	3.20
	Loc 9	Below Pyramid Lake	< 63 μm	8.5	8.57	0.002	5.30
	Loc 11	Piru Creek	Bulk	7.16	0.56	<0.002	1.00
	Loc 13	Torrey Rd. off CA-126	< 63 μm	8.25	4.96	0.007	3.50
	Loc 14	Sespe Creek	< 63 μm	8.22	5.45	0.011	4.60
	Loc 16	Ranch	< 63 μm	7.7	2.63	0.002	3.30
	Loc 16	Ranch	< 63 μm	8.09	3.35	<0.002	3.30
	Average background for SCR			8.20	4.79	0.005	2.91
Ventura River (VR)	Loc 20	Foster Park	< 63 μm	7.42	20.7	0.009	4.90
	Loc 21	Ventura River	< 63 μm	7.67	1.91	0.002	2.10
	Average background for VR			7.55	11.31	0.006	3.50
Santa Rosa Island (SRI)	CC1	Santa Rosa Island	< 63 μm	7.49	3.52	0.002	2.10
	WC1	Santa Rosa Island	< 63 μm	7.8	2.51	0.003	2.30
	Average background for SRI			7.65	3.02	0.002	2.20
Average background values for the Santa Barbara Basin*				8.07	4.98	0.004	2.84

***** The sediment flux contribution weights for Santa Clara River, Ventura River and the Channel Islands are 0.78, 0.07 and 0.15 (Warrick and Farnsworth, 2009).

B.4 References

Chelton, D.B., Davis, R.E., 1982. Monthly mean sea-level variability along the west coast of North America. Journal of Physical Oceanography, 12: 757-784.

Dickson, A.J., Cohen, A.S., Coe, A.L., 2012. Seawater oxygenation during the Paleocene-Eocene Thermal Maximum. Geology, 40(7): 639-642.

Feleischer, P., 1972. Mineralogy and Sedimentation history, Santa Barbara Basin, California. Journal of Sedimentary Petrology, 42(1): 49-58.

Frischknecht, M., Munnich, M., Gruber, N., 2015. Remote versus local influence of ENSO on the California Current System. Journal of Geophysical Research: Oceans, 120: 1353-1374.

Hennekam, R., de Lange, G., 2012. X-ray fluorescence core scanning of wet marine sediments: methods to improve quality and reproducibility of high-resolution paleoenvironmental records. Limnology and Oceanography: Methods, 10(12): 991-1003.

Jacox, M.G., Fiechter, J., Moore, A.M., Edwards, C.A., 2015. ENSO and the California Current coastal upwelling response. Journal of Geophysical Research: Oceans, 120: 1691-1702.

Marsaglia, K.M., Rimukus, K.C., Behl, R.J., 1995. Provenance of sand deposited in the Santa Barbara Basin at Site 893 during the last 155,000 years. In: Kennett, J.P., Baldauf, J.G., Lyle, M. (Eds.), Proceedings of the Ocean Drilling Program, Scientific Results.

Richter, T.O. et al., 2006. The Avaatech XRF core scanner: technical description and applications to NE Atlantic sediments. New techniques in sediment core analysis, 267: 39-50.

Ryan, W.B.F. et al., 2009. Global Multi-Resolution Topography synthesis. Geochemistry, Geophysics, Geosystems, 10(3): 1-9.

Tjallingii, R., Röhl, U., Kölling, M., Bickert, T., 2007. Influence of the water content on X-ray fluorescence core-scanning measurements in soft marine sediments. Geochemistry, Geophysics, Geosystems, 8(2): 1-12.

Warrick, J.A., Farnsworth, K.L., 2009. Sources of sediment to the coastal waters of the Southern California Bight. The Geological Society of America Special Paper, 454: 39-52.

Appendix C: Supplementary Information for Chapter 6

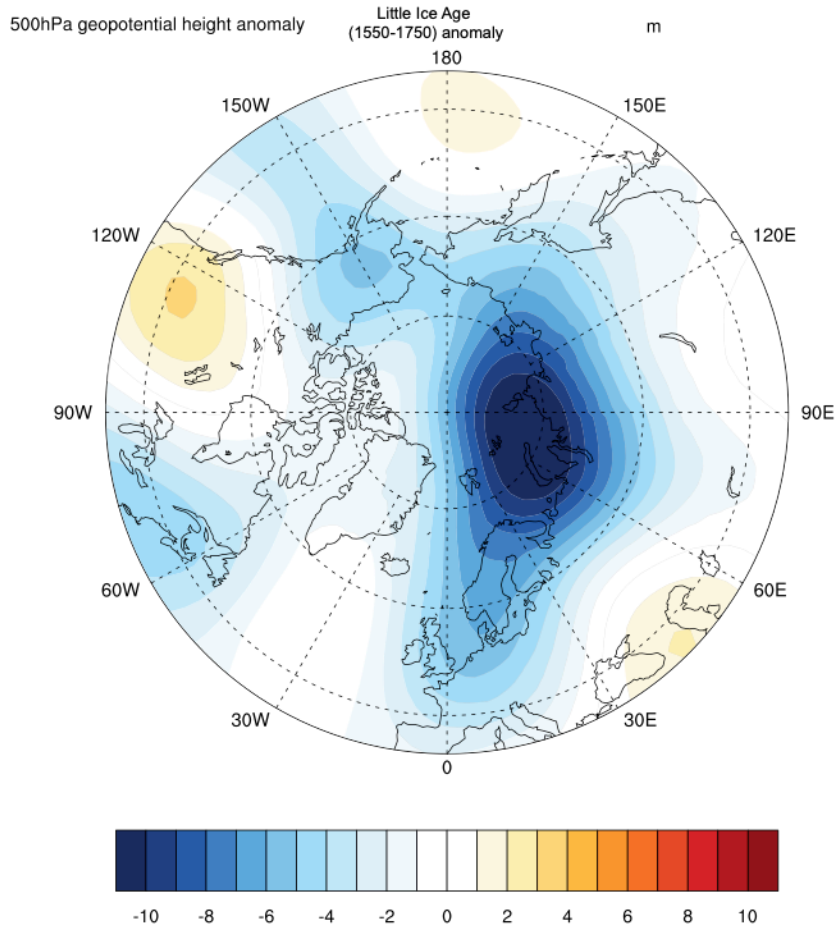

Figure C-1 500hPa geopotential height anomaly (m) of the late Little Ice Age (1550 – 1750 CE) with respect to the pre-1850 mean.

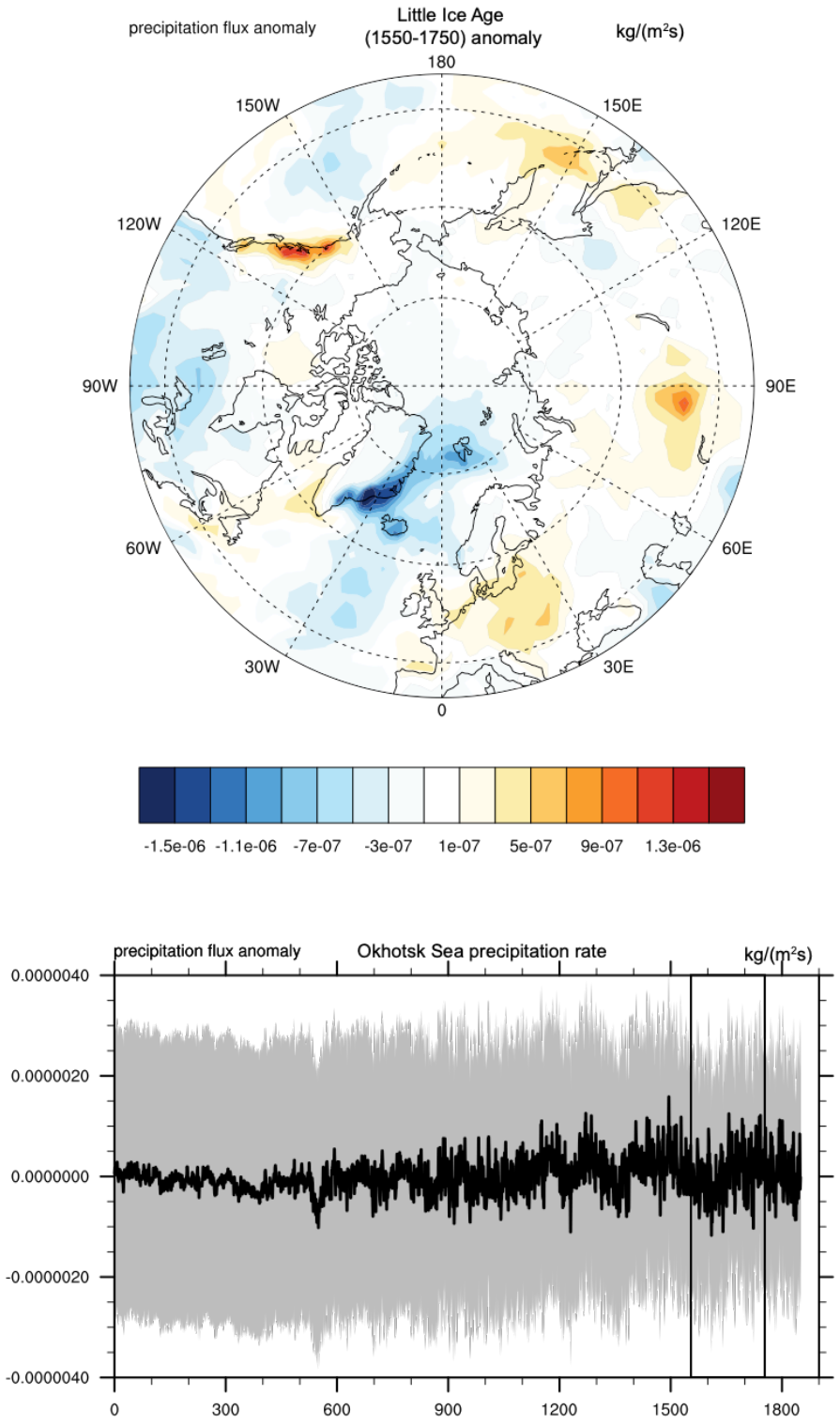

Figure C-2 Upper panel: Precipitation rate anomaly of the late Little Ice Age (1550 – 1750 CE) with respect to the pre-1850 mean. Lower panel: Area weighted precipitation rate anomaly time series over the Sea of Okhotsk (50 – 65°N, 135 – 170°E). The 1550 – 1750 CE interval is outlined in the black rectangle.

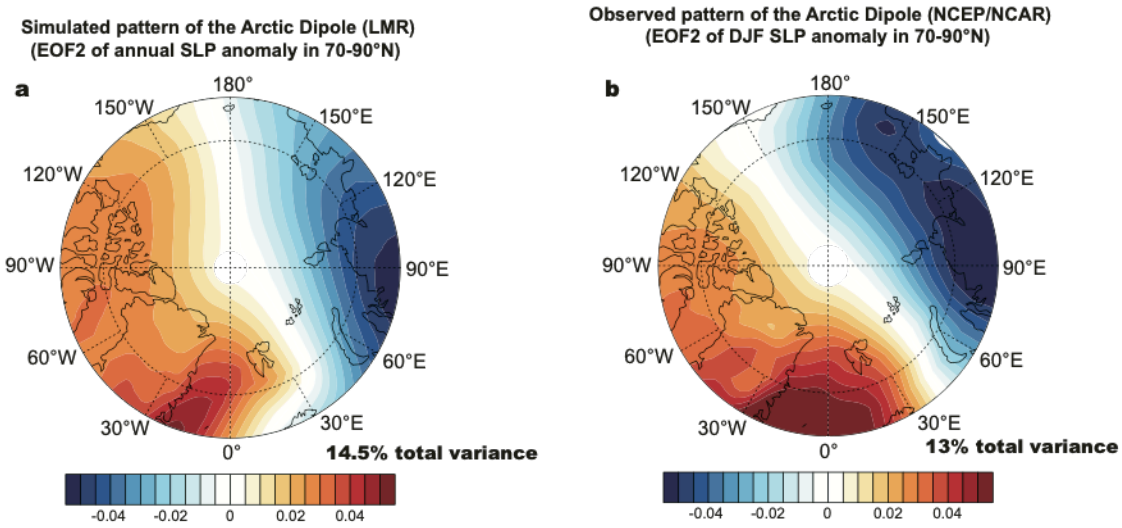

Figure C-3 Spatial patterns of simulated and observed Arctic Dipole. (a) Simulated positive AD pattern from the Last Millennium Reanalysis, as EOF2 of the annual sea level pressure (SLP) anomaly north of 70°N (14.5% of the total variance); (b) observed AO pattern from the NCEP/NCAR reanalysis from 1948 to present, as EOF2 of the December to February [DJF] SLP anomaly north of 70°N (13% of the total variance).

Appendix D: Supplementary Information for Chapter 7

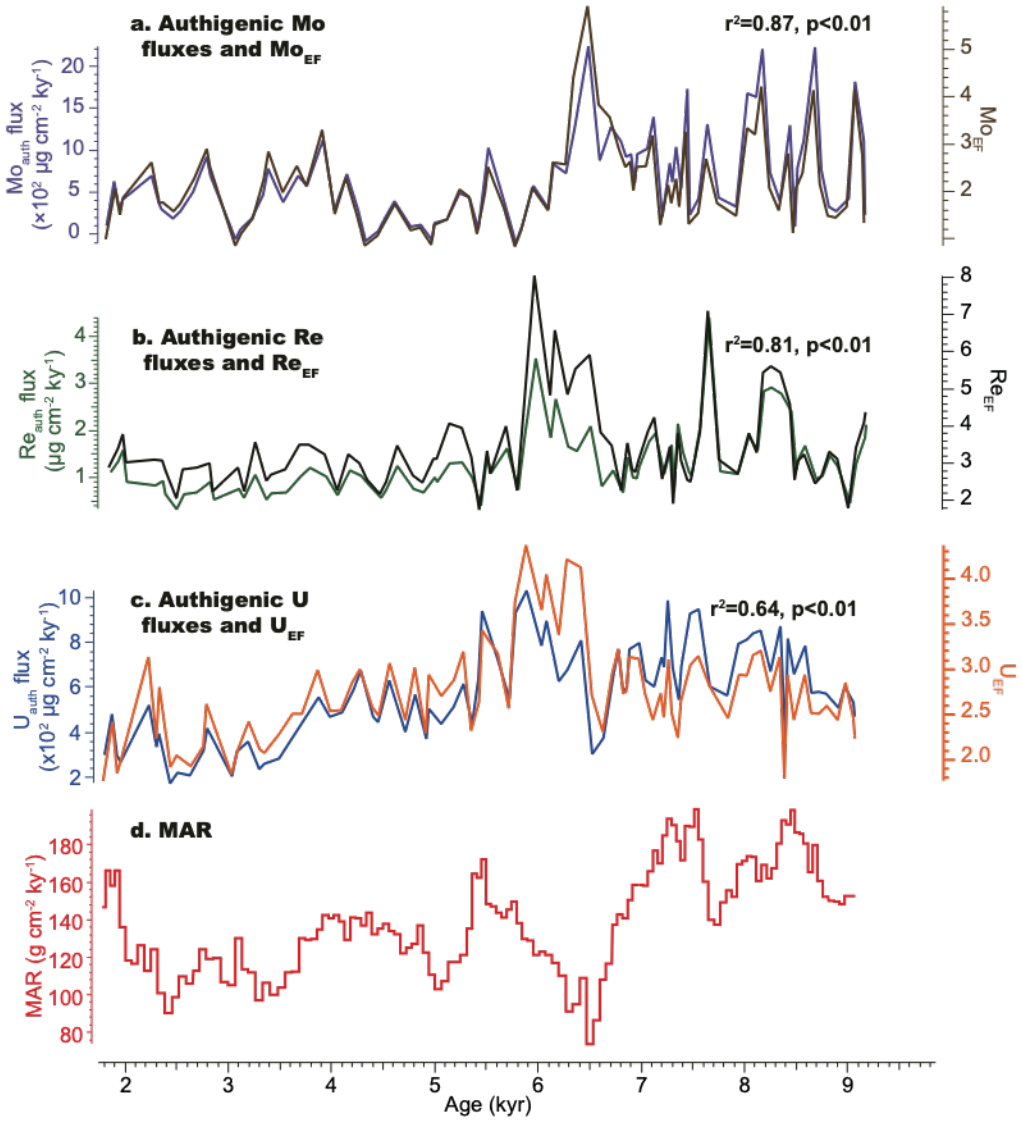

Figure D-1 Comparison of authigenic metal fluxes and metal enrichment factors ($Metal_{EF}$) under the influence of sedimentation rate changes. (a) Authigenic Mo fluxes (purple line) and Mo_{EF} (brown line); (b) authigenic Re fluxes (green line) and Re_{EF} (black line); (c) authigenic U fluxes (green line) and U_{EF} (orange line); (d) mass accumulation rates (MAR).

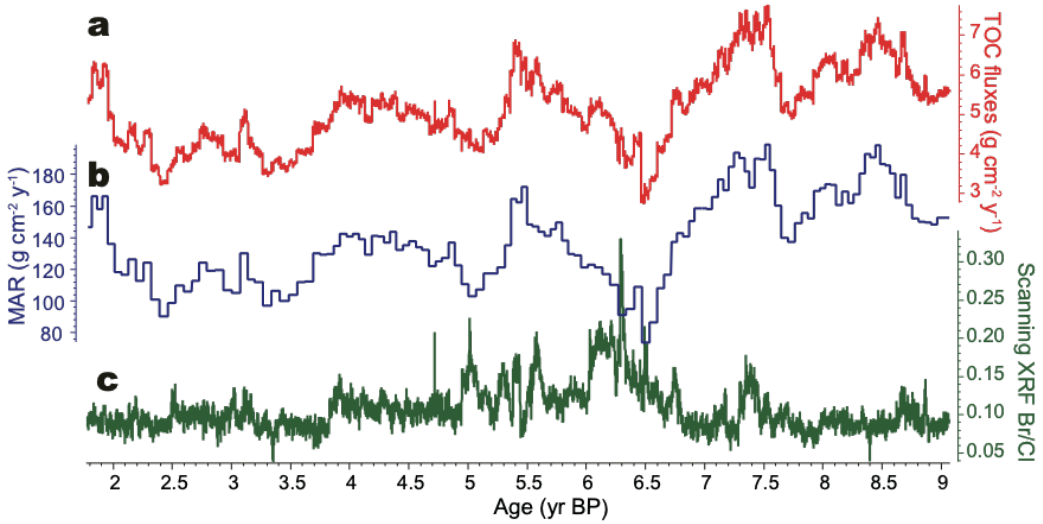

Figure D-2 Mass accumulation rates and TOC fluxes. (a) Calculated total organic carbon (TOC) fluxes (red line); (b) Mass accumulation rates (MAR) (blue line); (c) Scanning XRF Br/Cl (green line).

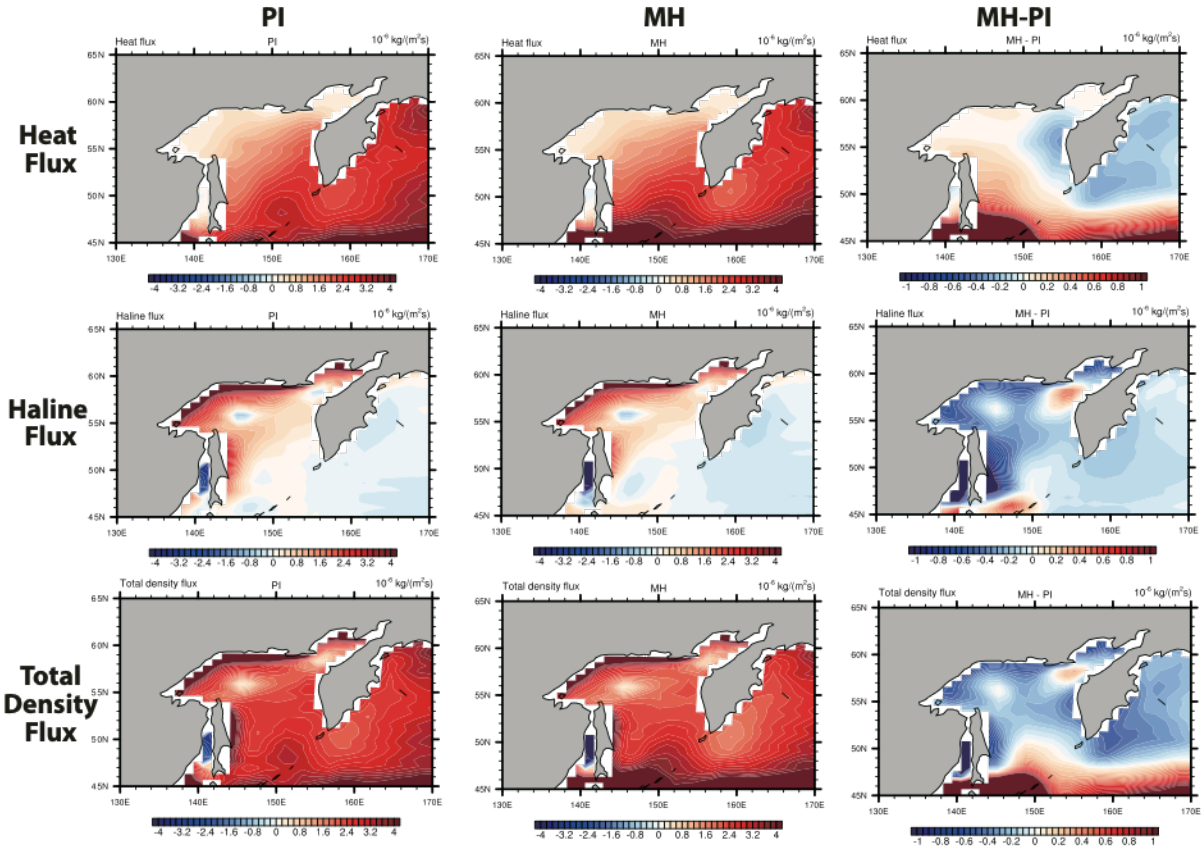

Figure D-3 Density flux decomposition in the region of 50 – 65°N and 135 – 170°E. Left column from top to bottom: heat fluxes (heat gain/loss), haline fluxes (precipitation, evaporation, and sea ice formation), and the total density fluxes for the Pre-industrial (PI) time slice. Middle column from top to bottom: heat fluxes, haline fluxes, and the total density fluxes for the mid-Holocene (MH, 6 ka) time slice. Right column from top to bottom: MH-PI difference of heat fluxes, haline fluxes, and the total density fluxes.

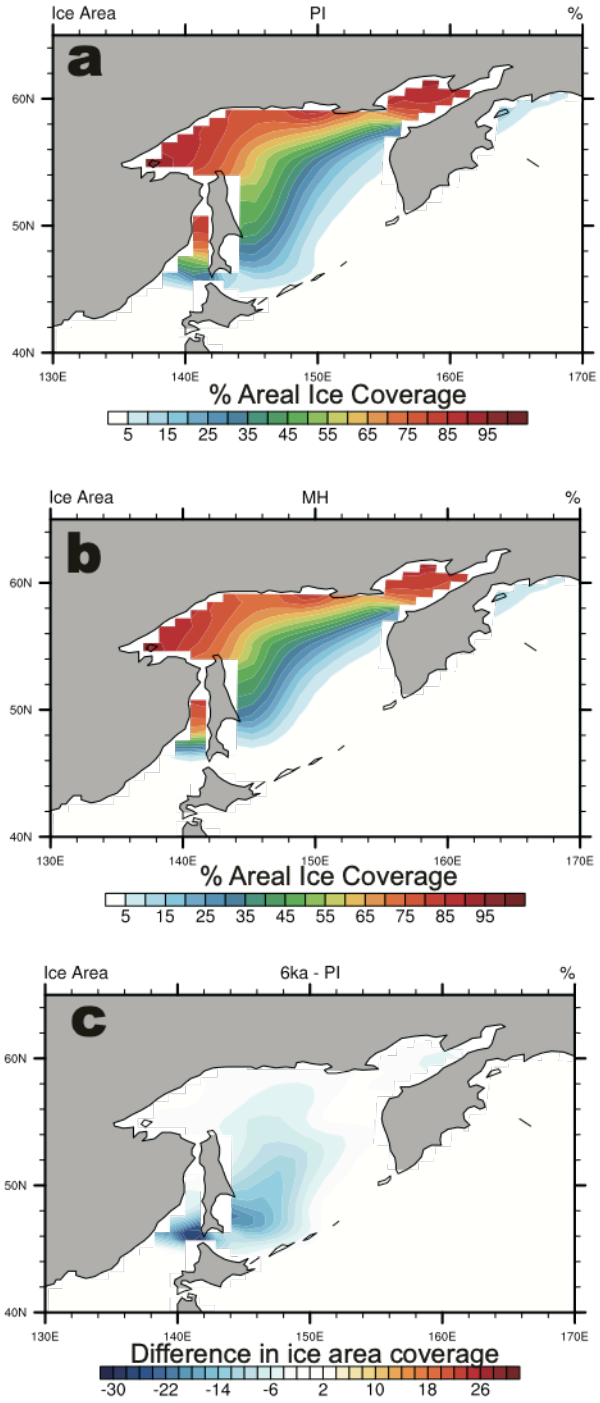

Figure D-4 CESM modeled ice area coverage (%) in the region of 50 – 65°N and 135 – 170°E. (a) Pre-Industrial (PI) time slice; (b) mid-Holocene (MH, 6 ka) time slice; (c) Difference of the ice area between MH and PI.

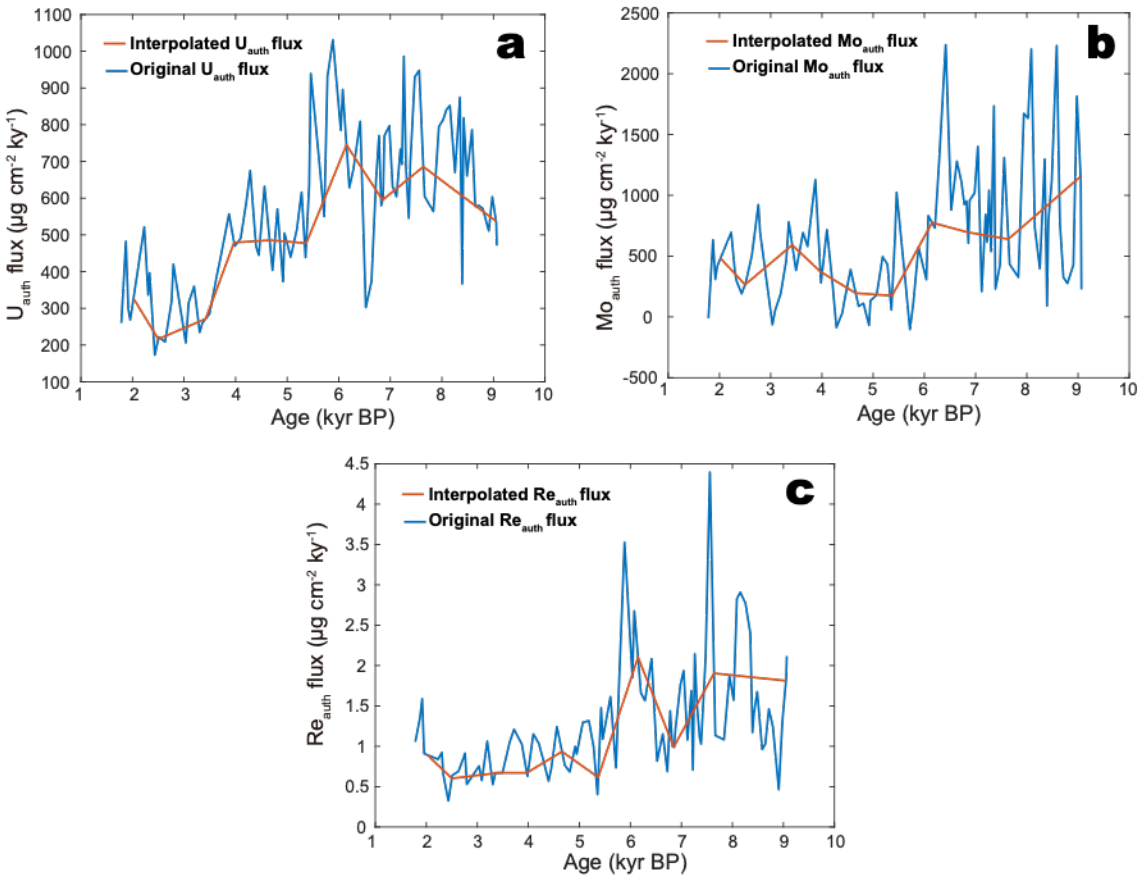

Figure D-5 Comparison of original (blue line) and interpolated (red) metal metal fluxes following the age model in Mix et al. (1991). (a), (b), and (c) show U, Mo, and Re authigenic fluxes, respectively.

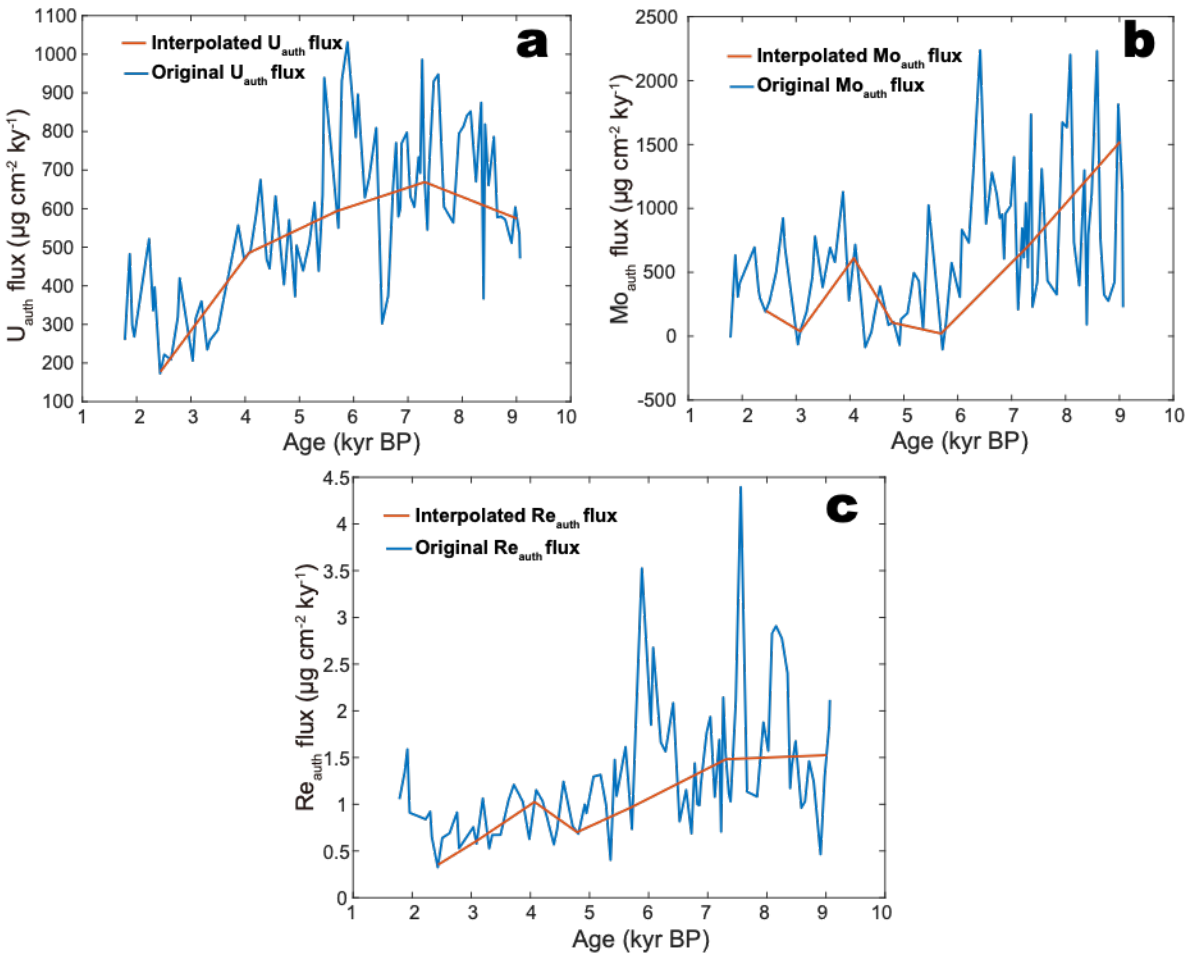

Figure D-6 Comparison of original (blue line) and interpolated (red) metal metal fluxes following the age model in Basak et al. (2010). (a), (b), and (c) show U, Mo, and Re authigenic fluxes, respectively.

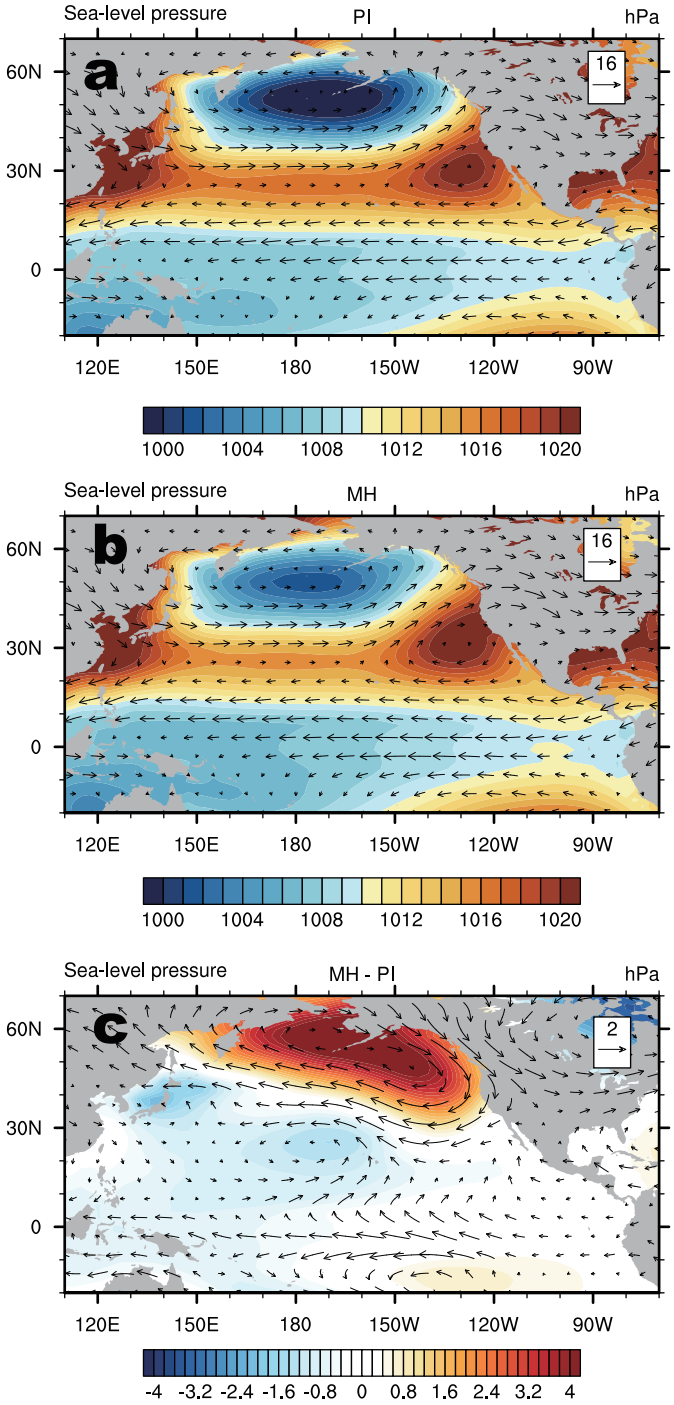

Figure D-7 CESM modeled sea-level pressure overlying with 850 hPa wind. (a) Pre-Industrial (PI) time slice; (b) Mid-Holocene (MH, 6 ka) time slice; (c) difference between MH and PI.

Table D-1 Southern California lithogenic background

Sediment Source	Sample Name	Location	Sample description	Al (%)	Mo (ppm)	Re (ppm)	U (ppm)	Ag (ppb)	Cd (ppm)	Cu (ppm)	Ni (ppm)	Pb (ppm)	Zn (ppm)	Mn (ppm)	Fe (%)
Santa Clara River	Loc 1	Santa Clara River	<63 µm	8.81	1.77	<0.002	1.40	150	0.12	133.5	35.5	20.3	173	1460	5.72
	Loc 2	Santa Clara River	<63 µm	9.31	8.47	<0.002	0.60	210	0.14	135.5	81.4	14.4	150	1060	5.44
	Loc 4	Discovery Park	Bulk	8.92	0.5	<0.002	0.50	30	0.02	6.4	7.6	7.6	51	1120	5.28
	Loc 3	Bouquet Canyon	<63 µm	6.93	8.74	<0.002	6.00	170	0.42	1440	149	97.1	277	2360	6.41
	Loc 5	Iron Hourse Trailhead	<63 µm	8.38	8.5	0.003	2.20	150	0.47	528	76.4	52.9	190	1080	5.12
	Loc 11	Piru Creek	Bulk	7.16	0.56	<0.002	1.00	30	0.03	3.1	3.5	16.3	35	363	1.48
	Loc 9	below Pyramid Lake	<63 µm	8.5	8.57	0.002	5.30	130	0.22	63.6	42.1	54.3	150	1060	5.2
	Loc 7	off CA-126/Newhall Ranch Rd.	<63 µm	8.07	3.97	<0.002	3.20	60	0.18	66.6	50.3	20	144	628	4.14
	Loc 13	Torrey Rd. off CA-126	<63 µm	8.25	4.96	0.007	3.50	240	1.02	298	49.7	42.3	223	1220	5.5
	Loc 14	Sespe Creek	<63 µm	8.22	5.45	0.011	4.60	90	0.45	47.4	44.1	19.2	118	545	3.89
	Loc 16	Ranch	<63 µm	7.7	2.63	0.002	3.30	70	1.02	27.6	29	18.5	96	824	3.79
	Loc 16	Ranch	<63 µm	8.09	3.35	<0.002	3.30	100	0.46	30.20	31.60	19.10	96.00	429	3.16
	Average			8.20	4.79	0.0050	2.91	119	0.38	231.66	50.02	31.83	141.9	1012.4	4.59
Ventura River	Loc 21	Ventura River	<63 µm	7.67	1.91	0.002	2.10	120	0.19	41.4	115.5	16.3	108	708	4.00
	Loc 20	Foster Park	<63 µm	7.42	20.7	0.009	4.90	190	1.60	99.80	136	18.6	179	507	4.29
	Average			7.55	11.31	0.0055	3.50	155	0.90	70.60	125.8	17.45	143.5	607.50	4.15
Santa Rosa Island	CC1	Santa Rosa Island	<63 µm	7.49	3.52	0.002	2.10	190	0.66	179.5	66	11.5	138	538	3.67
	WC1	Santa Rosa Island	<63 µm	7.8	2.51	0.003	2.30	160	0.87	113.00	53.20	11.40	180.0	393	3.44
	Average			7.65	3.02	0.0025	2.20	175	0.77	146.25	59.60	11.45	159.00	465.50	3.56
Santa Ynez River	Loc 24	Sage Hill Campground	<63 µm	7.21	6.47	0.003	3.4	180	1.55		71.9	10.4	127	566	4.26
	Loc 24 #2	Sage Hill Campground	<63 µm	6.7	9.1	0.004	4.5	360	3.42		87.9	17.6	136	713	3.52
	Loc 28	Ave. of Flags	<63 µm	6.14	3.47	0.002	3	310	1.68		210	27.6	103	688	3.53
	Loc 30	Riverbend Park	<63 µm	7.13	4.85	0.002	4	230	2.06		42.5	25.3	96	331	2.29
	Average			6.80	5.972	0.0027	3.72	270	2.178		103.1	20.22	115.5	574.5	3.4

Table D-2 Authigenic trace metal fluxes and enrichment factors

Authigenic Mo flux ($\mu g\ cm^{-2}\ kyr^{-1}$)	Authigenic Re flux ($\mu g\ cm^{-2}\ kyr^{-1}$)	Authigenic U flux ($\mu g\ cm^{-2}\ kyr^{-1}$)	Re_{EF}	Mo_{EF}	U_{EF}
-11.88	1.05	259.96	2.89	0.98	1.76
633.30	1.34	482.10	3.41	2.06	2.42
308.45	1.59	298.29	3.78	1.50	1.85
418.08	0.91	268.49	3.02	1.86	1.97
694.80	0.84	521.30	3.10	2.62	3.13
359.33	0.92	336.37	3.07	1.75	2.24
296.89	0.65	396.38	2.81	1.77	2.80
191.57	0.32	173.08	2.05	1.58	1.92
274.91	0.64	221.97	2.85	1.74	2.05
504.28	0.69	208.68	2.87	2.28	1.93
923.14	0.91	318.69	3.01	2.89	2.15
695.64	0.53	419.75	2.24	2.52	2.61
-63.70	0.75	206.20	2.88	0.85	1.84
54.89	0.58	314.89	2.24	1.11	2.11
190.20	1.06	359.85	3.57	1.43	2.42
463.15	0.53	234.81	2.53	2.25	2.11
780.10	0.67	259.47	2.70	2.85	2.08
383.38	0.67	284.77	2.83	1.97	2.27
692.50	1.04	385.22	3.49	2.54	2.50
579.97	1.21	446.41	3.50	2.12	2.51
1128.08	1.03	556.74	3.24	3.29	2.99
279.75	0.63	469.39	2.26	1.52	2.54
715.87	1.15	490.21	3.23	2.29	2.55
283.23	1.04	586.68	2.99	1.51	2.85
-86.72	0.85	674.59	2.55	0.85	3.00
31.99	0.57	468.30	2.17	1.06	2.57
159.14	0.73	444.85	2.50	1.30	2.49
388.94	1.24	631.99	3.48	1.72	3.07
87.19	0.76	403.53	2.67	1.18	2.44
111.24	0.68	570.35	2.48	1.22	3.02
-68.57	1.00	372.75	3.12	0.86	2.29
133.16	0.90	504.50	3.13	1.29	2.94
181.18	1.30	439.67	4.07	1.40	2.70
495.19	1.32	513.83	3.94	2.03	2.88
430.88	1.00	615.95	3.17	1.88	3.20
57.68	0.40	438.86	1.75	1.10	2.32
651.74	1.48	634.50	3.33	1.96	2.64
1024.21	1.09	939.00	2.73	2.51	3.43
374.92	1.61	717.60	3.99	1.65	3.17
-103.47	0.73	550.28	2.28	0.83	2.57
104.31	1.84	931.83	4.31	1.18	3.75
572.97	3.52	1031.23	8.05	2.07	4.37
306.58	1.85	785.02	4.83	1.59	3.66
831.77	2.68	895.80	6.57	2.61	4.05
732.12	1.66	628.65	4.84	2.58	3.38
1262.17	1.57	680.26	5.52	4.40	4.21
2237.26	2.08	808.97	5.92	5.92	4.12
880.25	0.82	302.35	3.82	3.84	2.71
1279.96	1.15	373.14	3.47	3.56	2.31
1107.20	0.69	653.27	2.26	2.89	2.95
923.96	1.44	770.16	3.54	2.52	3.23
952.88	1.00	579.64	2.83	2.62	2.73
606.62	0.99	600.36	2.77	2.01	2.76
956.78	1.22	769.22	3.07	2.52	3.14
1020.02	1.76	797.13	3.86	2.54	3.11
1400.33	1.93	631.73	4.24	3.18	2.73
209.50	1.08	604.29	2.57	1.28	2.44
844.29	1.69	733.10	3.45	2.14	2.74

615.07	0.71	692.38	1.92	1.74	2.47
1041.17	2.14	985.88	3.80	2.27	3.10
538.87	1.54	688.97	3.08	1.68	2.52
1734.37	1.10	545.34	2.55	3.26	2.25
230.50	1.03	695.37	2.50	1.31	2.66
422.89	2.10	930.01	3.84	1.53	3.05
1309.02	4.39	947.68	7.10	2.69	3.15
433.16	1.13	604.62	3.09	1.74	2.82
326.70	1.08	563.85	2.71	1.48	2.46
1673.14	1.88	794.95	3.80	3.33	2.94
1634.39	1.57	813.43	3.28	3.21	2.93
2201.98	2.83	840.98	5.44	4.22	3.16
735.51	2.91	851.99	5.60	2.08	3.21
396.88	2.77	670.23	5.45	1.59	2.76
1297.58	2.40	874.36	4.60	2.81	3.14
91.64	1.17	367.00	2.55	1.11	1.80
795.41	1.41	818.52	3.04	2.07	2.94
1116.41	1.68	660.63	3.23	2.39	2.44
2230.69	0.96	786.04	2.45	4.14	2.94
769.15	1.03	577.52	2.65	2.15	2.52
324.22	1.46	579.81	3.32	1.48	2.50
275.99	1.24	571.76	3.13	1.44	2.60
425.99	0.46	510.93	1.80	1.68	2.44
1813.00	1.30	603.69	3.43	4.17	2.85
1118.59	1.84	533.59	4.08	2.74	2.46
225.89	2.12	470.74	4.38	1.34	2.23

Table D-3 ODP Hole 1017E redox-sensitive metal enrichment factors

Age (yr BP)	Re_{EF}	U_{EF}	Mo_{EF}
0	3.89	0.66	0.26
134	5.33	0.77	0.26
269			
403	5.88	0.73	0.24
538	5.67	0.83	0.23
672	5.16	0.84	0.29
807	5.54	0.77	0.26
941	6.36	0.87	0.24
1075	5.77	1.01	0.28
1210	5.78	0.83	0.26
1344	7.46	1.17	0.32
1479	6.52	0.91	0.26
1568	8.31	1.05	0.26
1703	10.11	1.37	0.31
1837	9.55	1.45	0.36
1972	8.93	1.47	0.35
2106	7.54	1.31	0.28
2240	10.64	1.18	0.30
2375	9.66	1.19	0.31
2509	6.80	1.14	0.29
2599	8.16	1.21	0.36
2733	8.17	1.10	0.29
2868	6.27	1.13	0.37
3002	6.71	1.09	0.34
3137	6.78	1.11	0.34
3271	7.04	1.26	0.39
3406	6.57	1.05	0.41
3540	6.84	1.27	0.39
3630	7.24	1.20	0.42
3764	8.31	1.18	0.43
3898	9.79	1.23	0.45

4033	7.09	1.27	0.41
4167	7.28	1.12	0.44
4302	7.40	1.28	0.54
4436	7.07	1.27	0.60
4571	8.26	1.02	0.43
4660	7.47	1.43	0.58
4795	9.30	1.43	0.58
4929	9.67	1.15	0.50
5063	10.05	1.29	0.61
5198	7.56	1.13	0.47
5332	7.67	1.38	0.61
5467	8.29	1.13	0.52
5601	7.01	1.38	0.65
5691	9.77	1.29	0.82
5825	8.50	1.40	0.76
5960	6.91	1.22	0.58
6094	7.81	1.35	0.67
6228	7.48	1.22	0.80
6363	7.69	1.32	0.85
6497	8.18	1.22	0.70
6632	6.76	1.24	0.60
6721	6.90	1.15	0.53
6856	7.86	1.17	0.54
6990	8.34	1.31	0.55
7125	7.11	1.35	0.62
7259	6.15	1.04	0.46
7394	5.00	0.95	0.44
7528	5.02	1.07	0.52
7662	4.73	0.83	0.39
7752	5.54	0.96	0.43
7886	6.66	0.99	0.47
8021	6.44	1.01	0.47
8155	6.61	0.98	0.44
8290	5.45	0.93	0.41
8424	5.01	0.86	0.44
8559	5.14	0.96	0.45
8693	5.06	0.95	0.49
8783	4.94	0.97	0.53
8922	6.70	1.00	0.53
9062	7.17	0.90	0.38
9196	6.57	1.08	0.39
9374	7.40	1.09	0.32
9552	9.44	1.35	0.32
9730	8.63	1.29	0.27
9908	9.22	1.57	0.32
10027	8.71	1.20	0.24
10205	10.30	1.39	0.30
10383	7.52	1.19	0.22
10562	4.78	0.97	0.25
10740	4.51	0.93	0.21
10918	3.26	0.70	0.14
11096	3.64	0.78	0.16
11274	3.35	0.73	0.15
11393	3.37	0.73	0.15
11571	3.65	0.63	0.12
11749	4.81	0.89	0.16
11928	3.94	0.83	0.16